Merging microfluidics and micro-array concepts: from molecular to nematode-based bioassays

THÈSE N^{O} 6808 (2015)

PRÉSENTÉE LE 20 NOVEMBRE 2015

À LA FACULTÉ DES SCIENCES ET TECHNIQUES DE L'INGÉNIEUR

LABORATOIRE DE MICROSYSTÈMES 2

PROGRAMME DOCTORAL EN MICROSYSTÈMES ET MICROÉLECTRONIQUE

ÉCOLE POLYTECHNIQUE FÉDÉRALE DE LAUSANNE

POUR L'OBTENTION DU GRADE DE DOCTEUR ÈS SCIENCES

PAR

Matteo CORNAGLIA

acceptée sur proposition du jury:

Dr G. Boero, président du jury
Prof. M. Gijs, Dr T. Lehnert, directeurs de thèse
Prof. M. F. Yanik, rapporteur
Prof. J. Korvink, rapporteur
Prof. Ph. Renaud, rapporteur

ÉCOLE POLYTECHNIQUE
FÉDÉRALE DE LAUSANNE

Suisse
2015

Simplicity is the ultimate sophistication.

Leonardo da Vinci

Acknowledgements

First and foremost, I would like to express my gratitude to my advisor Prof. Dr. Martin Gijs, who gave me the opportunity to conduct research in his group. Through these years, I sincerely admired so many unique aspects of his guidance: the simplicity at which he looks at things, combined with his talent for immediately seeing the big picture; his kind yet determined leadership, together with his wide interdisciplinary competence and open-minded attitude in facing problems within many different scientific fields. I am very thankful to Martin for his constant support, but also for the large amount of freedom he allowed me to take in the framework of the various research projects I got involved in. I would also like to thank my co-advisor Dr. Thomas Lehnert, who was always available for any question or suggestion, both theoretical and practical, both in good and in bad times. Besides my advisors, I would like to thank the other members of my thesis committee: Prof. Dr. Jan G. Korvink, Prof. Dr. Philippe Renaud, Prof. Dr. Mehmet Fatih Yanik, and Dr. Giovanni Boero, for their insightful comments and genuine interest in my work, which resulted in a fruitful and pleasant scientific discussion. I thank moreover the European Union's FP7 funding programme, Marie Curie actions, and the European Research Council for the generous financial support of my research. My sincere thanks goes then to Prof. Dr. Johan Auwerx, for having generated the research collaboration which actually made most of this thesis possible, for his immense knowledge in the biomedical field and for his visionary attitude, which makes him a pacesetter in research and a great motivator. I am deeply thankful to my closest collaborator throughout these years, Dr. Laurent Mouchiroud, who introduced me to the world of *C. elegans*, and, since then, has always been my guru in the field. Thanks, Laurent, for getting more and more involved in my research, for strongly believing in the potential of our findings and, now, for pushing towards the next phase of our common project.

I am tremendously thankful, then, to all the people at LMIS2 who I had the great chance to work with. Cumhur, for being my first guide to the lab and making me active part of his “on-chip immunoassay” project. Hui, for the incredible kindness, competence and enthusiasm she always put in our collaborations and endless talks about photonics. Raphael, for his infinite patience and invaluable contribute to the “bead-scanning” project, but also for always having the right answer to any question I could imagine in any field. Cristina, Li, and Gergely for brilliantly taking over part of my research. All the master and semester students I had the pleasure to supervise during these years and from which I learned a lot as well: Gopal, Daniel, Alexis, Federico, Chiara, Dimitry, Edoardo, Shreya, and Marie-Pierre. Special thanks to Melis and Sylvie for our nice chats and for their so prompt and efficient help, whatever I needed. Finally, thanks to all my other present and former colleagues at LMIS2 and to all the past and present members of our LMIS2&4 lunch&sat-group: Rima, Diego, Pierre, Fabien, Guillaume, Stefano, Amélie, Elodie, Niccolò, Robert, Jagoda, Sophie, Sebastian, Bilge, Nader, Josias, Thomas, Tuan, Roger, Xiaopeng,… Thanks to the Lunaphore team,

in particular to Tuna, for many nice chats and for his always enlightening pieces of advice, to Déborah, for keeping answering with a smile my (many) business questions, to Pierre, for the great time spent together both at EPFL and outside (e.g. in Valais!), to Saska, simply for being the kindest office-mate ever. My gratitude also goes to the ATPR and CMi staff, for their contributes at the creation of my experimental setups and their help with the microfabrication processes, respectively. I am very thankful to Prof. Dr. Jeroen Lammertyn, head of the MeBioS-Biosensor group at KU Leuven and coordinator of the "BioMax" European project, which I had honor to be part of. I am really glad I had such a great opportunity to collaborate within a corsortium of world-class academic and industrial partners, to visit personally most of them and to become part of such a wide network of amazing people. Thanks to all the PIs of the consortium for their extremely valuable advice, coming from many different backgrounds and fields of expertise. And a huge thanks to all of you, "BioMax fellas" – Elena, Delfina, Fabiola, Iulia, Soledad, Tonge, Tamara, Malte, Stefano, Rory, Bedabrata, and Deniz – for the great time we had together. Thanks to all the people of the MeBioS group, for having "adopted" me as a visiting student for about four months: again Jeroen, Elena, Iulia and Tamara, and then Daan, Kim, Phalguni, Bert, Karen, Karel, Kris, Deborah, Bram, Federica, Dragana, Filip, Carlo, Steven, Evgeny, Nicolas, … you guys really made me feel like home during my whole stay in Leuven! And a special thanks to Malte for having shared with me his flat, scientific ideas, philosophical thoughts and many adventures during that period, as well as an on-going attempt of first purely Skype-based scientific collaboration.

Last but not least, an immense thank you to all my friends in Lausanne (and, some others, around the world), for all the incredible experiences we shared throughout these years. To Diego, who could have fit in any paragraph of these acknowledgements, having him been my office-and-flatmate for years and becoming close to a brother. To all "Les Amis" – Antonio, Lucian, Pietro, Hélène and Andrea – for really being like a family in these years and, then, to all our friends who extended this family: Sergio, Ombretta, Mario, Alessandra, Rima, Aldo, Cristina, Giovanna, Mariana, Patrizia, Ferdinando, Carla, Camilla, Andrea, Nicole,… for the countless unforgettable moments we spent together. I owe then a very special thank you to my childhood friends Gianluca, Marco, Alessio, Marcello, for always making me feel as I never left Bra every time I get back there.

Finally, my deepest gratitude goes to my parents and to my girlfriend, for their constant support, guidance, and unconditional love. Thank you mum and dad, Angela and Riccardo, for taking care of me throughout all these years and always believing so much in me. Thanks so much for having taught me and showed me the inestimable value of things such as fairness, integrity, responsibility, hard-work and faith. Thanks for having taught me to always care about human empathy and to always think critically. And then thanks to you, Bea, for believing so much in me and in us, in spite of any obstacle and of any distance. You taught me how to look at the world in a very different way, so bright and colorful and full of life; you showed me that everything has so many more facets than I thought. Thanks for being my girlfriend and best friend and love. Thank you.

Matteo Cornaglia

Lausanne, October 14th 2015

Abstract

Essential in biomedical research is the necessity of gathering statistically relevant data about large populations of specific biological entities – e.g. organisms, cells or molecules – while preserving detailed information about each single entity under investigation. This thesis deals with this need and proposes the combination of microfluidics and "micro-arraying" techniques in developing technological tools to conceive bio-assays at single molecule/cell/organism resolution.

First, we propose an on-chip immunoassay technique, through which we demonstrated detection of the biomarker tumor necrosis factor α in serum down to concentrations in the attomolar range (10^{-18} M). In particular, we provide a comprehensive predictive model of the assay, which employs micro-arrays of superparamagnetic beads. We introduce the concept of "magnetic particle-scanning", as a method for building immunoassays with extremely low limit of detection, down to the single-molecule level. Afterwards, we modified our bead micro-arraying technique, to make it suitable for the immobilization of particles and cells of various sizes and properties. Specifically, we present a method for the electrostatic self-assembly of dielectric microspheres in well templates, as a technique for fast and versatile fabrication of microlens arrays. By combining these arrays with microfluidics, we created a new tool for single-nanoparticle detection in flowing media, able to detect moving objects of sub-diffraction size through conventional low-magnification microscopes. An analogous micro-arraying method was then developed to seed large populations of non-adherent cells in isolated micro-compartments. In combination with an electrowetting-on-dielectric microfluidic platform, this technique allows implementing high-throughput cytotoxicity assays on yeast cells, at single-cell resolution.

Subsequently, we conceived technological solutions for the automated analysis of *Caenorhabditis elegans*, one of the most employed model organisms in biomedical research. First, we developed a microfluidic platform for on-chip nematode culture and creation of synchronized *C. elegans* embryo micro-arrays. Long-term multi-dimensional imaging in our device allows systematic phenotyping studies at single-embryo resolution. We could discriminate embryonic development variations with unprecedented accuracy and we successfully analyzed the impact of perturbations of the mitochondrial functions on the embryogenesis. A "second generation prototype" of the device is then presented, enabling long-term automated studies on *C. elegans* at single-nematode resolution and over the whole organism development, from early embryogenesis to adulthood. Finally, we introduce a "third generation prototype", which features: (i) a new microfluidic design tailored for the isolation of larvae at a desired developmental stage and for their successive culture and treatment; (ii) a method for reversible immobilization of nematodes, enabling long-term high-resolution imaging. We successfully employed this platform to analyze protein aggregation in a *C. elegans* model for human amyotrophic lateral sclerosis (ALS). The device allows precisely localizing

protein aggregates within the nematodes' tissues, as well as monitoring the evolution of single aggregates over consecutive days at sub-cellular level.

Keywords

Microfluidics, micro-array, protein detection, superparamagnetic bead, magnetic particle-scanning, electrostatic self-assembly, lens array, nanoparticle detection, yeast, single-cell, *Caenorhabditis elegans*, on-chip worm culture, multi-dimensional imaging, *C. elegans* embryo, reversible worm immobilization, long-term high-resolution imaging, neurodegenerative disease, protein aggregation, phenotyping.

Résumé

Dans le domaine de la recherche biomédicale, il est essentiel de pouvoir obtenir des données statistiques relatives à de larges populations d'entités biologiques – comme des cellules ou des molécules – tout en préservant les informations détaillées qui concernent les entités individuelles considérées. Ce travail de thèse traite de cette thématique en combinant l'utilisation des techniques de microfluidique et de mise en micro-matrice pour la réalisation de tests biologiques au niveau d'entités individuelles.

Nous avons ainsi pu établir un test immunologique sur puce, capable de détecter le facteur de nécrose tumorale α dans le sérum à des concentrations de l'ordre de l'attomolaire (10^{-18} M). Nous avons développé un modèle prédictif complet de cette technique basé sur l'exploitation de matrices de microparticules superparamagnétiques. Nous avons par la suite introduit le concept de "scansion de particules magnétiques" comme nouvelle méthode afin de créer des tests immunologiques aux limites de détection très basses, atteignant le niveau de la molécule unique. En outre, la technique de mise en micro-matrice de particules magnétiques a été adaptée à l'immobilisation de particules et cellules de tailles et propriétés différentes. Nous avons en effet développé une méthode d'auto-assemblage électrostatique de microsphères diélectriques dans des puits pour la production de matrices de microlentilles. En introduisant ces matrices dans un système microfluidique, nous avons pu créer un nouvel outil pour la détection de nanoparticules en flux. Ce système a permis d'identifier des objets en mouvement de taille inférieure à la limite de diffraction de la lumière, tout en utilisant des microscopes conventionnels à faible grossissement. Par la suite, nous avons établis une méthode pour distribuer dans des puits séparés des populations de cellules non adhérentes. Cette technique a été utilisée avec un dispositif microfluidique « electrowetting sur diélectrique » pour réaliser des tests de cytotoxicité sur des cellules de levure au niveau de la cellule individuelle.

Une seconde partie de ce travail de thèse a permis de concevoir des technologies dédiées à l'analyse automatisée du nématode *Caenorhabditis elegans*, un organisme modèle très utilisé en recherche biomédicale. Nous avons développé un dispositif microfluidique pour l'élevage de nématodes sur puce et la mise en micro-matrice d'embryons de *C. elegans*. À l'aide d'un processus d'imagerie multidimensionnelle, ce dispositif a permis l'analyse systématique de phénotypes chez l'embryon individuel, en particulier l'impact des perturbations des fonctions mitochondriales sur l'embryogenèse. Nous avons ensuite dessiné un second prototype, conçu pour l'analyse automatisée du développement de nématodes isolés, depuis l'embryogenèse jusqu'au stade adulte. Enfin, nous avons introduit un troisième prototype, qui se caractérise par: (i) une nouvelle architecture fluidique, conçue pour sélectionner des larves de taille spécifique, les élever et les traiter sur puce; (ii) une méthode d'immobilisation réversible des nématodes, permettant de les observer à

haute résolution et à long terme. Nous avons utilisé cette plateforme pour analyser l'agrégation de protéines chez un modèle *C. elegans* de sclérose latérale amyotrophique (SLA) humaine. Nous avons ainsi pu localiser précisément des agrégats spécifiques dans les nématodes et suivre leur évolution à un niveau subcellulaire au cours du temps.

Mots-clés

Microfluidique, micro-matrice, détection de protéines, particule super paramagnétique, scansion de particules magnétiques, auto-assemblage électrostatique, matrice de lentilles, détection de nanoparticules, levure, cellule unique, *Caenorhabditis elegans*, élevage de nématodes sur puce, imagerie multidimensionnelle, embryon de *C. elegans*, immobilisation réversible de nématodes, observation à long terme à haute résolution, maladie neurodégénérative, agrégation de protéines, phénotypage.

Sommario

Nell'ambito della ricerca biomedica è essenziale poter ottenere dati statistici relativi ad ampie popolazioni di entità biologiche specifiche – quali, ad esempio, organismi, cellule o molecole – preservando al tempo stesso informazioni dettagliate riguardo le singole entità considerate. Questa tesi tratta tale tematica e propone l'uso combinato di microfluidica e tecniche di "micro-compartimentazione" per lo sviluppo di strumenti tecnologici atti a realizzare test biologici con risoluzione a livello del singolo organismo, cellula o molecola.

Presentiamo innanzitutto un nuovo test immonologico "su microchip", in grado di individuare la presenza del biomarcatore fattore di necrosi tumorale α nel siero, fino a concentrazioni dell'ordine dell'attomolare (10^{-18} M). In particolare, forniamo un modello predittivo completo della tecnica, che si basa sull'uso di micro-matrici di particelle superparamagnetiche. Introduciamo il concetto di "scansione di particelle magnetiche", come nuovo metodo per ideare test immunologici con limiti di rilevazione bassissimi, fino al livello della singola molecola. In seguito, abbiamo modificato la nostra tecnica di micro-compartimentazione di particelle magnetiche per adattarla all'immobilizzazione di particelle e cellule di varie dimensioni e proprietà. Presentiamo un metodo di auto-assemblaggio elettrostatico di microsfere dielettriche in strutture ordinate di pozzetti, per la produzione rapida e versatile di matrici di microlenti. Inserendo poi queste matrici in un sistema microfluidico, abbiamo creato un nuovo strumento per il rilevamento di singole nanoparticelle all'interno di un flusso, che permette di identificare oggetti in movimento di taglia inferiore al limite di diffrazione della luce tramite microscopi convenzionali a basso ingrandimento. Abbiamo sviluppato inoltre un altro metodo di micro-compartimentazione analogo a quello presentato al fine di distribuire in pozzetti separati ampie popolazioni di cellule non-aderenti. Abbiamo usiamo questa tecnica in combinazione con l'uso di un dispositivo microfluidico di tipo "elettrowetting su dielettrico" per implementare test di citotossicità su cellule di lievito con risoluzione a livello della singola cellula.

Nella fase successiva del progetto, abbiamo ideato soluzioni tecnologiche per l'analisi automatizzata del *Caenorhabditis elegans*, uno degli organismi modello più utilizzati nella ricerca biomedica. Abbiamo dapprima sviluppato un dispositivo microfluidico per l'allevamento di nematodi "su microchip" e la micro-compartimentazione di embrioni di *C. elegans* sincronizzati in fase evolutiva. Un processo di imaging multidimensionale permette di condurre, nel nostro dispositivo, analisi fenotipiche sistematiche su singoli embrioni. Siamo riusciti a distinguere variazioni dello sviluppo embrionale a livelli di risoluzione senza precedenti; abbiamo inoltre studiato l'impatto di perturbazioni delle funzioni mitocondriali sull'embriogenesi. Presentiamo poi un secondo prototipo del dispositivo, concepito per studi automatizzati di lunga durata su *C. elegans*, con risoluzione a livello del singolo nematode e lungo l'intera durata del suo sviluppo,

dall'embriogenesi allo stadio adulto. Infine, introduciamo un terzo prototipo che presenta: (i) una nuova architettura microfluidica, progettata per selezionare larve ad un determinato stadio di sviluppo e, in seguito, allevarle e trattarle; (ii) un metodo di immobilizzazione reversibile dei nematodi, che permette la loro osservazione ad alta risoluzione. Abbiamo utilizzato questa piattaforma microfluidica per analizzare il processo di aggregazione proteica in un modello *C. elegans* per la sclerosi laterale amiotrofica (SLA) umana. Il dispositivo permette di localizzare precisamente aggregati proteici specifici all'interno dei tessuti dei nematodi e di osservare l'evoluzione di singoli aggregati a livello subcellulare per più giorni consecutivi.

Parole chiave

Microfluidica, micro-matrice, rilevamento di proteine, particella superparamagnetica, scansione di particelle magnetiche, auto-assemblaggio elettrostatico, matrice di lenti, rilevamento di nanoparticelle, lievito, singola cellula, *Caenorhabditis elegans*, allevamento di nematodi su microchip, imaging multidimensionale, embrione di *C. elegans*, immobilizzazione reversibile di nematodi, osservazione di lunga durata ad alta risoluzione, malattia neurodegenerativa, aggregazione proteica, analisi fenotipica.

Contents

List of Figures

List of Tables

List of Equations

Preface

Recent advances in science and technology at the micro- and nano-scale are rapidly and constantly changing the world, with enormous impact on people's everyday life. The advent of microelectronics in the late 1950s suddenly enabled engineers to incorporate a tremendous amount of additional functionality and flexibility into products than was previously even imaginable. This immediately resulted in the fastest technological revolution ever undertaken by human race, which produced, in a few decades only, the world as we see it, i.e. permeated by technological devices, machines and gadgets of any kind and – potentially – at everyone's disposal. From a socio-cultural point of view, the main effect of the micro/nano-science revolution is probably represented by the "democratization of technology": information, communication systems and functionalities that once were accessible to only a selected minority are now available to everyone. The icons of such democratization process are today represented by the Internet and the smartphones, but we are now wondering when exactly this revolution will involve another – from many facets, more important – aspect of human society: healthcare. Micro/nanoscience allows in fact nowadays good control and study of biological materials at the same dimensional scale of the individual entities under investigation, such as micro-organisms, cells or even single molecules – probably in vague analogy with what happened for the control of electrons in the early days of microelectronics. Moreover, microfluidics – the technology for manipulating small volumes of fluids – largely demonstrated its potential to miniaturize whole complex laboratory protocols onto single microchips, with substantial advantages over standard laboratory procedures. These technological solutions, usually named "lab-on-a-chip" (LOC) devices, moreover benefited from investments – from government funding agencies and venture capitalists – aiming at promoting their commercialization. Surprisingly, however, despite this convergence of favorable factors, only a few LOC-based products have been successfully introduced into the market, while most of them never left the research labs and were never made accessible to people. The limiting factor towards the implementation of the emerging technological tools in a novel class of "democratized" healthcare devices seems to reside in the commercialization process itself. One of the main bottlenecks preventing the lab-to-market transfer of technology is probably represented by the absence of standardized, versatile, fully automated solutions. In the last two decades, in fact, research efforts have been mainly directed towards the development of individual LOC components, tailored for specific applications, while fully functional integrated devices have been only rarely proposed. In the absence of standardized fabrication techniques and versatile adaptable solutions, even the most groundbreaking LOC components proved not to be suitable for commercialization, usually because of their fundamental mutual incompatibility. In the light of these considerations, I always focused my research efforts on the development of versatile, fully automated LOC tools, answering to this urgent need for future commercial solutions. I typically proved the capabilities of our

devices to address specific biomedical questions, but always carefully designed them to be mutually compatible and easily re-adaptable for manifold applications. A common feature of all the LOC devices that will be presented in this thesis is represented by the combination of microfluidics and "micro-arraying" approaches, as key elements towards standardization, full automation and easy scalability of the LOC technology. By means of the combined microfluidic/micro-array toolkit, together with my scientific collaborators, I addressed different topics and covered a quite large spectrum of applications, which range from the development of integrated immunoassays to the detection of nanobiomaterial, moving then towards the conception of whole organism-based bioassays. On the one hand, this research approach allowed me diving into a multitude of research domains, sometimes very far from each other, and this positively resulted in a fruitful cross-contamination of ideas among the different fields. On the other hand, however, a very large amount of work should now be cited for a comprehensive description of all the different topics which have been considered in this work. I believe that such an overview would be quite confusing for the reader if condensed in a single chapter of this thesis. For these reasons, I structured this document according to the main research themes considered in my work and extensively expanded each theme individually. Overall, the common thread of my work is represented by the combination of microfluidics and "micro-arraying" concepts, as a key approach for the isolation and accurate analysis of biological entities of different size and level of complexity – from molecules to nanomaterials, from cells to whole small model organisms.

In chapter 1, I describe a new on-chip immunoassay technique, based on the use of micro-arrays of superparamagnetic beads as substrates for enhanced specific protein capture, ideally enabling single-molecule detection in a simple microfluidic assay format. In chapter 2, then, I extend the concept of magnetic bead arraying by introducing a novel method for rapid self-assembly of large arrays of micro-entities of different nature and materials – from dielectric beads to non-adherent cells. In collaboration with other researchers at LMIS2 and at the biosensors department at KU-Leuven, we employed this method for two different applications: fabrication of microlens arrays for nanoparticle detection and single-cell analysis on yeast cells, respectively. In chapter 3, I introduce a new type of hydrodynamic micro-array system, designed for the automated isolation, long-term imaging and phenotyping of *Caenorhabditis elegans* embryos. I then demonstrate the use of this system for the investigation of a specific molecular pathway – i.e. the mitochondrial unfolded protein response (UPR^{mt}) – in *C. elegans* embryos. The concept of whole-organism phenotyping is further extended in chapter 4, where a new microfluidic arraying system is proposed, tailored for long-term studies on *C. elegans* nematodes at single-organism resolution and over their whole development – from embryogenesis to adulthood. In chapter 5, then, I present a complete microfluidic platform for controlled culture, reversible immobilization and long-term high-resolution imaging of nematodes. This final microfluidic design is conceived to maximize versatility and scalability of the platform, towards high-throughput applications and proves to be suitable for time-resolved monitoring of complex biological processes in *C. elegans*, such as the evolution of a neurodegenerative disease. At last, chapter 6 concludes this thesis, by providing the reader with an overview of the presented results and an outlook on future opportunities in the field.

Chapter 1 Superparamagnetic micro-particle arrays towards single-molecule detection

Abstract A novel protein detection method has been developed, based on magnetic and microfluidic manipulation of superparamagnetic beads, through which we recently demonstrated detection of tumor necrosis factor-α from spiked serum down to 60 attomolar (60×10^{-18} M) [1], thus attaining a limit of detection (LOD) comparable to PCR-based techniques, orders of magnitude more sensitive than conventional methods. Our technique extends the current knowledge of force differentiation immunoassays. Unlike previously reported bead-based "flow chamber" assays [2, 3], in fact, our method introduces the use of magnetic bead dipole–dipole interactions, combined with microfluidic viscous forces, to enhance the selectivity of specific antigen-antibody (Ag-Ab) immunocomplex formation and thus attain unprecedented limits of detection for this kind of assays. Moreover, by combining Finite Element Method (FEM) simulations with analytical calculations, we built a complete predictive model for our technique [4], to be employed as a guide for its further use, optimization and development. We corroborated the simulated results with experiments and we characterized the enhanced assay selectivity, both theoretically and experimentally. We eventually worked at a comprehensive theoretical model including considerations on the probability of the single immunocomplex formation, allowing investigating the assay kinetics and understanding the peculiar behavior of its dose-response curves [5, 6].

This chapter is an adapted version of the following publications:

- **M. Cornaglia**, R. Trouillon, H. C. Tekin, T. Lehnert, and M. A. M. Gijs, Dose-response curve of a microfluidic magnetic bead-based surface coverage sandwich assay, *New Biotechnol* 32, 433-440, doi: 10.1016/j.nbt.2015.03.008 (2015)
- **M. Cornaglia**, R. Trouillon, H. C. Tekin, T. Lehnert, and M. A. M. Gijs, Magnetic particle-scanning for ultrasensitive immunodetection on-chip. *Anal Chem* 86, 8213-8223, doi:10.1021/ac501568g (2014)
- **M. Cornaglia**, H. C. Tekin, T. Lehnert & M. A. M. Gijs. Fine-tuning of magnetic and microfluidic viscous forces for specific magnetic bead-based immunocomplex formation. *J Appl Phys* 114, doi: 10.1063/1.4817663 (2013)
- H. C. Tekin, **M. Cornaglia** & M. A. M. Gijs. Attomolar protein detection using a magnetic bead surface coverage assay. *Lab Chip* 13, 1053-1059, doi: 10.1039/C3lc41285g (2013)

1.1 Introduction

1.1.1 Immunoassays in clinical diagnostics

Immunoassays are essential in clinical diagnostics to differentiate between health and disease and for therapeutic monitoring. A major goal is disease detection at an early stage to minimize the invasiveness of the treatment and maximize the chance of healing [7, 8]. To reach this goal, the measurement of extremely low concentrations of proteins in serum is necessary [9-13]. At the same time, point-of-care medical diagnostics represents one of today's main challenges towards the promise of tests that can be carried out at the site of patient care [14]. From the immunoassay integration perspective, this has been translated in terms of miniaturization of the detection systems and reduction of the sample and reagent volumes needed for the analysis. The conjunction of these factors is dictating the need of a new generation of fast, cheap and minimally-invasive diagnostics tools, able to selectively detect dramatically low amounts of proteins – down to the limit of a single molecule – in complex media. For instance, clinically relevant concentration values of tumor necrosis factor α (TNF-α) or interleukins (e.g. IL-6) for early disease detection are in the femtomolar regime or lower ($<10^{-15}$ M) [15]. A minimally invasive immunoassay should ideally be performed starting from a sample volume the size of a blood droplet (typically 5 to 10 µL), thus containing at maximum a few thousand target Ags. Recent technological advances, in particular those enabled by microfluidics, have therefore been creating novel tools for detecting biomarkers at low concentrations and/or sample volumes in complex sample media and with a wide variety of assay read-outs [1, 3, 16-22]. Functionalized superparamagnetic particles have been shown to be ideally suited for the rapid and efficient capture and isolation of target molecules [23, 24]. Many of these magneto-microfluidic assays were based on a protocol, in which magnetic particles were immobilized in a flow and exposed to a series of sequential reagent exposure and washing steps, as inspired by a batch-type assay [25-27]. Also continuous flow microfluidic assays have been proposed, in which magnetic particles were moved through multilaminar reagent/washing solution flow streams to implement the assay protocol [28]. Furthermore, droplet-based systems have been proposed, which allowed storage of reagent/washing solutions in aqueous droplets surrounded by an immiscible oil phase and employed magnetic particles that were moved between the different droplets to perform the assay protocol [29, 30].

1.1.2 Magnetic bead-based surface-coverage immunoassays

Among the available immunoassay techniques, magnetic bead-based "surface-coverage" methods recently emerged for their relative ease of implementation and extremely low limits of detection. In this class of assays, magnetic particles are used as labels to detect the formation of Ag-Ab immunocomplexes on a substrate. Quantification of the surface-bound particles is used to provide a measure of the Ag concentration to be analyzed. In this context, S. J. Osterfeld *et al.* [31] designed a sequential assay in which Ags were first captured on a detection surface and bound to biotinylated Abs, on which streptavidin-coated magnetic beads were then incubated (**Figure 1.1**a). During such incubation, the magnetic particles formed streptavidin–biotin bonds and their capture dynamics could be monitored in real time via giant magnetoresistance (GMR) sensors [32].

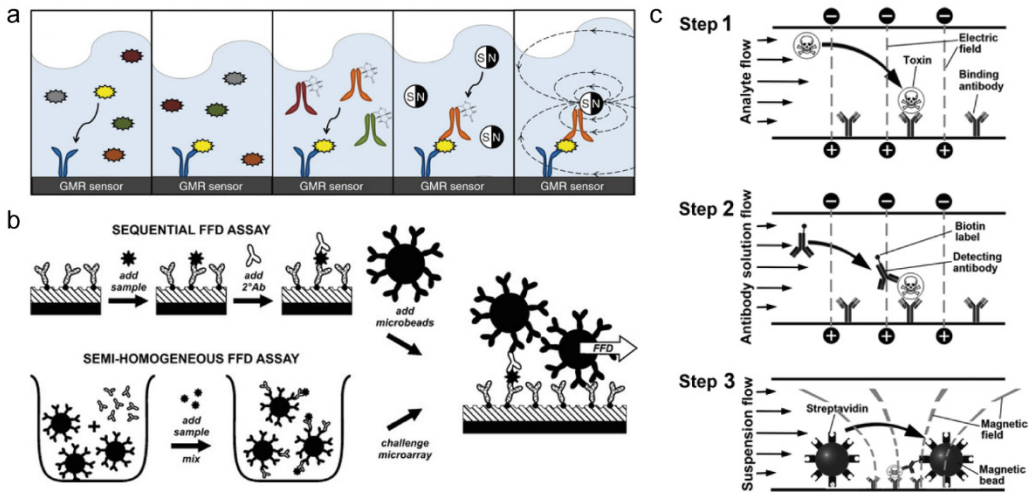

Figure 1.1 | Bead-based surface coverage immunoassays. (a) Schematic representation of the assay procedure described by Osterfeld *et al.* and Gaster *et al.* (reproduced from [17]). Legend: capture Abs = blue; target Ags = yellow; biotinylated detection Abs = orange. Streptavidin-labeled magnetic nanoparticles are bound to the biotinylated detection Abs and used as magnetic tags, since they are detected by the underlying GMR sensor. (b) Schematic description of the assay techniques reported by Mulvaney *et al.* (reproduced from [3]). Magnetic microbeads are used as labels for Ag detection, while fluidic force discrimination (FFD) is employed to reduce unspecific bead adsorptions. (c) Schematic representation of the assay procedure described by Shlyapnikov *et al.* (reproduced from [33]). Magnetic beads are used to label speficic immunocomplexes and detect bacterial toxins by direct bead counting via microscope observation.

By means of this method, Gaster *et al.* reached a LOD of 200 fg mL^{-1} for carcinoembryonic antigen (CEA) spiked in 50 µL mouse serum with a total assay time of 2.5 h [17].

S. V. Mulvaney *et al.* [3] presented magnetic bead-based surface coverage assays in both a sequential and a semihomogenous configuration (**Figure 1.1**b). In the sequential assay format, target Ags and detection Abs were incubated in separate steps on an Ab-covered detection surface. Ab-coated magnetic beads were then deposited over the detection surface, as labels for the formation of specific immunocomplexes, while a washing step was used to remove unspecifically bound beads via “fluidic force discrimination” (FFD). Then, target Ags were quantified by counting the number of remaining beads on the detection surface. A LOD of 100 fg mL^{-1} (3.5 fM) for staphylococcal enterotoxin B (SEB) was achieved in 2 µL PBS. In the semi-homogenous assay format, magnetic beads were instead mixed with target Ags before transporting them onto the detection surface. This resulted in improved assay sensitivity but much higher sample volume consumption, with a LOD of 1 fg mL^{-1} (35 aM) for SEB spiked in 1 mL PBS and 100 fg/mL (3.5 fM) in 1 mL canine serum samples.

Y. M. Shlyapnikov *et al.* [33] described a bead-based method for the detection of bacterial toxins (**Figure 1.1**c). Electrophoretic concentration of toxins on an Ab-coated surface was performed during a 3 min flow in a microfluidic channel. Afterwards, biotinylated Abs were transported over the surface-bound Ags for 2 min. In a third step, a permanent magnet was positioned below the device, to attract streptavidin-coated beads towards the surface, while they were injected into the device. This procedure promoted the specific capture of the beads by formation of Ab-Ag-Ab sand-

wich immunocomplexes. The number of surface-tethered beads was then measured by microscope observation of the substrate and subsequent image processing. By using this technique, cholera toxin (CT), staphylococcal enterotoxin A (SEA), SEB and toxic shock syndrome toxin (TSST) could be detected down to 0.1 pg mL^{-1}, while heat-labile toxin of *Escherichia coli* (LT) was detected down to 1 pg mL^{-1}, in tap water and water from pond and river. Significantly higher LODs (0.1 ng mL^{-1}) were achievable without the electrophoretic concentration of toxins. Electrophoretic focusing requires however particular sample conditions: for instance, meat and milk extracts need to be desalted before being analyzed with this method. The desalination procedures unfortunately resulted in a loss of toxins and increased the LOD of CT, SEA, SEB and TSST to 1 pg mL^{-1}.

1.1.3 Challenges and opportunities for ultra-sensitive protein detection

When assaying samples having an extremely low analyte concentration, the ratio between the amount of target molecules and the amount of particles used for their capture is usually very low. As a result, the percentage of particles carrying analyte molecules follows a Poisson distribution with very low mean value – i.e. particles generally carry either a single molecule or none. In this regime, quantification of the amount of molecule-carrying particles is based on single analyte molecule detection events [34]. However, the size mismatch between target molecules and particles may complicate the detection. For instance, the typical size of molecules of interest being in the nanometer range (the Stokes radius of a TNF-α monomer was estimated as 2.2 nm at pH=7.0) [35], a captured molecule occupies only ~10^{-7} of the surface of a 300 nm diameter particle. This ratio drops to ~10^{-9} and ~10^{-11} for 3 μm and 30 μm particles, respectively. If we intend to capture these particles on a substrate aiming to count them for single molecule immunodetection, these values are indicative of the – extremely low – probability of encounter between a particle-linked Ag and substrate-immobilized Abs. Since in such case both single Ag molecules (ligands) and capture Abs (receptors) are bound to surfaces, their recognition kinetics is substantially reduced as compared to freely diffusing species; therefore the formation of specific immunocomplexes would be very slow or probabilistically almost impossible [36]. However, solutions to this problem are offered on the nanoscale. A first option could be reducing the particles' size, ideally down to a few tens of nm, to reduce the size-mismatch. Although this would improve ligand-receptor encounter probabilities, it would result in much more challenging particle manipulation, capture and detection. In order to take advantage of the size of micrometer particles, an alternative solution is increasing the rotational diffusion of the Ag-carrying particles to enhance the Ag-Ab encounter probability. While this concept has been proposed for agglutination immunoassays in solution [36, 37], it is rather unexplored in surface-based assays.

In this chapter, we address this issue and we propose as a solution a novel surface-based immunoassay technique, which employs superparamagnetic microparticles in a microfluidic chip to attain ultrasensitive protein detection, down to the single-molecule level. In section 1.2 of this chapter, we present the technique and show its potential, by demonstrating detection of only 200 molecules of TNF- α in a serum sample volume of 5 μL, corresponding to a concentration of 60 attomolar or 1 fg mL^{-1}. In section 1.3, then, we identify the main forces governing the immunoassay performance and present a combined FEM/analytical model to predict and control these

forces, with the aim of maximizing the assay specificity and minimizing its "background noise". In section 1.4, we eventually introduce the concept of "magnetic particle-scanning", as new key mechanism to significantly increase the probability of immunocomplex formation in our assay, and, more in general, in other single molecule-based heterogeneous immunoassays.

1.2 A new method for ultrasensitive protein detection in serum

1.2.1 Overview of the technique

Our protein detection method is based on magnetic and microfluidic manipulation of superparamagnetic beads. A complete platform for the integration of this method in a microfluidic format was developed in the framework of a previous project [38] and its detailed description is out of the scope of this work. Here, a few technical aspects of the microfluidic device will be mentioned, while the whole process of development and optimization of the detection method itself will be presented in detail. Our technique is based on the following immunoassay protocol. First, "large" (2.8 µm) Ab-functionalized magnetic beads are used to specifically capture Ags from a serum matrix under active microfluidic mixing. Subsequently, the large beads are gently exposed to a surface pattern of fixed "small" (1.0 µm) Ab-coated magnetic beads (**Figure 1.2**a). During the exposure, attractive magnetic bead dipole–dipole interactions improve the contact between the two bead types and help the Ag-Ab immunocomplex formation (**Figure 1.2**bi), while non-specific large bead adsorption is limited by exploiting viscous drag forces in the microfluidic channel on the small-bead pattern (**Figure 1.2**bii). After exposure of the large beads to the pattern of small beads, the Ag concentration is detected by simply counting the number of surface pattern-bound large magnetic beads (**Figure 1.2**c).

The whole assay is performed in a microfluidic polydimethylsiloxane (PDMS) chip featuring microfluidic channels, pneumatic valves and a micro-mixing chamber [1]. The chip is connected via fluidic ports to syringe pumps for automated fluidic manipulations. Nemesys syringe pumps (Cetoni, Korbussen, Germany) were used for automated flow control. Complex microfluidic operations (e.g.: mixing, valve actuation, etc.) were handled through an in house-developed Labview (National Instruments, Austin TX, USA) software interface. A digital camera (Pixelink PL-P742) was mounted with 0.5× TV adapter (Zeiss product no. 456101) on an inverted microscope (Zeiss Axiovert S100) equipped with a 32× objective (Zeiss LD-Achroplan), to take optical micrographs of the (250 µm – wide and 2500 µm – long) surface pattern of fixed small beads, which we will refer to as "detection area". An electrostatic self-assembly method [39] was used to immobilize the small beads onto aminopropyl-trietoxysilane (APTES) dot structures (**Figure 1.2**d), previously microfabricated on glass substrates via standard lithography techniques [40] (**Figure 1.2**e). For each assay, about 3500 large superparamagnetic beads and a 5 µL sample solution were introduced into the micro-mixing chamber through reservoirs integrated in the microfluidic chip. On-chip active mixing was conducted to pre-concentrate Ags on the large bead surfaces. Ag-loaded beads were then transported in buffer solution through a (250 µm – wide, 60 µm – high) microfluidic channel to the detection area, under the presence of the magnetic field produced by a permanent magnet.

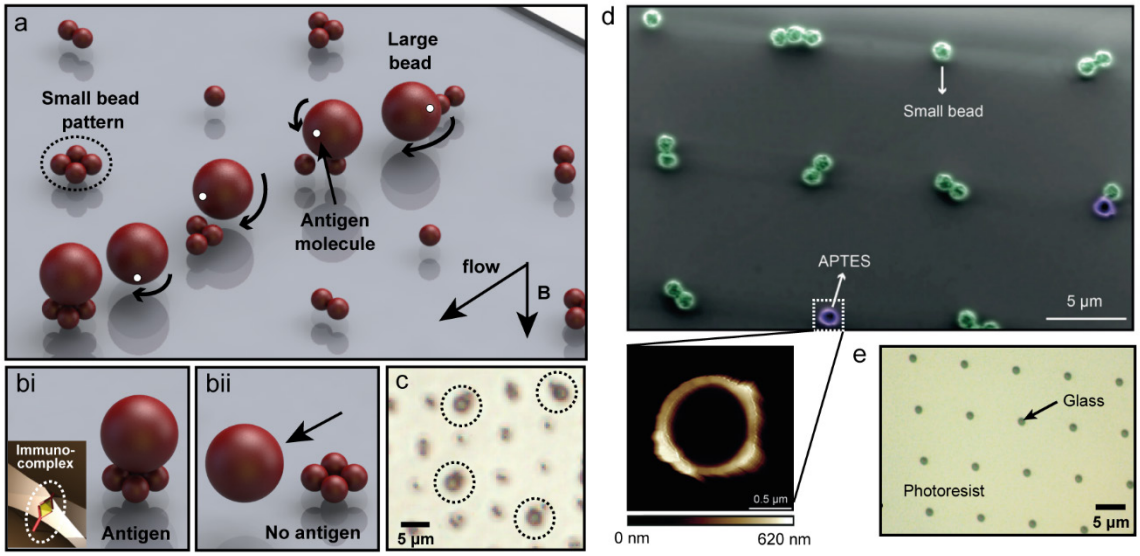

Figure 1.2 | Overview of the protein detection method. (a) Schematic representation of the time-lapse motion of a large bead exploring the detection area and interacting with the functionalized surface on the small beads through magnetic dipole-dipole forces. (b) Large bead capture mechanism: (bi) in absence of Ags, large beads are transported by the microfluidic flow through the whole detection area and washed away; (bii) if at least one Ag molecule is present on the large bead surface, the bead is captured onto the detection area via Ag-Ab binding. (c) Assay readout: counting of the captured large beads provides a measure of the number of molecules present in the sample under analysis; (d) Scanning electron microscopy (SEM) photograph of a part of the detection area after small bead patterning. The image is artificially colored to emphasize the small beads and APTES patterns. In zoom, atomic force microscopy (AFM) image of a 1.5 µm APTES dot after the photoresist lift-off process. (e) Micrograph of a detection chip covered with 600 nm – thick structured photoresist layer, used for depositing the APTES dot patterns.

It is worth noticing that, in principle, other micromagnetic structures could have been used to replace the immobilized small particle "landscape" and micropatterned magnetic structures [41], the surface of which can be bio-functionalized. However, a direct immobilization of pre-functionalized magnetic particles offers a very fast and reliable solution for getting patterning and functionalization done at the same time. Moreover, if particles are superparamagnetic, their magnetization can be accurately modulated by an external magnetic field, therefore offering an additional degree of freedom with respect to taking permanent micro- or nanomagnets. The magnetic landscape can be therefore accurately tuned by an operation as simple as changing the relative position between the immobilized particles and a permanent magnet.

1.2.2 Protein detection results

First, we used our system for the detection of biotinylated anti-streptavidin, spiked as Ag in fetal bovine serum (FBS). **Figure 1.3**a shows representative images of large bead counting for the analysis of different concentrations of spiked Ags, corresponding to specific numbers of Ag molecules to be detected inside each serum sample. The number of large beads bound to the detection area increases with the Ag concentration. **Figure 1.3**b reports the percentage of specifically captured beads, as a function of the total number of Ag molecules to be detected. To produce this graph, for each sample concentration, the number of specifically bound beads is calculated, as a differ-

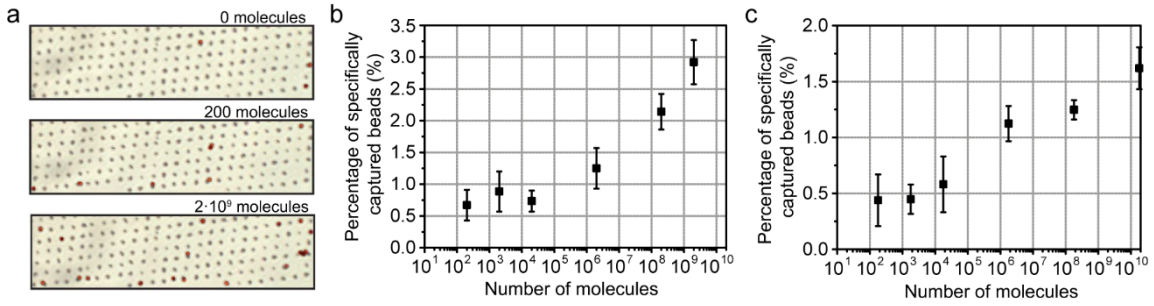

Figure 1.3 | Experimental results of protein detection. (a) Optical microscopy photograph of a small portion of the detection area using as Ag sample three different concentrations (i.e. three different amount of molecules to be detected: 0, 200, and $2 \cdot 10^9$ molecules, respectively) of biotinylated anti-streptavidin in FBS. Color enhancement is applied to the large beads for better visualization. (b, c) Experimental data for the detection of (b) biotinylated anti-streptavidin and (c) TNF-α in FBS (n= 3-4, the error bars are SD).

ence between the bead count in the presence of Ags spiked into the sample matrix and the average bead count with no (0 fg mL^{-1}) Ag (i.e. background signal). The obtained values are then divided by the total number of beads used for each assay (i.e.: 3500) and expressed as a percentage of this value. Data points represent the mean of 3–4 replicates with error bars = standard deviation (SD). Moreover, the LOD signal is taken as three times SD of the background signal [42] and it is calculated to be 6.5 attomolar, corresponding to the detection of down to ~200 biotinylated antistreptavidin molecules in the 5 µL serum sample.

Figure 1.3c shows instead the results of detection of TNF-α, spiked at different concentrations in FBS. TNF-α is a cytokine secreted from cells during inflammation [43], while the presence of excessive amounts of TNF-α molecules in the bloodstream can be linked to an increased risk of cancer, as well [44]. With our assay, we achieve a LOD of 1 fg mL^{-1} (60 attomolar), corresponding to the possibility of detectiong the presence of a few hundred TNF-α molecules in 5 µL serum samples.

1.3 Assay specificity enhancement and background noise reduction

A good specificity is a prerequisite for a low detection limit of the assay, as it translates directly into a low signal for the blank reference experiment and reduces noise caused by unspecific adsorption effects. To unravel the origin of the specificity in our immunoassay technique, we developed a physical model of the force balance involved in our “dual magnetic bead”-based protein detection format. We then validated experimentally our theoretical predictions and employed this model as a tool for the optimization of the assay performance.

1.3.1 Physical modeling

Figure 1.4a summarizes the forces involved at the moment of a single immunocomplex formation. Large beads are transported in the microfluidic channel by Poiseuille flow and thus subjected to a viscous drag force $\mathbf{F_{drag}}$. The presence of an external magnetic field and the magnetized small bead pattern generates on the large magnetic beads a force $\mathbf{F_{mag,\,ext}}$ and $\mathbf{F_{dip}}$, respectively, as will be described further. When a specific immunocomplex is formed, an extra retention force $\mathbf{F_{spec}}$ is established due to the presence of the Ag. The goal of the optimized immunoassay is to keep large

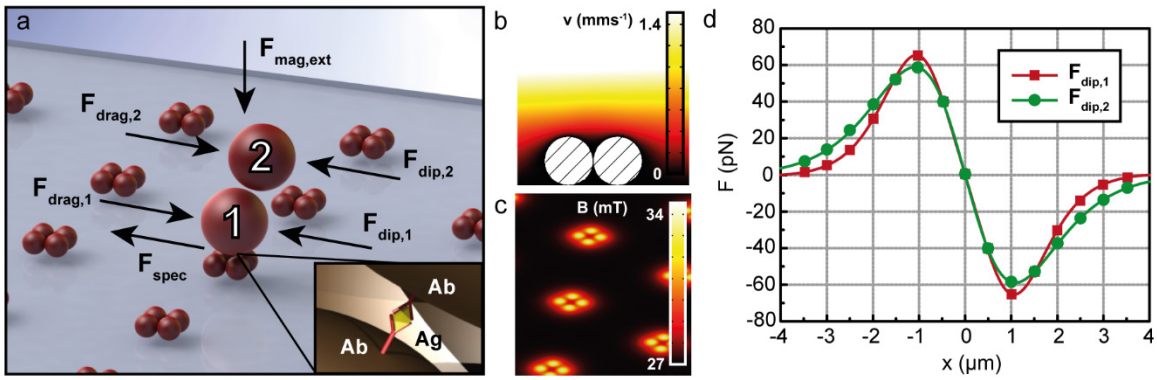

Figure 1.4 | Physical modelling for assay specificity enhancement. (a) Diagram of the main directions of the viscous ($\mathbf{F_{drag,1}}$ and $\mathbf{F_{drag,2}}$) and magnetic dipolar ($\mathbf{F_{dip,1}}$ and $\mathbf{F_{dip,2}}$) forces acting on two large magnetic beads. Bead 1 is translating just above the small bead pattern and bead 2 just above bead 1. Also the magnetic force $\mathbf{F_{mag,ext}}$ induced by the permanent magnet and the specific inter-bead binding force $\mathbf{F_{spec}}$ due to the formation of the Ab-Ag-Ab sandwich immunocomplex (in zoom) are indicated. (b) Side-view of the flow velocity in a microfluidic channel above a pattern of 4 small magnetic beads of 1 µm diameter, when applying a flow of 100 nL/s in a microchannel with section h×w = 60 µm×250 µm. (c) Magnetic induction at a position of 1 µm above the bottom of the microchannel when applying an external magnetic induction of 27 mT. The small beads locally increase the induction, which is the basis for the attractive dipolar force with a large bead. (d) x component of the magnetic dipolar force acting on 2 large magnetic beads, as indicated in **Figure 1.4**b ($\mathbf{F_{dip,1}}$ and $\mathbf{F_{dip,2}}$), moving with the flow along the x-direction. The centre position of the pattern of 4 small beads is chosen as x=0 µm. The forces are plotted with respect to the x-displacement of the large beads, for an external induction of 27 mT at the microchannel bottom.

beads attached to the small bead pattern only if an Ag is present, i.e. minimize non-specific adsorption while maximizing the specific bead capture.

The microfluidic environment is simulated via FEM using Comsol 4.2a (COMSOL Multiphysics, Zürich, Switzerland), by solving the Navier-Stokes equation for incompressible flow [45]. The presence of a small bead pattern at the channel bottom influences the flow, as represented in **Figure 1.4**b. The simulation allows extracting precise values of the local fluid velocity **v** for accurate estimation of the drag force acting on a large bead approaching the pattern. A "drag coefficient" f_D has to be employed to take into account the proximity of the large bead to the microfluidic channel wall. Therefore, the drag force acting on a large bead is calculated as:

$$\mathbf{F_{drag}} = 6\pi\mu R\mathbf{v}f_D \tag{1.1}$$

where $\mu = 8.9 \times 10^{-4}$ Pa s is the viscosity of the buffer solution used, $R = 1.4$ µm is the bead radius, and f_D the drag coefficient given by [23]:

$$f_D = \left[1 - \frac{9}{16}\left(\frac{R}{R+z}\right) + \frac{1}{8}\left(\frac{R}{R+z}\right)^3 - \frac{45}{256}\left(\frac{R}{R+z}\right)^4 - \frac{1}{16}\left(\frac{R}{R+z}\right)^5\right]^{-1} \tag{1.2}$$

with z the distance between the surface of the large bead and the contour of the small bead pattern that is fixed on the bottom of the microfluidic channel.

In the presence of a magnetic induction $\mathbf{B_{ext}}$, superparamagnetic particles get magnetized with magnetic moment $\mathbf{m}(\mathbf{B_{ext}})$, according to a non-linear, non-hysteretic magnetization curve, specific

for the bead type [46]. The magnetic force $\mathbf{F_{mag,ext}}$ acting on a large bead with magnetic moment $\mathbf{m_L}$ is given by [47]:

$$\mathbf{F_{mag,ext}} = (\mathbf{m_L} \cdot \nabla)\mathbf{B_{ext}} \tag{1.3}$$

Moreover, a magnetic dipolar force acting on a large bead in proximity of the small bead pattern can be calculated as the gradient of the total dipolar interaction energy [27]:

$$\mathbf{F_{mag,dip}} = -\nabla\left[\sum_{i=1}^{n} \frac{\mu_0}{4\pi|\mathbf{r_i}|^3}\left(\mathbf{m_i} \cdot \mathbf{m_L} - \frac{3}{|\mathbf{r_i}|^2}(\mathbf{r_i} \cdot \mathbf{m_i})(\mathbf{r_i} \cdot \mathbf{m_L})\right)\right] \tag{1.4}$$

where n is the number of small beads in the pattern, $\mu_0 = 4\pi \times 10^{-7}$ TmA^{-1} is the magnetic permeability, $\mathbf{r_i}$ is the distance vector between the center of the large bead and of the ith small bead, $\mathbf{m_L}$ and $\mathbf{m_i}$ are the magnetic moments of the large bead and of the ith small bead, respectively. If the derivative is calculated along the direction of the microfluidic flow (defined as x direction), this component of the magnetic dipolar force in equilibrium is opposite to the drag force. We therefore consider only the x-component of the magnetic force in the force balance equation.

Direct simulation of the complete physical model is complicated via standard simulation tools. However, the problem can be split into its different physical subdomains and three-dimensional (3D) FEM simulations can be combined with Matlab (The Mathworks Inc., Natick, MA) analytical calculations. First, the exact distribution of the magnetic induction on the patterned area is simulated via FEM using Comsol 4.2a. The magnetized small bead pattern generates a well-defined magnetic induction landscape, whose properties are defined by the external magnetic induction and by the specific pattern choice. In **Figure 1.4**c we report the FEM-calculated magnetic induction landscape for the conditions chosen in our experiments. The pattern of small beads results in a ~25% stronger magnetic induction at the beads' top surface, where immunocomplex formation occurs. However, we have only considered $\mathbf{B_{ext}}$ to calculate the magnetic moments of the different beads and have imported these data in the Matlab code for calculating the magnetic dipolar force on a large bead. In particular, a custom-made Matlab script was developed to simulate the force on a large bead at different x-positions (with 10 nm intervals) with respect to the location of the small bead pattern. As in the experiments, the distance between adjacent patterns is chosen to be large enough to ensure no magnetic cross-interaction. Each single pattern can be therefore considered as a modular unit of the array and simulated independently. The dipolar force acting on a large bead that is moving on top of a pattern of immobilized small beads is calculated using Equation (1.4), employing the "effective" dipole moment method, in which the magnetic moment $\mathbf{m_i}$ of a particle is the effective moment of an "equivalent" point dipole [48]. Full magnetization curves [46] are considered for the evaluation of the beads' magnetic moment. Different patterns of small beads have been considered in our simulations, as described further. For a direct comparison with our experimental conditions, we report here the specific case of a large bead moving above a pattern of 4 small beads, with an external induction of 27 mT at the microchannel bottom. Results are shown in **Figure 1.4**d, where the x component of the dipolar force acting on either bead 1 or bead 2 (see schematic of **Figure 1.4**a) is plotted with respect to their displacement. As

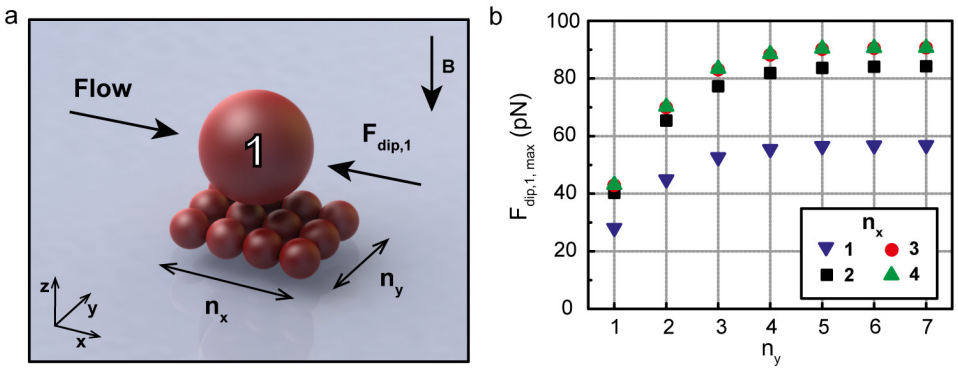

Figure 1.5 | Magnetic dipolar force calculations. (a) Schematic representation of the modeled geometry: a large bead is flowing on top of a $n_x \times n_y$ pattern of immobilized small beads, under the presence of a vertical magnetic induction B = 27 mT. (b) Maximum value of the x-component of the attractive magnetic dipolar force acting on bead 1, $\mathbf{F_{dip,1,max}}$, for rectangular small bead patterns consisting of a different number $n_x \times n_y$ of small beads.

expected, when bead 1 is brought in contact with the small bead pattern, it tends to be immobilized by magnetic interactions at the centre of the 4-bead pattern, where the force is zero. However, in the presence of a drag force, the large bead will be displaced from the centre and only kept on the pattern if the drag force does not exceed the maximum dipolar retention force (~ 65 pN in this case). Our approach allows easily simulating the magnetic dipolar forces versus displacement of the two types of large beads for any pattern of surface-immobilized small beads and magnetic field distribution. For a constant external magnetic field induction, the dipolar retention force exerted by the pattern on a flowing large bead varies with the size and the shape of the pattern. A comparison of the calculated forces for rectangular patterns of different size is reported in **Figure 1.5**.

1.3.2 Experimental optimization of the assay specificity

The validity and the precision of our model are corroborated experimentally on a microfabricated PDMS device. A microfluidic PDMS half-channel, 250 µm in width, 60 µm in height, is fabricated by standard soft-lithography technique [49]. 1.0 µm diameter MyOne Streptavidin C1 Dynabeads (Life Technologies, Zug, Switzerland) are used as the small superparamagnetic beads, and 2.8 µm diameter M-280 Streptavidin Dynabeads (Life Technologies, Zug, Switzerland) are used as the large superparamagnetic beads. Small and large beads are functionalized off-chip with biotinylated anti-tumor necrosis factor-α (anti-TNF-α) Ab (Life Technologies, Zug, Switzerland). Then the functionalized small beads are electrostatically fixed on a glass substrate, via a micropatterned aminopropyl-trietoxysilane (APTES) layer [39]. On circular APTES dots of 1.5 µm in diameter, 1 to 4 small beads are usually immobilized on each single dot, most of the dots showing 4 beads, as depicted in **Figure 1.4**a. In total the glass substrate carries ~8000 of these small bead patterns. The PDMS half-microchannel is then clamped on the glass substrate and connected via external tubing to a precision Nemesys syringe pump for the fluid manipulation. Strength and position of the permanent magnet have to be chosen to ensure, at the same time, gentle landing of the large beads onto the glass substrate and good bead capture efficiency. Magnets of different size and geometries are tested, in order to find the configuration that best fulfils both the aforementioned

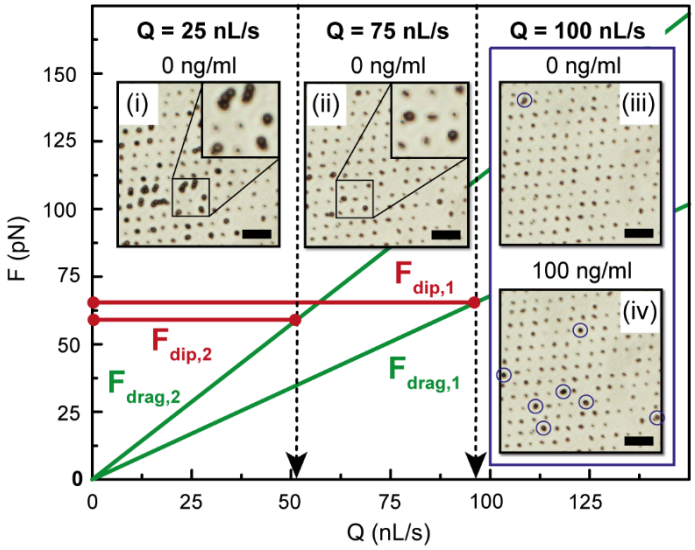

Figure 1.6 | Experimental optimization of the assay specificity. Force-flow rate diagram, indicating different regimes for the magnetic bead-based immunoassay, with insets of representative parts of the small bead pattern array. The x-components of the forces are indicated for the 2 types of large beads that were presented in **Figure 1.4**a. For flow rate Q < ~50 nL/s, the maximum intensity of the drag force $\mathbf{F_{drag,2}}$ is insufficient to remove the large magnetic bead(2) from the surface, leading to formation of bead chains (see inset (i)). For ~50 nL/s < Q < 95 nL/s, $\mathbf{F_{drag,1}}$ is insufficient to remove the large magnetic bead(1) from the surface, which leads to immobilization of single beads (see inset (ii)). For Q > 95 nL/s, drag forces are sufficient to remove non-specifically linked large magnetic beads (see inset (iii)), while, if a large bead is linked to the small bead pattern via an immunocomplex, it stays attached (see inset (iv)) and its presence can be used for Ag quantification. Circles are drawn around the captured large beads for better visualization. Scale bars in the insets are 20 µm.

requirements. Finally, a cylindrical permanent magnet (Supermagnete, Uster, Switzerland) is chosen, 1 cm in diameter, 3 mm in height, magnetized along its vertical axis, with magnetization of ~1040 kA/m. The magnet is positioned at 9 mm-distance from the glass substrate, thanks to a proper holder. The average magnetic induction at the glass surface level is measured via a gaussmeter (Pacific Scientific-OECO, Goleta, CA).

Experimentally, different regimes of the large bead transport mechanism can be identified, allowing investigating the origin of the good assay performance, as reported in **Figure 1.6**. From the theory, for a pattern of 4 small beads, maximum magnetic dipolar retention forces $\mathbf{F_{dip,1}}$ = 65 pN and $\mathbf{F_{dip,2}}$ = 59 pN are estimated for bead 1 and bead 2, respectively (see **Figure 1.4**d). These two values can be considered as force thresholds defining the different regimes of large bead transport and retention. For flow rate values below 50 nL/s, consistent grouping of large beads is observed, leading to uncontrollably high amounts of unspecific adsorption of large beads on the patterned area. In this flow rate range, in fact, large magnetic beads experience viscous drag forces lower than 35 pN when transported just above the small beads, where they are thus magnetically retained. Following the same reasoning, we can predict the vertical chaining of bead 2 to bead 1, the former being subjected to drag forces lower than 60 pN in this regime. The intensity of the dipolar interaction grows then with the number of beads chaining, according to Equation (1.4), hence the creation of even longer chains can be observed and large bead clustering is eventually

obtained (see **Figure 1.6** inset (i)). This working regime is clearly not applicable from an immunoassay perspective, as it is compromised by uncontrolled unspecific adsorption phenomena. However, this bead transport regime has been proven to be extremely interesting for other types of integrated bioassays and bio-studies, based on self-assembly of vertical chains of bio-functionalized beads [50, 51].

Instead, no vertical chains of large beads can be formed at flow rates larger than 50 nL/s. A second transport regime can be identified for flow rates between 50 nL/s and 95 nL/s, where isolated large beads are magnetically captured on the small bead pattern (see **Figure 1.6**, inset (ii)). For flow rates larger than 95 nL/s, viscous drag forces always exceed dipolar retention forces and large beads cannot be magnetically immobilized on the array anymore. In this regime, therefore, the capture of a large bead occurs only when an extra force comes into play. In case of reference tests (no Ags on the large beads), these extra forces can be only provided by unspecific interactions. For Ag-carrying beads (in our case the Ag is recombinant mouse TNF-α obtained from Life Technologies, Zug, Switzerland), instead, the formation of specific immunocomplexes at the beads' interface is responsible for the retention force $\mathbf{F_{spec}}$. While magnetic attraction between beads is known to act in favor of the immunocomplex formation [36], specific bonds can be disrupted by a too large drag force acting on the large beads, resulting in signal loss. Therefore, drag forces exerted on the large beads have to be minimized, so that they are just sufficient to remove non-specifically adsorbed large beads. The rupture force of the TNF-α – anti-TNF-α Ag-Ab pair has not been investigated under shear stress conditions. However, since for the biotin-streptavidin bond this force has been measured to be ranging between 3 pN and 11 pN [52], we can assume to be working with forces approximately in this range of values or slightly lower. Optimized assay specificity for this biomarker can be therefore expected for flow rate values around 100 nL/s. For this flow rate a clear difference of bead capture is observed between no TNF-α-carrying beads (0 ng/ml TNF-α) (see **Figure 1.6**, inset (iii)) and TNF-α-carrying beads (100 ng/ml TNF-α) (see **Figure 1.6**, inset (iv)).

1.4 Enhancement of specific immunocomplex formation

In the previous section, we described a physical modeling tool conceived for the optimization of the assay selectivity and the reduction of its background noise. In this first description of our immunoassay technique, superparamagnetic beads were considered as translating point-like dipoles, since this approximation allows readily estimating the balance of the forces acting on the particles involved in each immunocomplex formation event. When estimating, however, the probability of the occurrence of each one of this events, a more sophisticated modeling approach needs to be built, in which the rotation of each particle in the 3D space needs to be considered as well. In this section, we introduce the concept of "magnetic particle-scanning": in our assay, large particles are actually subjected to successive stochastic reorientations in the engineered magnetic energy landscape established by the regular pattern of small magnetic particles, while transported by hydrodynamic forces in the microfluidic system. In this mechanism, as the moving particle slides over the immobilized ones, the point of contact between the two particles continuously explores, or "scans", a section of the particle surface. If this inter-particle interaction is repeated

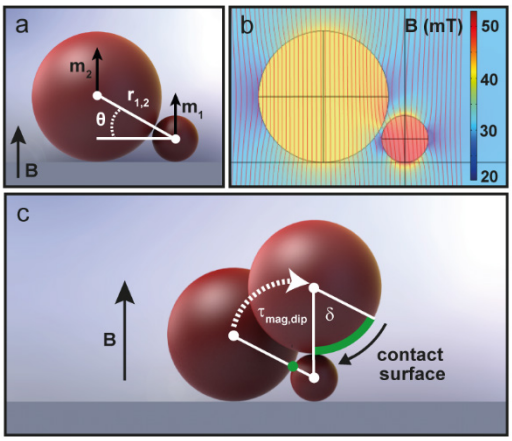

Figure 1.7 | Simulations of the 3D inter-particle interaction. (a) Schematic of a small and a large magnetic particle with magnetic moment $\mathbf{m_1}$ and $\mathbf{m_2}$, respectively, and indicating the angle θ and the position vector $\mathbf{r_{1,2}}$. (b) FEM simulation of the field lines for a large and small magnetic particle, placed in an external magnetic induction of 30 mT. (c) Contact of the large particle sliding over a small particle under influence of the torque $\tau_{mag,dip}$ as indicated by the arc corresponding to the angle δ.

several times, a large fraction of the moving bead surface can be interrogated, until the presence of a bound Ag triggers the particle binding. We explore this phenomenon in a custom-built magneto-microfluidic chip. Finally we introduce a random walk-based model for describing the magnetic particle-scanning process, explaining the particular dose-response curves of our protein detection experiments over the whole tested concentration range. Moreover, our analysis provides understanding of the features of other particle-based heterogeneous immunoassays.

1.4.1 Magnetic particle-scanning model

We will first describe the physics of the inter-particle interactions leading to the particle-scanning mechanism. When two superparamagnetic particles are placed in a constant magnetic induction **B**, they acquire each a magnetic moment, $\mathbf{m_1}(\mathbf{B})$ and $\mathbf{m_2}(\mathbf{B})$ respectively, and interact via dipolar forces. If the first particle is immobilized on a substrate that is normal to **B**, the second particle will be subjected to a torque, the size of which can be calculated as the first angular derivative of the dipolar interaction energy between the two particles, as follows:

$$\tau_{mag,dip} = -\frac{\mathrm{d}}{\mathrm{d}\theta}\left[\frac{\mu_0}{4\pi\left\|\mathbf{r_{1,2}}\right\|^3}\left(\mathbf{m_1}.\mathbf{m_2} - \frac{3}{\left\|\mathbf{r_{1,2}}\right\|^2}(\mathbf{r_{1,2}}.\mathbf{m_1})(\mathbf{r_{1,2}}.\mathbf{m_2})\right)\right] \tag{1.5}$$

where θ is the angle formed by the position vector between the center of mass of the two particles ($\mathbf{r_{1,2}}$) and the substrate plane (see **Figure 1.7**a), $\mu_0 = 4\pi \times 10^{-7}$ T m A^{-1} is the permeability of vacuum, and $\mathbf{m_1}$ and $\mathbf{m_2}$ are the magnetic moments of the two particles that we consider to be point-like dipoles. A stable situation is reached when $\mathbf{m_1}$ and $\mathbf{m_2}$ are aligned along the field direction (θ = 90°). **Figure 1.7**b shows the intensity of the magnetic induction **B** and the spatial distribution of the magnetic induction lines within a large and small magnetic particle for an externally applied induction of 30 mT, as calculated using a 3D FEM simulation (Comsol Multiphysics). We used a magnetic susceptibility χ of 0.7 and 1.4 for the large and small magnetic particle, respectively [46].

Our calculation shows that the perturbation of the vertical magnetic field lines due to the presence of the particles is minimum, thus supporting the assumption that both magnetic moments are oriented along the z-direction, as implicitly assumed in Equation (1.5). As domain reorientations in a magnetic particle, which consists of an ensemble of magnetic nanocrystals in a non-magnetic matrix, are relatively slow [53], $\mathbf{m_1}$ and $\mathbf{m_2}$ are not expected to change their orientation with respect to the particle surfaces on the time scale of their interaction, leading to a "pinning" of the magnetic moments to the particles. As a consequence, an increasing part of the large particle will be in contact with the small particle, when the former slides over the latter under influence of the torque $\tau_{mag,dip}$. The distance on the large particle surface over which this contact takes place is indicated by the arc defined by the angle δ (see **Figure 1.7**c).

Moreover, as the induced displacement of the large particle occurs in a liquid with viscosity μ, a "magnetic tangential velocity" $v_{mag,tan}$ arises from instantaneous equilibrium [23] between magnetic and drag forces applied to the particle, as follows:

$$v_{mag,tan} = -\frac{\tau_{mag,dip}}{\left\|\mathbf{r_{1,2}}\right\| \cdot 6\pi\mu R f_D} \tag{1.6}$$

where R is the particle radius and f_D is the corrective drag coefficient taking into account the vicinity of the particles to the substrate. When the substrate is placed at the bottom of a microfluidic channel, in which a constant flow is applied, a Poiseuille flow develops in the microchannel and the local fluid velocity v can be calculated by solving the Navier-Stokes equation for incompressible flow in the microfluidic channel [45]. An additional viscous drag force will act therefore on the moving particle, and can be calculated using Equation (1.1), with v conveniently taken as the velocity of the unperturbed Poiseuille flow at the center of mass of the particle [23]. Because of the parabolic velocity profile in the microchannel, the drag force acting on the large particle will be strongest once it is on top of the small particle. As shown in section 1.3, this microfluidic viscous force can be tuned to detach the large particle, when no additional tethering forces are introduced to keep the two particles linked.

1.4.2 Experimental observation of the inter-particle interaction

To verify our theoretical model experimentally, we designed the simple magneto-microfluidic system shown in **Figure 1.8**a. Functionalized small superparamagnetic particles are patterned on a glass substrate, which is clamped to a PDMS half-microchannel. A constant vertical field at the glass substrate, as induced by a permanent magnet placed above the chip, imposes a constant magnetic moment to the immobilized particles. In particular, size, shape and position of the permanent magnet employed in our setup are dictated by two main needs: (i) a uniform magnetic induction at the glass surface over the whole detection area, with the same intensity of the one observed in all our previous protein detection experiments; (ii) an efficient light exposure to the immobilized particles, for accurate time-lapse observation of the magnetic particles via a high-speed camera. A ring magnet (10 mm outer diameter, 4 mm inner diameter, 5 mm height), with magnetization of ~1040 kA/m, positioned above the chip at 10 mm distance from the glass substrate allows satisfying both the aforementioned requirements. The central hole allows perfect

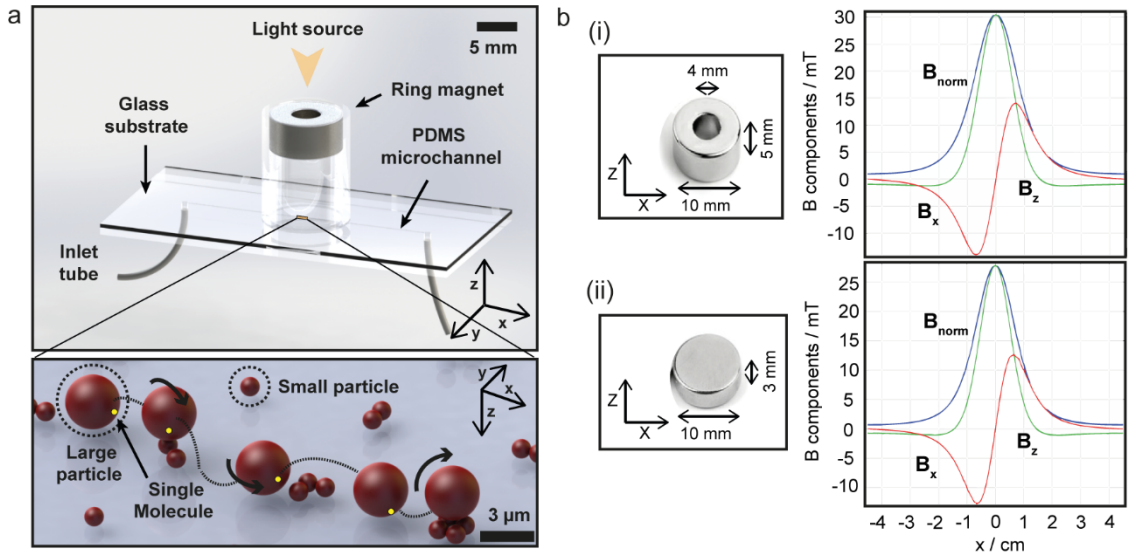

Figure 1.8 | Microfluidic platform for the experimental observation of magnetic particle-scanning. (a) Schematic representation of the magneto-microfluidic device used for investigating the "magnetic particle-scanning" mechanism. (b) Spatial distribution of the magnetic induction components ($\mathbf{B_x}$ and $\mathbf{B_z}$, according to the axis system defined in text) and the total intensity ($\mathbf{B_{norm}}$) along the bottom of the microfluidic channel, as simulated via 3D FEM for 2 different magnet geometries: a ring magnet (I) and a disc magnet (ii), positioned respectively 10 mm and 9 mm below the channel bottom. In both cases the detection area is centered with respect to the magnet top face, at x=0.

light transmission through the magnet. The size of the magnet and its position with respect to the detection area are adjusted according to the results of 3D FEM Comsol simulations of the magnetic induction distribution for different configurations. In **Figure 1.8**bi we report the spatial distribution of the magnetic field induction components at the glass chip surface, for the magnet configuration used in our experiments and mentioned above. At 10 mm distance from its top face, the ring magnet produces a magnetic induction profile on the detection area which is basically equal to the one of a disc magnet of same magnetization and similar dimensions (**Figure 1.8**bii), as the one employed in our previous microfluidic experiments (section 1.3). A peak of 27-30 mT in the central region of the magnet is obtained in both cases, as further confirmed via Gauss meter measurements.

In our experiments, a diluted suspension of large superparamagnetic particles is injected in the microchannel at 100 nL/s flow rate, this value being obtained from the previously described optimization process of the assay specificity (section 1.3). Under these magnetic and drag force conditions, large particles gently slide over the substrate and interact with the small particles, as described further and shown in **Figure 1.9**.

Figure 1.9a describes the behavior of a large particle in vicinity of a small particle, as obtained from the modeling corresponding to the described experimental conditions. Three distinct phases are defined for an inter-particle contact event: (i) transport of a large particle by viscous drag forces (in the time interval t_2-t_1); (ii) encounter with a small particle (at t_2) and contact during a time interval t_3-t_2, when the large particle is subjected to the magnetic torque; and (iii) large particle release inside the channel, in case no tethering force is linking the two particles. The contact

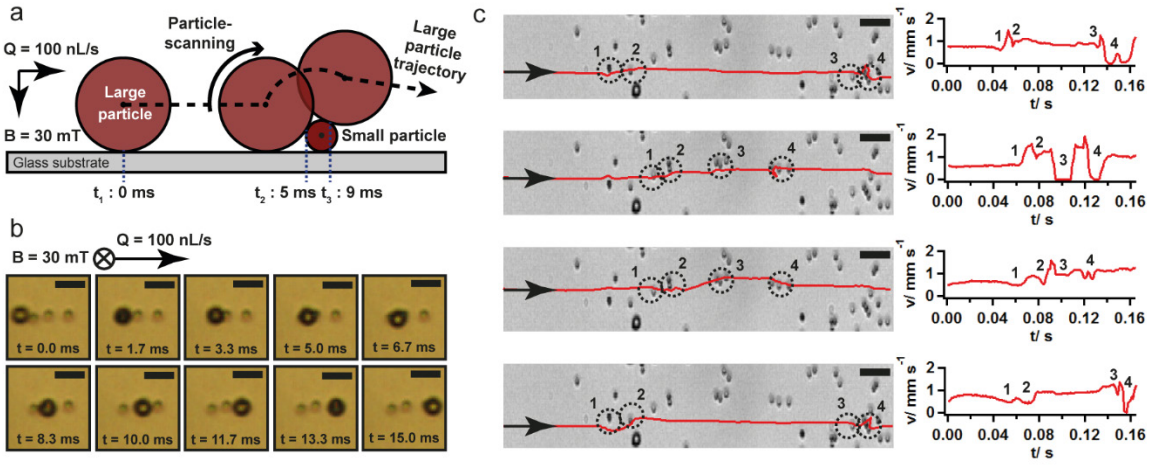

Figure 1.9 | Experimental observation of magnetic particle-scanning. (a) Schematic motion of a large particle in the detection area in the presence of a small particle, as obtained from a Matlab simulation, for an external magnetic field B = 30 mT and flow rate Q = 100 nL s^{-1}. A total contact time of ~4 ms is estimated between the two particles. (b) Motion of a large particle over the detection area, for B = 30 mT, Q = 100 nL s^{-1}, as experimentally observed via a high-speed camera. Scale bar = 5 µm. (c) Experimental tracks and velocity profiles for four different large particles, for B = 30 mT, Q = 100 nL s^{-1}, extracted from a video taken at 1200 fps. At each encounter with an immobilized small particle, a large particle undergoes both in-plane and out-of plane displacements. Scale bar = 10 µm.

time between the two particles is estimated by taking into account two contributions: the local velocity v of the fluid, as simulated by FEM, and the magnetic tangential velocity $v_{mag,tan}$ of the rotatory movement, calculated in Matlab using Equation (1.6). Neither in the experiment nor in the model, ligand-receptor forces between the two particles are included, yet. A contact time of approximately 4 ms between the two particle surfaces is calculated, in good agreement with the experimental result of **Figure 1.9**b.

In **Figure 1.9**c we report the trajectories of four different large particles, taken from a 1200 fps video, as they flow over the small particle-patterned area. Multiple in-plane reorientations and trajectory deviations of each flowing particle can be observed at each encounter with a small particle. Moreover, the velocity plot associated to each trajectory allows extracting further information about the out-of-plane particle movements. Large particles flow at relatively constant velocity (0.8-1 mm/s) on the glass surface and abruptly decelerate while in close proximity to any immobilized particle. The small peaks in the velocity profiles correspond to sudden increases of the velocity upon detachment of a large particle sitting on top of a small particle (time t_3 in **Figure 1.9**a), where hydrodynamic flow and drag force is maximum.

1.4.3 Increasing the ligand-receptor encounter probability

In this subsection we estimate the gain in ligand-receptor encounter probability induced by the scanning mechanism, under our standard experimental conditions. **Figure 1.7**c already showed the increase of contact area of a large particle with an immobilized small particle due to the sliding motion induced by the magnetic torque. In this schematic picture, all the elements of the system were aligned along a symmetry plane defined by the flow direction and the vertical axis, i.e. the

trajectory of the large particle is constrained within this plane. However, in reality, as already suggested by **Figure 1.9**c, this symmetry is rarely conserved. The contact between a large and a small particle mainly occurs out of this symmetry plane, giving rise to a lateral displacement and extra lateral components of the magnetic and hydrodynamic forces. In successive contact events with a number of small particles, this gives rise to the scanning of a significantly larger part of the surface of the large particle than shown in **Figure 1.7**c. **Figure 1.10**a, case i. (top) shows the contact of the large particle while moving in the presence of the magnetic field that pins the magnetic moment, but without the immobilized small particles. In this case, the particle simply slides over the flat substrate and "probes" it with only one point, because of the spherical geometry, as already demonstrated by others [2]. Therefore the ligand-receptor encounter probability is expected to be very low, especially for single molecule detection. When the large particle moves in the symmetry plane and small particles are present, the contact point describes a line on the surface of the large particle (**Figure 1.7**c), increasing somewhat the chance for ligand-receptor encounter (**Figure 1.10**a, case ii. (center)). Even when multiple small particles are explored, as the orientation of the large particle is not altered, the same portion of the large particle surface is each time scanned. If we now consider the real case, where lateral displacements of the large particle occur, a different section of the large particle surface is explored at each interaction with a small particle dot (**Figure 1.10**a, case iii. (bottom)). It is interesting to note that, up to now, we assumed that the particles are solely exposed to magnetic and hydrodynamic forces. Nevertheless, other surface interactions of different origin, such as electrostatic, chemical or friction forces, may introduce an additional torque [54], which would even be more beneficial for enhancing this reorientation phenomenon.

The attempt frequency of ligand-receptor binding corresponds to the rate of large particle reorientation events and can be strongly enhanced by precisely controlling the arrangement of the immobilized small particles. In particular, we designed different regular patterns of immobilized small particles and developed a particle-tracking Matlab code to predict the trajectory of the large particles over them (see subsection 1.5.5). **Figure 1.10**b shows an array of isolated dots of four small particles at 9 µm inter-distance, allowing a high density of small particles while still avoiding magnetic cross-interaction between adjacent dots, with the trajectories of five large particles moving over the pattern. A 6.5° tilting angle of the dot pattern with respect to the flow direction **Figure 1.10**c) was found to be a good choice for increasing the number of encounters, in comparison to the geometry shown in **Figure 1.10**b. Again, we fabricated this optimized small particle array via electrostatic self-assembly on a micropatterned APTES layer [39]. The full array is made up of ten 250 µm × 250 µm sections, for a total number of ~8000 small particle dots. Under our standard experimental conditions ($B_{ext,z}$=27-30 mT, Q=100 nL/s), we found that a single large particle encounters on average 20 small particle dots over the length of each section (**Figure 1.10**d), resulting in about 200 encounters over the full length of the array (**Figure 1.10**e).

To estimate the gain in ligand-receptor encounter probability induced by the scanning mechanism, we calculate below the probability to successfully bind the large particle $P_{capture}$ for the three cases described in **Figure 1.10**a, adapted to our real experimental conditions. As shown in **Figure 1.10**f, the scanning mechanism is expected to introduce a dramatic enhancement of the particle capture

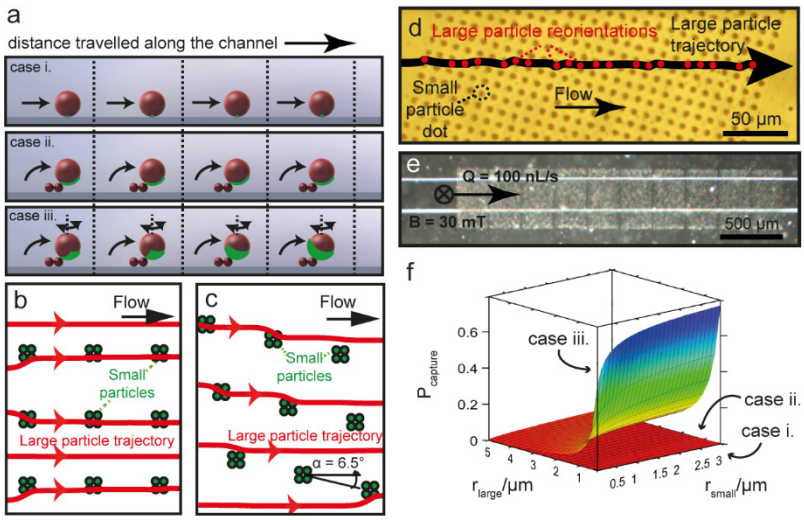

Figure 1.10 | Estimation of ligand-receptor encounter probability. (a) Large magnetic particle moving in a magnetic field that pins its magnetic moment (top) in absence of immobilized small particles, (center) in presence of small particles, but only moving in the symmetry plane (no lateral displacements) and (bottom) under our experimental conditions, where lateral displacements of the large particle occur as well. In the last case, a different section of the large particle surface is explored at each interaction with a small particle dot. (b,c) Simulated large particle trajectories on (b) a non-tilted and (c) a 6.5° tilted regular array of 4 small particles per pattern, iteratively traced by combining FEM simulations and Matlab analytical calculations. The tilted pattern guarantees more frequent encounters between immobilized small particles and flowing large particles. (d) Trajectory of a large particle on a tilted small particle array, under our standard experimental conditions ($B_{ext,z}$=27-30 mT, Q=100 nL/s), as experimentally observed using a high-speed camera. Red dots are used to visualize the large particle reorientation events (~20 over a 250 µm-long array). (e) Optical microscopy photograph of the particle array used for protein detection experiments. (f) Capture efficiency $P_{capture}$ calculated for the three situations of **Figure 1.10**a as function of the radii of the large and small particles using Equation (1.7),(1.8) and (1.9), taking N=1 and r_{ligand} = 2.2 nm. The cases i. and ii. are not easily distinguishable on this graph (even though case i. always induces a smaller $P_{capture}$ than case ii. by at least two orders of magnitude) so that this representation merely emphasizes the increased $P_{capture}$ from case iii.

probability. The large particles can be in first approximation considered as spheres where only a fraction of the surface is covered by ligands and can be bound to the receptors on the small particles. We also assume that the surface concentration of ligands is well below saturation, so that there is no interaction between ligands. Ideally, capture is immediately triggered when a ligand-covered part of the surface encounters the dot pattern. The probability to successfully bind the large particle $P_{capture}$ is therefore directly related to the capability of the device to intercept this small area over the whole particle surface. To estimate $P_{capture}$, we consider three situations:

(i) No scanning (Figure 1.10a, case i. (top)): in this case, the large particle surface is not scanned by small particles, as detailed above. However, its orientation is still pinned by the magnetic field. Hence, as detailed by others [2], and assuming a perfectly spherical geometry, the contact between the large particle and the sensing surface is reduced to a single point and $P_{capture}$ is the ratio of the part of the particle surface that is effectively covered with ligands over the whole particle surface:

$$P_{capture} = \frac{N \cdot r_{ligand}^2}{4 \cdot r_{large}^2} \tag{1.7}$$

with *N* the number of ligands on the large particle surface, r_{ligand} the average radius of a ligand molecule and r_{large} the radius of the large particle. This probability is evidently extremely low for single molecule carrying particles.

(ii) Scanning, but no lateral forces (Figure 1.10a, case ii. (center)): all the forces and displacements are constrained into a single vertical plane, thus preventing the lateral rotational reorientation described earlier. Hence, even if the large particle is scanned by many successive small particle dots, the output will be the same for each encounter, and the same fraction of the large particle surface will be examined. The particle is expected to keep the same orientation during its trajectory across the full surface of the device. In this case, the length of the device does not enhance $P_{capture}$, as only the initial contact point of the arc that is defined by the angle δ will be determining for successful capture. Hence:

$$P_{capture} = \frac{N \cdot \delta \cdot r_{ligand}}{\pi \cdot r_{large}} \tag{1.8}$$

(iii) **Scanning and reorientation** (**Figure 1.10a, case iii. (bottom)):** if the full scanning mechanism is enabled, the orientation of the large particle can change at every encounter with any of the N_{dots} dots composed of the small particles. Hence, if $P_{capture,i}$ is the probability that the large particle is captured on the ith dot of small particles, we can write that:

$$P_{capture} = \sum_{i=1}^{N_{dots}} P_{capture,i} \tag{1.9}$$

Given the sequential scanning of the large particle by the array of dots, a binding at the ith dot is equivalent to (i-1) non-binding encounters with the (i-1) previous dots in the trajectory of the large particle, followed by a successful encounter on the ith dot. If we introduce P_{SB}, the probability of a successful binding of the large particle upon an encounter with a small particle dot, we obtain the following expression for $P_{capture,i}$:

$$\mathrm{P_{capture,i}} = \mathrm{P_{SB}}(1 - \mathrm{P_{SB}})^{\mathrm{i}-1} \tag{1.10}$$

Hence, $P_{capture}$ can be written as:

$$\mathrm{P_{capture}} = \mathrm{P_{SB}} \sum_{\mathrm{i}=0}^{\mathrm{N_{dots}}-1} (1 - \mathrm{P_{SB}})^{\mathrm{i}} = 1 - (1 - \mathrm{P_{SB}})^{\mathrm{N_{dots}}} \tag{1.11}$$

This expression is equivalent to considering the large particle immmobilization event as a stochastic process in which the binding is tested N_{dots} times, with a probability of success P_{SB}, until a successful event is obtained. As expected, this value tends to 1 as N_{dots} increases towards infinity. Furthermore, P_{SB} is the probability of ligand-receptor binding upon inter-particle encounter. The

probability P_{SB} can therefore be evaluated using the expression of $P_{capture}$ detailed for case ii (Equation (1.8)). The Equation can also be linearized, assuming that P_{SB}<<1, so that:

$$P_{capture} = 1 - \left(1 - \frac{N \cdot \delta \cdot r_{ligand}}{\pi \cdot r_{large}}\right)^{N_{dots}} \sim N_{dots} \frac{N \cdot \delta \cdot r_{ligand}}{\pi \cdot r_{large}} \tag{1.12}$$

In **Figure 1.10**f, $P_{capture}$ has been calculated for these three situations, using the full equation for situation iii., with r_{small} the radius of the small particle, taking N=1 and r_{ligand} = 2.2 nm (the Stokes radius of TNF-α monomer was estimated as 2.2 nm at pH=7.0) [35], showing indeed the dramatically higher $P_{capture}$ for case iii.

Finally, it has been here assumed that the large particle can fully rotate, and none of its degrees of freedom is constrained. As the orientation of the large particle is magnetically pinned, this assumption can be refined by multiplying the expressions of $P_{capture}$ detailed in the text by a factor η, equal to the ratio of the large particle surface accessible to the small particle scanning to its total surface. Indeed, due to the magnetic pinning, the top section of the large particle ideally will never encounter the small particle dots. The value for η can be obtained from the angle δ defining the length described by the inter-particle point of contact during large and small particle interactions (see **Figure 1.7**c):

$$\delta = \arccos\left(\frac{r_{large} - r_{small}}{r_{large} + r_{small}}\right) \tag{1.13}$$

The surface of the large particle that is accessible for contact with a small particle dot, $S_{accessible}$, is described by the solid angle obtained by the rotation of δ around the vertical axis, so that

$$S_{accessible} = 2\pi r_{large}^2\big(1 - \cos(\delta)\big) \tag{1.14}$$

Hence,

$$\eta = \frac{2\pi r_{large}^2\big(1 - \cos(\delta)\big)}{4\pi r_{large}^2} = \frac{1 - \cos(\delta)}{2} = \frac{r_{small}}{r_{large} + r_{small}} \tag{1.15}$$

While this simple model already shows that both the scanning and the reorientation of the large particles improve the capture probability, however, this is only an approximation for the behavior of the real system. Indeed, in this estimation it was assumed that the changes in the orientation of the particle between the interactions with the immobilized surfaces were completely random. In our system, these interactions are more appropriately described by a single point of contact that is randomly diffusing over the surface of the particle until it hits a bound Ag. A random walk description would therefore be a much better approximation than a succession of independent tests of the stochastic variable. During a true random walk, the probability for the next movement is the same for any direction. In our case, as the molecule is moving in the direction of the flow, a movement of the point of contact on the surface of the particle in the direction of the flow is more likely. However, as detailed in the previous description, the system is not perfectly symmetric, and random rotation along the z axis, changes in direction, out-of-plane contacts, *etc*. are all expected

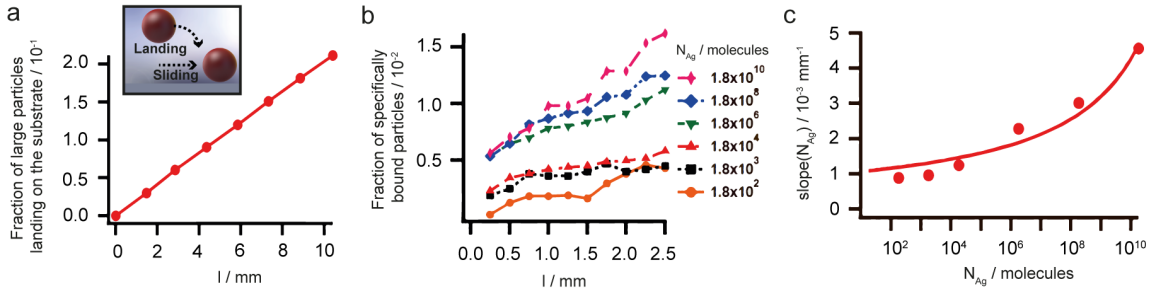

Figure 1.11 | Study of the particle capture efficiency vs. length of the channel. (a) Calculation of the fraction of the large particles that have landed on the substrate as a function of the distance in the microchannel for our standard experimental conditions. Insert: schematic illustration of the "landing" and "sliding" regimes of a large particle. (b) Experimental fraction of large particles captured as a function of the channel distance, for different concentrations of TNF-α molecules spiked in FBS under our standard experimental conditions. (c) Slopes obtained from the experimental curves shown in (b) as a function of the number of Ag molecules. The full line shows a fit of the experimental data with the model established in Equation (1.24).

to enhance the reorientation rate of the bead, so that the trajectory of the point of contact on the surface of the sphere is not a straight line in the direction of the flow, but is actually randomized by the constant rotation and re-orientation of the particle. Hence, the point of contact can potentially then move in any direction, even though the direction of the flow would be the one associated to the highest probability. We hence assume that this behavior can be modelled as a random-walk. Overall, this approximation is found to describe accurately the behavior of the system and to be in good agreement with the experimental data, thus supporting this hypothesis (see further).

1.4.4 Evaluation of the particle binding along the detection area

As the number of particles specifically captured on each section of the small particle dots landscape can be easily assessed by microscopic observation, this analysis allows for the study of the capture probability as a function of the distance travelled within the channel. As shown in the insert of **Figure 1.11**a, two different regimes can be identified when a particle is injected into the detection channel. First, it is transported by the parabolic flow, while magnetophoretically attracted to the bottom of the channel by the external magnetic field. We refer to this as the "landing" regime. The graph of **Figure 1.11**a shows the fraction of the large particle population that has reached the substrate as a function of the distance in the microchannel for our typical experimental conditions (see subsection 1.5.5 for details of the model calculation). Once a particle has "landed" on the substrate, the scanning mechanism starts, during which the former slides over the surface of the substrate, at a speed v_0~0.8-1 mm/s for our typical experimental conditions, until it is eventually captured by a small particle dot.

Figure 1.11b shows the experimental fraction of large particles captured as a function of the channel distance, for different concentrations of TNF-α molecules spiked in FBS. To emphasize the capability of the device for detection of very low amounts of target molecules, we report, instead of the concentration, the number of molecules present in the 5 µL sample injected in the chip N_{Ag}. The fraction of large particles is experimentally obtained by simply counting the number of particles present on each 250 µm long section of the small particle dot pattern (see **Figure 1.10**e). As

expected, this fraction increases linearly with distance, and the slope of this line increases with N_{Ag}. In our experiments, the captured fraction *vs.* distance curves show an initial offset at the beginning of the sensing region (i.e. a non-zero fraction at x=0 mm on **Figure 1.11**b), increasing with N_{Ag}. This offset can be explained by the important number of large particles that have landed in the micro-channel region upstream of the small particle landscape and are moving over the substrate. Upon their encounter with the first small particle detection section, a relatively high amount of large particles is therefore initially captured.

The curves of **Figure 1.11**b are linearly fitted and the slope (≡ *slope(N_{Ag})*) of these fits is presented as a function of N_{Ag} in **Figure 1.11**c. Very strikingly, the dependence of *slope(N_{Ag})* on N_{Ag} is strongly sub-linear, i.e. lower concentrations are much more effectively detected than higher ones. We will see in the next section that the physical quantity *slope(N_{Ag})* can be conveniently used to quantify $P_{capture}$. Furthermore, the result *output(N_{Ag})* of our assay, defined as the fraction of all injected large particles captured over the ten small particle detection sections, is found in good approximation to be proportional to *slope(N_{Ag}).* The coefficient of proportionality was evaluated as 4.4±0.5 mm (for the 5 datasets corresponding to concentrations above the LOD, average ± standard deviation (SD)). The variation of this coefficient is found to be very small (about 11% of the average) over the 8 orders of magnitude considered in our assay.

1.4.5 Random walk description of the scanning process

In agreement with previously reported results [55, 56], we assume that the binding probability of the large particle $P_b(l)$, as a function of the distance l travelled in the microchannel along the small particle landscape, satisfies a 1st order reaction kinetics law:

$$P_b(l) = P_0\left(1 - e^{-l/L}\right) \tag{1.16}$$

where L is the characteristic distance of successful binding and P_0 the probability of binding for a large particle for $l \to +\infty$. The factor $P_0 \leq 1$ can be evaluated from the geometry of the system, and can be approximated by η, the ratio of the large particle surface accessible to scanning to the small particle dots to its total surface (see above). The data of **Figure 1.11**b show that we are in the linear part of the function of Equation (1.16), i.e. $l \ll L$, and that $P_b(l)$ can be approximated by the quantity $P_0 l/L$. This fact is also confirmed by the low fraction (< 2%) of particles captured over the length of the channel. The linear-like curves shown in **Figure 1.11**b also allows one to relate the variations of *slope(N_{Ag})* (i.e. the captured fraction vs. l) to $P_b(l)$ and hence to the inverse of the characteristic length L. As the particle is moving at an average speed v_0 in between the small particle dots, the value of L can be related to a characteristic binding time $\tau \equiv L/v_0$, so that *slope(N_{Ag})* and Equation (1.16) can be readily expressed as function of time.

The interactions between the large particle and the immobilized small particle dots can be approximated by a random walk of the contact point over the surface of the large particle, as illustrated in **Figure 1.12**a. This stochastic displacement is assumed to stop when the point of contact

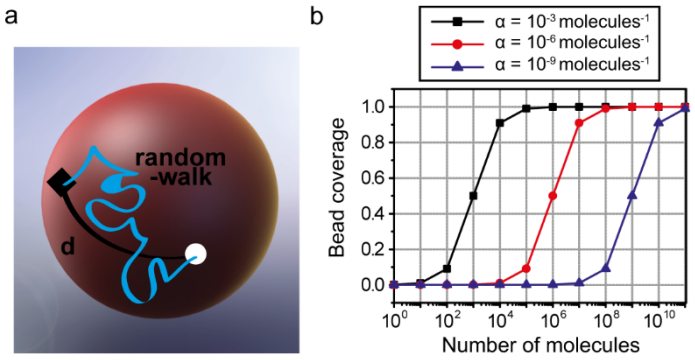

Figure 1.12 | Random walk description of the particle scanning. (a) Schematic representation of the random walk modeling approach: the contact point between large and small beads describes a random-walk on the surface of the large beads, from the initial contact point to the location of a captured ligand molecule. (b) Calculation of the large bead coverage of captured ligand molecules, assuming a Langmuir relationship for molecule capture, and different values of the parameter α (10^{-3}, 10^{-6} and 10^{-9} molecule^{-1}).

between a large and a small particle coincides with the position of an Ag bound to the large particle. Mathematically, the mean first passage time (t_{MFP}) for a point randomly walking over the surface of a sphere from a starting point to a target position can be generally expressed as [57]

$$t_{MFP} \propto A + B\ ln(d) \tag{1.17}$$

where d is a dimensionless distance separating the starting point of the walk on the sphere from its target position, and A and B are constants depending on the scales of the system. Additionally, it can be proven that the factor A is significant only for low d [57]. We therefore formulate the assumption that the contribution of A can be neglected, in agreement with the observation that $P_b(l)$ is low (L is large), and hence the random walk length d necessary to encounter an Ag is large as well. This approximation is highly suited for low densities of bound Ags on the large particle surface, and especially for single molecule detection. The distance d can be approximated by considering the optimal uniform distribution of $N_{Ag,bound}$ points, which correspond to locations of Ags bound on the surface of a sphere. We assume here a homogeneous distribution of Ag over the surface of the particle with radius r_{large}. In this case, it can be demonstrated that [58, 59]

$$d \sim \left(\frac{8\pi}{\sqrt{3}}\right)^{1/2} \frac{r_{large}}{\sqrt{N_{Ag,bound}}} \tag{1.18}$$

and hence that

$$t_{MFP} \propto ln(\gamma'\ N_{Ag,bound}) \tag{1.19}$$

where γ' is a constant. To express $N_{Ag,bound}$ as a function of N_{Ag}, we assume a Langmuir relationship between these two values [60, 61], with α being a constant and $N_{Ag,bound\ max}$ the maximum number of Ag that can be bound to the particle surface:

$$N_{Ag,bound} = N_{Ag,bound\ max} \frac{\alpha N_{Ag}}{1 + \alpha N_{Ag}} \propto \frac{\alpha N_{Ag}}{1 + \alpha N_{Ag}} \tag{1.20}$$

The Langmuir relationship typically describes the amount of molecules adsorbed onto a surface in equilibrium with a solution of known concentration. For low amounts of Ag molecules, the relation between the amount of free and bound Ag is linear. Above a certain concentration of Ag, the response saturates, as all the possible adsorption sites are occupied. **Figure 1.12**b shows profiles obtained from Equation (1.20) for different values for α. The Langmuir equation shows a sigmoid shape when displayed with a logarithmic abscissa axis. In this case, the parameter α controls the Ag concentration at which the system switches from the linear to the saturated response. It largely accounts for the affinity of the ligand to the receptor as well as the mixing efficiency in the chip. The system saturates at lower Ag concentrations for larger α values.

Finally, t_{MFP} can be expressed as a function of the experiment-derived time τ. To do so, we define the instantaneous capture probability $p_c(t)$, i.e. the probability that the particle is captured exactly at the time t. The latter is by definition the probability density function of $P_b(t)$:

$$p_c(t) \equiv \frac{dP_b}{dt}(t) \tag{1.21}$$

As we assumed that the random walk stops when the point of contact between a large and a small particle coincides with the position of an Ag bound to the large particle, the first passage of this point of contact at the position of an Ag will result in the binding of the large particle. Hence, t_{MFP} can be evaluated from $p_c(t)$ following

$$t_{MFP} = \int_0^{+\infty} u\, p_c(u) du = \int_0^{+\infty} u\, \frac{dP_b}{du}(u) du \tag{1.22}$$

And, by solving the integral by partial integration, we find that $t_{MFP} = P_0 \tau$ and t_{MFP} is directly proportional to τ. We can therefore write the following expression for $slope(N_{Ag})$:

$$slope(N_{Ag}) = \frac{P_0}{L} = \frac{P_0}{\tau\, v_0} = \frac{{P_0}^2}{t_{MFP}\, v_0} \tag{1.23}$$

As $output(N_{Ag})$ is proportional to $slope(N_{Ag})$, and using the expression for t_{MFP} (Equation (1.22)), we can write that

$$output(N_{Ag}) = \frac{\beta}{ln(\gamma \frac{\alpha N_{Ag}}{1 + \alpha N_{Ag}})} \tag{1.24}$$

where β and γ are constants. For N_{Ag}=0, an output value of 0 is obtained.

This analysis shows that α, which is obtained from the Langmuir equation, controls the concentration from which the Ag coverage over the bead is sufficiently high, so that the assumption $l << L$ is not satisfied anymore. As shown in **Figure 1.13**a, the curves actually diverge towards +∞ for $N_{Ag} = 1/(\gamma - 1)\alpha$. The parameter therefore accounts for the binding affinity and the mixing efficacy in the system. The effect of the negative parameter β is shown in **Figure 1.13**b. Here, no

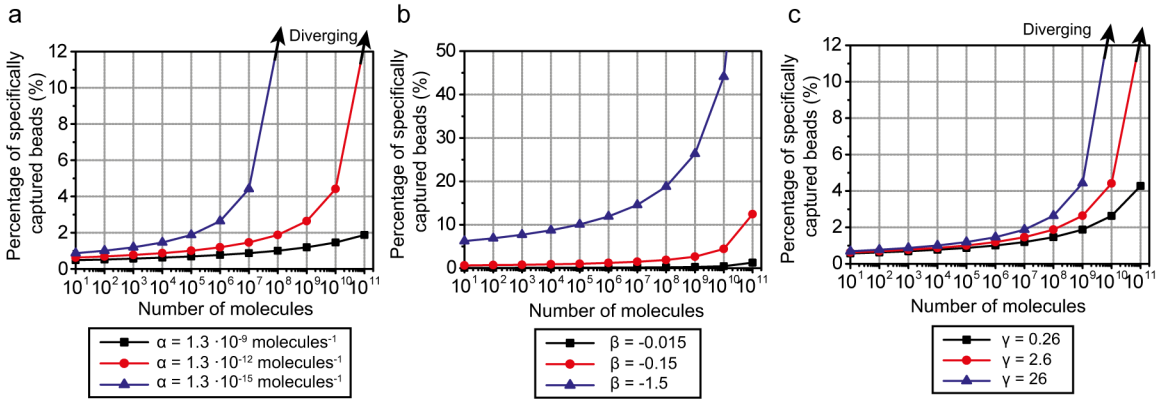

Figure 1.13 | Analysis of the model fitting parameters. Plots of the function describing the assay readout (Equation (1.24)), for different values of the fitting parameters (a) α is a parameter, β= -0.15, γ =2.6, (b) β is a parameter, α= 1.3x10^{-12} molecule^{-1}, γ=2.6, and (c) γ is a parameter, β= -0.15 and α= 1.3x10^{-12} molecule^{-1}.

obvious effect can be observed, as this is merely a multiplication constant which scales the magnitude of the response. More importantly, it is expected that this value depends on P_0 and v_0, from Equation (1.23), and more generally on the beads size. Indeed, through the intercept angle δ, these can modulate the surface of the large bead that is accessible to the small bead, and therefore the overall capture probability. This parameter also accounts for the random walk over the bead surface (Equation (1.17)). In this case, a slower random walk (or a larger t_{MFP}) would indicate a larger parameter B in Equation (1.17), and a smaller β. This would result in a lower output, at fixed N_{Ag}. This also corresponds, qualitatively, to an increase in L. Finally, in the case of γ (**Figure 1.13**c), a behavior similar to α is observed. High γ values induce a divergence of the curve for lower N_{ag}. From Equation (1.19), γ accounts for the distribution of the ligands over the large bead surface (Equation (1.18)). It is therefore determined by the geometry of the large bead. Large γ values therefore indicate a faster saturation of the large bead surface with Ag because of a shorter inter-adsorbed Ag distance d (Equations (1.18) and (1.19)).

As stated above, this model is valid only for low Ag amounts. At higher concentrations, Equation (1.16) cannot be linearized anymore, and a different expression for the *output*(N_{Ag}) function is expected. Moreover, the Ag concentration is largely assumed to be a continuous function in the model, whereas it actually describes a low number of discrete molecules. The result from this fact is that the response of the system is discrete too. For instance, if only one Ag is injected, only two results can theoretically be obtained for *output*(N_{Ag}), 0 and 1/3500 (as 3500 large beads were injected). In this case, it is expected that the result obtained from *output*(N_{Ag}) would then be better described by the average of several experiments. We can therefore speculate that, at very low Ag amounts, the output of the assay would be seen as a stochastic variable with two states (*output*(N_{Ag})= 0 and *output*(N_{Ag})= 1/3500) and the model would return the expected value of this random variable. Technically, this case was not encountered in our analysis, as the LOD of the assay was found to be ~200 Ag and the signal obtained for this value is at least an order of magnitude above 1/3500.

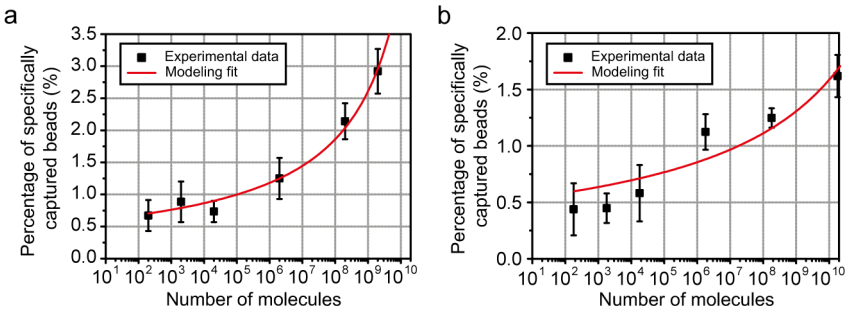

Figure 1.14 | Explanation of the assay dose-response curves. Experimental data for the detection of (a) biotinylated anti-streptavidin and (b) TNF-α in FBS (n= 3-4, the error bars are SD), with the corresponding fitting curves. The solid lines are fit to the experimental values following the expression for *output(N_{Ag})* detailed in Equation (1.24). The R^2 values are 0.99 and 0.86 for the fittings of the biotin/streptavidin and TNF-α datasets, respectively.

1.4.6 Explanation of protein detection experiments

The biotin/streptavidin binding experiments performed in FBS can be now fitted with Equation (1.24), as shown on **Figure 1.14**a. Furthermore, the data obtained for the detection of TNF-α in FBS are also fit with this model (**Figure 1.14**b). The different values obtained from the fitting, i.e. the parameters α, β and γ and the maximum coverage of the particles over the range of concentrations considered in the experiment, as described by the Langmuir equation, are presented in **Table 1.1**. The critical factor for this fitting, the Langmuir adsorption constant α, is found to be much higher for the biotin/streptavidin ligand/receptor system than the one computed above for the TNF-α system (**Table 1.1**). This result is in good agreement with the very high binding affinity of biotin to streptavidin, in comparison to an Ag/Ab system. **Table 1.1** shows, in addition to the fit parameters, some representative dissociation constants K_D reported in the literature for the different systems detailed in this study. As mentioned above, α is an indicator of the efficacy of the Ag binding. A high α and a low K_D indicate a high binding affinity, as observed from the values shown on **Table 1.1**. Furthermore, the low values found for α are still in good agreement with the central assumption in the random walk model, i.e. that the coverage of Ag on the large particle surface is low. This guarantees that the system is far from saturation, and that Equation (1.16) can be approximated by a linear behavior.

It is interesting to compare our protein detection method with other magnetic particle-based techniques. Several recent reports have highlighted the capabilities of magnetic micro- and nanoparticles as carriers of the Ag or as detection labels for sensitive analyses [23, 24]. In a first class of devices, the Ag are initially bound to the surface of a microchannel, and are then detected by injecting Ab-labeled particles (“Ag on substrate”, see **Figure 1.15**). Other devices, like the one discussed here, present the specificity of tethering the Ag of interest on the particles and bringing the latter to the detection area by a microfluidic flow (“Ag on particles”). First of all, both approaches of these so-called “surface coverage” assays have resulted in an extremely low limit of detection. However, by comparing the dose-response curves, obtained over similar ranges of concentrations for these two types of devices (“Ag on substrate” vs “Ag on particles”), different behaviors have been observed.

Table 1.1 | Fitting parameters obtained from the data shown in Figure 1.14. The "maximum coverage" parameter shows the maximum fraction of the surface of the large particle covered by Ag over the experimental concentration range, assuming that this value follows a Langmuir isotherm dependence over N_{Ag}. Some representative values of the dissociation constants K_D of these ligand-receptor systems are also reported for comparison.

System	α / molecule^{-1}	β / a.u.	γ / a.u.	Maximum coverage	K_D / M
Biotin/ streptavidin in FBS	1.3×10^{-12}	-1.5×10^{-1}	2.6	2.5×10^{-3}	4×10^{-14} from ref. [62]
TNF-α in FBS	3.6×10^{-14}	-1.6×10^{-1}	1.3×10^{-1}	6.4×10^{-4}	2.2×10^{-9} – 7.8×10^{-9} from ref. [63]

In the 'Ag on substrate' setup (**Figure 1.15**), the Ag is bound to the bottom of a channel. Here, the detection process can be reduced to particles scanning linearly the surface of the channel, until they encounter an Ag. At low Ag concentrations, if enough particles have passed in the channel, so that all the adsorbed Ag are detected, the output is the amount of particles adsorbed onto the surface. As a consequence, the calibration curve is an adsorption isotherm, such as the Langmuir equation described on Equation (1.20). Interestingly, for this type of device, the concentration response drawn over a logarithmic scale typically is a sigmoid saturating at high concentrations [33, 64]. We note that a sigmoid is a good approximation of a Langmuir isotherm on a logarithmic scale. The flattening of the curve typically limits the capabilities of these chips at very high concentrations. For a Langmuir adsorption isotherm, this saturation theoretically occurs for concentrations larger than $1/\alpha$ (where α is the Langmuir constant from Equation (1.20)). It is important to note that the $1/\alpha$ parameter is actually setup-dependent. As seen from the curves shown in refs. [33, 64], the $1/\alpha$ value is quite low in this type of devices (below 10^{10} Ag). The plateau, on the right side of the sigmoid, can be observed on the same range of concentrations considered in our device, indicating concentrations above the $1/\alpha$ limit. However, for comparable ranges of concentrations, the "Ag on particles" setup is not saturating, even at the highest concentration considered, which are still below their $1/\alpha$ limit (**Table 1.1**). This phenomenon is beneficial for widening the dynamic range of the device, and stems from the sub-saturation coverage of the Ag on the large magnetic particles. The regime of this device is therefore sub-linear, but saturation of the output will nevertheless occur if N_{Ag} exceeds $1/\alpha$. Furthermore, the particle surface scanning process, described extensively before, is expected to improve the behavior of the device especially at low Ag surface coverage, as indicated by the graphical representation of $P_{capture}$ (**Figure 1.10**f), and by the comparison of Equation (1.7) and (1.12). It is important to notice that, for both geometries, the dose-response curves are expected to flatten for extremely high concentrations. This can be due to saturation of the binding sites or steric hindrance effects and is taken into account by the adsorption isotherm, present in the two different designs, describing the binding of the free Ag to their substrate. Also, in this high concentration limit, steric hindrance related to the size of the large particle will comparatively limit the efficiency of substrate binding as, above a certain Ag concentration on the surface of a large particle, not all Ags can contribute in improving the binding efficiency of the particle.

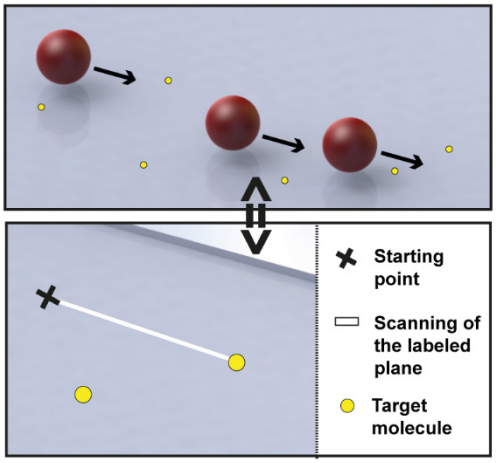

Figure 1.15 | Principle of the "Ag on substrate" magnetic particle-based system. The target Ag molecules are bound on the substrate and Ab-functionalized large particles scan the surface for detection. Counting of the immobilized particles quantifies the number of ligand-receptor bindings and hence the Ag concentration on the surface.

1.5 Materials and Methods

1.5.1 Chemicals and materials

4-inch 550 µm thick Si and float glass wafers, de-ionized water (DIW) were obtained from the Center of Micro- and Nanotechnology of EPFL. GM 1075 SU-8 negative photoresist was purchased from Gersteltec (Pully, Switzerland). AZ ECI 3027 positive photoresist was purchased from AZ Electronic Materials (Wiesbaden, Germany). PDMS Sylgard 184 was acquired from Dow Corning (Wiesbaden, Germany). 1 mL borosilicate H-TLL-PE syringes were purchased from Innovative Labor Systeme (Stutzerbach, Germany). Micro-line ethyl vinyl acetate tube with 0.51 mm inner and 1.52 mm outside diameters was bought from Fisher Scientific (Wohlen, Switzerland). Neodymium magnets were acquired from Webcraft (Uster, Switzerland): (i) disc magnets with 6 mm diameter, 2 mm thickness (product no: S-06-02-N, magnet-magnet attraction force: ~ 10 N); (ii) disc magnets with 10 mm diameter, 3 mm thickness (product no: S-10-03-N, magnet-magnet attraction force: ~ 18 N); (iii) ring magnets with 4 mm inner and 10 mm outer diameters, 5 mm thickness (product no: R-10-04-05-N, magnet-magnet attraction force: ~ 25 N) The APTES solution (product no. 440140), Phosphate Buffered Saline (PBS) 10x concentrate solution (product no. 5493), Tween-20 (product no. 1379) and biotin (product no. B4501) were purchased from Sigma-Aldrich (Buchs, Switzerland). Dynabeads MyOne Streptavidin C1 (small particles), Dynabeads M-280 Streptavidin (large particles), recombinant mouse TNF-α, biotinylated polyclonal rabbit Ab specific to mouse TNF-α and FBS dialyzed were purchased from Life Technologies (Zug, Switzerland). Biotinylated goat anti-streptavidin and streptavidin were obtained from Vector Laboratories (Reactolab SA, Servion, Switzerland). Fetal Bovine Serum (FBS) standard quality was bought from PAA Laboratories (Chemie Brunschwig AG, Basel, Switzerland) and Pluronic F-127 was purchased from BASF (Basel, Switzerland). A PBS (0.15 M NaCl, 0.01 M phosphate, pH 7.4) solution was prepared by diluting a PBS 10x concentrate solution. PBS-Tween 1% solution was made by diluting 1% (volume / volume) Tween-20 in PBS. A buffer solution was prepared by diluting 0.08% (weight/volume)

Pluronic F127 in PBS. To reach Ag concentration levels used in the experiments, the biotinylated anti-streptavidin was diluted in PBS or FBS dialyzed and mouse TNF-α was prepared in FBS standard quality.

1.5.2 Fabrication of the glass detection chip via electrostatic self-assembly of magnetic particles

0.6 µm thick AZ ECI 1512 photoresist was patterned on a glass wafer using standard photolithography techniques [40].The pattern features a 250 µm x 2.5 mm area containing ~8000 dots, 1 µm in diameter, with a 10 µm inter-distance between adjacent dots. The wafer was diced into chips with 28 mm × 25 mm area. The chip surface was activated in air plasma for 40 s at 12 W and 1 mbar pressure. 1 % (volume / volume) APTES solution diluted in DIW was spin-coated at 5000 rpm. The chip was baked at 100°C for 10 min. The resist was ultrasonically removed in acetone for 2 min. The chip having a pattern of 1.5 µm APTES dots was stored at -18°C until further use. For small particle patterning, the chip was reversibly bonded to a dedicated PDMS chip, containing a microfluidic channel with 60 µm height and 500 µm width. The glass detection chip and this PDMS chip were tightly clamped for leak-proof sealing. For electrostatic binding of the small particles to the APTES dot pattern, a 10 µL solution of small particles was introduced inside the microfluidic channel at a 150 nL s^{-1} flow rate using a syringe pump. Hereafter, a 30 µL PBST 1% washing step was conducted at 5 µL s^{-1}. Finally, the glass detection chip was separated from the PDMS and was ready to be clamped to the PDMS microfluidic chip.

1.5.3 Fabrication of the microfluidic chip for the experimental analysis of the magnetic-particle scanning

PDMS microchannels were replicated using SU-8 microstructures on Si wafers. First a 60 µm-thick SU-8 layer was patterned through photolithography processes. Liquid PDMS mixture (10:1 base:cross-linker weight ratio) was degassed, poured on the SU-8 mold and cured at 100 °C for 1 h. The cured PDMS layer was peeled off from the mold and the fluid injection holes were punched through the chip. The PDMS chip was then surface-activated with air plasma at 12 W for 1 min, together with a glass support, to which the PDMS was successively bonded. For experiments with magnetic particles patterned on APTES (i.e. glass detection chips), the cured PDMS piece was instead clamped to the glass substrate by using a custom-made polymethylmetacrylate (PMMA) holder. PDMS channels used for these analyses size 60 µm in height and 250 µm in width.

1.5.4 Magneto-microfluidic setup for the experimental analysis of the magnetic-particle scanning

1 µm-diameter superparamagnetic particles were randomly patterned at the bottom of the microfluidic channel by strong unspecific adsorption on the glass substrate. A ring magnet (10 mm outer diameter, 4 mm inner diameter, 5 mm height) was positioned below the microfluidic chip, at 10 mm distance from the channel bottom, by using a custom-built PMMA holder. This resulted in a constant vertical field induction $B_{ext,z}$ = 30 mT over the substrate detection zone at the level of the immobilized particles, as measured via Gauss meter and simulated by FEM. The full assembly was flipped upside down and positioned on the stage of an inverted microscope (Zeiss Axiovert

S100), to allow light transmission through the ring magnet and light collection from below the chip, via a high magnification objective (LD EC Epiplan-Neofluar, 50x, Zeiss). The flow manipulation in the microfluidic channel was performed by precision syringe pumps (Nemesys, Cetoni, Korbussen, Germany). 3 μm-diameter superparamagnetic particles were diluted in buffer solution to a final concentration of 0.01 mg (~7×10^4) particles per mL. The particle suspension was then injected in the microchannel at 100 nL/s flow rate. High-speed camera tracking (MC-1363 camera, Mikrotron, Unterschleissheim, Germany) was used to accurately monitor individual particles during their transport in the microchannel, at 1200 frames-per-second rate. The gradient of the external magnetic field in the direction normal to the substrate plane resulted in the effective magnetophoretic attraction of the particles towards the glass substrate. The field intensity was chosen to be weak enough not to capture large particles on the glass surface, where they could hence still move and being transported by the flow across the small particle pattern. Image analyses were performed using the ImageJ software (Bethesda, Maryland, USA).

1.5.5 3D particle tracking in the magneto-microfluidic chip

Magnetophoretic separation of magnetic particles in microfluidic channels has been previously explored both experimentally and via numerical calculations [65]. The transport of superparamagnetic particles through a two-dimensional potential energy landscape has been empirically and numerically studied as well [66]. In this work, however, we propose a new versatile simulation method, which allows predicting and analyzing both these phenomena with the same approach. Our method is based on three main steps: (i) a finite element method (FEM) calculation of the 3D magnetic field landscape using COMSOL 4.2a software (COMSOL Multiphysics, Zürich, Switzerland); (ii) a FEM calculation of the 3D velocity distribution in the microfluidic flow, using COMSOL 4.2a; (iii) importing the magnetic and fluidic results in Matlab (Mathworks, Natick MA, USA), for the analytical calculation of the magnetic particle trajectories. Specifically, to construct the large particle trajectories reported in **Figure 1.10**b-c, the values of magnetic induction in the presence of the small particle pattern are first simulated by FEM (see **Figure 1.7**b). Discrete values of magnetic flux density components are extracted in a 3D grid format (with 200 nm spacing between adjacent points) and imported in Matlab, where intermediate values inside the grid can be obtained by 3D interpolations among adjacent points. A zoom on the central portion of the channel is considered, and a flow velocity v of about 1 mm/s is calculated via FEM over the whole selected area, for the portion of the fluid in proximity of the small particle pattern, where the large particles are flowing. The magnetophoretic velocity of a large particle at each specific location is successively calculated on Matlab, by imposing instantaneous equilibrium between magnetic and drag forces acting on the particle. A few trajectories for different particles are iteratively traced, with a sampling time of 1 μs, by tracking particle positions and recalculating velocities at every step. The same approach is employed to simulate the magnetophoretic attraction of the particles towards the glass substrate upon their injection in the microfluidic channel (**Figure 1.11**a). The magnetic induction distribution inside the full microchannel volume in the presence of the permanent magnet is calculated via COMSOL, as well as the fluidic flow profile. Discrete values of magnetic flux density components in the 3D microchannel space are then imported in Matlab, together with the

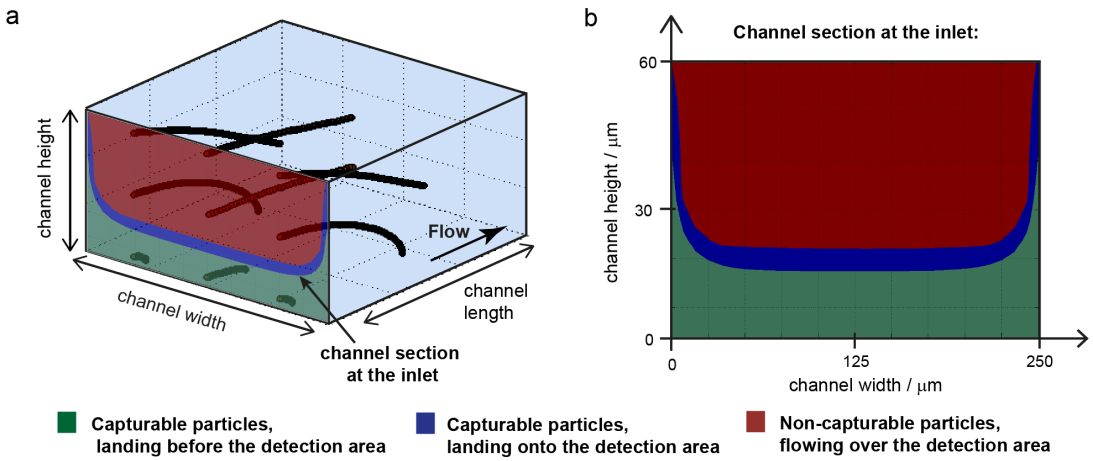

Figure 1.16 | Simulated 3D trajectories of superparamagnetic particles. (a) Magnetophoretic trajectories of 9 large particles entering the microfluidic channel at different locations, as iteratively traced by employing our 3D particle tracking approach, for our standard experimental conditions. (b) Projection of the large particle trajectories on the channel inlet section. The trajectories of particles entering the channel at each possible position are simulated to predict their landing location inside the microchannel. If a homogeneous distribution of particles is assumed at the channel inlet, this simulation directly allows estimating the number of particles effectively reaching the detection area (**Figure 1.11**a).

values of the local fluid velocity components. Trajectories for large particles entering the channel at different locations are iteratively traced, with a sampling time of 1 µs (**Figure 1.16**a).

In our assay, only the central region along the microchannel width (from 50 µm to 200 µm on **Figure 1.16**b), corresponding to flow velocities higher than 90% of the maximum velocity, was considered for the particle counting. From the 3D tracking presented here, we evaluate than only ~22% of the large particles enter in contact with this area and are therefore potentially taken into account for the Ag detection. As detailed in the main text, for the lowest concentration of Ag detected (about 200 molecules), about 0.5 % of the 3,500 large particles, i.e. ~18 large particles, are captured on this region. If we now assume that all the large particles, instead of only 22 % of the total number, were to land on this detection zone, this would mean that about 80 large particles would be captured, corresponding to the detection of 80 single molecules out of 200. This fact further emphasizes the capabilities of our technique at low Ag concentration.

1.6 Conclusions

We presented a novel magnetic bead surface coverage assay, in which “large” (2.8 µm) antibody (Ab)-functionalized magnetic beads captured their antigen (Ag) from a serum and these Ag-carrying beads were subsequently exposed to a surface pattern of fixed “small” (1.0 µm) Ab-coated magnetic beads. When the system was placed in a magnetic field, the magnet dipole attractive interactions between the two bead types were used as a handle to approach both bead surfaces and assist with the Ag-Ab immunocomplex formation, while unspecific binding (in absence of an Ag) of a large bead was limited by the viscous drag forces in the microfluidic flow. Despite the fact that this novel immunoassay technique showed unprecedented performance, an extensive understanding of its enhanced specificity and sensitivity were still lacking. Therefore, a predictive

model for the engineering and optimization of this type of assay was highly desirable, as it would have become the key towards a further assay development and exploitation.

We first focused on the understanding and enhancement of the assay specificity, mainly aiming at optimizing the main parameters of the assay ptotocol (i.e.: magnetic fields, flow rates,…), to minimize its background noise signal. By combining FEM simulations with analytical calculations, we built a predictive model of the force balance acting on the two types of superparamagnetic beads employed in our method. We demonstrated that the fine-tuning of magnetic dipolar and microfluidic viscous forces acting on the microparticles represents the key for extremely selective protein detection in our assay. The dynamic nature of the detection method is moreover believed to be crucial, as well. Thanks to our model, in fact, the perfect balance between magnetic dipolar and viscous forces could be set during the whole assay time, so that Ag-carrying beads do not have to be first immobilized and then washed out of the detection area to eliminate the unspecifically adsorbed ones. This dynamic way of operating, where the “washing step” occurs somehow at the same time of the immunocomplex formation itself, allows not only minimizing unspeficic Ag-Ab binding, but also reducing the overall assay time and complexity. These results were confirmed by experimental observations.

In a second phase of the project, we dealt with a more sophisticated modeling of the assay, where the whole 3D motion of the microparticles was considered, to enhance the probability of specific immunocomplex formation and, hence, further increase the assay sensitivity. In this context, we introduced and investigated the principle of “magnetic particle-scanning” for on-chip detection of biomolecules. We experimentally observed this phenomenon in a new custom-built magneto-microfluidic chip and theoretically described it by a random walk model. This analysis emphasizes the basic mechanisms controlling our type of assay. As the ligand and receptors are bound to surfaces, it is critical to increase the probability that they encounter each other, thus triggering recognition and a capture event. Simulating the trajectory of the point of contact with a random walk can account well for the behavior of the system. This fact also suggests that the working principle of the whole immunoassay can, under certain assumptions, be reduced to this stochastic motion of the contact point. Our model shows that magnetic particle-scanning results in a very high probability of immunocomplex formation for very low Ag concentrations, which directly translates into an extremely low limit of detection, down to the single molecule-per-particle level. On the other hand, for high Ag concentration the binding efficiency is lowered, which is key to the large dynamic range of the dose-response curves. This new modelling approach finally allowed to fully understand key unexplained features of the dose-response curves of our assay: (i) its ability to detect an output signal (i.e. the bead number count) for extremely low Ag concentrations, and (ii) an output signal of the assay that was non-linear with respect to the Ag concentration. Our full theoretical description resulted in the accurate fit of experimental dose-response curves obtained previously for two different ligand-receptor systems (biotin/streptavidin and anti-TNF-α/TNF-α).

Our modeling tools moreover allowed better understanding the behavior of other types of particle-based heterogeneous immunoassays, which also exhibited very low limits of detection. Several so-called “magnetic surface coverage immunoassays” based on fluidic flow discrimination have in

fact recently shown extreme sensitivity [1, 3, 19]. We can now assert that this may be related to the possibility of fine-tuning immunocomplex-induced binding forces between the magnetic beads and the surface, and viscous drag forces induced by the flow that remove/wash non-specifically attached beads from the substrate. Also the rapid and dynamic extraction of target Ags from the raw sample, and subsequently processing the magnetic beads in clean buffer solution is in favour of reproducibility and accuracy of an assay. Although ultrasensitive protein detection has been demonstrated generally at the cost of more complex and sophisticated assay principles and protocols, we think that the mentioned magnetic bead surface coverage assays will provide interesting options for the development of future sensitive and accurate immunoassays. Besides sensitivity, robustness, low-cost, large dynamic range, accuracy and multiplexing capability are other important criteria that will determine the success of such analytical system, and these mostly outstanding issues will have to be addressed in future.

Overall, we therefore think that, despite the specific nature of the magnetic particle scanning principle we proposed, our analysis has wider application potential and will be helpful for designing and explaining new types of on-chip surface coverage immunoassays, which exploit the binding of a particle to a substrate via an Ag.

Chapter 2 Microwell templates for lens-array and cell-array self-assembly

Abstract We propose a novel versatile method for the rapid and versatile fabrication of arrays of microspheres to be used as lenses of desired geometry and optical properties. Our method is based on the electrostatic self-assembly of dielectric microspheres in Parylene-C/glass well templates, with the array geometry patterned in the Parylene-C layer via standard microfabrication techniques. While different particle sizes and materials can be used to tune the light focusing properties of the microlenses, we demonstrate here a process that uses 3 µm size melamine spheres. We use optical tweezers to assess the electrostatic nature of the microsphere binding mechanism by manipulating the patterned spheres. We demonstrate that our method ensures extremely fast and reliable array formation and offers moreover the possibility to reversibly assemble and disassemble the lens array by tuning the pH of the microsphere patterning and washing solutions. We then successfully employ our self-assembled lens arrays to detect gold and fluorescent nanoparticles (NPs) during their motion in water-based medium, through a standard low magnification/low numerical aperture microscope objective. The same technique could also used for immunodetection of biomolecules immobilized on gold NPs in buffer and, in future, it may develop into a versatile tool to detect nanometric objects of environmental and biological importance, such as toxic nanomaterials, viruses or other biological agents. An analogous self-assembly strategy is then proposed for isolating yeast cells (*Saccharomyces cerevisiae*) in femtoliter wells for subsequent analyses within the microwell array at single-cell resolution. In this work, the single-cell patterning technique is combined with the use of a digital microfluidic (DMF) platform to create a tool for conducting studies on isolated non adherent cells in a high-throughput way and with enhanced spatio-temporal resolution.

This chapter is an adapted version of the following publications:

- **M. Cornaglia**, H. Yang, T. Lehnert, and M.A.M. Gijs. Electrostatic self-assembly of microsphere lens arrays. MNE 2014 - the 40th International Conference on Micro and Nano Engineering, Lausanne, Switzerland, September 2014.

- H. Yang, **M. Cornaglia**, and M. A. M. Gijs, Photonic Nanojet Array for Fast Detection of Single Nanoparticles in a Flow. *Nano Lett* 15, 1730-1735, doi: 10.1021/Nl5044067 (2015)

- P. Tewari Kumar, K. Vriens, **M. Cornaglia**, M. A. M. Gijs, T. Kokalj, K. Thevissen, A. Geeraerd, B.P.A. Cammue, R. Puers and J. Lammertyn, Digital microfluidics for time-resolved cytotoxicity studies on single non-adherent yeast cells. *Lab Chip*, doi: 10.1039/C4LC01469C (2015)

2.1 Introduction

Different methods for the fabrication of microlenses and microlens arrays have been developed in the last years, reflecting the key role of optics, opto-electronics and photonic systems at enhancing the performance of communication, processing, sensing and display systems [67]. Most of these techniques are however rather expensive, time-consuming and definitely not suitable or versatile enough for fast prototyping of lab-on-a-chip systems. Furthermore, considerable interest recently arose for high-resolution sensing systems that can detect nano-objects and even individual molecules in liquids [68, 69]. Advanced optical techniques have been proposed for sensitive detection of nano-objects, but typically required high-end, expensive, and bulky experimental setups [70, 71]. If direct optical detection of NPs in liquids could be possible using a standard microscope, this would lead to more affordable and portable sensing applications. However, conventional optics only permits detecting relatively large objects, because the scattered light intensity decreases with decreasing size and the light collection capability of a standard microscope objective is limited by its numerical aperture (NA) [72]. Therefore only NPs that are either larger than several hundred nanometers or having extremely enhanced scattering probability can be detected. While a microsphere is known to act as a focusing microlens [73], when it has a refractive index contrast relative to the fluid medium that is less than 2:1 and a diameter between several to tens of wavelengths (λ), a highly-focused propagating beam from the shadow-side surface of the microsphere is generated due to constructive interference of the light field [74]. This beam is termed as “photonic nanojet” and has a sub-λ full-width-at-half-maximum (FWHM) transverse dimension and typically is several λ in length. A very interesting predicted property of a photonic nanojet is that the presence of a particle, much smaller than λ and positioned within the nanojet, significantly enhances back-scattering of the light through the microsphere. High-refractive index microspheres embedded in a PDMS medium containing dispersed 50 nm size gold NPs confirmed a back-scattering intensity two times larger than that caused by the isolated microsphere itself indeed [75]. If appropriate microspheres could be integrated into microfluidic devices for direct detection of objects with a dimension much smaller than λ, this could be of high interest for many environmental and biological sensing applications.

Yang *et al.* [76] recently demonstrated the use of 3 and 9.75 µm dielectric microspheres as *in situ* lenses for the enhancement of fluorescent signals for on-chip immunoassays (**Figure 2.1**a). In their system, fluorescent immunocomplexes were built by successive incubation steps on APTES microstructures, which were patterned on a glass substrate, at the bottom of a microfluidic channel. Microparticles were then carefully positioned on top of the immunocomplexes for signal amplification, by transporting them through the microfluidic channel via a 2 nL/s flow. Such a very low flow rate value had to be used to allow the particles’ temporary immobilization on top of the patterned microstructures by weak electrostatic interactions with the APTES features themselves. For direct nanoparticle observation within the microfluidic flow, a more robust and versatile method for the on-chip microsphere integration was however highly desirable. Among other techniques for particle micropatterning, an interesting approach was recently proposed by Witters *et al.* [77]. In their method, a droplet containing the microparticles to be immobilized is transported multiple times above a microwell array, by means of electrostatic droplet actuation on a DMF

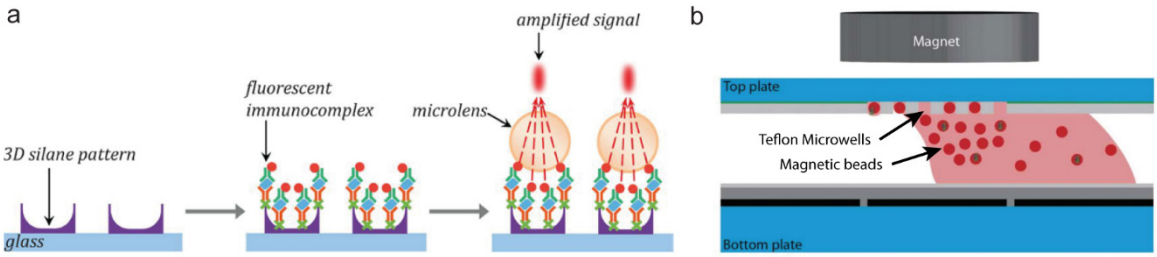

Figure 2.1 | Microsphere optical properties and micropatterning technique. (a) Schematic representation of the use of microlenses for on-chip immunofluorescence amplification, as reported by Yang *et al.* (reproduced from [76]). Fluorescent immonocomplexes are immobilized onto APTES microstructures. Dielectric particles are then used as spherical microlenses to amplify the fluorescent signals, therefore enhancing the immunoassay sensitivity. (b) Schematic representation of the magnetic bead patterning technique described by Witters et al. (reproduced from [77]). Beads are attracted inside a microwell array by an external magnetic field, while transported by a DMF actuated microfluidic droplet.

platform (**Figure 2.1**b). As the microwell size is designed to host single microparticles, this technique ideally allows "printing" isolated particles over the whole array area. However, a relatively low patterning efficiency was observed in absence of additional forces pulling the particles towards the microwells' side. High loading yield was only demonstrated for magnetic beads, in combination with external magnetic forces, while the patterning of dielectric particles still remained an open question.

To provide an answer to the aforementioned needs, we developed a new method for rapid and versatile fabrication of dielectric microsphere arrays at the bottom of microfluidic channels. Our technique relies on the electrostatic self-assembly of the microspheres in a microfabricated Parylene-C template on a glass substrate. The chip was then illuminated through an optical microscope for the generation of photonic nanojets in the microfluidic medium, where we tested the capability of our device of detecting moving NPs. Furthermore, we managed to generalize our microsphere patterning method to create a more versatile technique for micro-arraying various entities of similar size, being them particles of different materials, shapes and properties or even single non-adherent cells.

Such a technological development brought us at addressing another crucial biological question by means of our micro-arraying technique. An emerging need in the bio-medical research community is in fact represented by the development of platforms that support single-cell analysis of non-adherent cells with high spatio-temporal resolution. The free-floating nature of non-adherent cells usually complicates their analysis with respect to the case of adherent cells. When large populations of non-adherent cells have to be studied at single-cell level, flow-cytometry is usually the preferred solution, which however does not allow obtaining data which are spatially and temporally resolved [78]. Moreover, only a few systems are currently available for precise positioning of non-adherent cells. Hence, many microfluidic-based solutions are currently being proposed as new tools for cell manipulation, by means of hydrodynamic forces [79, 80] or forces of other nature, such as, for instance, electrical [81], optical [82] or gravitational [83]. Nevertheless, most of these solutions still suffer from a combination of drawbacks: (i) the demand for large sample and reagent consumption for cell manipulation and analysis; (ii) microchannel clogging events when

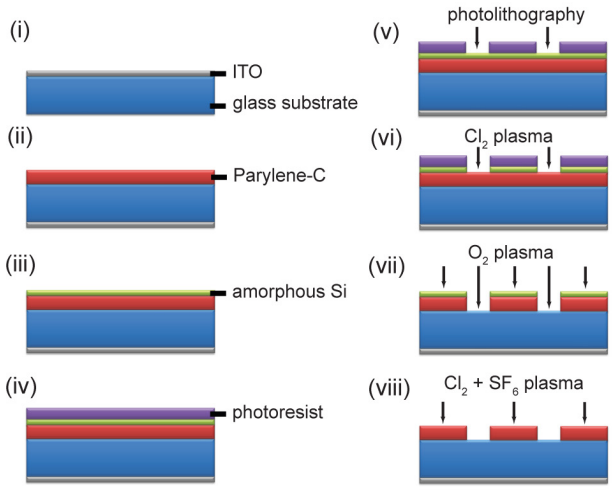

Figure 2.2 | Microfabrication process flow for Parylene C/glass well templates. (i) ITO is deposited on the back-side of the glass wafer, followed by the deposition of (ii) Parylene-C and (iii) amorphous Si on the front-side of the wafer. (iv) Photoresist is spin-coated on the wafer and (v) patterned by standard photolithography processing. (vi) Amorphous Si is etched by a Cl_2 plasma. (vii) The photoresist layer and Parylene-C are etched by an O_2 plasma. (viii) The amorphous Si hard-mask is etched by a Cl_2 plasma and the Parylene-C layer is treated by SF_6 plasma to enhance its hydrophobicity.

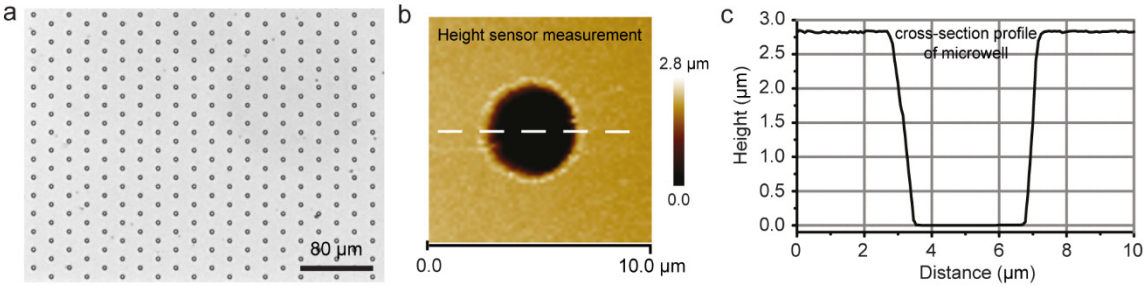

Figure 2.3 | Characterization of microfabricated array templates. (a) Micrograph of the microwell array template after fabrication. Microwells with a diameter of 3 µm are interspaced by 20 µm in both *x*- and *y*-directions. (b,c) AFM measurement on a 3 µm microwell, showing (b) the topography and (c) the profile along the dashed line in (b).

cell-rich samples have to be handled [84]; (iii) undesired biological effects, such as cell stresses, introduced by fluidic shear forces or other forces. To solve these issues, we developed a modified version of our microsphere self-assembly technique, which proved to be a new powerful tool to create micro-arrays of isolated non-adherent cells, for their study at high spatio-temporal resolution.

2.2 Microlens arrays for single-nanoparticle detection

2.2.1 Microwell template fabrication

Fused silica glass wafers (Ø4 in., 525 µm in thickness), photoresist AZ 1512, Parylene-C dimer, A174 silane and DIW were obtained from EPFL's Center of MicroNanoTechnology. The main fabrication steps of the template are schematically illustrated in **Figure 2.2**. A transparent and colorless layer (100 nm in thickness) of indium tin oxide (ITO, 90 wt% In_2O_3 and 10 wt% SnO_2) was first

deposited on the backside of a clean wafer via magnetron sputtering (Pfeiffer SPIDER-600, Pfeiffer Vacuum, Switzerland) and used as conductive layer for upcoming inductively coupled plasma (ICP) etching. After the silanization of the wafer by A174, the back-side was protected by ultraviolet (UV) tape. Then, a Parylene-C layer (3 µm in thickness) was coated on the glass wafer by chemical vapor deposition (Comelec C-30-S Parylene deposition system, Comelec, Switzerland). Afterwards, the UV tape was removed from the back-side of the wafer, leaving the Parylene-C membrane only on the front-side. An amorphous silicon hard mask (100 nm thickness) was deposited on the front side of the wafer by sputtering. This hard mask was then patterned by standard photolithography using AZ1512 positive photoresist (1.1 µm thickness) and ICP Cl_2 plasma etching (STS Multiplex ICP etcher, Surface Technology Systems, Newport, UK). The exposed Parylene-C was etched by O_2 plasma, and the photoresist layer was removed at the same time. The amorphous silicon hard mask was stripped by Cl_2 plasma, leaving the microwell array on the glass substrate. As the last step, the Parylene-C layer was treated with SF_6 plasma for 30 sec to increase its hydrophobicity [85]. Afterwards, the glass wafer was diced into small chips (16 mm × 30 mm) that were ready to be used for microsphere patterning.

In our design, microwells with a diameter of 3 µm were arranged over an area of 2 × 6 mm^2 in a hexagonal pattern, and separated in the x- and y-directions by an interspacing of 20 µm. The fabricated microwell array template is shown in **Figure 2.3**a. The topography of the microwells was characterized by AFM at room temperature using a Bruker FastScan AFM (Bruker AXS Inc., Madison, USA). **Figure 2.3**b shows the height measurement on a microwell, while the corresponding cross-section profile is shown in **Figure 2.3**c. The measurements show that the depth of the microwell after the fabrication is 2.86 µm and the diameter of the microwell is ~3 µm, which ensures single-microsphere-per-well patterning and accurate positioning of the microspheres.

2.2.2 Patterning of the dielectric microspheres

After the fabrication of the microwell array on the glass chip, the dielectric microspheres were patterned with an off-chip experimental protocol. Carboxyl-functionalized melamine microspheres with diameter of 3 µm were selected to be patterned into the microwells to generate a microlens array due to their high refractive index (n = 1.68), low light absorbance, and optimum light focusing capability in water [76]. According to previously published work [76], 3 µm diameter melamine microspheres generate maximum light intensity and smallest transverse dimension of the photonic nanojet, when the microspheres are immersed in water. For the patterning of the microlenses, the carboxyl-functionalized melamine microspheres were suspended in a droplet, which was then transported over the microwell surface multiple times (see **Figure 2.4**a). While the droplet was repelled from the hydrophobic surface of the Parylene-C, single microspheres were trapped inside the microwells, having hydrophilic glass bottoms.

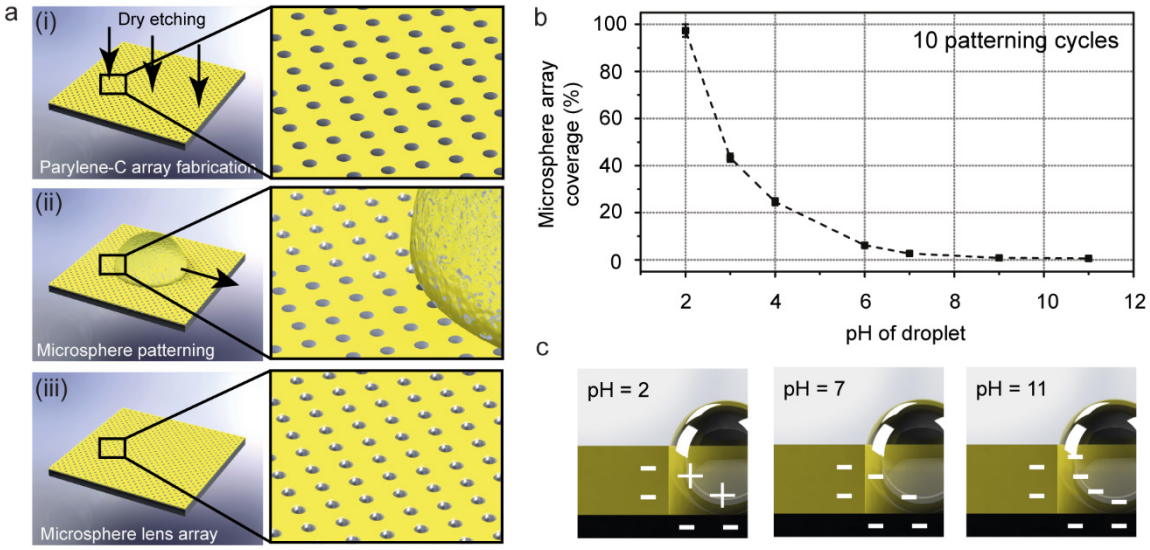

Figure 2.4 | Electrostatic self-assembly of dielectric microsphere arrays. (a) Schematic representation of the microsphere patterning process: (i) microfabricated Parylene-C microwell array; (ii) a droplet with suspended microspheres is transported over the hydrophilic microwells multiple times, during which microspheres get trapped; (iii) due to the geometry and surface charge of the microwells, the microspheres stay immobilized in the microwell pattern, also after removal of the droplet. (b) Microsphere loading efficiency as function of pH of the droplet. (c) Schematic illustration of the microsphere patterning at different pH conditions, indicating the electrostatic charges involved in the patterning process.

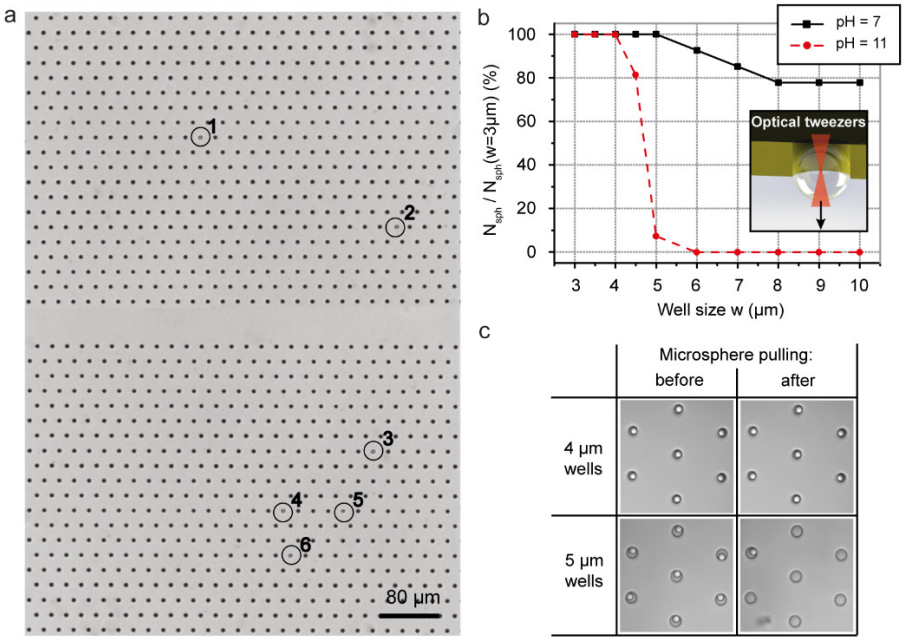

Figure 2.5 | Analysis of lens patterning and immobilization efficiency. (a) Micrograph of a representative microwell array after microsphere patterning at pH = 2. Over an area comprising 1160 microwells, only 6 microwells do not contain a microsphere after patterning (i.e.: patterning efficiency ~99.5 %). (b) Number of microspheres N_{sph} left within the microwell array as a function of well size *w* after application of optical tweezer forces, at relatively high pH conditions (pH>7). At constant pulling force, lower pH values and well size closer to the sphere size are beneficial for stronger electrostatic self-assembly forces, so that less microspheres can get removed from the microwells. (c) Representative micrographs of portions of 4 µm and 5 µm well arrays with patterned microlenses, before and after the application of optical tweezer forces on the spheres.

We investigated the electrostatic nature of the microsphere patterning mechanism by performing the experiments with microspheres diluted into buffer with different pH values. The working buffer was prepared by mixing different amounts of HCl or NaOH into PBS buffer. Thereafter, the stock solution of the carboxyl-functionalized melamine microspheres was 10× diluted into buffer samples at different pH values, ranging from 2 to 11. For each sample at different pH condition, a 6 µL droplet was transported over the microwell array for 10 patterning cycles (1 cycle = 1 passage of the droplet over the array) by using a pipette. As shown in **Figure 2.4**b, the microsphere loading efficiency strongly depends on the pH of the buffer used for patterning, which revealed the electrostatic nature of the patterning process. Indeed, higher loading efficiencies were obtained for lower pH values, as confirmed by considering the isoelectric point of the microspheres (~ 3), the Parylene-C layer (< 2) and the glass substrate (< 3) [86, 87].The best loading efficiency was obtained at pH = 2, condition at which the microspheres carry a positive surface charge (see **Figure 2.4**c**)**. By this patterning procedure a very high loading efficiency (> 99%) could be achieved, as shown in **Figure 2.5**a. Moreover, perfect lens immobilization was achieved, since all the microspheres stayed captured inside the microwells during the NP detection experiments – which were instead performed at pH=7.

A further analysis of the lens immobilization efficiency was moreover carried on by employing optical tweezers (NanoTracker, JPK instruments AG, Germany) to exert a constant pulling force on single patterned microspheres, immobilized within microwells of different sizes (**Figure 2.5**b,c). This analysis illustrates the crucial role of the interaction between spheres and microwell walls for the stable lens immobilization as well as the possibility of reversibly assemble and disassemble the lens array via electrostatic forces. In fact, all the microspheres are perfectly locked inside the microwells for well sizing less than 4 µm in diameter, while for larger microwells, the spheres can be still extracted from the template at relatively high pH values (i.e. pH ≥ 7). The strong dependence of this phenomenon on the pH of the microsphere solution is a further evidence of the electrostatic nature of the sphere “locking mechanism” inside the microwell template.

2.2.3 Microlens effect of the dielectric microspheres and NPs detection

In order to be employed for detection of NPs in a flow, the microsphere array was embedded in a microfluidic stream, by clamping the glass substrate to a PDMS half-channel. In order to verify the lens effect of the microspheres, PBS solution was first introduced into the microfluidic channel and the chip was illuminated by a mercury arc lamp from the bottom of the glass substrate (**Figure 2.6**a). A 20× objective with NA of 0.22 was used to image the top of the microsphere array, focusing on the focal plane of the microspheres. The microscopic image (see **Figure 2.6**b) indicated that the optical signal propagating through a microsphere is focused in a highly localized spot with enhanced intensity, i.e. the photonic nanojet, and the light intensity obtained along the cross section of the microsphere demonstrated that the microlens can provide a >3-fold light focusing capability, as shown in **Figure 2.6**c.

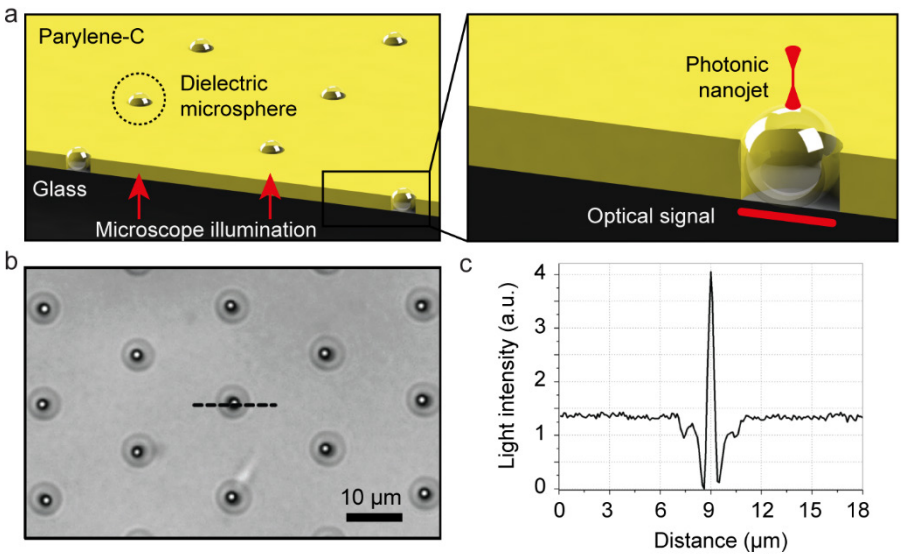

Figure 2.6 | Light focusing property of the microlens array. (a) Schematic representation of an array of microspheres while illuminated through a microscope objective. The light source beneath each microsphere is focused in a highly localized and intense spot, also named "photonic nanojet". (b) Microscopic image focused onto the plane of the nanojets emitted from the melamine microspheres (the focal plane corresponds to the plane at which the nanojets have maximum light intensity). The light intensity along the dashed line in (b) is shown in (c): the intensity of a photonic nanojet is typically >3 times higher than the background signal coming from the area with no microlenses.

We successfully employed our microlens array to detect the presence of gold and fluorescent nanoparticles in the microchannel, with NP size down to 50 nm and 20 nm respectively – i.e. well below the diffraction limit of the 20× microscope objective used for the detection. By using an array format for the microlenses, the same NP can be transported through a sequence of photonic nanojets placed in the same flow stream. The optical signal obtained from a row of lenses is then easily correlated to unambiguously prove the transit of even a single moving NP. Another advantage of using an array is that a larger region of the microfluidic channel is probed, which is advantageous for detecting low NP concentrations. First gold NPs in the 50-400 nm range were dispersed in DIW and introduced into the microfluidic channel at a flow velocity of ~10 µm/sec. **Figure 2.7**a shows that the presence of a 400 nm gold NP in the nanojet results in a back-scattered light intensity that is significantly enhanced with respect to that of a NP outside of the nanojet. **Figure 2.7**b shows the results obtained for 50 nm gold NPs: direct optical microscopy (without the microspheres) cannot resolve these NPs, which are instead still observable through the microlens array. We further tested our technique by using calibrated polystyrene fluorescent NPs with emission wavelength λ_{em} = 515 nm. NPs with size from 20 nm to 460 nm were dispersed in phosphate buffered saline (PBS)-Tween 20 (0.5% v/v) solution and introduced into the microfluidic channel. **Figure 2.8** shows the experimental results for NPs with diameter of 460 nm and 20 nm. When a fluorescent NP passed through a photonic nanojet, its fluorescent excitation was highly enhanced. For the used flow conditions, the NPs were typically exposed to the strong optical field in the nanojet for ~20 milliseconds. The fluorescent emission of the NPs was extremely bright, so that NPs down to 20 nm in diameter could be still distinguished when passing through a nanojet.

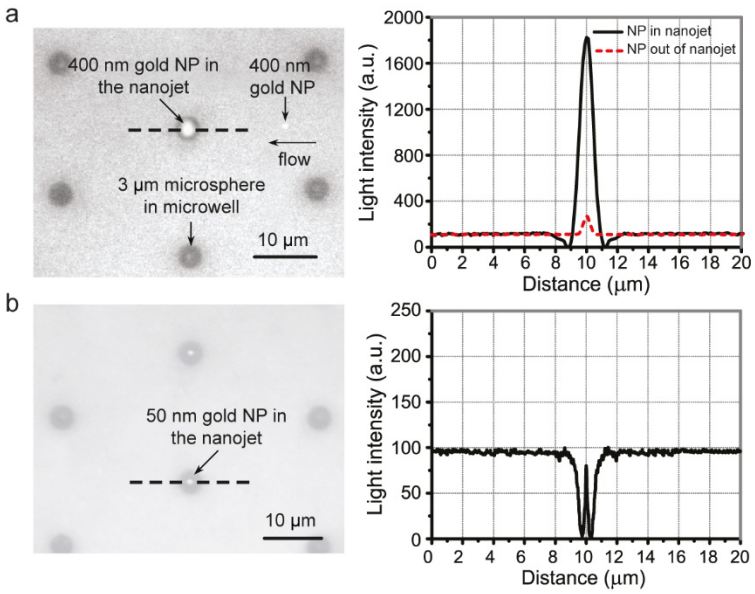

Figure 2.7 | Detection of gold NPs in a microfluidic flow. Backscattering intensity from gold NPs under white-light illumination. Microscopic images (left column) and intensity profiles along the dashed lines in the left panels (right column) for gold NPs sizing (a) 400 nm and (b) 50 nm. 400 nm gold NPs are still detectable when they are outside a nanojet, and their intensity profile is plotted on the corresponding right panel too.

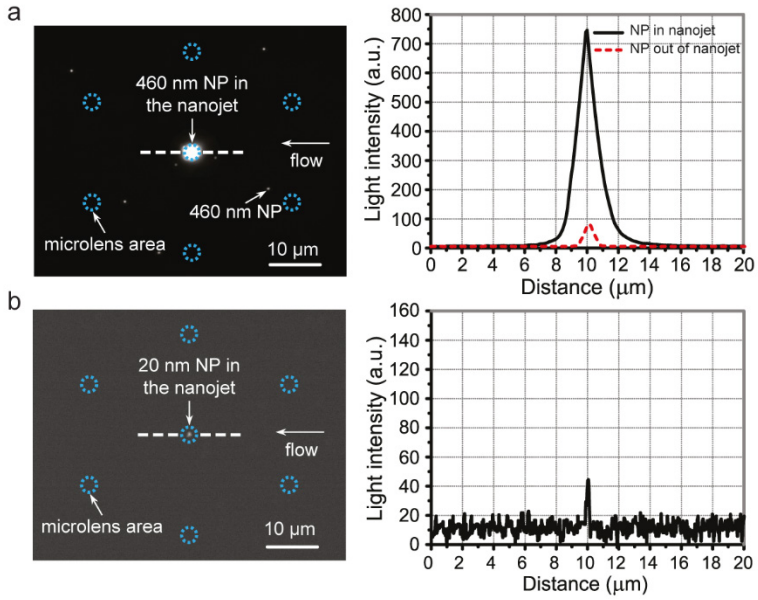

Figure 2.8 | Detection of fluorescent NPs in a microfluidic flow. Emission at λ_{em}=515 nm of fluorescent NPs when excited at a wavelength of λ_{ex}=505 nm. Microscopic images (left column) and intensity profiles along the dashed lines in the left panels (right column) for fluorescent NPs sizing (a) 460 nm and (b) 20 nm. 460 nm fluorescent NPs are still detectable when they are outside a nanojet, and their intensity profile is plotted on the corresponding right panel too.

2.3 Non-adherent cell patterning for single-cell analyses

2.3.1 Microwell template fabrication and well size optimization

For this set of studies, microwell templates were fabricated at the ESAT-MICAS cleanroom facility at KU Leuven (Leuven, Belgium), according to the process flow described by Witters and colleagues. [77] This microfabrication process flow is similar to the one described in **Figure 2.2**, with some process modifications related to the use of different materials for the template fabrication. In particular, microwells are here etched in a Teflon-AF® layer, deposited on an aluminum-coated glass substrate. This choice is dictated by the fact that, for this application, microwell templates are designed to be integrated in a DMF platform, instead of in a "channel-based" microfluidic device. Specifically, the microwell templates are employed in an electrowetting-on-dielectric (EWOD) DMF platform, which allows manipulating discrete liquid droplets on hydrophobic surfaces, by locally controlling the surface hydrophobicity via application of electric fields [88]. To ensure reliable droplet displacement, highly hydrophobic surfaces – such as Teflon-AF® layers – need to be used, while contacts for the local application of the electric field are patterned in the underlying aluminum layer.

The microwell size had to be tailored to allow fast reproducible patterning of single yeast cells of the *Saccharomyces cerevisiae* strain BY4741. The cell size distribution of this strain was measured via flow cytometry (BD Biosciences, San Jose, CA, USA) and ranges between 3.5 µm and 8 µm, with the majority of cells included in the 4.5-5.5 µm size interval. Cell seeding on the EWOD platform was first simulated off-chip, by displacing multiple times a droplet of cell suspension over the microwell template, similarly to what is described in **Figure 2.4**a. Templates with different microwell sizes where tested and microwells sizing 5.3 ± 0.1 µm resulted to be the most suitable for patterning single yeast cells over the whole array (see **Figure 2.9**). An interspace of 14 µm among adjacent wells was eventually chosen to prevent undesired contact among budding seeded cells, which could prevent correct cell isolation or extract seeded cells from the microwells at successive droplet passages.

2.3.2 Single cell seeding and cytotoxicity assays on the DMF platform

After the off-chip protocol optimization, the cell seeding technique was transferred onto the DMF platform and used for the rapid assembly of large arrays of thousands single-cells, for subsequent on-chip cytotoxicity assays. Specifically, this method was used to investigate the response of single yeast (*Saccharomyces cerevisiae*) cells to Amphotericin B (AmB), a cell membrane permeabilizing antifungal drug, able to induce programmed cell death when applied over a certain dose. A detailed description of the DMF device operation and of the performed assays is presented in [89]. Here only an overview of this work will be reported.

Briefly, 1 hour before seeding the yeast cells within the microwell array, cells were pre-treated with AmB at different concentrations, ranging from 0 µM to 200 µM, in a dimethyl sulfoxide (DMSO) background of 1 % (v/v). Afterwards, for each pre-treated sample, a 2.7 µL cell suspension

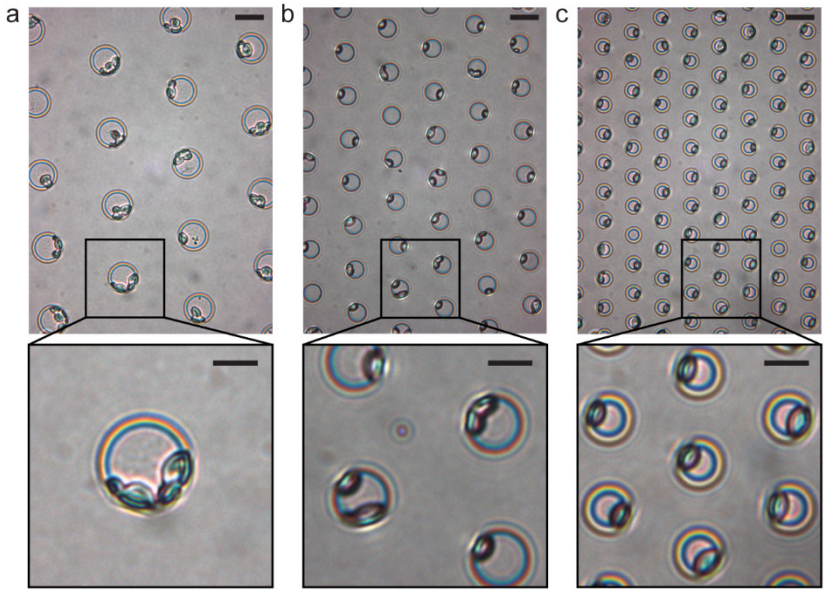

Figure 2.9 | Microwell size optimization for single-cell patterning. Micrographs of microwell templates upon off-chip cell patterning, with wells sizing (a) 12 µm, (b) 8 µm and (c) 5.3 µm. Both 12 µm and 8 µm well sizes result in patterning of multiple cells per well (see zooms of picture (a) and (b)). 5.3 µm wells allow instead patterning single cells in every microwell (see zoom of picture (c)), with high cell loading efficiency (e.g. ~97% in this case). Picture scale bars = 10 µm; zoom scale bars = 5 µm.

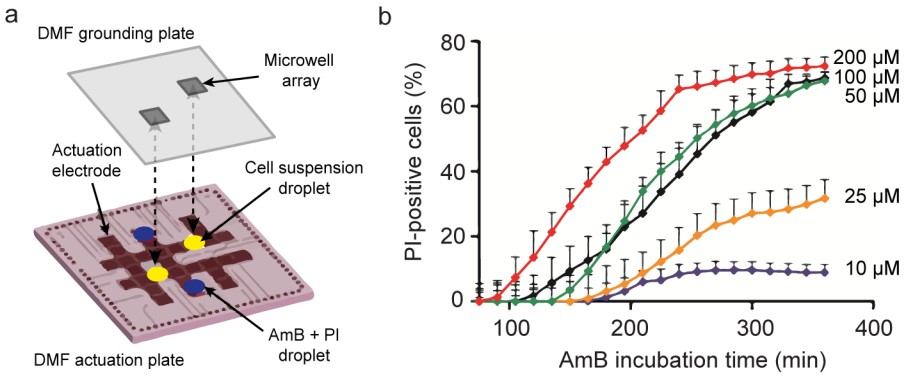

Figure 2.10 | Cytotoxicity assays on the DMF platform. (a) Schematic representation of the DMF platform configuration and (b) experimental results of the cytotoxicity assays.

droplet was dispensed on the DMF chip actuation plate, aside another droplet containing the corresponding AmB concentration and 2 µg/mL propidium iodide (PI) in 1/5 YEPD (1 % Yeast Extract; 2 % Peptone; 2 % Dextrose, diluted in distilled water).

The DMF grounding plate, where the microwell template was fabricated, was then assembled to the chip, with the cell suspension droplet positioned below the microwell array and sandwiched between the two DMF plates (**Figure 2.10**a). To prevent droplet evaporation and cell drying, the air gap between the 2 plates was filled with 80 µL silicon oil. The chip was then flipped upside down and incubated for 10 min at room temperature to allow the sedimentation of the cell suspension onto the microwell array. At this point, the cell seeding protocol was reproduced on-chip,

by displacing multiple times the cell suspension droplet over the array, by means of EWOD actuation. Successively, the cell suspension droplet was moved away from the array, and replaced by the second droplet, in order to incubate the patterned cells within the AmB/PI medium. AmB can induce cell death either via necrosis – a type of non-apoptosis in which cells die with a compromised cell membrane – or through apoptosis – i.e. programmed cell death [90]. PI is used as a fluorescent marker for non-apoptotic cell death, since it can enter the cells only if their plasma membrane is compromised. For each AmB concentration, the response of the cells to the treatment was monitored by counting the number of PI-positive cells each 15 min, for 5 hours. Afterwards, the whole array was exposed to intense UV irradiation for 20 min to abruptly kill and permeabilize all the cells and render them PI-positive, to easily count the total number of cells seeded in the array. A dose-dependent increase of the number of PI-positive cells over time was observed (**Figure 2.10**b). Furthermore, higher dosages of AmB (200 µM) resulted in faster membrane permeabilization with respect to lower AmB dosages (< 50 µM). This result further highligths the importance of time-dependent analyses for screening purposes, for instance towards the identification of fast-killing antifungal agents.

2.4 Materials and Methods

2.4.1 Fabrication and assembly of microfluidic chips for NPs detection

Upon microsphere patterning on a glass substrate, the substrate was ready for clamping to a PDMS half-channel, which was replicated from a SU-8 structure that was fabricated on a silicon wafer. A 5:1 mixture of PDMS prepolymer and curing agent (Dow Corning) was cast over the SU-8 mold and cured at 70 °C overnight. Then the PDMS replica was peeled off from the mold, resulting in a microfluidic half-channel with a height of 20 µm, a width of 800 µm and a length of 24 mm. Two PMMA plates were used to clamp the PDMS replica and the glass chip with the Parylene-C microwell array containing the microlenses.

2.4.2 Image acquisition for NPs detection

An Axiovert S100 (Carl Zeiss) inverted microscope, equipped with a 20× objective with NA of 0.22 (Zeiss Objective LD EC Epiplan-Neofluar 20×/0.22 DIC M27, 422452-9900), was used for illumination and signal detection. The microscope was configured with a mercury vapor arc lamp (X-Cite 120, Carl Zeiss) and appropriate fluorescent filter sets. Image acquisition and light detection were achieved using a CCD camera (ORCA-C4742-80ER, Hamamatsu Photonics). The integration time for recording an image was set to 20 milliseconds, which was determined by the flow velocity (~10 µm/sec) and the FWHM of the photonic nanojet (~240 nm). This integration time was just long enough to record the signal intensity of the NP during its full transit at the best focused part of the nanojet.

2.4.3 Yeast cell culture

Saccharomyces cerevisiae strain BY4741 was used in all experiments. Reagents were supplied by Lab M Ltd. (Lancashire, England), unless stated otherwise. Media used were YEPD (1 % Yeast Extract; 2 % Peptone; 2 % Dextrose) or 1/5 YEPD (YEPD diluted in distilled water). A yeast overnight

culture grown at 200 rpm and 30°C, was diluted to an optical density (OD) measured at λ=600 nm of 0.15 in a flask containing 50 mL YEPD and further cultured at 200 rpm and 30°C for 5 hours to obtain exponentially grown cells. Cells were then pelleted by centrifugation at 4000 rpm for 3 min, washed and re-suspended in 1/5 YEPD to OD 3.

2.4.4 Fabrication of DMF plates and platform operation

Fabrication of DMF chips was performed in the ESAT-MICAS cleanroom facility of KU Leuven, as described in [89]. For the fabrication of the actuation plate, cleaned glass wafers (1.1 mm thickness) were sputter coated with chromium (100 nm) and patterned using standard photolithographic processes. The plates were cleaned in acetone and isopropyl alcohol (IPA) twice, and the surface was plasma-activated (O_2-plasma, 150 mtorr, 100 W). To promote adhesion, the plates were primed with silane A174 and then coated with a layer of Parylene-C (3 µm) using chemical vapour deposition. A thin layer of Teflon-AF® (approx. 200 nm thickness using 3 % w/w in Fluorinert FC-40) was subsequently spin-coated (1200 rpm) on top of the Parylene-C layer, baked for 5 min at 110°C and 5 min at 200°C. Crenelated actuation electrodes of 2.8 mm × 2.8 mm were selectively actuated to manipulate individual droplets of 2.7 µL. The grounding plate of the DMF device was fabricated as follows: cleaned glass wafers (1 mm thickness) were coated with aluminium electrodes (40 nm) using thermal evaporation, leaving two 2.5 × 2.5 mm visualization windows. The surface was then coated with the fluoroalkylsilane F8263, followed by spin-coating Teflon-AF® (approx. 3 µm). Fluoroalkylsilane improved the adhesion between Teflon-AF® and aluminium. In order to pattern the Teflon-AF® surface, a hard mask was developed by depositing Parylene-C (1 µm) and aluminium (60-80 nm). A thin layer of AZ1505 photoresist was then spin-coated on the aluminium hard mask. Using standard photolithography processes, the aluminium was patterned and etched. Finally, for transferring the pattern from aluminum to Teflon-AF®, the plates were subjected to O_2 plasma (150 mtorr, 100 W) for 10 min. At last, the aluminum-Parylene-C mask was peeled off using tweezers, revealing the two microwell arrays (1.9 mm × 1.9 mm) on a single grounding plate, consisting of 22,000 microwells each. The patterned microwells measured approximately 5.3 µm in width and 3 µm in depth, and were arranged in a hexagonal pattern with a pitch distance of 14 µm.

For DMF platform operation, a double-sided sticky tape of 160 µm thickness was applied on the actuation plate as a spacer and for adhering the grounding plate to the actuation plate. The assembled plates were installed in a custom-made DMF microfluidic chip holder. The actuation sequence of electrodes was controlled with a customized Labview program (National Instruments Corp., Austin, TX, USA) and an in-house developed Matlab based program (MathWorks Inc., Natick, MA, USA). Droplets were driven by an AC-voltage of 120–130 Vrms, an activation time of 1 s and a relaxation time of 40 ms. The AC-actuation voltage was realized by the oscillating waveforms, produced by the function generator operating at 1 kHz (GFG-8216A-ISO-TECH, England) and further amplified by an amplifier (FLC Electronics A600, Origin Sweden).

2.5 Conclusions

In this chapter we presented a new general method for rapid self-assembly of large arrays of micro-entities of different nature and materials – from dielectric microbeads to non-adherent cells. In our technique microfabricated well arrays are used as templates for micro-entity patterning. We exploit lateral capillary forces to simultaneously "seed" thousands of single beads/cells per microwell template, starting from a droplet of bead/cell suspension which is simply deposited on top of the template and transported over the microwell surface multiple times. The hydrophobic nature of the template surface allows moving the droplet, while wetting of the inner volume of the microwells – and, thus, access of the micro-entities to the wells – is triggered by the hydrophilic nature of their bottom surface. The whole patterning process can be performed off-chip in a few seconds and the obtained bead/cell micro-arrays can then be readily integrated within microfluidic devices, such as a PDMS channel or a DMF platform.

By using Parylene-C/glass well templates to pattern melamine microspheres, we moreover introduced the use of electrostatic forces to improve the self-assembly process and enhance the immobilization of the patterned spheres within the microwells. This specific combination of materials was chosen to generate robust microlens arrays for the detection of NPs in a microfluidic flow. Specifically, we achieved the detection of NPs with a size far below the classical diffraction limit in a microfluidic device by using a conventional brightfield and fluorescence microscope. In contrast to optical detection-based analytical techniques, such as those that use laser excitation and light scattering, our technique did not rely on complex experimental setups and had the ability to easily distinguish individual NPs and do live counting of these NPs by using a standard microscope setup. In our experiments, the microscope objective was used in combination with the dielectric microsphere array to generate an array of photonic nanojets. When NPs were transported by a flowing medium through a nanojet, their light scattering or fluorescence intensity was typically enhanced by a factor ~40, allowing the detection of gold particles down to 50 nm and fluorescent particles down to 20 nm. All the further developments of this work have become subjects of a new PhD project at the LMIS2 laboratory.

By using the same patterning method with Teflon/glass well templates, we then managed to isolate yeast cells (*Saccharomyces cerevisiae*) in femtoliter wells for subsequent analyses within the microwell array at single-cell resolution. The versatility of our patterning method was once again confirmed by the fact that for these experiments the cell arrays were used in combination with a microfluidic platform of a completely different format, i.e. a DMF platform. This part of the project was performed in collaboration with the biosensors group at KU-Leuven (Leuven, Belgium), where further developments of this work are currently being carried on by two other PhD students.

Chapter 3 Hydrodynamic micro-arrays for long-term imaging and phenotyping of *C. elegans* embryos

Abstract Studies of the real-time dynamics of embryonic development require a gentle embryo handling method, the possibility of long-term live imaging during the complete embryogenesis, as well as of parallelization providing a population's statistics, while keeping single embryo resolution. We describe an automated approach that fully accomplishes these requirements for embryos of *Caenorhabditis elegans*, one of the most employed model organisms in biomedical research. We developed a microfluidic platform which makes use of pure passive hydrodynamics to run on-chip worm cultures, from which we obtain synchronized embryo populations, and to immobilize these embryos in incubator micro-arrays for long-term high-resolution optical imaging. We successfully employ our platform to investigate morphogenesis and mitochondrial biogenesis during the full embryonic development and elucidate the role of the mitochondrial unfolded protein response (UPR^{mt}) within *C. elegans* embryogenesis. Our method can be generally used for protein expression and developmental studies at the embryonic level, but can also provide clues to understand the aging process and age-related diseases in particular.

This chapter is an adapted version of the following publications:

- **M. Cornaglia**, L. Mouchiroud, A. Marette, S. Narasimhan, T. Lehnert, V. Jovaisaite, J. Auwerx, and M. A. M. Gijs, An automated microfluidic platform for *C. elegans* embryo arraying, phenotyping, and long-term live imaging, *Sci Rep* 5, 10192, doi: 10.1038/srep10192 (2015)

- **M. Cornaglia**, L. Mouchiroud, A. Marette, S. Narasimhan, T. Lehnert, V. Jovaisaite, J. Auwerx, and M. A. M. Gijs, Multi-dimensional imaging and phenotyping of *C. elegans* embryos via an automated microfluidic device. Proc. of 19th International Conference on Miniaturized Systems for Chemistry and Life Sciences (microTAS 2015), Gyeongju, Korea, October 2015.

3.1 Introduction

3.1.1 New model organisms for drug discovery

Improving human health and evaluating the health status is nowadays a completely multi-disciplinary topic, involving research fields from medicine and biology, to physics, chemistry and engineering. At the core of the main issues concerning human health, still resides the lack of a global understanding of the physiology of whole organisms, due to an extreme complexity that is very hard to grasp without multiple-parameter and integrated analytical techniques. Many efforts are constantly being done to progressively dig deeper into the secrets of the human biology to better treat diseases. Obviously, there is no possibility to directly conduct this research on humans as a whole. Hence, researchers mainly base their work on studies performed on cells and tissues, which are however not able to preserve the full information about the entire organism they originate from. When this information is absolutely necessary, thus, scientists need to address analyses on entire organisms such as mice, rats, pigs, monkeys, etc, which represent the so-called "model organisms" for investigating the different aspects of human health. Nevertheless, this approach fairly originates inevitable ethical concerns and, from a practical viewpoint, raises several other issues in terms of time and cost of the analyses. These studies, in fact, cannot involve a high number of specimens and they are therefore usually not suitable for high-throughput analyses, which are however more and more crucial for the healthcare domain. For all these reasons, in recent years, the so-called "small model organisms" are gaining particular attention in the field, since they allow circumventing most of these issues [91, 92]. Analyses on small animals such as *Caenorhabditis elegans*, *Drosophila melanogaster*, *Danio rerio*, or *Xenopus laevis* provide in fact a high amount of biological information about the organization of a full organism, while avoiding time, cost and, often, ethical concerns. The small size of these animals, however, highly complicates these analyses, especially when only the traditional manual pick-and-place and other manipulation techniques are available, which lack the reproducibility and throughput standards required for massive usage of the technique. Microfabricated solutions, though, can definitely solve this last issue, since they allow directly operating on the same length-scale of the organisms under test, paving the way towards absolute control over the protocols and the high-throughput-type analyses required by this field.

3.1.2 *C. elegans* as an emerging model organism

Among the small model organisms, the nematode *C. elegans* has some particularly interesting features, which give it increasing attention in the whole biomedical research community. Established as a model organism by Sydney Brenner in 1965, *C. elegans* was the first animal to get its genome entirely sequenced in 1998[93]. Since then, it has become a widely accepted model for investigations into different bio-medical fields, while key discoveries made in *C. elegans* have already been awarded with 3 Nobel Prizes. Many biological processes have been conserved between worms and humans and high-level biological questions about complex human diseases can be addressed by studies on *C. elegans*. Interestingly, in fact, *C. elegans* and human beings share a high amount of genes and molecular pathways (e.g. 40% of worms' genes have their human counterpart) [93]. Therefore, through the years, the *C. elegans* research community has generated an

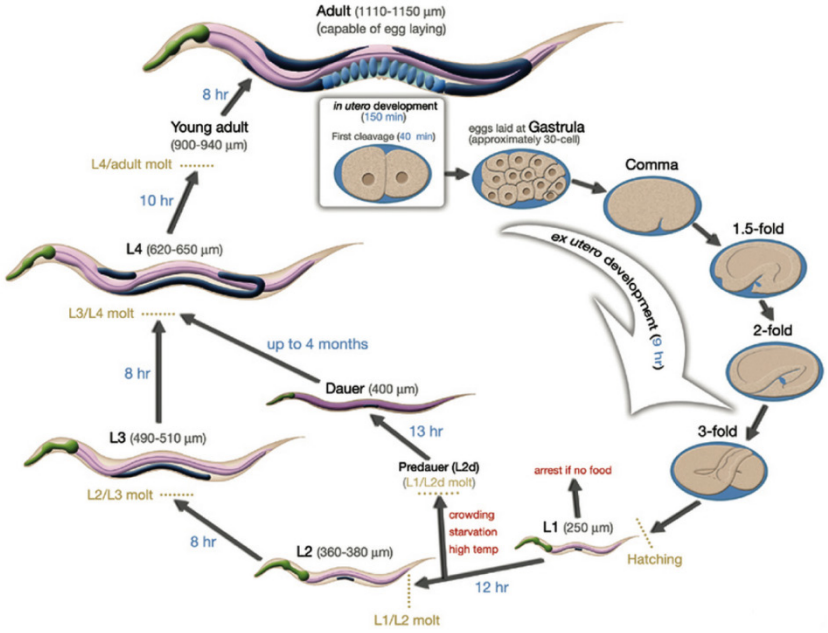

Figure 3.1| Life cycle of wild-type *C. elegans* at 22°C, in agar plate culture conditions. 0 min is fertilization. Numbers in blue along the arrows indicate the length of time the animal spends at a certain stage. First cleavage occurs at about 40 min postfertilization. Eggs are laid outside at about 150 min postfertilization and during the gastrula stage. The length of the animal at each stage is marked next to the stage name in micrometers (Reprinted from [96]).

extensive library of mutant strains as well as a broad toolkit for worms' genetic manipulation. RNA interference (RNAi), for instance, can be implemented in a relatively easy way in worms – i.e. by feeding them with bacteria expressing double-stranded RNA (dsRNA) for the gene of interest – and represents a powerful technique for gene silencing and investigation of loss-of-function phenotypes [94]. Moreover, *C. elegans* nematodes are transparent at all their developmental stages and a large amount of fluorescent reporter-gene strains has been made available to visualize gene expression and signaling patways in real-time. *C. elegans'* relatively short life cycle (**Figure 3.1**) and lifespan (around 20 days in laboratory conditions) makes it a very convenient model organism for the investigation of developmental processes and for the aging research as well. *C. elegans* hermaphrodite adults have 959 somatic cells and their complete lineage is known [95]. 302 of these cells are neurons and their selective ablation has been demonstrated as well, for both nerve regeneration analyses and nervous system disease investigation. *C. elegans* possesses one of the simplest central nervous systems and by far the best characterized. Despite this simplicity, both physiological behaviors – e.g. feeding, locomotion, egg-laying – as well as complex behavioral traits – e.g. sensory responses, social behaviors, learning – can be observed and studied in worms.

As mentioned before, microfluidic-based technologies operate on the same length-scale of *C. elegans* size and hold therefore enormous potential for improving *C. elegans* manipulation and studies in terms of both automation and accuracy. In this context, a significant amount of work has been done in the last 5 to 10 years and some excellent reviews have been recently published to provide overviews of the advancements in this field. The potential of microfluidic technologies for phenotyping, imaging and screening of multicellular organisms has been reviewed by Yanik *et al.* [97], Crane *et al.* [98], Wlodkowic *et al.* [99], Chronis *et al.* [100], and Baker [101]. Bakhtina *et al.*

presented a wide overview of the microfluidic solutions which have been proposed so far to enhance *C. elegans* manipulation and studies [102]. Sivagnanam *et al.* reviewed the use of microfluidic systems for the exploration of living multicellular organisms, organs, and tissues [103]. Hulme *at al.* provided then an interesting analysis about *C. elegans* as a platform for integrating chemical and biological research [104].

3.1.3 Challenges and opportunities for *C. elegans* embryogenesis analysis

Before reaching the adult stage and upon egg hatching, *C. elegans* nematodes pass through four larval (L1-L4) stages (**Figure 3.1**). In most oganisms, exposure to particular environmental conditions during early life is often decisive for their successful development. In *C. elegans*, events occurring during larval stages are known to have a strong impact on the animal's lifespan [105]. Whether conditions in the embryonic phase of life have an influence on the later development is however a much more challenging question to answer, mainly because systematic *C. elegans* embryonic morphogenesis studies are still difficult from a technical point of view. In fact, *C. elegans* worm culture is performed on the surface of nematode growth medium agar plates covered with *Escherichia coli* bacteria for feeding. This technique proves especially tedious if large numbers of animals are to be analyzed. Moreover, for embryonic studies, currently available protocols are based on animal dissection and embryo mounting on agar pads [106], which typically require specialized and advanced skills and lacks reproducibility and high-throughput potential. Recently, it has been shown that various aspects of functional exploration of *C. elegans* can be significantly improved using microfluidics [102-104, 107-109]. "Worm-chips" have successfully demonstrated their high potential at enhancing worms' handling and accurate imaging, for applications in lifespan studies [110], phenotyping and screening [111, 112], nerve regeneration analyses [113], as well as for the investigation of worms' behavioral dynamics [114]. So far, however, such robust methods to study *C. elegans* embryos do not exist yet, whereas a microfluidic solution has been only proposed to study early embryo development for larger size model organisms, namely fruit fly (*Drosophila melanogaster*) [115] and zebrafish (*Danio rerio*) [116].

Chung *et al.* [115] recently proposed a microfluidic array for large scale ordering and orientation of *Drosophila* embryos. Their microfluidic device uses hydrodynamic forces to immobilize hundreds of embryos in a vertical position, exploiting their anisotropic embryonic shape (**Figure 3.2**a). By means of this method, the authors could quantify morphogen gradients in the dorsoventral patterning system of the embryos, a task that was before complicated by the technical challenge of manually orienting individual *Drosophila* embryos, featuring about 0.5 mm in size. By using an analogous embryo-trap approach and chip geometry, Akagi *et al.* [116] proposed then a mesofluidic device for the immobilization, drug perfusion and high-resolution imaging of zebrafish embryos (**Figure 3.2**b). The authors then demonstrated that the "embryo-array technology" can be effectively used for the analysis of anti-angiogenic compounds using transgenic zebrafish lines.

C. elegans embryos are 10-100 times smaller than those of the other small model organisms and thus basically impossible to handle manually. However, no technological solution for their manipulation and study has been proposed so far. To enable systematic analysis of *C. elegans* embryonic

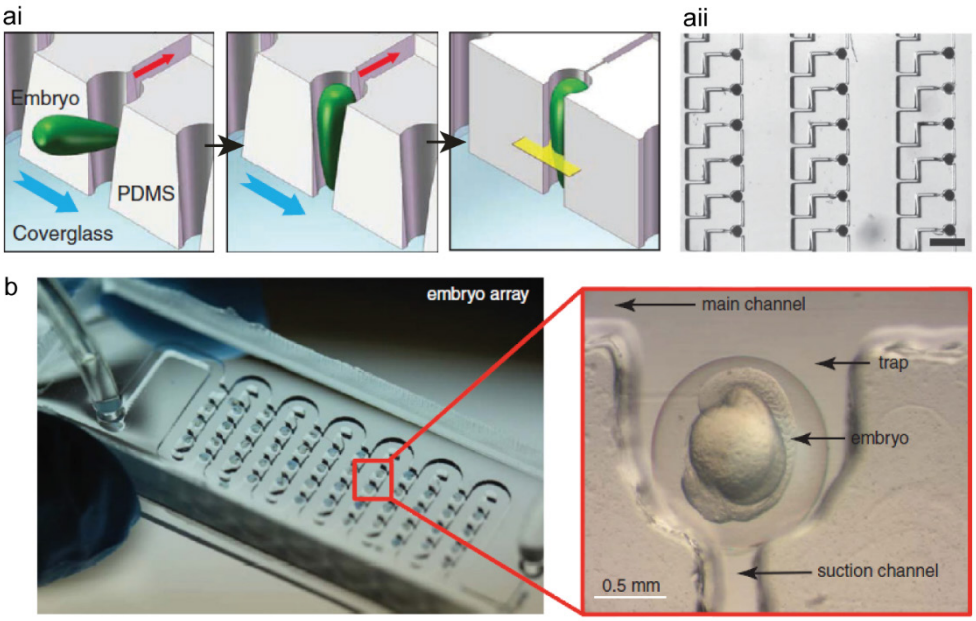

Figure 3.2| Embryo-array technologies for *Drosophila* and zebrafish studies. (ai) Schematic representation of the *Drosophila* embryo trapping process proposed by Chung *et al.* (reproduced from [115]): an embryo is first guided into the trap and vertically oriented by fluidic forces; the trap then contracts for the embryo immobilization and imaging (yellow plane = imaging focal plane). (aii) A section of the array with trapped embryos. Scale bar = 500 µm. (b) Picture of the mesofluidic device for zebrafish embryo arraying, as proposed by Akagi *et al.* (reproduced from [116]). The right panel depicts a magnified section of the device with a single trap holding an immobilized zebrafish embryo.

morphogenesis, we hence developed a microfluidic platform for automated on-chip worm culture, creation of synchronized embryo arrays, and for long-term parallel live imaging at the single embryo level. We successfully employed our platform to investigate mitochondrial biogenesis during the embryonic development. Using our method to study a large number of embryos of different wild-type and mutant worm strains, we elucidated an outstanding issue regarding the role of UPR^{mt} during early worm embryogenesis.

3.2 Microfluidic platform design and automated operation

3.2.1 Overview of the microfluidic device

The robustness and automation of our system completely relies on passive hydrodynamics, with no need of any active component on-chip, such as integrated valves. This approach allows simplifying fluidic protocols and significantly minimizing fabrication constrains of the device, which simply consists of a monolithic PDMS microfluidic chip, sealed to a ~150 µm-thick glass coverslip. Our microfluidic chip features two main components: a “worm culture chamber” and an “embryo-incubator array" (**Figure 3.3**a,bi). External flow control through four independent inlets is achieved via computer-controlled syringe pumps, while two external valves are used to open and close two separate outlets. The worm culture chamber is delimited by specific microfluidic channel arrangements for generating uniform flow distributions in the chamber and for filtering entities of different size (**Figure 3.3**bii): a “worm injection filter”, for gentle insertion of mixed worm suspensions

into the chamber; a “worm synchronization filter”, to select the age of the worm population to be tested, by only retaining either adult worms or L4 larvae inside the chamber; an “*E. coli*/drug delivery filter”, to homogeneously introduce feeding and treatment solutions inside the chamber; an “embryo transfer filter”, to reliably displace embryos from the chamber to the embryo-incubator array upon egg laying. The embryo-incubator array consists of a serpentine channel in which each pair of branches is connected by isolated micro-compartments, specifically tailored for the trapping of *C. elegans* embryos and their high-resolution imaging through the glass coverslip (**Figure 3.3**biii).

Embryos, which are transferred to the embryo-incubator array are automatically positioned in the micro-incubators by passive hydrodynamic trapping (**Figure 3.3**c). The design of this section of the chip is optimized according to both general microfluidic rules and specific needs related to the characteristics of *C. elegans* embryos, as it will be extensively discussed in the next subsections. Overall, our fluidic design results in enhanced efficiency of capture and stable positioning of single embryos, with unprecedented performance in terms of control and reliability of the trapping mechanism for non-spherical objects. The flow rate distribution inside the array has to ensure the capture of a single embryo for each micro-incubator. Since the number of available embryos is being limited by the egg production inside the chamber, a perfect efficiency of the hydrodynamic trapping method has to be established in order to recover all eggs. At the same time, however, high trapping efficiency is typically associated to higher fluidic pressures through the micro-incubators. Therefore, forces exerted on the incubated eggs have to be considered as well, to prevent the flow from introducing undesired mechanical stresses on the captured embryos.

A crucial role for the system performance is clearly played by the geometry of the micro-incubators, hence different types of micro-incubators have been fabricated and tested (details of this optimization process are reported in subsection 3.2.4). For high-resolution parallel time-lapse imaging of the whole embryo population and automated image processing, all the embryos have to be perfectly arrayed in stable positions and kept correctly aligned and well-oriented for several hours. We optimized the incubator size and shape mainly according to these needs, with our final design featuring elongated semicircular incubators, which are 35 µm wide, 38 µm long and 35 µm high (**Figure 3.3**d). Using these dimensions, single embryos can be reliably positioned and aligned inside the incubator array (**Figure 3.3**e). Only slight variations in their angular positions are observed, given the natural size variability of the embryos (see subsection 3.2.4).

The whole incubator array features 20 micro-incubators, which are progressively filled by embryos as soon as they are naturally laid. This number is chosen to provide a significant data statistics for each experiment, while still maintaining a good level of age-synchronization among all the embryos in the array. For a worm culture which is at the peak of its egg production, complete filling of the incubator arrays typically takes around 1 hour. The whole embryo population is studied using fully automated multi-dimensional imaging, covering six independent dimensions: the 3 spatial coordinates, the development time, the exposure (brightfield, fluorescent) duration, and the embryo number in the array (**Figure 3.3**f).

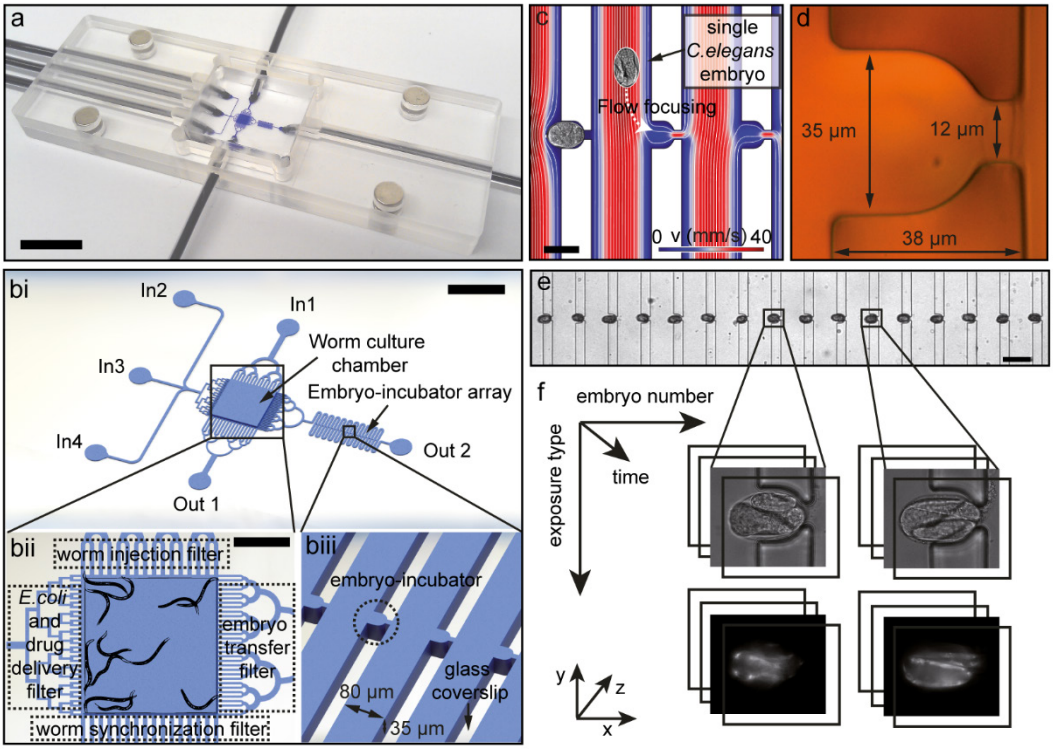

Figure 3.3 | Overview of the microfluidic device. (a) Picture of the microfluidic device, sizing 25 mm x 75 mm (standard microscope slide size), including lateral microfluidic connections, which make the device compatible for imaging with every upright or inverted microscope. Scale bar = 10 mm (bi) Schematic representation of the central part of the microfluidic chip, having as main constitutive parts: the worm culture chamber, the embryo-incubator array, four inlets (In1 to In4) and two outlets (Out1 and Out2). Scale bar = 2 mm (bii) Zoom on the worm culture chamber, including a drawing of young adult *C. elegans* for size comparison. The chamber is delimited by specific microfluidic channel arrangements, tailored for different functions: (top) worm injection, (bottom) worm synchronization, (left) *E. coli* / drug delivery and (right) egg transfer. Scale bar = 1 mm (biii) Three-dimensional schematic zoom on a portion of the embryo incubator array. (c) FEM simulation (Comsol Multiphysics) of the fluid dynamics in the incubator array region, showing the principle of passive hydrodynamic arraying of single embryos. Fluidic velocity and streamlines are calculated for a flow rate of 100 nL/s at the inlet In3. Scale bar = 50 µm (d) Micrograph of a single incubator on the SU-8/silicon master mold used for PDMS casting. (e) Micrograph of a section of the array with immobilized embryos. Scale bar = 100 µm (f) Illustration of the multi-dimensional imaging that is enabled on the array of embryos and spans six dimensions: the 3 spatial coordinates, time, exposure type and embryo number in the array.

3.2.2 Multi-functional cross-shaped culture chamber

In our chip, the cross-shape of the worm culture chamber (**Figure 3.4**) is designed to decouple the worm loading/washing protocols from the embryo transfer operations, by allowing liquid flows through the chamber along two orthogonal directions (In1-Out1 and In2/3/4-Out2, respectively). Since both the aforementioned operations rely on precise flow rate thresholds for their correct functioning, a crucial requirement is represented by flow uniformity across the whole width of the chamber, in both directions. For this reason, the chamber is connected to its inlets and outlets by binary trees of microfluidic channels, in which any inflow – or outflow – is symmetrically split – or merged – in equal portions, hence ensuring controlled and homogeneous flow speed across the chamber. For worm loading, this channel configuration is particularly crucial not to damage the

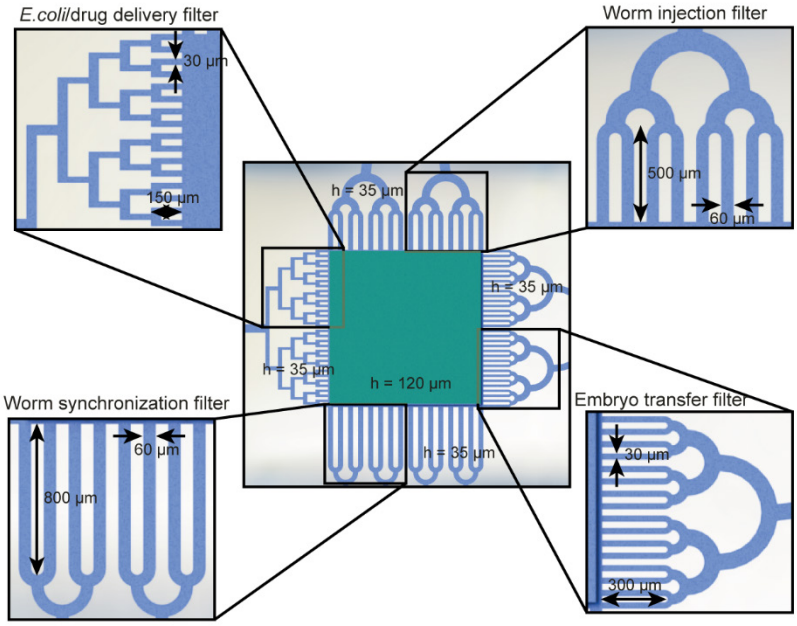

Figure 3.4 | Geometry of the worm culture chamber. Schematic representation of the worm culture chamber, with zooms on the surrounding microfluidic channel arrangements and their specific dimensions.

worms during the injection, since it ensures uniform worm distribution across the In1-Out1 filters, avoiding their accumulation at narrowing channels which might cause unpredictable flow patterns and overpressures over their bodies. During the progeny transfer, flow speed homogeneity ensures then that all the embryos present in the chamber are subjected to similar drag forces. This allows moving them all towards the incubator array, without losing some of them in the worm chamber or damaging some of them by excessive forces.

3.2.3 Design of the hydrodynamic trapping micro-array

The efficiency of the hydrodynamic trapping mechanism in the embryo incubator can be estimated by calculating the ratio between Q_1 and Q_2, i.e. the volumetric flow rates through each incubator and its bypass channel, respectively (**Figure 3.5**ai). This can be done by first considering the pressure drop between points A and B, along the two different fluidic paths and then imposing equal pressure drop along them (ignoring minor losses due to channel bends, widening/narrowing, etc.) [117]. At steady-state flow conditions, for incompressible Newtonian fluids flowing through straight microchannels (i.e. Poiseuille flow), this operation actually corresponds to calculating the inverse of the ratio between the hydraulic resistances of the two paths, R_2/R_1. For straight channels with rectangular cross-sectional shape, the hydraulic resistance can be calculated as [45]:

$$R = \frac{12\mu L}{1 - 0.63\,(\frac{h}{w})}\frac{1}{h^3 w} \tag{3.1}$$

where μ is the fluid viscosity, L the channel length, h and w the channel height and width, respectively.

Table 3.1 | Microfluidic designs to test embryo capture efficiency. Geometrical parameters, as defined in **Figure 3.5**aii, Q_1/Q_2 ratio, and experimental embryo capture efficiency of two microfluidic designs.

	W_c (µm)	L_c (µm)	W_i (µm)	L_i (µm)	W_d (µm)	L_d (µm)	Q_1/Q_2	E (%)
Design A	100	1000	35	50	12	8	~4	~50
Design B	80	1200	35	30	12	8	~13.5	~100

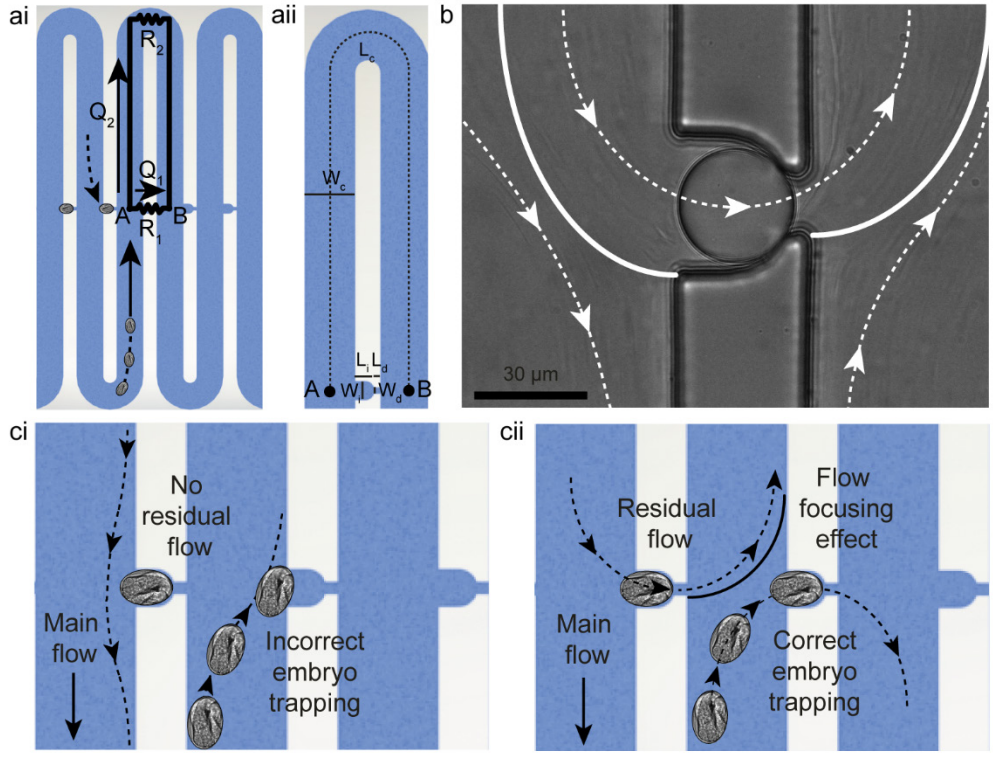

Figure 3.5 | Design of the hydrodynamic trapping micro-array. (a) Schematic representation of the design of the hydrodynamic embryo trapping system, with (ai) indication of the flow rates Q_1 and Q_2 through a trap and a bypass channel, respectively, and (aii) definition of the geometrical parameters. (b) Optical micrograph of an *E. coli* suspension flowing through an embryo incubator, in which a 30 µm PMMA bead has been trapped to study the hydrodynamic trapping mechanism. Flowing *E. coli* bacteria allow visualizing the flow streamlines and assessing the presence of residual flow through the occupied incubator. Dashed white lines trace a few of the streamlines, while the solid lines are guides to the eye that indicate the boundary between the main flow in the bypass channel and the residual flow in the incubator. (c) Schematic representation of the embryo trapping mechanism, (ci) in absence and (cii) in presence of residual flow through an occupied incubator. The residual flow enhances the correct embryo orientation and positioning inside the next incubator of the array.

It has been shown that, for spherical objects (e.g. micro-beads), good trapping efficiencies are achieved for ratios $Q_1/Q_2 = R_2/R_1 > 3$ [117]. However, no data were available on the hydrodynamic trapping of non-spherical objects for an incubator/bypass microfluidic design. Hence, we first estimated the trapping efficiency of our device for different array geometries and then fabricated

two microfluidic devices with different Q_1/Q_2 ratios to experimentally evaluate their capturing efficiency for *C. elegans* embryos. The efficiency E is defined as the number of experimentally captured embryos over the total amount of embryos injected into the microfluidic device.

The geometrical parameters of **Table 3.1**, as defined in **Figure 3.5**aii, have been chosen following specific needs related to the capture of *C. elegans* embryos. For instance, the bypass channel width has to be large enough to allow the passage of embryos at any orientation and avoid channel clogging, even when a group of embryos is flowing through the serpentine. Another constraint is the height of the microchannels (h = 35 µm in our design), as the microfluidic device must allow stable and flat embryo positioning inside the incubators, while still avoiding squeezing of the captured embryos. The exact geometry of the embryo incubator plays here an important role, as discussed in detail in subsection (3.2.4). From our experimental analysis, we concluded that the Q_1/Q_2 ratio of ~13.5 guarantees 100% embryo trapping efficiency, while for a ratio of ~4, only 50% of the flowing embryos are typically trapped. We mainly attribute this behavior to the fact that the bypass channel width has to be designed large enough with respect to the embryo size for the reasons explained above.

Another option to reduce mechanical stresses on captured embryos could have been the reduction of the height of the bypass channel with respect to the incubator's one. This would result in enhanced sealing of the incubator, when occupied by an embryo [118]. However, while spherical objects simply need to be directed towards an empty incubator to be trapped, egg-shaped objects must be properly oriented, in order to ensure their correct capture and positioning in the incubator. By setting equal trap and bypass channel heights, we therefore deliberately allowed the presence of a residual flow through occupied incubators (**Figure 3.5**b). Such residual flow modifies the flow pattern in the vicinity of the subsequent downstream trap and generates an additional flow that is beneficial for guiding the embryo towards its correct re-orientation and trapping into the adjacent empty incubator (**Figure 3.5**c).

Another hydrodynamic trapping design has been recently proposed, in which multiple incubators were positioned side-by-side in between adjacent serpentine branches [115]. On the one hand, this design undoubtedly allows optimizing the number of captured embryos in a given field of view, but, on the other hand, it does not allow deterministically setting a 100% trapping efficiency, mainly because of the undesired residual flow through occupied incubators, perturbing the expected flow rate through the unoccupied ones. As a result, we considered this alternative design to be less suitable for our application, where the number of available embryos is limited and where trapping efficiency and accuracy are more important than having a larger number of trapping sites.

3.2.4 Optimization of the embryo incubator geometry

The design of an embryo incubator that perfectly matches the requirements of our application is based on the following considerations. The incubator width (W_i in **Figure 3.5**aii and **Figure 3.6**a) has to be large enough to gently accommodate a single *C. elegans* embryo, while not introducing any lateral pressure on it during its complete development. On the other hand W_i cannot be too large with respect to the average width of an embryo, to guarantee its alignment exactly along

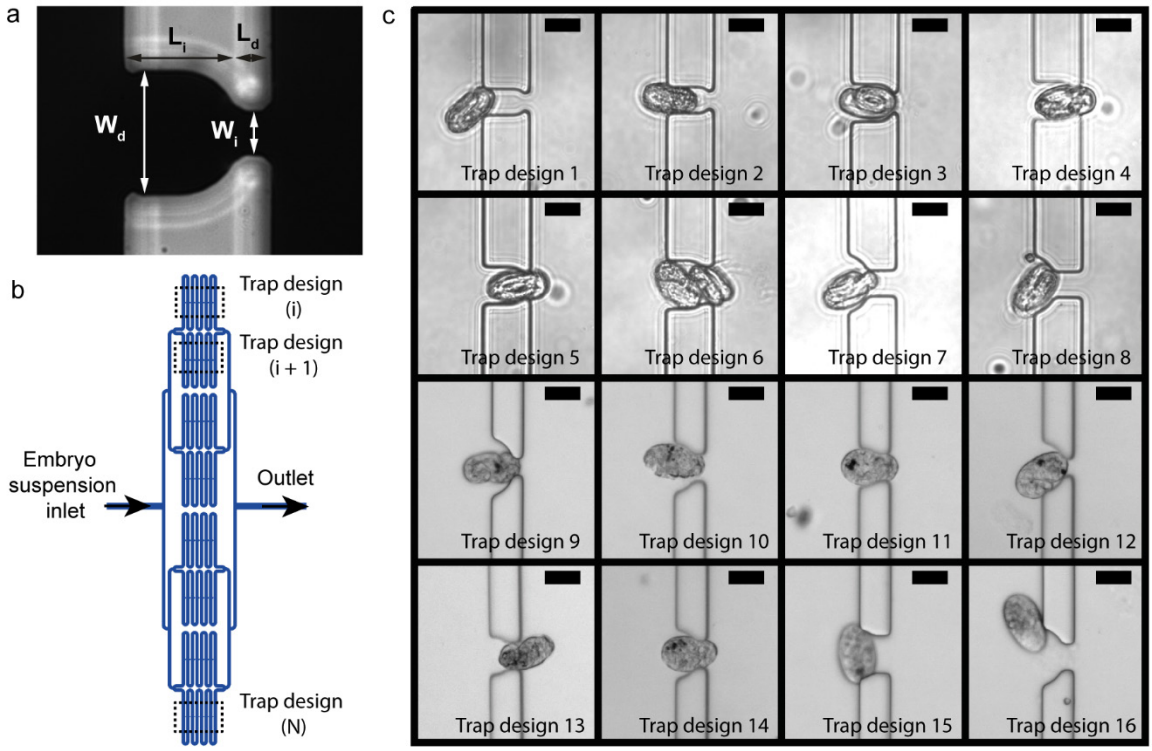

Figure 3.6 | Optimization of the embryo incubator geometry. (a) Picture of a PDMS embryo incubator, with main geometric features the incubator width (W_i) and length (L_i), and drain width (W_d) and length (L_d). (b) Schematic representation of the microfluidic device designed and fabricated for the experimental characterization of different embryo incubator geometries. (c) Representative pictures of 16 different embryo incubator geometries, showing possible issues in single embryo trapping, positioning and imaging, such as mechanical stress induced on the captured embryo, wrong embryo positioning/orientation, multiple embryo capture, etc.. Scale bars = 30 µm.

the same direction, which represents an important requirement for the automated parallel imaging over the whole incubator array. The incubator length (L_i in **Figure 3.5**aii and **Figure 3.6**a) has been chosen taking into account that long incubators would result in multiple embryo trapping at a single incubator site, while too short ones would expose each captured embryo to flow patterns that would change its position during the imaging process or even remove it from the incubator. Dimensions of the drain connecting each incubator to the adjacent branch of the main serpentine channel (W_d and L_d in **Figure 3.5**aii and **Figure 3.6**a) also need to be carefully designed, as *C. elegans* embryos have a limited mechanical stiffness and can be squeezed through the drain by excessive fluidic pressures. On the one hand, the drain has to be narrow and long enough to retain the embryo inside the incubator, even at the relatively high flow rates used for their capture, while, on the other hand, its fluidic resistance has to be sufficiently low for efficient hydrodynamic trapping.

In order to take into consideration all the aforementioned constraints, we designed a dedicated microfluidic device for studying the optimization of the embryo incubator size and shape (**Figure 3.6**b). Our device features parallel arrays of embryo incubators with different geometries for experimentally studying the embryo capture, positioning and imaging for the different designs. *C. elegans* embryo suspensions in M9 buffer were prepared following standard biological protocols

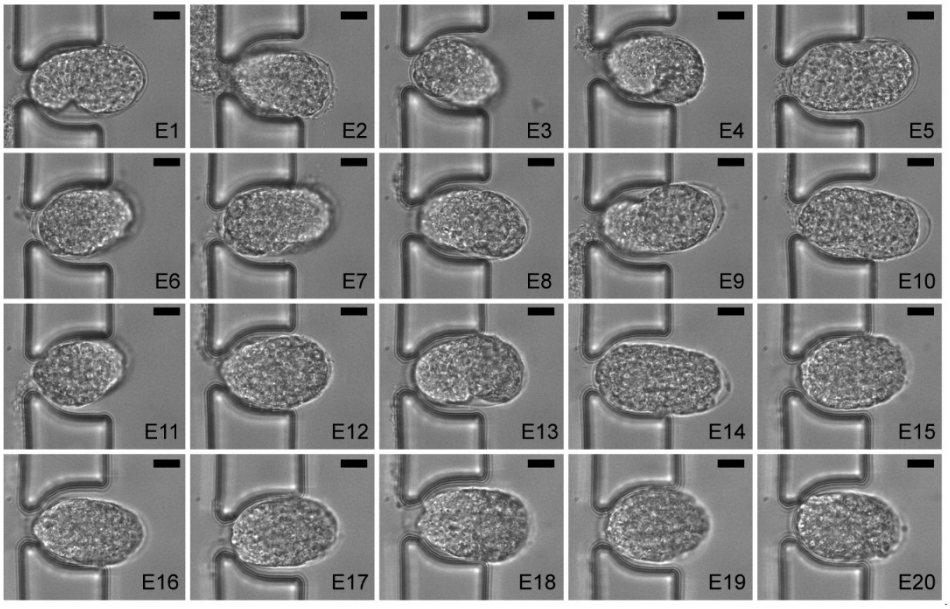

Figure 3.7 | Angular position of embryos inside the incubators. Pictures of a representative array of embryos (E1 to E20), upon complete filling of the incubator array. The hydrodynamic trapping mechanism results in stable embryo positioning, with angular deviations within a 5-10° solid angle, due to the natural size and shape variability of the embryos themselves. Scale bars = 10 µm.

[119] and directly injected into the microfluidic device. The various aspects and artefacts, which were theoretically predicted and described above, were experimentally observed indeed (**Figure 3.6**c). Among the tested incubators, we eventually selected, as optimized design, an elongated semicircular incubator with W_i = 35 µm, L_i = 30 µm, W_d = 12 µm, L_d = 8 µm (**Figure 3.3**d). Interestingly, our final design allows moreover emptying the full array in a few seconds, by expelling the captured embryos from the incubators by means of a flow pulse at relatively high flow rate (5-10 µL/s).

Computer-controlled image processing was used on our platform to further extend its analytical possibilities towards fully automated real-time screening and phenotyping. To enable this possibility, however, the exact positioning of each embryo inside the incubator array has to be carefully considered, since image processing tools should always be able to automatically recognize and analyze the embryos in the array. In our device, only slight variations in the embryo angular position inside its incubator are observed (**Figure 3.7**). This variations are dictated by the natural size variability of the embryos themselves, sometimes resulting in slight vertical tilting (**Figure 3.7**, panel E3, where the embryo seems to have a more circular shape resulting from the vertical tilt angle) or horizontal tilting (**Figure 3.7**, panel E9), but always these angles are lower than 10°.

3.2.5 Automated operation of the platform

A live-cell microscopy environmental control system (Visitron, Puchheim, Germany) allowed controlling the chip temperature over the whole duration of each experiment. The microfluidic operations were controlled using Nemesys syringe pump control software (Cetoni, Korbussen, Germany). Experimentally, the microfluidic chip was first filled with Pluronic F127 solution, incubated for 30 min inside the device, to prevent *E. coli* sticking and accumulation inside the microchannels

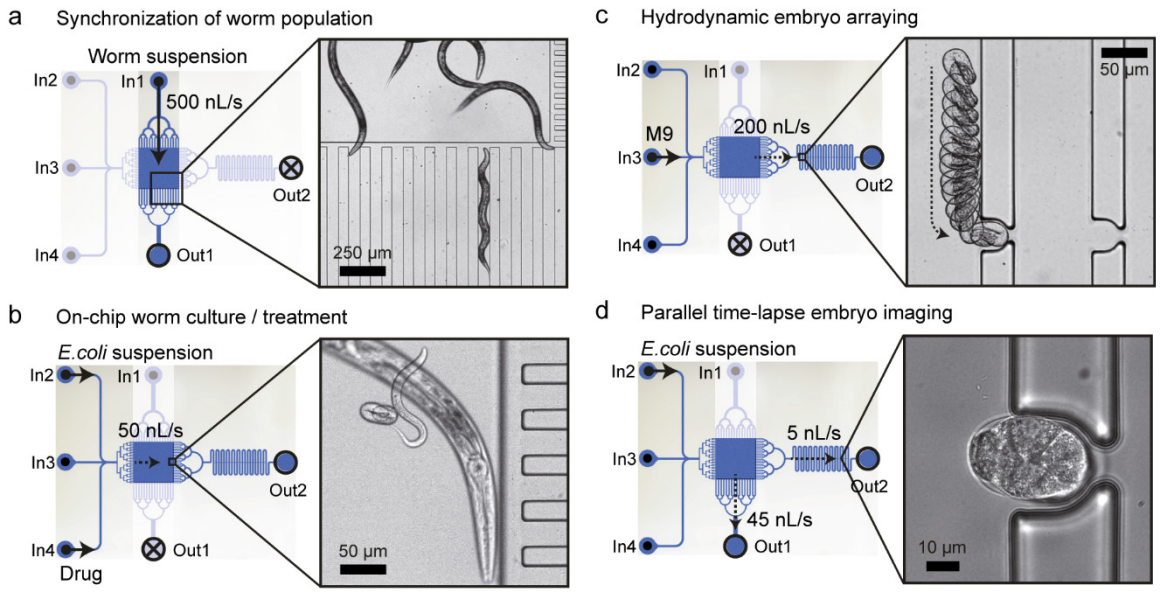

Figure 3.8 | Operation of the microfluidic device. (a) First a 10 µL suspension of worms in M9 buffer is injected into the microfluidic device along the In1-Out1 direction at a flow rate of 500 nL/s. Symbols used for the in- and outlets: dot and arrow = syringe in use (e.g. In1); dot = syringe not in use (e.g. In2); circle = open valve (e.g. Out1); cross and circle = closed valve (e.g. Out2). The "worm synchronization filter" is tailored to retain inside the chamber only adult worms, as selected by their larger size and their better swimming abilities (see picture in zoom). (b) Subsequently worm culture is controlled by periodically injecting *E. coli* in M9 buffer along the In2-Out2 direction, typically at 50 nL/s flow rate. This ensures normal development of the worms in the liquid environment and continuous embryo production during their adult life span (see picture in zoom). Optionally, drugs or chemicals can be introduced at the In4 inlet for on-chip worm treatment. (c) Injection of M9 buffer at 200 nL/s flow rate along the In3-Out2 direction triggers the transfer of all the eggs present in the chamber towards the incubator array, where they are captured by passive hydrodynamics, as shown by the superposition of 13 video frames in the zoom. (d) The perfusion of *E. coli* suspension towards both Out1 and Out2 simultaneously ensures proper worm feeding inside the culture chamber and stable embryo positioning inside the incubators, enabling parallel time-lapse imaging of the embryos at cellular resolution (see picture in zoom).

[120]. Few worms from a non-synchronized population were suspended in 10 µL of M9 buffer and sucked in a microfluidic tube, which was then connected to the device. From this point on, the system was completely controlled by software, through the automated sequential steps described in **Figure 3.8**.

In each experiment, worms and embryos are manipulated via sequences of fully automated operations. A worm suspension is first injected into the microfluidic device through the top port (In1 of **Figure 3.8**a) and directed towards the "worm synchronization filter" by opening the valve at "Out1". The geometry of the chip is optimized for retaining inside the worm culture chamber only adult worms by simply selecting the correct flow rate for the sample injection. In practice, at a flow rate of 500 nL/s, in a few tens of seconds, all the larvae present in the suspension are directly washed out of the chip, while adult worms are kept inside the chamber both due to their larger size and their better swimming abilities/resistance against the flow (zoom of **Figure 3.8**a). The number of worms retained inside the chamber is controlled by the concentration of young adults in the worm suspension injected into the device (typically, 5 to 10 young adults per 10 µL suspension). Alternatively, a L1-L4 larvae suspension can be injected at a flow rate of 100 nL/s to retain

just L4 larvae inside the chamber. When needed, the number of captured worms can be adapted by running an optional "washing step", where M9 buffer is injected for a few seconds along the In1-Out1 direction at higher flow rates (1 to 5 µL/s).

Upon isolation of a defined worm population inside the chamber, worms are cultured and can be eventually treated on-chip with specific drugs or chemicals (**Figure 3.8**b). For worm culture/treatment, an *E. coli* suspension is injected in the chamber at a desired rate, through the In2-Out2 direction, while drugs or chemicals can be introduced in the chip at controlled concentration and precise instants of the worms' lifespan. A simple increase of the flow speed inside the chamber along the In3-Out2 direction is then used to transfer the eggs present in the chamber towards the embryo-incubator array. In practice, a 200 nL/s flow of M9 buffer allows recovering all the eggs present in the chamber and isolating each of them in a single micro-incubator via passive hydrodynamic trapping up to complete array filling (**Figure 3.8**c). Parallel time-lapse imaging is then started, either for the full array or by scanning each individual embryo at high resolution, at desired frame rate, magnification and light wavelength, depending on the analysis of interest (**Figure 3.8**d). Alternatively, parallel time-lapse imaging could be started at the beginning of the embryo collection phase, in order to monitor each embryo from the first moment of its trapping on. Brightfield imaging of the 20 trapped embryos takes 20 seconds, and this procedure is repeated every minute. In the fluorescence experiments, combined brightfield and fluorescent imaging of the 20 trapped embryos is done in 180 seconds, and this procedure is repeated every 15 minutes, to avoid phototoxicity effects on the embryos. The synchronization point in the development for all embryos can be chosen by using either the appearance of the bean stage or hatching.

During live imaging, we apply a slow flow (5-10 nL/s) of M9 buffer along the In3-Out2 direction to assure stable positioning of the embryos in the array. Because of the large section difference between chamber and incubators, the flow speed is slower inside the culture chamber and this very gentle flow is strong enough to keep captured eggs in position, but not fast enough to transfer new eggs from the chamber to the array. Optionally, for sequential studies on embryo populations produced by the same worms at different periods of their full adult lifespan, worm culture can be maintained in the chamber by the perfusion of *E. coli* from In2 inside the chip. Both the valves at Out1 and Out2 are left open in this case, and the different hydrodynamic resistances of the two orthogonal directions result in a partitioning of the flow between the two outlets, with most of the liquid flowing through Out1. This establishes a slow flow through the incubator array, ensuring stable positioning of the embryos over long periods, while still reducing *E. coli* accumulation in the array area, which could compromise the results of embryo fluorescent imaging, because of the autofluorescence of *E. coli* bacteria.

3.3 Embryogenesis studies at single-organism resolution

3.3.1 Automated analysis of embryonic morphogenesis

A microscopy environmental control system maintains a constant temperature on the chip (typically 25°C) over the whole duration of each experiment. An automated xy-positioning stage is used

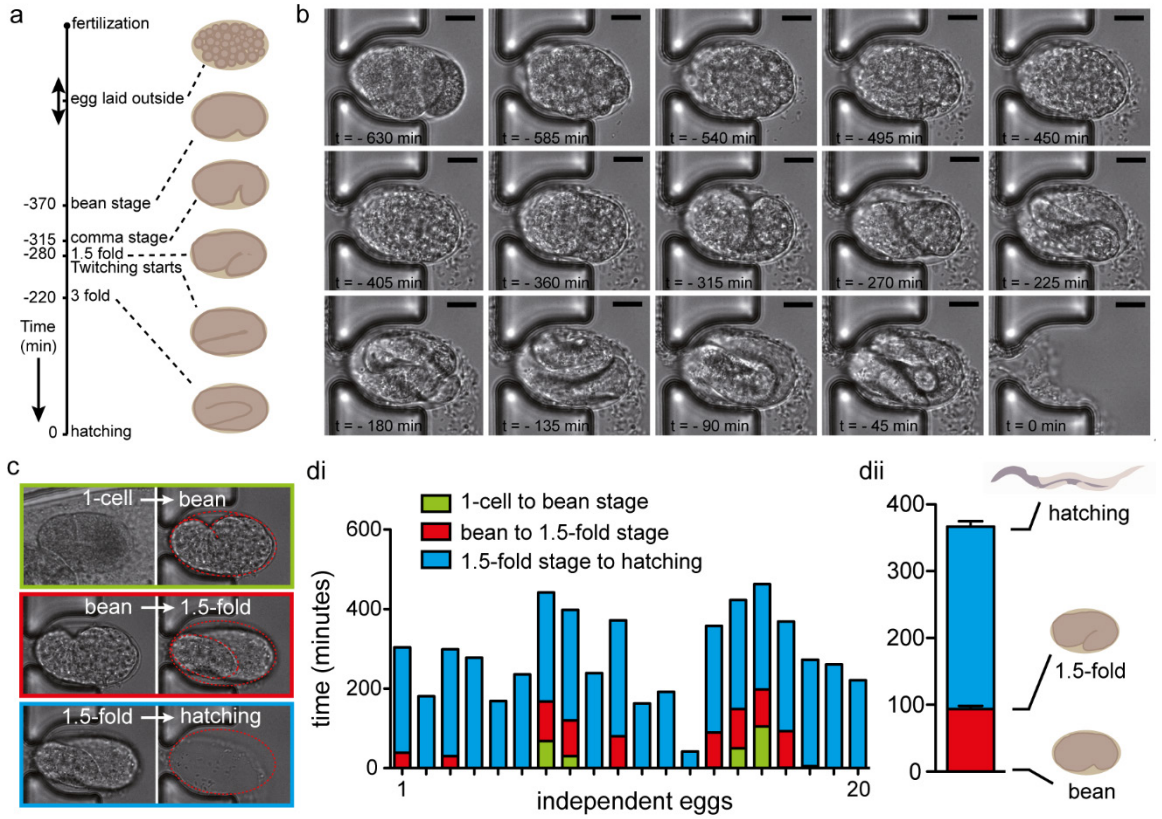

Figure 3.9 | Study of *C. elegans* embryogenesis for wild-type worms. (a) Time-lapse of the main embryonic stages of development with typical time indications for T= 25°C and wild-type worms. (b) Full embryonic development from egg capture in the incubator till hatching, as observed in a sequence of brightfield microscopy images (63× oil immersion objective, NA 1.4) taken from a movie (1 frame per minute) at 45 min intervals for a N2 wild-type worm strain at 25°C; the hatching time defines t=0. Scale bars = 10 µm (c) Illustration of main embryonic development phases –1 cell to bean; bean to 1.5-fold; 1.5-fold to hatching– that are clearly morphologically distinguishable. (d) Duration of development phases, as observed for an array of 20 embryos for a N2 wild-type worm strain at 25°C; (di) variation of the time duration the embryo spends in an incubator, originating from differences in the exact moment of egg laying and trapping of the embryo; (dii) average duration of development phases, as obtained from the data in (di).

to scan sequentially all positions of interest on the embryo-incubator array. Embryos can be monitored at cellular resolution through a 63x, NA 1.4 oil immersion objective, thus allowing accurate observation and analysis of *C. elegans* embryonic morphogenesis stages (**Figure 3.9**a) over the whole time-span, from egg capture to hatching (**Figure 3.9**b). Two key events with clearly different morphological changes in the embryo shape can be distinguished: (i) the onset of the so-called "bean stage", beginning of morphogenesis (**Figure 3.9**c, top), and (ii) the onset of the "1.5-fold stage", followed by the twitching inception (**Figure 3.9**c, middle). Together with egg hatching (**Figure 3.9**c, bottom), these morphological changes could be detected by software-controlled pattern recognition codes, for the full automation of the image processing.

We recorded the duration of the two last development phases of **Figure 3.9**c for full arrays of embryos (n=20) belonging to different strains. Our platform allowed accurate measurement of the duration of these phases for individual N2 wild-type embryos at 25°C (**Figure 3.9**di). The apparent variability is an indication of variations in the exact moment of egg laying (and subsequent trapping) of each embryo, which represents another interesting phenotype to be studied with our

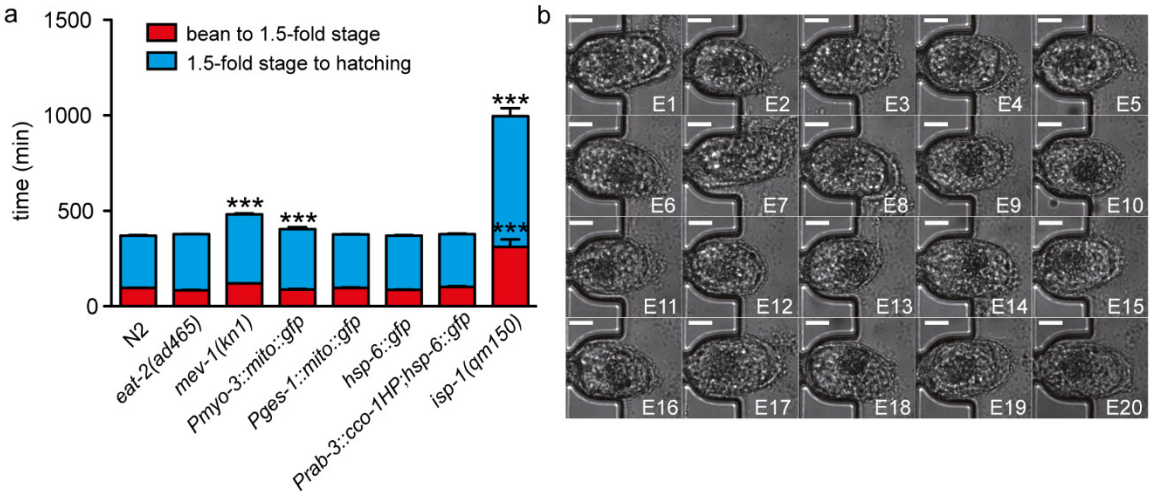

Figure 3.10 | Study of *C. elegans* embryogenesis for transgenic, mutant and treated worms. (a) Duration of different development phases –bean to 1.5-fold; 1.5-fold to hatching– for the N2 wild-type strain of worms and a number of transgenic strains and mutants. Bar graphs are expressed as mean+SEM, *** $p \leq 0.001$. (b) Pictures of a full array of 20 embryos taken 600 min after trapping in the incubators, illustrating the blocked development when the embryos are laid by N2 wild-type worms that were exposed in the culture chamber to 2 mM of the anticancer drug 5-fluorouracil (5-FU) in M9 buffer. Scale bars = 10 µm.

method as well. The average duration of the development phases could be monitored with good accuracy, even from this single array experiment (**Figure 3.9**dii). Moreover, as worms could be cultured and maintained on the same chip for several days, we demonstrated the capability of our device to be employed for studying age-related changes in worm reproduction and progeny development. Wild-type worms were used for these proof-of-concept experiments. A mixture of L1-L4 larvae was injected into the microfluidic device, to isolate a small population of 5 to 10 L4 larvae inside the worm culture chamber. Worms were then cultured on chip during their full adult lifespan and different embryo populations were isolated at different moments of the worms' reproductive period. We compared then arrays of embryos shortly captured after the start of egg production (Day 1) with other arrays that have been filled approximately 72 hours later (Day 4). For the first generation of embryos (Day 1), about 50% of the captured eggs were in phase 1 or phase 2 (i.e. before the bean stage or before the onset of twitching, respectively). As worms get older, however, we observed a general decrease in egg production and brood viability, as well as an increase of the average age of the embryos at laying. These observations are in good agreement with off-chip results (data not shown).

In a further set of studies, we systematically investigated the duration of the different development phases for several transgenic strains and mutants (**Figure 3.10**a). In particular, we used SJ4100, SJ4103 and SJ4143 transgenic strains of worms, which express Green Fluorescent Protein (GFP) under the control of the *hsp-6* (homolog of mtHSP70 in mouse), the *myo-3* (homolog of Myosin-3 in mouse) and the *ges-1* (homolog of Carboxylesterase in mouse) promoters, respectively, in a N2 wild-type background [121, 122]. These strains are typically employed for the study of the gene expression level and/or localization, either through the GFP quantification or imaging approaches. Also we used the transgenic strain AGD1073 obtained by crossing *hsp-6::GFP* reporter worms with a neuron-specific *cco-1* hairpin line [123]. The resulting *Prab-3::cco-1HP;hsp-6::gfp*

strain of worms displays a specific *cco-1* (homolog of the cytochrome c oxidase-1 subunit Vb/COX4 in mouse) silencing in the neurons driven by the pan-neuronal promoter *rab-3*. Finally, we investigated the TK22, DA465 and MQ887 strains, carrying a loss-of-function mutation in the *mev-1, eat-2* and *isp-1* genes, respectively [124-126]. *mev-1* encodes the cytochrome *b* large subunit (Cyt-1/ceSDHC) in complex II of the mitochondrial electron transport chain. The *mev-1* mutation was shown to shorten lifespan and the mutants display a large panel of age-related phenotypes and metabolic disorders [127]. *eat-2* encodes a ligand-gated ion channel subunit closely related to the non-alpha-subunits of nicotinic acetylcholine receptors (nAChR). Mutation in the *eat-2* gene affects primarily pharyngeal pumping rates, slowing pumping down to 10–20% of the normal rhythm, which mimics a caloric restriction state and increases the lifespan [128]. *isp-1* encodes a Rieske iron sulphur protein, which is a subunit of complex III of the mitochondrial electron transport chain. A mutation in this gene affects the rates of physiological processes like reproduction and development, and extends the longevity [126].

As for the wild-type, we could reliably determine the average duration of the bean to 1.5-fold stage phase (phase 2) (~90 min) and the average duration of the 1.5-fold stage to hatching phase (phase 3) (~280 min) in the *eat-2(ad465)*, *Pges-1::mito::gfp*, *hsp-6::gfp* and *Prab-3::cco-1HP;hsp-6::gfp* strains. A weak increase of the phase 3 was measured with the *Pmyo-3::mito::gfp* transgenic strain, which is in accordance with the slight developmental delay observed during the larval stage (data not shown). A more significant 1.3-fold increase of phase 3 is instead observed in the *mev-1* mutants, while for the *isp-1(qm150)* mutants, both phases 2 and 3 were more than two times longer compared to the control worms. These results already highlight the importance of the mitochondrial electron transport chain function during embryogenesis.

Eventually, the possibility of automated on-chip chemical or drug treatment was validated by exposing the worms to the anticancer drug, 5-fluorouracil (5-FU). This compound induces cell-cycle arrest and apoptosis of germ-line cells in *C. elegans* [129]. In our experiment, wild-type worms were isolated in the culture chamber at the L4 larval stage and treated on-chip with 5-FU at a concentration of 2 mM, while being cultured at 25°C towards the adult stage. After washing the chamber with clean M9 buffer, successively laid embryos were transferred to the incubator array and monitored for 12 h. All embryos prematurely died, proving the efficiency of the drug exposure of the worms in the culture chamber of the chip (**Figure 3.10**b).

3.3.2 Study of mitochondrial biogenesis during embryonic development

Knowing that the knockdown of many mitochondrial genes can induce embryonic lethality or result in an infertile phenotype, we investigated mitochondrial function and biogenesis during embryogenesis, focusing on the molecular pathway known as mitochondrial unfolded protein response (UPR^{mt}). The latter is an adaptive response that monitors and subsequently repairs abnormal proteostasis within the mitochondria and, as such, ensures the proper function and integrity of the mitochondria [130, 131]. In *C. elegans*, it has been shown that UPR^{mt} is most effective when triggered during larval development, resulting in a permanent adaptive protection of the mitochondria throughout life and, as such, increasing the animal's survival rate (**Figure 3.11**). This care-

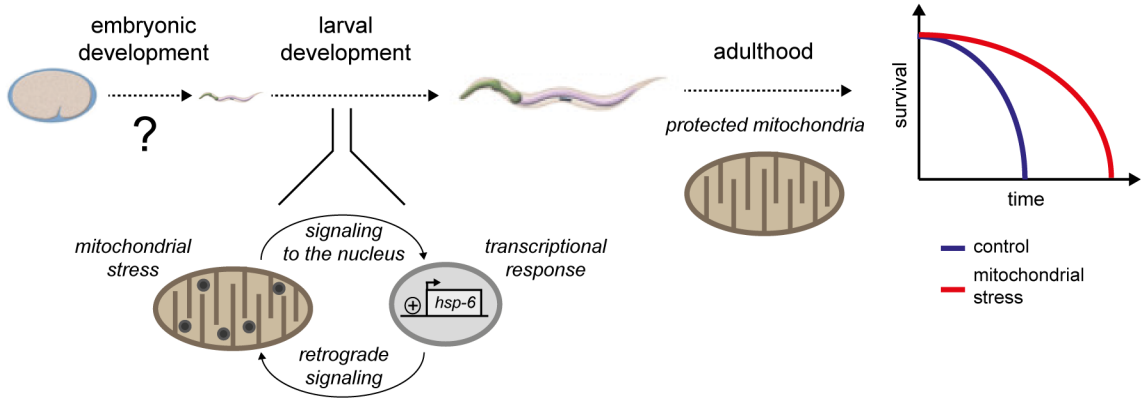

Figure 3.11 | Mitochondrial unfolded protein response. (a) Schematic representation of the mitochondrial unfolded protein response (UPR^{mt}), as known for the larval and adult stages of the nematode *C. elegans*.

ful control of mitochondrial activity early in life seems to setup a proper rate of aging, which persists throughout life, probably through the establishment of epigenetic imprints [132]. However, it is still unknown whether the UPR^{mt} is operational during the earliest phases of the life, *i.e.* embryonic development. As tackling this problem requires the careful analysis of multiple parameters in a spatio-temporal controlled fashion in a living embryo, we used our platform to address this challenging question.

Before measuring the UPR^{mt} activity, we first investigated whether mitochondrial biogenesis could be detected and monitored in two different tissues in embryos, i.e. the muscle and the intestine. Indeed, a proper mitochondrial activity is a prerequisite for the induction of a mitochondrial stress. Two transgenic strains of worms were used, expressing GFP either in the mitochondria of the body wall muscle cells, i.e. the *Pmyo-3::mito::gfp* worm strain SJ4103, or in the intestinal cells, i.e. the *Pges-1::mito::gfp* worm strain SJ4143 [122]. Larvae or adult worms of these strains are commonly used to monitor the mitochondrial activity, proliferation and morphology [133, 134]. Brightfield and fluorescent pictures of the same embryo were quasi-simultaneously recorded and superimposed, permitting accurate localization of the fluorescent signal. Interestingly, our analysis revealed that mitochondrial proliferation takes place in both muscle and intestinal cells (**Figure 3.12**a-f and **Figure 3.12**g-l, respectively). The mitochondrial biogenesis looks different in terms of intensity between muscle and intestinal cells, probably due to the different number and role of mitochondria, as it is clear when comparing **Figure 3.12**a-c with **Figure 3.12**g-i. Indeed, after the 1.5-fold stage of embryogenesis, most cellular proliferation and migration of the body wall muscles are completed and the worm starts twitching in the eggshell, requiring a sustained energy supply provided by the mitochondrial activity [135]. Beside the intensity of mitochondrial biogenesis during embryogenesis, our study revealed that mitochondrial proliferation behaves independently of tissue morphogenesis. While genetic markers of the body wall muscle and the intestinal cells significantly appear before the bean stage [136], we observed a rather large delay regarding the onset of mitochondrial proliferation, highlighting a specific increase of the energy supply during the late phase of the embryo development (**Figure 3.12**d-f and **Figure 3.12**j-l). Further-

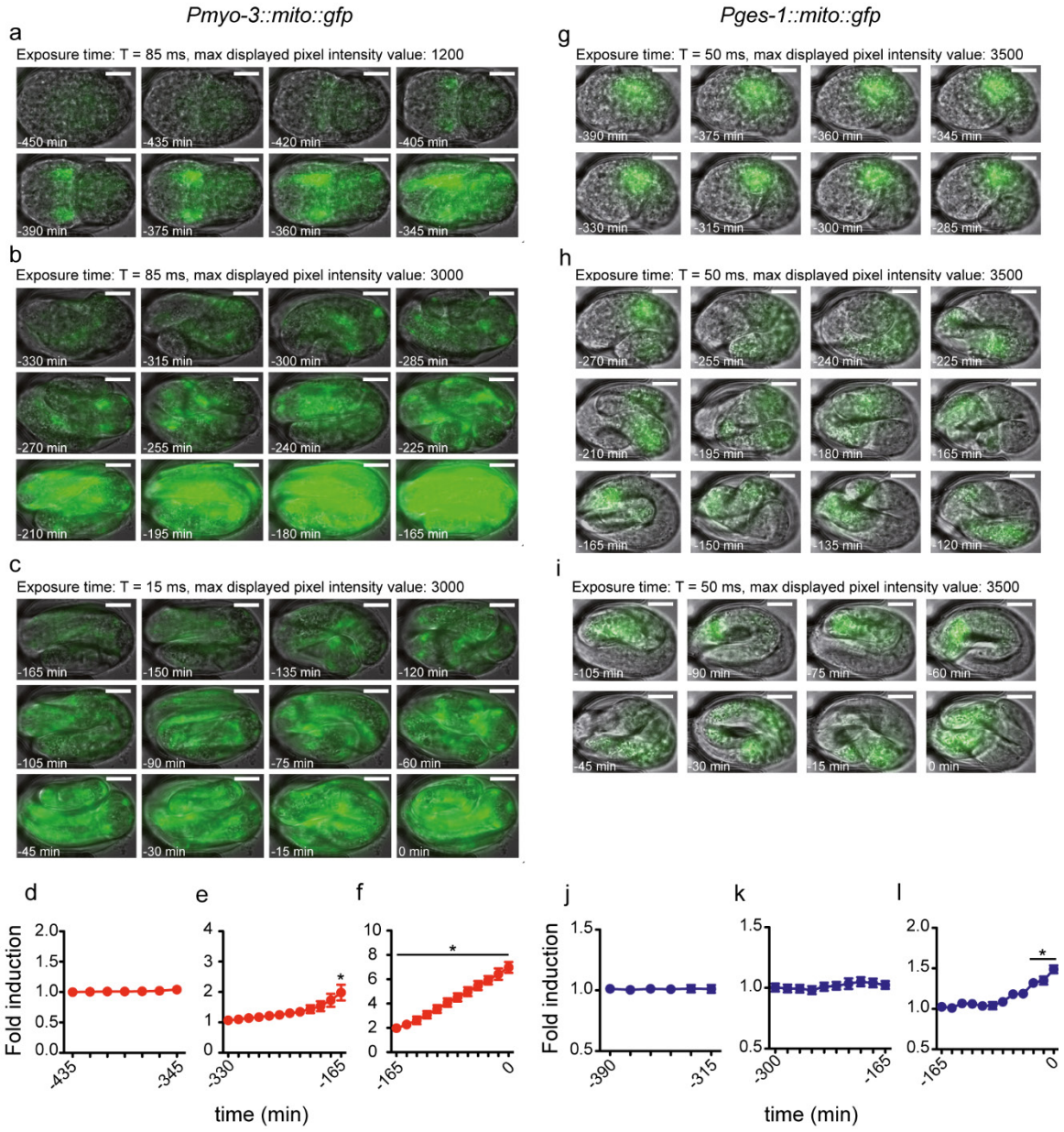

Figure 3.12 | Study of mitochondrial biogenesis. (a-c) Merges of optical brightfield and fluorescent pictures of the *Pmyo-3::mito::gfp* embryos and (d-f) the corresponding GFP quantification over the whole time-span from embryo capture to hatching (n=4). Pictures are grouped in blocks of same experimental observation and image representation conditions (exposure time and maximum displayed pixel intensity). (g-i) Merges of optical brightfield and fluorescent pictures of the *Pges-1::mito::gfp* embryos and (j-l) the corresponding GFP quantification over the whole time-span from embryo capture to hatching (n=14). Pictures are grouped in similar blocks as for the *Pmyo-3::mito::gfp* embryos. For (d-f) and (j-l), the curves correspond to the relative GFP induction compared to the initial time point in (d) and (j), respectively, of the experiments. Bar graphs are expressed as mean+SEM, * p≤0.05, points below a horizontal line are significantly different from the corresponding control. Scale bars = 10 µm.

more, as already observed in mouse embryos, this late proliferation of mitochondria could coincide with the pronounced structural and functional differentiation of the mitochondria within the different tissues [137].

Interestingly, a previous study showed that the mitochondrial DNA copy number – which is indicative of the relative number of mitochondria in the organism – remains unchanged from the late embryo stage up to the L3 larval stage, whereas a five-fold increase occurs with the transition from L3 to L4 [138]. Our experimental observations suggest that a first increase in mitochondrial biogenesis actually takes place earlier, during the embryogenesis (**Figure 3.12**f and **Figure 3.12**l). Although embryonic mitochondrial biogenesis is less pronounced compared to that occurring during the L3 to L4 transition, it is significant and we speculate that it provides the necessary amount of mitochondria and energy, required for the first steps of the larval development.

3.3.3 Study of mitochondrial unfolded protein response during embryogenesis

We investigated whether the UPR^{mt} can also be detected during embryogenesis. To monitor the mitochondrial stress response in living embryos, we used a transgenic strain of worms that reports on the activity of the UPR^{mt} with integrated GFP genes driven by the regulatory DNA region of the mitochondrial chaperone *hsp-6* [121]. In these transgenic worms, an increase of *hsp-6::gfp* expression is indicative of the presence of a mitochondrial stress and the subsequent induction of the UPR^{mt} [123, 139]. We first examined the UPR^{mt} induction in unstressed embryos. Despite a pronounced mitochondrial proliferation occurring during the late phase of the embryogenesis, we did not observe a matching increase of *hsp-6::gfp* expression (**Figure 3.13**a,d). This result is in agreement with previous reports showing an activation of the UPR^{mt} during the L3 to L4 transition period, where a similar burst of mitochondrial biogenesis occurs only when a mitochondrial stress is experimentally induced [123, 138]. Nevertheless, a careful monitoring and surveillance of mitochondrial stress is fundamental for the embryogenesis, as the loss of function of some UPR^{mt} mediators, such as *hsp-6* and *dve-1*, has been reported to lead to an early death of the worm embryos[140, 141].

Studies performed at the larval stages indicated that the UPR^{mt} can be robustly induced by applying direct mitochondrial stress. These stresses include oxidative stress and the inhibition of the mitochondrial transcription and translation machinery, resulting in the disturbance of the mitonuclear proteostatic balance [121, 139, 142]. Mitonuclear imbalance results from the disruption of the stoichiometric balance between components of oxidative phosphorylation (OXPHOS) complexes encoded by the mitochondrial and/or the nuclear genome and robustly activates the UPR^{mt} [139]. Examples of such a mitonuclear imbalance are provided by the loss-of-function mutation of the nuclear-encoded complex III protein, *isp-1*, and/or the complex IV protein, *cco-1*, which induces a robust UPR^{mt} and extends worm lifespan. These genetic manipulations deplete single components of specific OXPHOS complexes, overloading the mitochondrial matrix with their respective partner proteins, which cannot be assembled into multiprotein complexes.

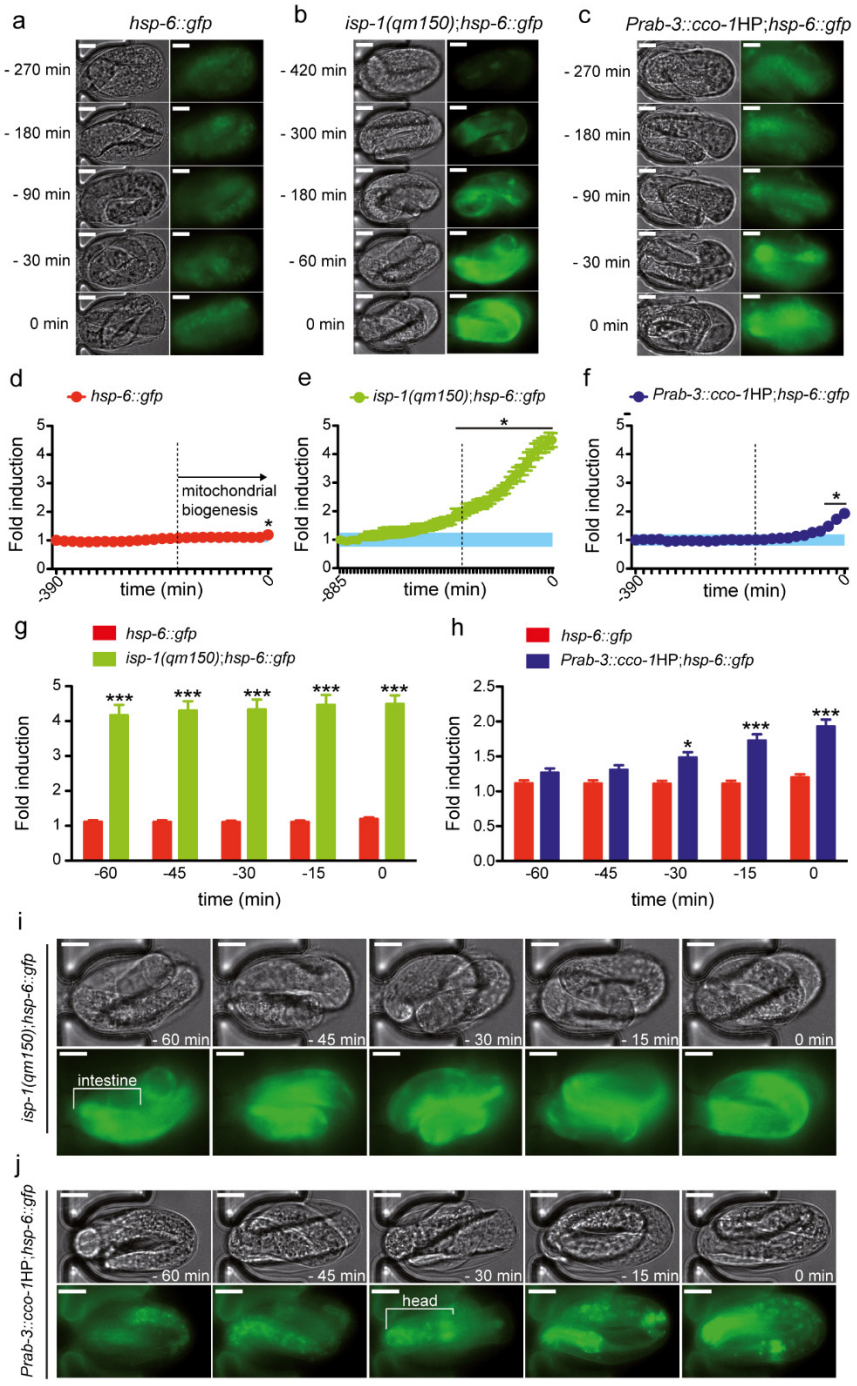

Figure 3.13 | Study of mitochondrial unfolded protein response (UPR^{mt}) during embryogenesis. (a-c) Representative optical brightfield and corresponding fluorescent pictures that show the *hsp-6::gfp* expression in (a) wild type, (b) *isp-1(qm150)*, and (c) *Prab-3::cco-1HP* strains. (d-f) Quantification of the *hsp-6::gfp* induction in (d) wild type, (e) *isp-1(qm150)* and (f) *Prab-3::cco-1HP* strains over the whole time-span from embryo capture to hatching (n=17, 7, and 21, respectively). The curves correspond to the relative GFP induction compared to the initial time point of each experiment. The blue area in each graph represents the base level 95% interval of confidence for each experiment. Bar graphs are expressed as mean+SEM, * p≤0.05, points below a horizontal line are significantly different from the corresponding control. (g-h) Comparison of the relative wild type hsp-6::gfp induction with the one of the (g) isp-1(qm150) and (h) *Prab-3::cco-1HP strains*. Bar graphs are expressed as mean+SEM, * p≤0.05, *** p≤0.001. (i-j) Localization of the *hsp-6::gfp* expression in the embryonic tissues, as observed in a period starting 60 min before hatching, for the (i) *isp-1(qm150)* and (j) *Prab-3::cco-1HP* strains. Scale bars = 10 µm.

To trigger a potential constitutive UPR^{mt} in embryos, we first used the mutant strain MQ887 carrying a mutation in the *isp-1* gene, which we crossed with the *hsp-6::gfp* worms. The resulting *isp-1(qm150);hsp-6::gfp* strain showed a constitutive activation of *hsp-6::gfp* in larvae and adult worms, revealing a strong and continuous mitochondrial stress [123]. By monitoring the *hsp-6::gfp* expression during the embryo development, we observed a 4- to 5-fold induction of the UPR^{mt}, which matches the onset of mitochondrial biogenesis (**Figure 3.13**b,e,g). Interestingly, this mitochondrial stress response seems to be more pronounced in the intestinal cells, which is in accordance with previous observations in larvae and adults and confirms that this tissue is one of the prime sites for the activation of the UPR^{mt} (**Figure 3.13**i) [123].

While UPR^{mt} can be activated in a cell-autonomous manner, as here illustrated in the intestine, this stress response can also be triggered in a cell-non-autonomous manner [123]. To explore this hypothesis, we used the *hsp-6::gfp* strain of worms carrying an additional transgene, which drives the knockdown of the mitochondrial gene *cco-1* only in neurons, i.e. the *Prab-3::cco-1HP;hsp-6::gfp* worm strain AGD1073. In this strain, the down-regulation of cco-1 in neuronal cells induces not only a localized mitochondrial stress and UPR^{mt} in the nervous system, but also induces a so-called “mitokine” signal, which will relay and induce UPR^{mt} in peripheral tissues, such as the intestine [123]. This mitochondrial communication between central and distal tissues seems to be fundamental, as it can synchronize the rate of aging for the whole organism independently of the cell-autonomous functions [143]. In the post-embryonic phase of worm development, the silencing of *cco-1* exclusively in neurons is sufficient to promote a mitochondrial stress that is propagated in distal tissues [123]. In this regard, we asked whether a similar mitochondrial cross-talk between tissues would already occur during the embryogenesis. One would in fact expect that the perfect organisation of this developmental period could involve a watchful communication between tissues in terms of mitochondrial biogenesis and stress response regulation. We observed a robust 2-fold induction of UPR^{mt} when *cco-1* is silenced in neuronal cells during the embryogenesis (**Figure 3.13**c,f,h). Interestingly, the activation of the mitochondrial stress response seems independent of the *rab-3* promoter activity – *rab-3* starts being expressed in the early cell division stages [136] – but rather a consequence of the concomitant mitochondrial proliferation and *cco-1* knockdown. Furthermore, while the UPR^{mt} induction takes place in the intestinal cells of the *isp-1(qm150)* embryos, neurons seem to be the primary cells for the mitochondrial stress response in the case of *cco-1* silencing in the neuronal system (**Figure 3.13**j). This difference between embryos and larvae concerning the lack of cell-non-autonomous activation of UPR^{mt} could be explained by the fact that the neuronal and hormonal signalling pathways required for signal transmission are not yet fully developed at the embryonic stage.

3.4 Materials and methods

3.4.1 Chemicals and Materials

4-inch 550 µm thick Si wafers and DIW were obtained from the Center of Micro- and Nanotechnology of EPFL. GM 1070 SU-8 negative photoresist was purchased from Gersteltec (Pully, Swit-

zerland). PDMS Sylgard 184 was acquired from Dow Corning (Wiesbaden, Germany). 1 mL borosilicate H-TLL-PE syringes were purchased from Innovative Labor Systeme (Stutzerbach, Germany). Microline ethyl vinyl acetate tube with 0.51 mm inner and 1.52 mm outside diameters was bought from Fisher Scientific (Wohlen, Switzerland). Pluronic F-127 was purchased from BASF (Basel, Switzerland*).* M9 buffer was obtained by adding 3 g KH_2PO_4, 6 g Na_2HPO_4, 5 g NaCl, 1 mL 1 M $MgSO_4$, H_2O to 1 litre and sterilization by autoclaving. Pluronic F127 solution was prepared by diluting 0.02% (weight/volume) Pluronic F127 in M9.

3.4.2 *C. elegans* strains and culture

C. elegans strains were cultured at 20°C on nematode growth media agar plates seeded with *Escherichia coli* strain OP50, unless stated otherwise. Strains used were wild-type Bristol N2, DA465 *eat-2(ad465)* II, MQ887 *ips-1(qm150)* XX, SJ4100 (zcIs13[hsp-6::GFP]), SJ4103 (zcIs14[*myo-3*::GFP(mit)]), SJ4143 (zcIs17[ges-1::GFP(mit)]), TK22 *mev-1(kn1)*. Strains were provided by the Caenorhabditis Genetics Center (University of Minnesota). The AG1073 (*Prab-3::cco-1HP;hsp-6::gfp*) strain of worms was kindly provided by Andrew Dillin (UC Berkeley, CA, USA). Worms were suspended in M9 solution prior to each microfluidic experiment. Microfluidic worm synchronization procedures are detailed in **Figure 3.8**.

3.4.3 Fabrication of the microfluidic chips

Microfluidic devices were prepared by soft lithography [144] using 2-layer SU-8 molds. Briefly, conventional photolithography was used to pattern a 35 µm-thick layer of SU-8 photoresist on 4-inch wafers. A 85 µm-thick layer of SU-8 was then patterned on top of the first one. The silicon mold was then diced in 15 mm × 18 mm microchips, which were inserted at the bottom of an aluminum/PMMA mold for PDMS casting. 1.5 mm diameter steel pins were used to define the lateral connections of the device for the external tubing insertion. A liquid PDMS mixture (10:1 base:cross-linker weight ratio) was degassed, injected into the mold and cured at 100 °C for 1 h. Upon extraction from the mold, each PDMS chip was bonded by plasma-activation to a 150 µm-thick glass coverslip. The chip was then connected to external tubing and enclosed in a PMMA holder (**Figure 3.3**a), designed for the observation of the device through any upright or inverted microscope and with any kind of objective.

3.4.4 Image acquisition and processing

The microfluidic chip was integrated onto an inverted microscope (Axio Observer, Zeiss) equipped with two illumination systems: (i) a precisExcite High-Power LED Illumination system (Visitron, Puchheim, Germany) for brightfield imaging and (ii) a Lambda DG4 illumination system (Sutter instruments, Novato, CA, USA) for fluorescence imaging. The microscope had a motorized xy-stage, equipped with an ASI piezo controller for z-displacement (Visitron, Puchheim, Germany) and the automated imaging process was controlled using VisiView Premier Image acquisition software (Visitron, Puchheim, Germany).

To start the automated imaging process, the position of the first egg in the array was set as initial point of the xy-stage scanning, while the locations of the other eggs were automatically determined by the interdistance between adjacent incubators (118 µm). A "wavelength program" was set on the software, to automatically switch between brightfield and fluorescent imaging modes, by controlling both the illumination systems. "Time-lapse" and "stage position" programs were set to automatically perform scanning and imaging over the full array at a desired rate, hence resulting in parallel time-lapse imaging of all the embryos. To avoid phototoxicity effects during these fluorescence imaging experiments, we minimized the exposure time of the embryo to the fluorescent excitation light ($t < 100$ ms) and pictures were recorded at a single focal plane of the microscope (i.e. at a single z value), despite the possibility of taking z-stacks with our setup. The movement of the embryo inside its eggshell during the twitching phase could sometimes introduce instantaneous modulations in the collected fluorescent intensity, because of the time-dependent positioning of the developing larva inside the focal volume of the microscope objective, but variations of the average fluorescent intensity of the embryo in a given xy-plane remained relatively small. The fluctuations in fluorescent intensity due to twitching of the embryo are smaller than the error bars in **Figure 3.12** and **Figure 3.13**. For each fluorescent picture, GFP intensity values were measured as average pixel intensity over the area occupied by the single embryo under observation. A background value was then measured for each picture as average pixel intensity over the microchannel area and this value was subtracted from the previously calculated one, to exclude the influence of any external autofluorescence sources from the measurement. Moreover, unspecific GFP expression is avoided by the use of tissue-specific promoters, e.g. the myo-3 promoter triggers GFP expression in the body wall muscles, while the ges-1 promoter in the intestinal cells only.

A simple Matlab script (MathWorks, Natick, MA, U.S.A) was written to reorder the large amount of data of each experiment according to the image xy-coordinates, time, light wavelength and exposure time. Image processing was performed with Fiji software (http://imagej.nih.gov/ij; version 1.47b).

3.5 Conclusions

In our platform, a well-defined and synchronized *C. elegans* embryo population can be isolated from an on-chip worm culture and studied in a fully automated way at extremely high spatial and temporal resolution. The device allows operation and analysis at the single-organism level, thus preserving the identity of each individual embryo, while at the same time providing statistics of the complete population. We demonstrate the capability of our platform to accurately analyze the real-time dynamics of different phases of the embryonic development, to monitor live protein expression in developing embryos during the complete embryogenesis, and to perform systematic studies that address outstanding issues in developmental biology.

Our approach allows suppressing the bleaching step in the classical method, which is used for embryo harvesting and could affect the embryo integrity. Furthermore, our on-chip embryo synchronization allows using a minimal amount of gravid worms to obtain an accurate number of laid eggs. Finally, the limitation of the manual handling and the full automation of our protocol provide

great advantages compared to the actual standard procedure, requiring several manual preparation steps (maintenance of a large worm population on solid agar plate, recovery of this worm population with the bleaching solution, washing of the egg preparation, egg transfer, etc.).

In particular, we validated our platform by characterizing development, mitochondrial biogenesis and UPR^{mt} in worm embryos at a precision that would have been very difficult or impossible to achieve with standard techniques. The imaging and monitoring of the embryogenesis require specific techniques, which imply single embryo isolation and its mounting [106]. Our microfluidic device was specifically designed to simplify and automate embryo handling, and only requires loading of a few adult worms into the chip. Furthermore, classical protocols for embryo analysis do not allow the concomitant monitoring of multiple replicates in identical biological conditions. The incubator array format of this platform provides a unique opportunity to study the intra-embryo variability in terms of viability, development or gene expression. This platform allows the identification in a reproducible and accurate manner of the different phases of the *C. elegans* embryogenesis that occur after the egg laying, from the early cell division stages to hatching. We were able to discriminate variations in terms of embryonic development and describe how perturbations of the mitochondrial functions can profoundly impact on the embryogenesis.

In *C. elegans*, the mitochondrial biogenesis mainly occurs during the late larval phase, *i.e.* during the L3 to L4 larval transition [138]. Here we described that another burst of mitochondrial biogenesis takes place during the last phase of the embryo development. This late embryonic proliferation of mitochondria seems to overlap with the differentiation of the mitochondria within the tissues, as revealed by the different profiles in term of biogenesis intensity and timing observed in muscle and intestinal tissues. Furthermore, while the mitochondrial biogenesis that occurs during the embryogenesis is less intense compared to the L3 to L4 transition, it is tempting to speculate that this late event in the embryo could be a prerequisite for the first steps of the larval development, by providing the required amount of mitochondria and energy. The crucial importance of the late phase of embryonic mitochondrial biogenesis is corroborated by the observation that several disturbances of the mitochondrial function during this specific period can impact later in the worm life [145].

In addition, we demonstrate that such perturbations of the mitochondrial function can trigger the UPR^{mt} pathway in embryos. The activation of this specific mitochondrial stress response matches the onset of mitochondrial biogenesis, which is in accordance with what is observed in larvae. Furthermore, the UPR^{mt} seems to work mainly in a cell-autonomous manner in embryos, probably because the signalling pathways required for the signal transmission between neurons and the distal tissues are not yet fully developed at this stage of life. These observations are the first proof that UPR^{mt} is functional during the embryogenesis. One could hypothesize that a mitochondrial stress restricted to the late phase of the embryo development could trigger a beneficial effect during the rest of the life, opening the concept of a potential “mitochondrial imprinting” during the first step of the organism’s life.

In the future, due to the versatility of our platform design, its live imaging capability can be readily extended to include other types of microscopies, like differential interference contrast microscopy, for high-contrast brightfield live imaging, and confocal microscopy to achieve extreme spatial resolution. Finally, we expect that similar microfluidic designs will be used to perform live imaging of a multitude of development events, like gastrulation and tissue morphogenesis during embryogenesis in other species of nematodes or other model organisms.

Chapter 4 Microfluidic culture chamber arrays for embryo-to-adulthood studies of *C. elegans* at single-organism resolution

Abstract In small-animal model research, a common issue for most of the applications is represented by animal isolation and monitoring, as well as by their age synchronization. In most of the biological laboratories these operations are manually performed via long and tedious protocols, prone to low reproducibility due to human errors and low control on the environmental conditions. For *C. elegans* research, this issue is amplified by the particularly small size of this model organism, which further complicates its manipulation and study. Thus, microfluidic tools for the automated handling of nematodes are recently gaining a lot of attention in the whole *C. elegans* research community. However, all the existing techniques for *C. elegans* isolation and monitoring – both manual and microfluidic-based – still base their population synchronization protocols on the selection of worms of different larval stages (typically L1 or L4), with no universally accepted standards and complete loss of information about all the developmental stages occurring prior to the synchronization itself. To solve these issues, we introduce a new microfluidic device which uses passive hydrodynamic trapping of *C. elegans* embryos as a method for worm isolation and age synchronization, for subsequent monitoring of the full development of the isolated worms at single-organism resolution. Our method allows synchronizing and starting monitoring a worm population at the earliest possible stage – i.e. upon laying of the embryos – and could thus set a new standard in the field. In our device, all the operations are driven via computer controlled syringe-pumps and performed inside a monolithic PDMS microfluidic chip. In this chapter, we discuss the microfluidic chip design and working principles and we describe an automated on-chip protocol for embryo isolation and transfer to individual microfluidic chambers, tailored for single-worm culture, treatment, and phenotypic study. With our device, we demonstrate the possibility of monitoring the whole development – from embryogenesis to adulthood – of individual worms at unprecedented levels of accuracy and automation. Moreover, being the embryos collected upon on-chip egg-laying (see chapter 3), the link between each worm population and its previous generation is conserved and can be tracked. Therefore, we foresee the use of our platform for transgenerational and epigenetic studies across successive worm generations.

4.1 Introduction

4.1.1 Microfluidic tools for long-term longitudinal studies on *C. elegans*

Biological processes are dynamic by their nature and the possibility of performing accurate time-resolved analyses of biological phenomena is a key need in the biomedical field. Many biological processes can be successfully studied in cell systems and several technological solutions have been proposed in the last years for long-term observation of dynamic phenomena in living cells [146-149]. However, to investigate time-dependent processes in which the interaction between multiple cells and/or different tissues plays a crucial role, long-term longitudinal studies of full organisms are required. The nematode *C. elegans* represents one of the best model organisms for this kind of analyses, mainly because of its very fast life cycle, combined with the ease of its genetic manipulation. Complex biological processes related to human dysfunctions developing throughout many years – such as metabolic or neurodegenerative diseases – can be potentially investigated in *C. elegans* in a matter of a few days or even hours [150]. Such an outstanding possibility triggered the development of different micro-technological tools for improving *C. elegans* handling and increasing the throughput of their analyses [103]. For instance, several miniaturized devices have been recently proposed to study worms' neurobiology [151], chemical sensitivity [152], behavior [153], and development [120], whereas different microfluidic designs offered the possibility of on-chip worm sorting [154], culture [110], immobilization [155], imaging [156], and/or screening [157].

A "worm-clamp" microfluidic device has been developed by Hulme *et al.*, with the goal of arraying and immobilizing *C. elegans* [158]. This system consisted of a PDMS-based array of gradually tapered microfluidic channels, with width ranging from 100 μm down to 10 μm, over 5 mm length. All these microchannels were merging into a common inlet on one side and a common outlet on the other side. As the animals were introduced into the microchannel network, they were pushed at the end of the tapered channels, where they got stuck. Almost all the trapped worms could moreover be eventually removed from the clamps by reversing the flow direction inside the device. In another study, then, the same group added circular confinement chambers to each branch of the microfluidic array described above (**Figure 4.1**a) [110]. In this chip, worms could be cultured in the different chambers and immobilized for imaging at the adult stage by suction in the worm-clamps. Each line of the array could be selectively addressed using prefabricated screw valves [159]. To prove the suitability of this device for performing longitudinal studies/measurements, individual worms were loaded via suction at the fourth larval stage (L4) into each confinement chamber and investigated over their lifespan.

Applicability of droplet-based microfluidic devices for creating an array of droplets containing *C. elegans* was also demonstrated. Clausell-Tormos *et al.* managed to encapsulate *C. elegans* eggs, along with *E. coli* bacteria as animal feed, inside 660 nL aqueous plugs. This system was then employed to monitor the larvae after egg hatching, during the various phases of their development [160]. While, on the one hand, this droplet-based system is relatively simple to design and does not require a complex microfluidic architecture, on the other hand, it lacks of flexibility, since it cannot isolate mother animals from their own progeny. In another work, Shi *et al*. designed a

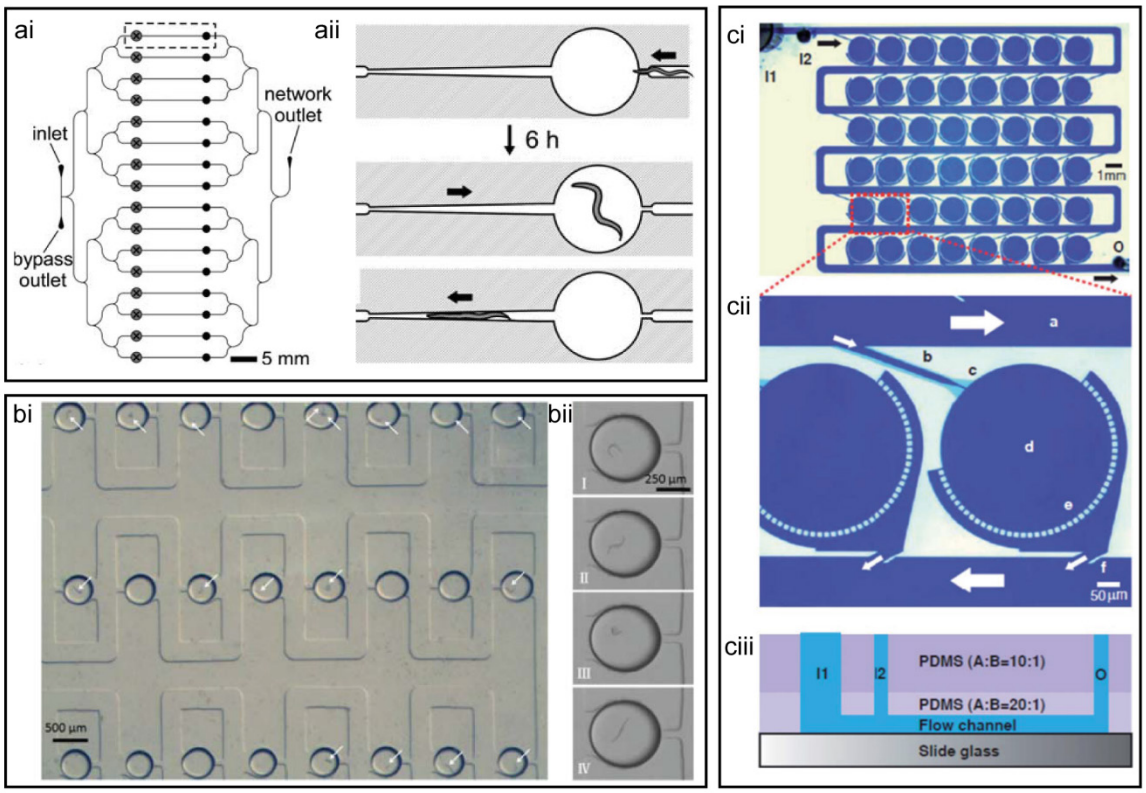

Figure 4.1 | Worm-chips for longitudinal studies at single-worm resolution. (a) Schematic representation of (ai) the "lifespan chip" geometry and (aii) the worm handling process proposed by Hulme *et al.* (reproduced from [110]). Worms are loaded into the chip at the L4 larval stage, cultured towards the adult stage and periodically sucked into a narrowing channel for temporary immobilization and imaging. (b) Pictures of the droplet-based system for *C. elegans* assays proposed by Shi *et al.* (reproduced from [161]): (bi) droplets encapsulated with worms and (bii) representative images of worms during an on-chip motility test. (ci-cii) Optical micrographs of the worm chamber array device proposed by Chung *et al.* (reproduced from [162]). A "loading channel" associated to each chamber is used for worm injection. (ciii) Schematic drawing showing a cross-section of the device, with 2 different PDMS compositions to tune the elasticity of the microchannels.

microfluidic device for worm encapsulation in isolated droplets and subsequent droplet immobilization in a trap array [161] (**Figure 4.1**b). This microfluidic device consisted of a T-junction droplet generator combined with a serpentine microchannel, short-circuited at each branch by a cavity for droplet trapping. The different fluidic resistances of the main flow path and the cavity-based short-circuited flow path ensured efficient droplet trapping, while around 60% of the trapped droplets contained a single worm.

Chung *et al.* [162] proposed then a "chamber array" microfluidic design for behavior-based chemical screening on *C. elegans* (**Figure 4.1**c). The specific geometry of the device was tailored for the injection of single adult worms in separated chambers and their subsequent exposure to chemical stimuli with precise temporal control. As a proof of concept, worms were exposed to sodium azide at different concentrations and the time-dependent descrease in their locomotion was quantified by determining the worms' body bend frequency over time.

4.1.2 Challenges and opportunities for *C. elegans* synchronization and lifespan studies

Most of the platforms conceived for *C. elegans* lifespan studies rely on worm synchronization at the L4 larval stage and allow monitoring the duration of worms' adult life, but do not provide any information about their embryonic and larval development. Very few platforms have been presented for *C. elegans* studies starting from earlier larval stages, while there is no currently available technological solution for monitoring the actual *full* worms' lifespan, i.e. from embryogenesis to death. This operation is particularly challenging since it requires accurate manipulation of biological entities of very different sizes and motilities. Embryos are 30-50 µm in size and they are enclosed in their eggshells: they have to be gently and accurately transported by fluidic forces if they need to be displaced at specific locations within a microfluidic chip. During larval development, both worms' length and diameter increase by a factor of about 10. *C. elegans* are moreover very motile: their overall force increases together with their size, while their motility is significantly amplified in liquid culture conditions (i.e. swimming gait) with respect to solid media cultures (i.e. crawling gait). All these factors need to be carefully taken into account when designing chip geometries for confinining and studying worms during their whole development from the embryonic to the adult stage. Starting from the experience achieved by developing on-chip solutions for *C. elegans* embryogenesis analyses (see chapter 3), we propose here a new microfluidic platform which aims at extending the worms' monitoring and analysis period from its embryonic development to its complete lifespan.

4.2 Microfluidic device design and automated operation

4.2.1 Overview of the microfluidic device

The geometry of our microfluidic device is conceived according to two main design rules: (i) a monolithic PDMS chip structure, ready to use upon a single bonding step (**Figure 4.2**a); (ii) use of pure passive hydrodynamics to carry on a full set of automated microfluidic operations. The first requirement is set to fasten and ease the chip preparation, by avoiding tedious manual operations, such as chip-by-chip alignment and bonding of several PDMS layers. The second rule allows minimizing the device connections and simplifying its control: first, our device does not need any extra-circuit or tubing for pneumatic valve control; second, all the microfluidic operations are handled by controlling inflow speed via automated syringe-pumps and outflow direction through two external valves. The absence of any active component in our device is however possible only by careful design of all the constitutive parts of our planar microfluidic geometry (**Figure 4.2**b).

Our chip is made up of two main building blocks: (i) the "parents' culture chamber", tailored for the isolation of young adult worms from a mixed population and their successive culture and treatment (**Figure 4.2**c); (ii) the "progeny's culture chamber matrix", featuring 16 micro-compartments for the capture of 16 embryos laid in the parents' chamber and their subsequent culture and phenotyping over several days, at single-worm level (**Figure 4.2**d). The parents' culture chamber is connected to arrangements of microfluidic channels of different size and geometry, de-

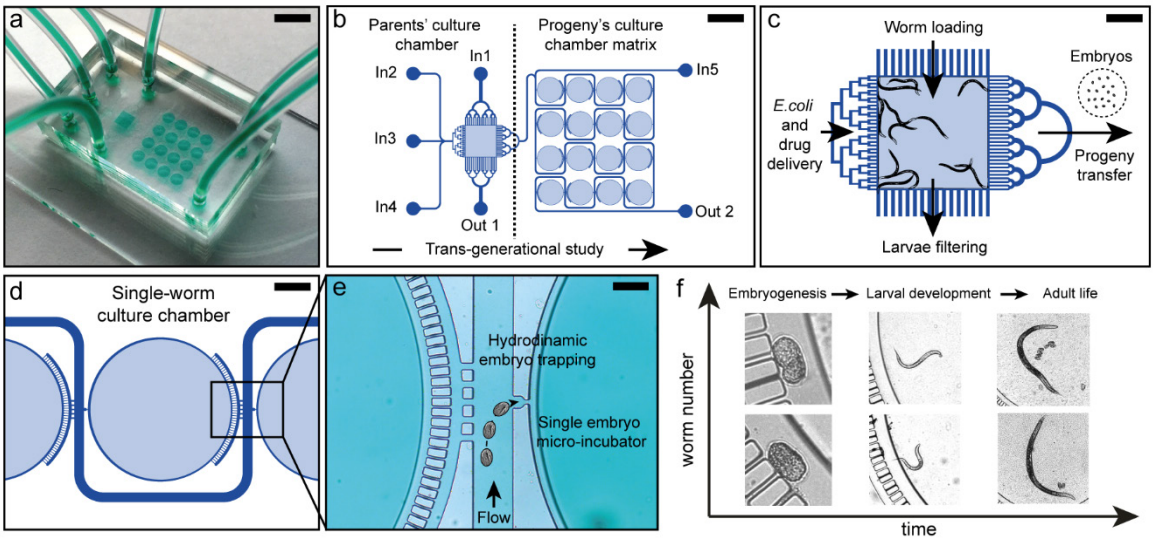

Figure 4.2 | Overview of the microfluidic device. (a) Picture of the microfluidic device. Scale bar = 5 mm (b) Schematic representation of the microfluidic chip layout, featuring as main constitutive parts: the parents' culture chamber, the progeny's culture chamber matrix, five inlets (In1 to In5) and two outlets (Out1 and Out2). Scale bar = 2 mm. (c) Zoom on the parents' culture chamber, including a drawing of young adult *C. elegans* for size comparison. The chamber is delimited by specific microfluidic channel arrangements, tailored for different functions: (top) worm injection, (bottom) worm synchronization, (left) *E. coli* / drug delivery and (right) egg transfer. Scale bar = 500 µm. (d) Schematic representation of a portion of the progeny's culture chamber matrix (Scale bar = 200 µm), with (e) a further zoom on a single embryo micro-incubator, used for hydrodynamic trapping of one *C. elegans* embryo for each chamber (Scale bar = 100 µm). (f) Illustration of the parallel time-lapse imaging that is enabled on the array of worms within the progeny's culture chamber matrix. Single worms are accurately monitored from embryogenesis to adult life.

signed for different specific functions, as previously described in chapter 3. A mixed worm population is loaded into the chamber from the channels connected to the In1 inlet: adult worms are retained inside the chamber by the filter associated to the Out 1 outlet, while larvae are directly washed out of the chip. Three separate inlets (In 2-4) are used to inject into the chip *E. coli* suspension, S-medium and chemicals, respectively. The adjacent channel arrangement promotes uniform liquid perfusion through the culture chamber, while preventing any passage of worms towards the inlets. Finally, the filter geometry connecting the parents' chamber to the progeny's chamber matrix is designed to ensure efficient transfer of embryos towards the matrix, while retaining all the worms inside the parents' chamber.

Each embryo which is transported through the serpentine channel connecting the 16 culture chambers is redirected towards the first empty micro-incubator and captured there by passive hydrodynamic trapping (**Figure 4.2**e). This mechanism allows automatically associating a single embryo to each culture chamber. The 16 captured embryos are then transferred to each dedicated chamber, for their successive hatching, culture towards the adult stage, monitoring and phenotyping at single-worm resolution (**Figure 4.2**f).

4.2.2 Automated device operation

The device is operated through sequences of automated processes (**Figure 4.3**). At the beginning of each experiment, a worm suspension is injected into the microfluidic chip from the In1 inlet

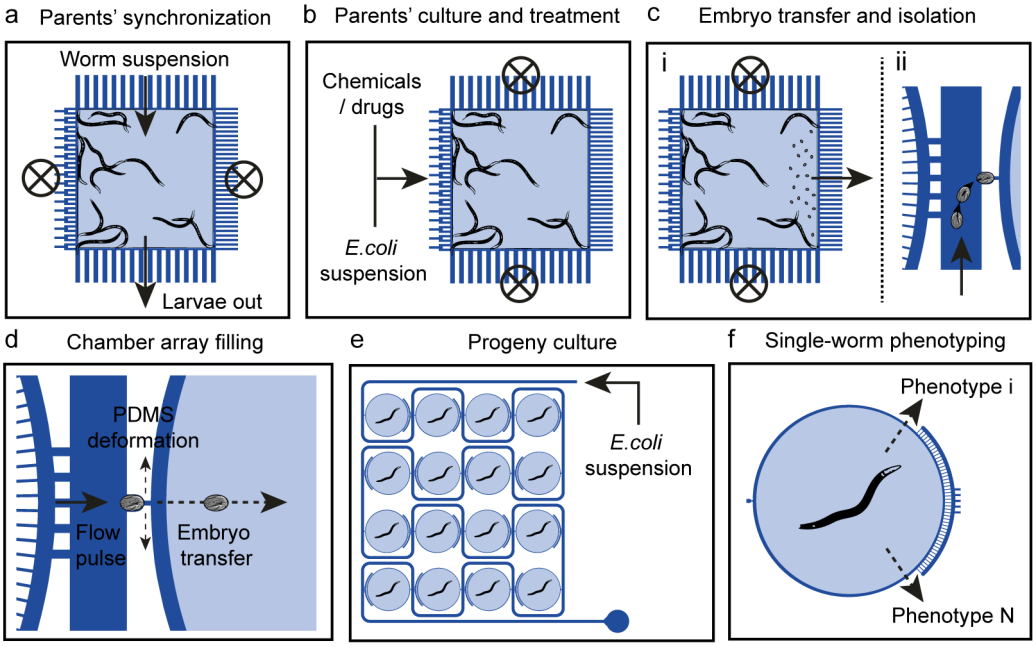

Figure 4.3 | Operation of the microfluidic device. (a) First a 10 µL suspension of worms in M9 buffer is injected into the microfluidic device along the In1-Out1 direction at a flow rate of 500 nL/s. Symbols used for the in- and outlets: arrow = flow; cross and circle = closed valve. The "worm synchronization filter" is tailored to retain inside the chamber only adult worms, as selected by their larger size and their better swimming abilities. (b) Subsequently worm culture is controlled by periodically injecting *E. coli* in M9 buffer along the In2-Out2 direction, typically at 50 nL/s flow rate. This ensures normal development of the worms in the liquid environment and continuous embryo production during their adult lifespan. Optionally, drugs or chemicals can be introduced at the In4 inlet for on-chip worm treatment. (ci) Injection of M9 buffer at 200 nL/s flow rate along the In3-Out2 direction triggers the transfer of all the eggs present in the chamber towards the progeny's culture chamber matrix, where (cii) they are captured by passive hydrodynamics in single micro-incubators. (d) A flow pulse is used to simultaneously trigger the transfer of all the captured embryos from a micro-incubator to the adjacent chamber. (e) The perfusion of *E. coli* suspension across the whole progeny's culture chamber matrix ensures proper worm feeding and development, while (f) automated parallel time-lapse imaging is used to trace multi-phenotipic profiles of the worms at single-worm resolution.

towards the Out1 outlet (**Figure 4.3**a). We typically employ 10 µL suspensions containing about 10 adult worms. For flow rates in the 500-1000 nL/s range, the geometry of the filter at the Out1 outlet (800 µm long straight channels, 60 × 35 µm^2 in section) ensures that all the larvae which are present in the suspension are simply washed through the chip towards the Out1 outlet, while adult worms are retained in the culture chamber, because of their larger size and better resistance against the flow. Afterwards, adult worms are cultured on-chip by perfusing *E. coli* suspension through the chamber (from In2), whereas for worm treatment, drugs or chemicals can be introduced in the chip as well (at In4) (**Figure 4.3**b).

For 10 young adults at their peak of reproduction, tens of eggs are typically laid inside the parents' culture chamber in about 1 h upon their loading on-chip. At this point, a 200 nL/s flow rate of S-medium buffer along the In3-Out2 direction is used to transfer all the embryos present in the chamber towards the progeny's culture chamber matrix. As will be detailed further, the geometry of this part of the chip is conceived to ensure the isolation of a single embryo aside each round

culture chamber, by positioning it in a specifically designed micro-incubator via passive hydrodynamic trapping (**Figure 4.3**c). Complete filling of the array of 16 micro-incubators is achieved in a few seconds, and the remaining eggs are automatically directed towards the Out2 outlet. As a final step of the embryo transfer protocol, a 2 s pulse of 40 µL buffer is injected towards Out2. Because of the relatively high fluidic resistance of the chamber matrix, this single flow pulse builds temporary overpressure inside the chip and slightly deforms the PDMS structure of the micro-incubators to trigger the transfer of each embryo to its chamber (**Figure 4.3**d).

Successively, perfusion of *E. coli* suspension from the In5 inlet towards the Out2 outlet allows distributing bacteria across the whole chamber matrix and feeding of the 16 worms after egg hatching (**Figure 4.3**e). At the same time, liquid flow along the In5-Out2 direction allows decoupling the use of the two sections of the chip, so that parents and progeny could be cultured at the same time, with no further transfer of embryos or worms from one side to the other. Alternatively, the parents' can be easily washed out of the chip after the embryo transfer inside the progeny chambers. Flow pulses of 5-10 µL/s along the In1-Out1 direction allow in fact inducing the passage of adult worms through the filter at Out1, with no perturbation of the progeny inside the 16 chambers aside. Worms in the progeny's chamber matrix can be cultured, monitored and analysed over consecutive days, at single worm resolution, while extracting precious phenotypic information – e.g. growth rates, protein expression, motility, etc. – related to all the different phases of its development, from early embryogenesis to adulthood (**Figure 4.3**f).

Finally, it is worth noticing that the whole presented set of complex microfluidic operations is allowed in our chip by mere changes in flow rate and/or in direction of the injected flows, controlled via software by automated syringe pumps. In this chip, the protocol complexity is transferred towards the chip engineering and design optimization, rather than to the multiplication of active controls and operations.

4.3 Engineering of the chip functionalities

4.3.1 Single embryo hydrodynamic trapping

In our device, when a *C. elegans* embryo is transferred to the progeny's chamber matrix, it first enters a 80 µm wide serpentine channel, interconnecting the 16 chambers. The geometry of the system is optimized to guarantee that each embryo flowing through this channel will get trapped aside the first available culture chamber, i.e. the chamber associated to the first empty micro-incubator along the path. Moreover, to ensure single-worm resolution for the successive analyses, the design needs to guarantee the trapping of a single embryo per incubator and that all the embryos transferred after the complete filling of the array will be directed towards Out2 and washed out of the chip. Finally, the trapping system must be optimized to maximize its capture efficiency. To control the transgenerational passage and prevent perturbations of the egg laying process, embryos are in fact transferred towards the trapping sites only upon their natural egg laying in the parents' culture chamber. This limits the number of available synchronized embryos per experiment, so that the loss of even a few embryos during their transfer could compromise the experiment and should be avoided.

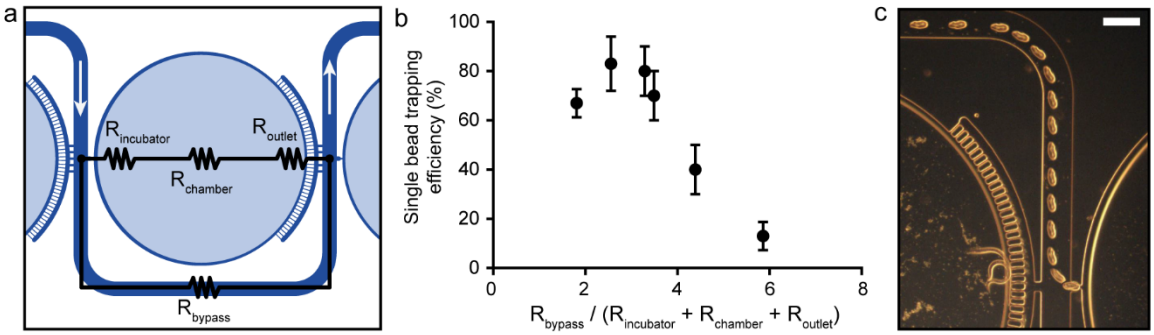

Figure 4.4 | Engineering of the hydrodynamic trapping system. (a) Schematic representation of the design of the hydrodynamic embryo trapping system, with indication of the hydraulic resistances associated to the different parts of the microfluidic geometry. (b) Experimental characterization of the trapping efficiency of the system for 6 similar microfluidic designs (characterized by different hydraulic resistances in their main constitutive parts). The "single bead trapping efficiency" is measured as the percentage of traps capturing a single 30 µm bead over the total number of available trapping sites. (c) Video frames superposition showing a single embryo trapping event in the device design with higher capture efficiency. Scale bar = 100 µm.

The efficiency of our embryo trapping mechanism can be predicted by calculating the ratio between the volumetric flow rates through each chamber and its bypass channel, respectively. In very first approximation, this ratio can be theoretically estimated by considering the pressure drop between inlet and outlet of each chamber along the two parallel fluidic paths and imposing equal pressure difference along them, assuming Poiseuille flow conditions [117]. This calculation, however, ignores losses due to channel bends, widening/narrowing, etc., which are indeed quite relevant in our design because of its composite geometry. In particular, spreading flow profiles at the boundary of pinched and broadened segments are completely neglected under this assumptions, which make therefore this calcualtion a very rough estimate of the real situation. Nevertheless, we decide to employ these calculations as a tool for a first approximated dimensioning of our chips, whose architecture is then refined through the results of a systematic experimental characterization (see further).

Assuming Poiseuille flow conditions, the ratio between the flow rate through a chamber and the one through its bypass channel can be calculated as the inverse of the ratio between the hydraulic resistances of the two fluidic paths (**Figure 4.4**a). For a straight channel with rectangular cross-sectional shape, the hydraulic resistance can be calculated using Equation (3.1). In our case, the resistance of the bypass channel, R_{bypass}, can be approximated using (3.1), while the fluidic path across the culture chamber is calculated as a series of 3 main resistances (**Figure 4.4**a): (i) $R_{incubator}$, including the resistances of a single-embryo trap and its drain connection to the chamber; (ii) the chamber resistance, $R_{chamber}$ and (iii) R_{outlet}, made up of two interconnected series of parallel resistances. We estimated the trapping efficiency for 6 similar versions of our device and fabricated them to experimentally determine the hydraulic resistance ratio which maximizes the capture efficiency in our geometry. For these tests, we employ 30 µm polymeric beads as trapping objects and define the capture efficiency as the percentage of traps containing a single bead over the total number of available trapping sites, for a constant amount of beads injected into the microfluidic device. From our experimental analysis, we conclude that a ratio R_{bypass} / ($R_{incubator}$ + $R_{chamber}$ + R_{outlet}) of ~2.6 maximizes the system trapping efficiency (**Figure 4.4**b). After ensuring similar results by

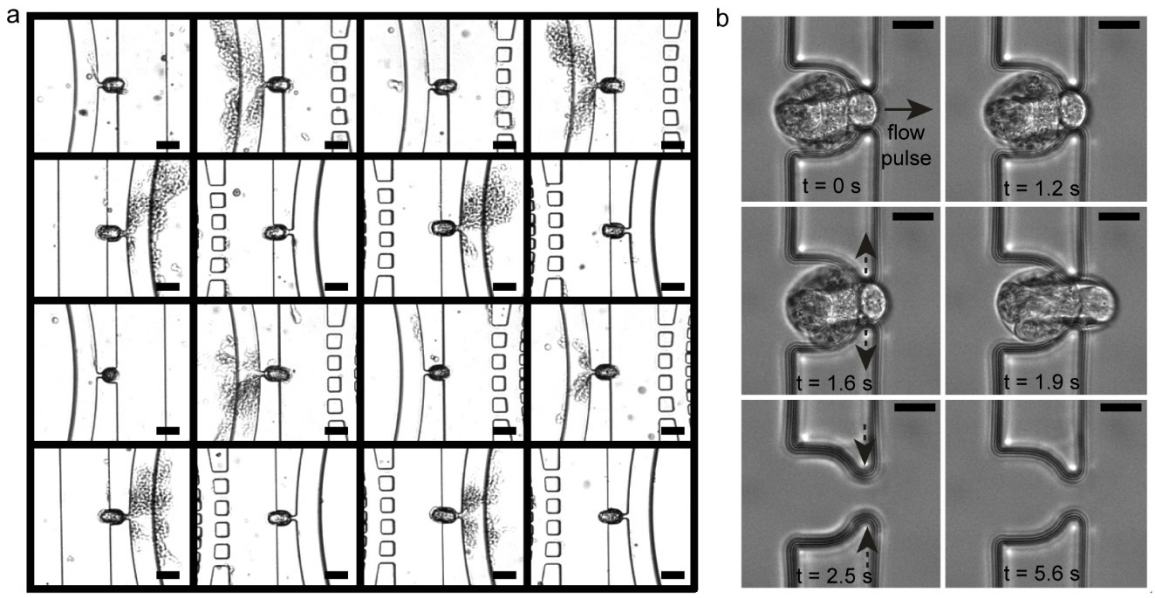

Figure 4.5 | Embryo isolation and parallel transfer to microfluidic chambers. (a) Pictures of a representative array of embryos, upon complete filling of the incubator array. The hydrodynamic trapping mechanism results in stable embryo positioning, with a single embryo associated to each culture chamber. Scale bars = 50 µm. (b) Time-lapse pictures of a micro-incubator, during the injection of an embryo into the adjacent chamber. A 1 s flow pulse triggers a fast reversible enlargement of the drain, allowing the transfer of the embryos inside their dedicated chambers. The PDMS structures get back to their undeformed shape in about 5 s.

using *C. elegans* embryos, we hence selected the chip geometry associated to this hydraulic resistance ratio as preferred choice for our successive chip designs. The selected geometry ensures in fact both correct embryo reorientation and positioning inside each micro-incubator (**Figure 4.4**c) and reliable assembly of matrices of 16 embryos upon their transfer from the parents' chamber (**Figure 4.5**a).

4.3.2 Parallel transfer of embryos from incubators to chambers

Size and shape of the micro-incubators are designed to gently accommodate single *C. elegans* embryos in a horizontal position, aligned along their longitudinal direction. As reported in chapter 3, elongated semicircular incubators (35 µm wide, 30 µm long) prove to be perfectly suitable for this purpose, each one associated to a 12 µm wide, 8 µm long drain connection for correct embryo trapping and stable positioning. In our chip, we now add a new functionality, since, upon its trapping in a micro-incubator, each embryo need to be transferred to its dedicated culture chamber. We rely on PDMS elasticity to control a fast reversible deformation of micro-incubators and drains and trigger the delivery of the embryos inside the chambers. We optimize this protocol according to some key requirements: (i) perfect embryo viability after the transfer; (ii) fast simultaneous displacement of all the trapped embryos; (iii) simple operations, automatically handled via syringe pumps. We find that a 1 s flow pulse of 20 µL along the In5-Out2 direction ensures the reliable transfer of the whole embryo matrix from incubators to chambers, according to all the aforementioned requirements (**Figure 4.5**b). Because of the relatively high fluidic resistance of our chip geometry, this flow pulse induces in fact enough deformation of our structures, with no need of

multiple PDMS layers fabricated at different “curing agent vs base” compositions to tune their stiffness [162].

4.4 Embryo-to-adulthood worm imaging at single-organism resolution

4.4.1 Embryogenesis monitoring

When embryos are transferred inside the progeny’s culture chambers, each of them is directed towards the central part of the outlet filter by the microchannel arrangement itself. The specific geometry of these filters is in fact designed to generate a flow focusing effect across the central portion of each chamber. Thanks to this feature, a relatively slow flow – typically 5-15 nL/s – along the In5-Out2 direction allows retaining the embryos at stable positions in each chamber, for their long-term imaging via high-magnification objectives (**Figure 4.6**a). If *E. coli* suspension is used, moreover, such a flow allows distributing bacteria across the chamber matrix, to provide the worms with their first food source upon egg hatching.

In our device, embryos can be transferred to their dedicated chambers at any time during their development, prior to egg hatching. In our experiments, the transfer is either performed upon full array filling or after all the embryos have reached the twitching phase. Although the former option is readily compatible with full protocol automation, the latter is usually preferred for two main reasons: (i) higher imaging stability is ensured when embryos are observed inside the micro-incubators; (ii) no mechanical stress is introduced on the embryos during early – and more delicate – phases of their development. Even when subjected to the transfer at very early developmental stages, embryos in our device proved to undergo normal development and perfect viability, in line with previously reported results [163], showing therefore no effect of any possible stress introduced by the transfer process itself.

As in the device presented in chapter 3, also in this chip, the different phases of the full embryonic development can be monitored and studied with extreme accuracy (**Figure 4.6**b).

4.4.2 Worm growth and development monitoring

The gentle flow (5-15 nL/s) used to retain the embryos at stable positions, in combination with the narrow size of all the microfluidic connections around the chambers, prove to be suitable to ensure the confinement of each worm in its chamber at any developmental stage, therefore enabling long-term studies at single-worm resolution. Only at the L1 larval stage, in fact, the worms’ section is still comparable in size with the one of the incubator drain, so that a flow is needed to ensure their permanence in the same chamber. Starting from the L2 larval stage, worms are instead geometrically confined within the chambers by their own larger size and food delivery can be pursued via periodical flow activation at desired rate. In particular, about 5 µL *E. coli* suspension is injected into the chip every 10 minutes, at $1.4 \cdot 10^9$ bacteria/mL concentration. This feeding protocol proves to ensure quite reproducible worm development, in good agreement with results reported in literature [96] (**Figure 4.6**c). For worm growth monitoring, we usually take time-lapse

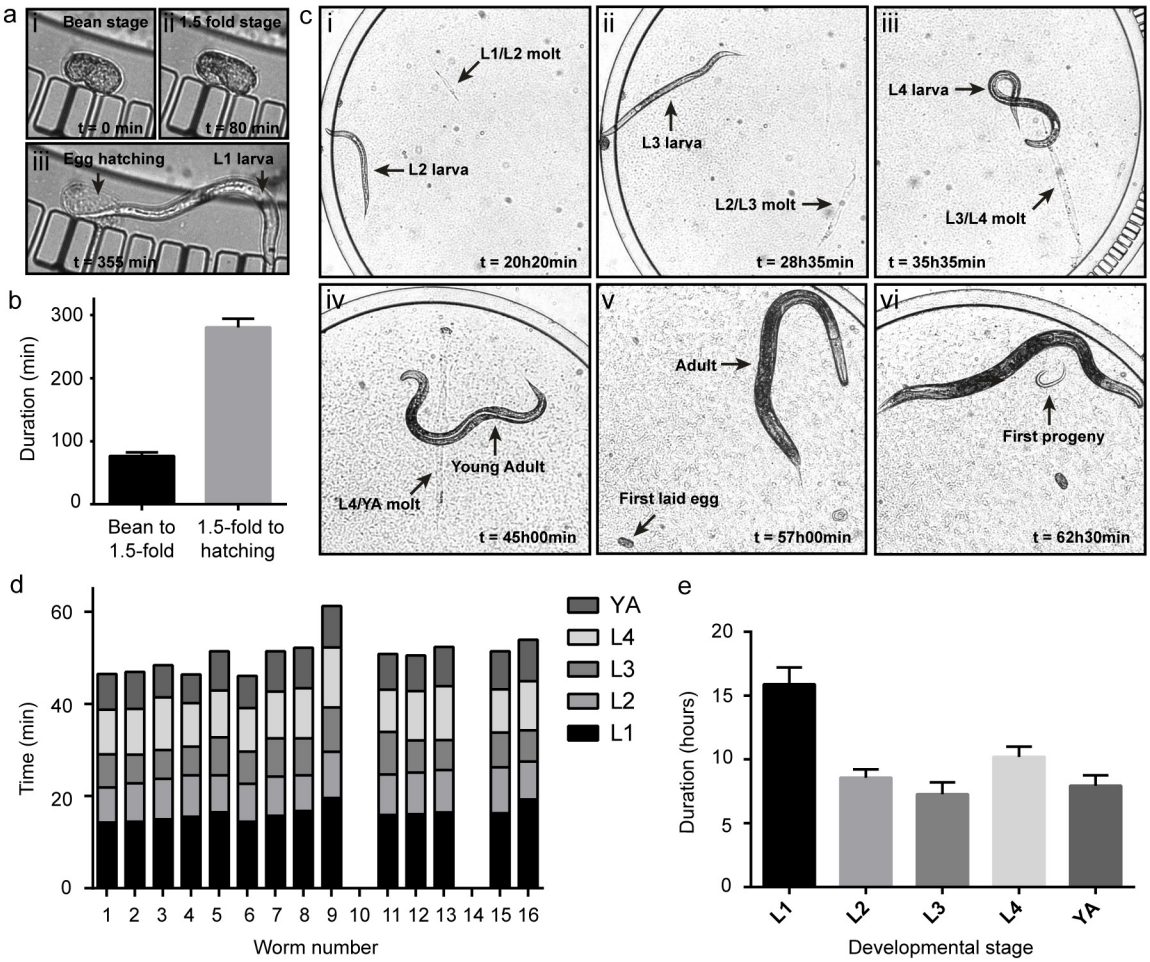

Figure 4.6 | Embryo-to-adult worm monitoring at single-organism resolution. (a) Embryonic development within a worm culture chamber, from (ai) bean stage to (aii) 1.5-fold stage till (aiii) hatching, as observed in a sequence of brightfield microscopy images (40× NA 0.6 objective) taken from a movie with 12 frames per hour. (b) Average duration of main embryonic development phases – bean to 1.5-fold; 1.5-fold to hatching –, as observed for an array of 16 embryos for a N2 wild-type worm strain at 25°C. Bar graphs are expressed as mean+SD (c) Full development of the worm in (a), as observed in a sequence of brightfield microscopy images (4× NA 0.1 objective) taken from a movie with 4 frames per hour. Accurate identification of the onset of the different developmental stages – (ci) L2, (cii) L3, (ciii) L4, (civ) young adult – is achieved by observation of the molting events. Progeny analysis – (cv) first laid egg, (cvi) first progeny – is demonstrated as well. (d) Duration of the main development phases – L1, L2, L3, L4, young adult (YA) – as observed for an array of 14 worms for a N2 wild-type worm strain at 25°C. The end of YA stage is defined by the appearance of fertilized eggs within the worm body. Variations of the time durations are commented in the main text; (e) average duration of development phases, as obtained from the data in (d). Bar graphs are expressed as mean+SD.

pictures of each chamber at 15 min intervals. Fully automated operations for this processs are allowed by a computer-controlled xyz-scanning microscope stage.

The presence of a single worm per chamber allows easily identifying the molting time of each worm and therefore accurately defining every transition from/to a different larval stage, up to the worms' adulthood. By analysing series of time-laspe pictures for each chamber, each molt can be found either attached to a worm tail during the molting itself or floating inside the worm culture chamber, if the picture was taken upon the molting (**Figure 4.6**c). These molting events represent a very accurate way to identify the actual biological transitions amongst the different larval stages

(L1-L4), up to the young adult (YA) stage. Other parameters could have been monitored to define these transitions – such as worm size or the apparition of specific features within the worms' tissues – but these alternative methods can be strongly affected by the variability of these parameters among different worm strains or conditions. In our device, the whole on-chip larval development can be hence monitored at an unprecedented combination of resolution and level of automation (**Figure 4.6**d-e). The duration of the YA stage is instead here defined as the time interval between the L4/YA molting and the appearance of the first fertilized eggs inside the worm.

The results of the representative experiment reported in **Figure 4.6**d are chosen to highlight some remaining issues and future applications of our device. As previously mentioned, if the microfluidic flow across the chamber array is temporarily stopped during the L1 phase, worms are still capable of escaping from the chambers, as it happened in this case for worms 10 and 14 (missing bars in the graph of **Figure 4.6**d). A further optimization of the worm feeding protocol for this device is moreover desirable, since variations of the duration of the different development phases may likely be induced by some non-uniformities in the *E. coli* distribution across the chamber array. The extreme sensitivity of our measurements to the food delivery method suggests however novel interesting applications for our device, which could in fact be readily employed for accurate caloric restriction studies, combined with developmental analyses. This possibility is further confirmed by the observation of the time-lapse development of worm 9 of **Figure 4.6**d. This nematode got accidentally blocked at a fixed location of its chamber – and hence experienced food deprivation – for several hours during the L1 phase. This "accident" has a very clear impact on its whole development, which is accurately detected by our device (see **Figure 4.6**d).

4.5 Materials and methods

4.5.1 Chemicals and Materials

4-inch 550 µm thick Si wafers and DIW were obtained from the Center of Micro- and Nanotechnology of EPFL. GM 1070 SU-8 negative photoresist was purchased from Gersteltec (Pully, Switzerland). PDMS Sylgard 184 was acquired from Dow Corning (Wiesbaden, Germany). 1 mL borosilicate H-TLL-PE syringes were purchased from Innovative Labor Systeme (Stutzerbach, Germany). Microline ethyl vinyl acetate tube with 0.51 mm inner and 1.52 mm outside diameters was bought from Fisher Scientific (Wohlen, Switzerland). Pluronic F-127 was purchased from BASF (Basel, Switzerland*).* M9 buffer was obtained by adding 3 g KH_2PO_4, 6 g Na_2HPO_4, 5 g NaCl, 1 mL 1 M $MgSO_4$, H_2O to 1 litre and sterilization by autoclaving. Pluronic F127 solution was prepared by diluting 0.02% (weight/volume) Pluronic F127 in M9.

4.5.2 *C. elegans* strains and culture

C. elegans strains were cultured at 20°C on nematode growth media agar plates seeded with *Escherichia coli* strain OP50, unless stated otherwise. The wild-type Bristol N2 worm strain was provided by the Caenorhabditis Genetics Center (University of Minnesota). Worms were suspended in M9 solution prior to each microfluidic experiment.

4.5.3 Fabrication of the microfluidic chips

Microfluidic devices were prepared by soft lithography [144] using 2-layer SU-8 molds. Briefly, conventional photolithography was used to pattern a 35 µm-thick layer of SU-8 photoresist on 4-inch wafers. A 85 µm-thick layer of SU-8 was then patterned on top of the first one. A liquid PDMS mixture (10:1 base:cross-linker weight ratio) was poured onto the mold, degassed, and cured at 100 °C for 1 h. Each PDMS chip was then cut along its sidewalls with a scalpel, gently detached from the SU-8 mold and bonded by plasma-activation to a glass microscope slide. The chip was then connected to syringes through external tubing.

4.5.4 Image acquisition and processing

The microfluidic chip was integrated onto an inverted microscope (Axio Observer, Zeiss) equipped with a precisExcite High-Power LED Illumination system (Visitron, Puchheim, Germany) for bright-field imaging. The microscope had a motorized xy-stage, equipped with an ASI piezo controller for z-displacement (Visitron, Puchheim, Germany) and the automated imaging process was controlled using VisiView Premier Image acquisition software (Visitron, Puchheim, Germany). To start the automated embryo imaging process, the position of the first egg in the array was set as initial point of the xy-stage scanning, while the locations of the other eggs were automatically determined by the interdistance between adjacent incubators. A 40× NA 0.6 objective, corrected for 1 mm-thick glass slides (LD Plan-Neofluar 40x/0.6 Corr Ph2 M27), was typically used for this imaging. “Time-lapse” and “stage position” programs were set to automatically perform scanning and imaging over the full array at a desired rate, hence resulting in parallel time-lapse imaging of all the embryos. An analogous protocol was set for the automated worm monitoring, performed through a 4× NA 0.1 objective. A simple Matlab script (MathWorks, Natick, MA, U.S.A) was used to reorder the large amount of data of each experiment according to the image xy-coordinates and time. Image processing was performed with Fiji software (http://imagej.nih.gov/ij; version 1.47b).

4.6 Conclusions

The device presented in this chapter further extends the analytical possibilities enabled by the microfluidic platform presented in chapter 3. In this device, a well-defined and synchronized *C. elegans* population can be isolated from an on-chip worm culture and studied in a fully automated way, starting from worms’ early embryogenesis up to their adult stage. The device allows operation and analysis at the single-organism level, thus preserving the identity of each individual worm during its whole development, while at the same time providing statistics of the complete population, thanks to the multi-chamber array format. We demonstrate the capability of our platform to accurately analyze the real-time dynamics of different phases of the embryonic development, as well as monitoring all the successive larval stages at unprecedented resolution and level of automation.

To the best of our knowledge, this is the first microfluidic device in which worms are isolated directly upon egg laying and then longitudinally monitored, potentially for their complete lifespan – i.e. from early cellular divisions to death. This will allow not only setting new standards in terms

of on-chip *C. elegans* culture and long-term analysis, but will also open the new possibility of accurately correlating developmental parameters, gene expression and any other phenotypic traits among all the different phases of worm growth, including the embyogenesis. Simultaneaous on-chip culture of the "parent worms" of each experiment will instead pave the way for fully automated on-chip transgenerational studies. For full lifespan studies at single-worm resolution, worms can be treated on-chip with 5-FU (see chapter 3), to prevent the development of the "third generation progeny" in the chamber matrix and preserve the identity of the 16 worms under test. Alternatively, the "third generation progeny" could be washed out of the chambers at the L1 stage, transported by relatively fast flow pulses through the microchannels at the otlet of each chamber (similarly to what will be presented in chapter 5). Eventually, to increase the throughput of each test, a new chip comprising more than 16 chambers could be easily designed and fabricated, thanks to the modularity of the presented microfluidic geometry and its regular array format, which ensure high device scalability.

All the further developments of this work have become subjects of a new PhD project at the LMIS2 laboratory.

Chapter 5 Microfluidic platform for high-resolution imaging of *C. elegans* and longitudinal monitoring of neurodegenerative disease

Abstract While many biological studies can be performed on cell-based systems, the investigation of molecular pathways related to complex human dysfunctions – e.g. neurodegenerative diseases – often require long-term studies in animal models. The nematode *C. elegans* represents one of the best model organisms for many of these tests and, therefore, versatile and automated systems for accurate time-resolved analyses on *C. elegans* are becoming highly desirable tools in the field. Here we describe a new multi-functional platform for *C. elegans* analytical research, enabling automated worm isolation and culture, reversible worm immobilization and long-term high-resolution imaging, and this under active control of the main culture parameters, including temperature. We employ our platform for *in vivo* observation of biomolecules and analysis of protein aggregation in a *C. elegans* model for amyotrophic lateral sclerosis (ALS). Our device allows automatically monitoring the growth rate and development of individual worms within a matrix of microfluidic chambers. We demonstrate the progression of specific protein aggregates – mutated human SOD1-YFP fusion proteins in the body wall muscles, in particular – for each worm over several days. Moreover, by combining reversible worm immobilization and on-chip high-resolution imaging, the device allows precisely localizing the expression of biomolecules within the worms' tissues, as well as monitoring the evolution of single aggregates over consecutive days at the sub-cellular level. This chapter is an adapted version of the following publications:

- **M. Cornaglia**, G. Krishnamani, L. Mouchiroud, T. Lehnert, J. Auwerx, and M.A.M. Gijs., Automated longitudinal monitoring of *in vivo* protein aggregation in a neurodegenerative disease *C. elegans* model, *Mol Neurodegener*, under revision
- **M. Cornaglia**, G. Krishnamani, M. Meurville, L. Mouchiroud, T. Lehnert, J. Auwerx, and M.A.M. Gijs. A microfluidic device for longitudinal studies of *C. elegans* neurodegenerative models. Proc. of 19th International Conference on Miniaturized Systems for Chemistry and Life Sciences (microTAS 2015), Gyeongju, Korea, October 2015.
- **M. Cornaglia**, G. Krishnamani, M. Meurville, L. Mouchiroud, T. Lehnert, J. Auwerx, and M.A.M. Gijs. An automated microfluidic platform for long-term high-resolution imaging of *C. elegans*. Proc. of 18th International Conference on Miniaturized Systems for Chemistry and Life Sciences (microTAS 2014), San Antonio, TX, USA, October 2014.

5.1 Introduction

5.1.1 Microfluidic tools for worm immobilization and high-resolution imaging

Because of the small size of *C. elegans* nematodes (a few hundreds of microns), high-magnification imaging is usually needed to extract relevant biological information, while studies on transgenic animals often require the accurate observation of highly localized fluorescent signals inside the worms. Hence, during imaging, animals have usually to be fully immobilized to prevent any movement, which otherwise would result in image distortion. Moreover, to observe the dynamics of biological processes, the same worm has to be immobilized repeatedly in a reversible manner. This should be done under normal physiological conditions in order to ensure minimal impact during the imaging phase. For high-throughput analyses, automation of this process is highly preferable. Some microfluidic-based worm immobilization methods have been recently proposed, based on worms' confinement in microchannels [164], suction flows [111], mechanical compression [165], CO_2 delivery [166], temperature decrease [112], electrotaxis [167], surface acoustic waves [168], and thermosensitive polymers [169].

More in detail, the first microfluidic solutions for *in vivo C. elegans* immobilization and imaging first appeared in the late years 2000s. Chronis *et al.* introduced the so-called "olfactory" and "behavior" devices, able to trap single worms and monitor their neuronal and behavioral activity (**Figure 5.1**a) [164]. These devices were fabricated in PDMS and their main constitutive part was represented by "worm-traps", optimized in size for hosting young adult worms (approximately 1 mm long and 70 μm in diameter), and characterized by a tapered end to block the worm, while still permitting analysis of its locomotion patterns in the wider section of the microfluidic channel [170].

Rohde *et al.* introduced then "high-speed microfluidic sorters", to immobilize single *C. elegans* for screening phenotypic features at sub-cellular resolution in physiologically active animals [111]. These microfluidic devices were based on separated flow and control layers, made from flexible polymers. Microchannels were used as a flow layer, to deliver reagents and manipulate worms, while the control layer consisted of a second set of microchannels built above the flow layer. (**Figure 5.1**bi) When pressurized, the channels of the control layer provided a valving function by deflection of a membrane into the flow channel, used for blocking or redirecting the flow. In these devices, worm immobilization was based on suction flows (**Figure 5.1**bii).

Krajniak *et al.* presented then a method for reversible immobilization of worms based on the use of a thermosensitive polymer [169]. Their PDMS microfluidic device consisted again of separate flow and control layers. The flow network featured culture chambers, isolated by inlet and outlet valves, for selectively retaining and culturing the worms inside the chip. The control layer of the device comprised instead the pneumatic circuitry for valve control and a second series of channels for flowing a pre-heated solution on top of the flow layer, to precisely control its temperature. Pluronic F127 block copolymer was injected into the culture chambers for selective immobilization of the worms by temperature-dependent gelation of the Pluronic solution (**Figure 5.1**c).

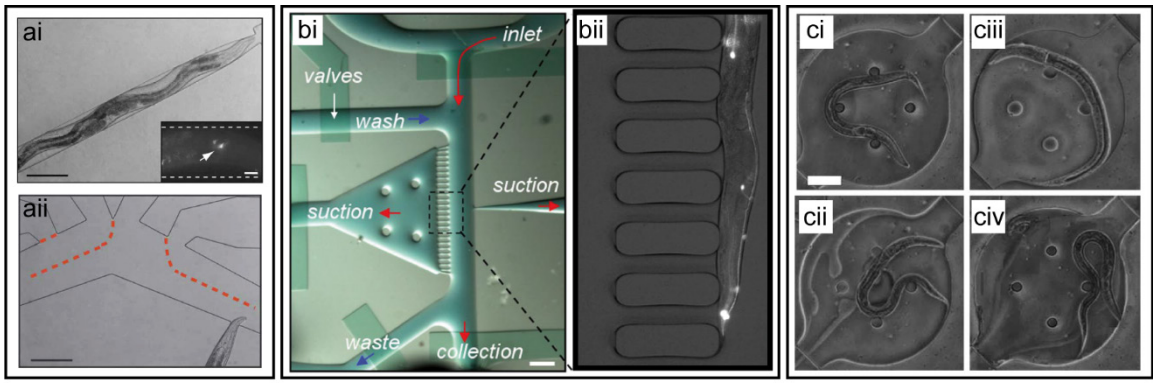

Figure 5.1 | Examples of microfluidic chips for *C. elegans* immobilization and imaging. (a) Pictures of (ai) the "behavior" and (aii) the "olfactory" chips proposed by Chronis *et al.* (reproduced from [164]). Worms are here confined in narrowing microfluidic channels. (bi) Picture of the microfluidic worm sorter proposed by Rohde *et al.*, with (bii) a zoom of a worm immobilized on suction channels (reproduced from [111]). (c) Pictures of the chip-gel hybrid microfluidic device proposed by Krajniak *et al.,* during (ci) worm culture, (cii) PF127 solution injection, (ciii) worm imaging, and (civ) worm release. (reproduced from [169]).

5.1.2 Challenges and opportunities for studies on *C. elegans* neurodegenerative models

The growing incidence of neurodegenerative diseases (NDs) urges for a complete understanding of the molecular processes underlying neurodegeneration, as a first step towards the final promise of a new class of therapeutics for these diseases. Cellular models have been exploited for some of these studies [171, 172], but the high complexity of the molecular mechanisms implicated in NDs increasingly demands *in vivo* models for the investigation of complex phenotypes, which are determined by the interplay among different tissues and pathways [173]. The nematode *C. elegans* represents a perfect model organism for such *in vivo* tests, mainly because of its very fast life cycle, combined with the ease of its genetic manipulation and the relatively high level of conserved mechanisms between *C. elegans* and humans [174]. In the last two decades, several protein-misfolding disorders, including age-related NDs, have been successfully modeled in *C. elegans* indeed [175]; libraries of transgenic worms are currently available for the research of the molecular mechanisms underlying Alzheimer's, Parkinson's and Huntington's diseases, as well as ALS [173]. Transgenic expression of disease genes in *C. elegans* is typically visualized via fluorescently tagged proteins within its transparent tissues. In most of the NDs, specific proteins self-assemble into aggregated species and cellular toxicity can be induced by the protein misfolding and aggregation process itself [173]. Therefore, the spatio-temporal-resolved observation of protein expression and aggregation, associated with the quantification and localization of these aggregates is a key analytical method for the *in vivo* monitoring of disease evolution. Unfortunately, conventional *C. elegans* handling and imaging techniques do not allow accurate monitoring of aggregate progression in individual worms over time, since nematodes are typically cultured in large populations on agar plates and irreversibly immobilized by means of anesthetics for high-resolution imaging.

Nevertheless, several miniaturized devices already proved their potential in neurobiology studies, such as the investigation of *C. elegans* oxygen sensation [176], olfactory [177] and chemosensory [112] neuronal activity, exploratory and learning behavior [178], neurotoxin-induced responses

[179], neuromuscular function [180], and nerve regeneration [181, 182]. In the neurodegeneration research field, Càceres et al. [183] recently proposed a microscale system for high-throughput visual screens on worms. This system exploited a curved microchannel geometry to trigger the positioning of nematodes into lateral orientations and facilitate the inspection of D-type motor neurons. Although this device allowed efficiently screening mutants carrying neurodegenerative defects, it did not permit longitudinal monitoring of the worms. Other microfluidic platforms have instead demonstrated the feasibility of continuous worm culture and observation. For example, Krajniak et al. [169] showed the microfluidic culture of L1-L3 larvae over periods of 12 to 36 h. However, protein aggregation monitoring within ND disease models typically requires worm culture and repeated high-resolution imaging of the same worm over significantly longer time periods (e.g. > 3 days). This imposes severe requirements in terms of system robustness and automation, related to the simultaneous and strict control of environmental conditions, like worm feeding, fluidic exchanges, temperature of the microfluidic environment, etc.. In this perspective, Rohde et al. [184] demonstrated an elegant automated system for *in vivo* time-lapse imaging and high-throughput screening of *C. elegans* in standard multiwell plates, which employed an in-well cooling apparatus for reversible worm immobilization. However, the use of this device for protein aggregation monitoring at single animal resolution is less trivial, as it did not have microfluidics on-board and could not exploit brightfield transmission microscopy as analytical tool.

Here we introduce a microfluidic platform for long-term and high-resolution monitoring of protein aggregation and automated analysis of *C. elegans* ND models. Specifically, we demonstrate the feasibility of *in vivo* observation over 4 days at single-animal resolution of superoxide dismutase 1 (SOD1) aggregation in the AM725 *C. elegans* transgenic strain, which we use as a biological model system for the investigation of the human ALS disease. This is enabled by our microfluidic platform, which co-integrates the following features and functionalities: (i) a method for fast confinement of worms of desired age in microfluidic chambers, by means of pure passive hydrodynamics with no need of any active components, such as integrated valves; (ii) a technique for continuous worm feeding and progeny removal, to preserve the on-chip worm identity over long-term studies; (iii) a method for reversible *C. elegans* immobilization using a hydrogel, enabling high-resolution imaging at arbitrarily selected moments of their whole lifespan; (iv) an integrated active temperature control system, both to set precise environmental conditions for *C. elegans* maintenance and to automatically steer the worm immobilization/release process; (v) a compact device assembly, readily adaptable to host different microfluidic designs and suitable for automated multi-dimensional imaging on any upright or inverted microscope.

5.2 Worm culture and imaging platform overview

Our worm culture and imaging platform features different components (**Figure 5.2**a). Worms are manipulated inside a monolithic PDMS microfluidic chip, conceived as a simple 1-layer device and operating via pure passive hydrodynamics, with no need of any active valving system. The chip is bonded to a standard 150 µm-thick glass coverslip for accurate worm imaging through high-magnification oil immersion objectives. An aluminum frame is specifically designed to host the chip and set a well-defined temperature distribution over its 3D geometry. Both the frame and the top

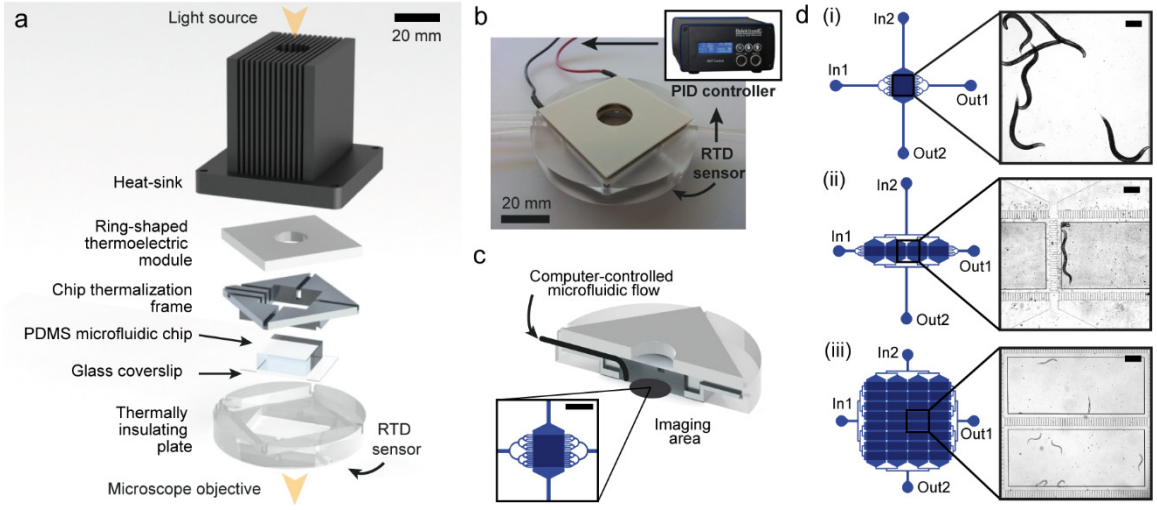

Figure 5.2 | Overview of the microfluidic device. (a) Schematic representation of the main constitutive components of the microfluidic platform. (b) Photograph of the device, with schematic picture of the closed-loop temperature control system. (c) Section view of the device assembly, with a zoom on a microfluidic design within the imaging area. Scale bar = 2 mm. (d) Representative microfluidic geometries for use with the platform, featuring matrices of worm culture chambers, tailored for the isolation of either (i) L4, (ii) L2 or (iii) L1 *C. elegans* larvae. Scale bars = 200 µm.

of the PDMS chip are positioned in contact with a thermoelectric module used to set the temperature of the assembly. A central hole in the Peltier module allows light transmission through the PDMS chip, therefore enabling worm imaging via transmission microscopy. A well-dimensioned heat sink ensures the dissipation of excess heat produced by the thermoelectric module; a thermally insulating holder allows positioning the device on the microscope stage while preventing thermal dissipation. The entire structure is held together by screws and springs at the four corners, in order to ensure good thermal contacts throughout the stack. A resistive temperature detector (RTD), in contact with the glass substrate, is employed to sense the temperature of the microfluidic device. The signal measured by the sensor is exploited to set the power provided to the thermoelectric module in a closed-loop configuration, for active control and constant monitoring of the temperature experienced by the worms inside the chip. The feedback loop management is committed to a portable proportional-integral-derivative (PID) controller (**Figure 5.2**b), provided with a software interface. The microfluidic flow inside the device is regulated by computer-controlled syringe pumps.

The tubings connecting the chip to the external syringes are directly plugged to the sidewalls of the PDMS device. To get this peculiar configuration, we casted PDMS inside a specifically designed mold, allowing to shape its whole 3D structure (see subsection 5.6.3). Lateral tubing connections are employed to partially embed the tubes in the aluminum thermalization frame, therefore putting them in contact with the Peltier module as well (**Figure 5.2**c). This allows pre-thermalizing the liquids prior to their injection inside the PDMS chip and opens the possibility of tuning the chip temperature through the injected liquid as well, as will be clarified further. Moreover, the lateral positioning of the microfluidic tubing makes our device readily suitable for imaging on both upright and inverted microscopes. Size and shape of the device holder allow perfect fit with any microscope stage or equipment compatible with standard 60 mm Petri dishes. The imaging area

available for transmission microscopy has about 15 mm in diameter, corresponding to the central hole of the thermoelectric module (**Figure 5.2**c). This represents the only geometrical constrain in the design of the PDMS chip, thus offering full versatility in using multiple microfluidic layouts. In particular, for our studies, we use three different microfluidic architectures, featuring matrices of worm culture chambers of different shapes and sizes (**Figure 5.2**d).

5.3 Engineering of the device temperature control system

5.3.1 Theoretical considerations

We investigate the performance of our temperature control system both theoretically and experimentally. The setup can be operated either in "closed-loop configuration" – by means of the PID controller – or in "open-loop mode", i.e. by providing the Peltier module with a constant electrical power. The former configuration results in fully automated control of the setup temperature, the latter option has the advantage of allowing device operation with no need of a feedback sensing system. When electrical power is supplied to the thermoelectric module, heat exchange is induced through the assembly, resulting in the heating or cooling of the chip, for positive and negative electrical powers, respectively. The temperature distribution achieved in the device satisfies the following equation in time:

$$\rho C_p \frac{\partial T}{\partial t} + \nabla(-k\nabla T) = Q \tag{5.1}$$

with density ρ, heat capacity C_p, and thermal conductivity k, varying according to the material (a scalar or a tensor for an isotropic or anisotropic material, respectively). In our case the temperature T is modulated by the heat source Q (unit: W/m^3), represented by the Peltier module. Further heat exchange occurs then via convective heat transfer at the boundaries of the assembly through the surrounding air, according to:

$$q = h(T_{ext} - T) \tag{5.2}$$

where q is the convective heat flux through a boundary (unit: W/m^2), h is the heat transfer coefficient and T_{ext} the temperature of the ambient air, far from the boundary. Because of the composite geometry of our device, including different materials with complex 3D shapes, Equations (5.1) and (5.2) are best solved via 3D FEM modeling, as will be detailed further.

5.3.2 Steady state temperatures in "open-loop" mode

To extract the "open-loop" calibration curve of our device, we first characterize its response for different constant cooling electrical powers (**Figure 5.3**a). In this study, the temperature is measured by means of a 1.6 × 2.5 mm^2 Pt1000 sensor positioned on the bottom face of the glass coverslip, aligned with the center of the microfluidic chip (at x=y=0 in the insert of **Figure 5.3**b). Because of the reduced thickness of the glass substrate, negligible temperature variations are expected between top and bottom face of the coverslip. As expected, for different cooling power in the "open-loop" configuration, the system is cooled down to specific steady-state temperatures, set by the equilibrium between thermoelectric cooling and heat convection in the surrounding air.

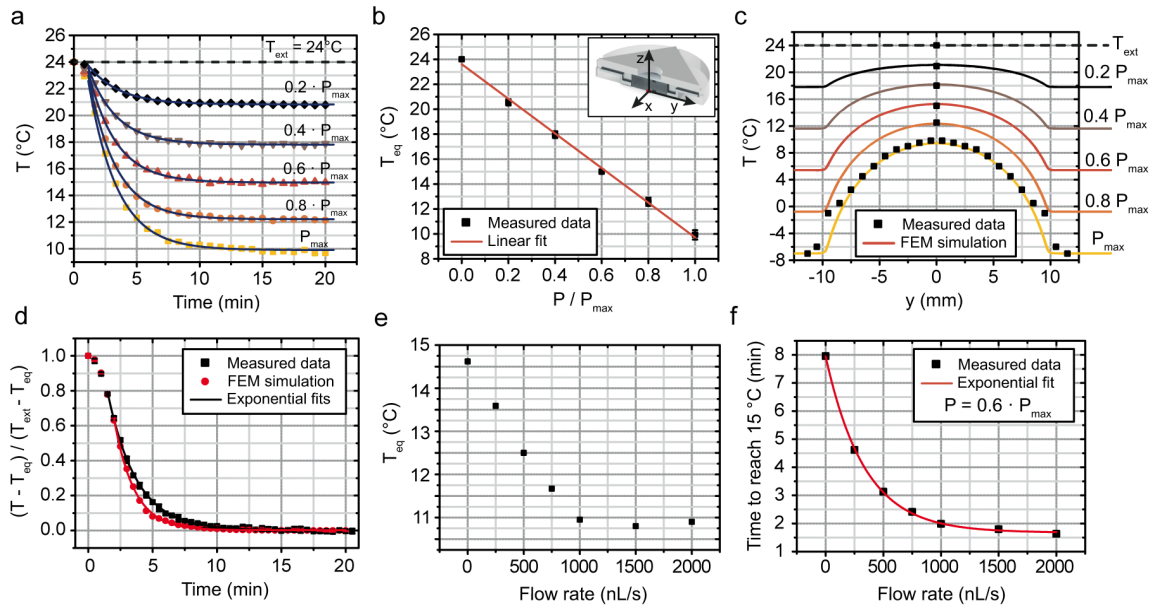

Figure 5.3 | Temperature control system characterization. (a) Experimental characterization of the device cooling performance in "open-loop" configuration, for different cooling power applied to the thermoelectric module starting from t=0 and an external temperature of 24 °C (temperature sensor positioned at the chip center). (b) Measured equilibrium temperature T_{eq} at the chip center (x=y=0) for different constant cooling power and starting from an external temperature T_{ext} = 24 °C. N=3, errors are SD. (c) Spatial temperature distribution across the chip area, both measured experimentally and simulated via FEM. (d) Temporal evolution of the "normalized chip temperature". Experimental data are obtained by plotting the curves of (a) normalized in the form of $(T - T_{eq})/(T_{ext} - T_{eq})$; each experimental point represents the average of all normalized data points for a specific time. (e) Measured equilibrium temperature T_{eq}, and (f) time to reach T = 15 °C during liquid injection at different flow rates at constant cooling power ($P = 0.6 \times P_{max} \sim 24$ W).

Starting from an ambient temperature of 24°C, stable temperatures down to 10 °C can be reached at the chip center, with a clear linear dependence on the electrical power that is applied to the Peltier module (**Figure 5.3**b). Because of the specific geometry of the device, the spatial temperature distribution is not constant throughout the chip area, as observed via measurements at different locations from the coverslip center (**Figure 5.3**c). By fitting these data with the corresponding simulated results, we empirically extract the heat transfer coefficient *h*, which models heat convection in our system (Equation (5.2)). A slight deviation in the fit between measured and simulated data is observed only close to the PDMS chip edge (y = ± 10 mm). This is attributed to imperfections of the contact surfaces between the chip and the metallic frame. We moreover simulate the spatial temperature distribution for different cooling powers, showing again good agreement between theoretical and experimental results (**Figure 5.3**c).

5.3.3 Heat exchange dynamics

The dynamics of heat exchange in our system can be efficiently studied by normalizing the curves of **Figure 5.3**a with respect to the external temperature T_{ext} and the steady-state temperature T_{eq} for each applied power. Normalized data prove to be independent from the electrical power and allow defining the calibration curve that describes the temperature evolution of the device in the "open-loop" configuration (**Figure 5.3**d). The same result can be obtained via FEM by plotting the temperature at the chip center using a time-dependent simulation. In this analysis, the coefficient

of performance (COP) of the thermoelectric module needs to be carefully taken into account, with COP typically defined as the ratio between the effective cooling power and the supplied electrical power. In our case, when the maximum allowed electrical power is provided to the thermoelectric module (P_{max} ~ 40 W), its COP is inversely proportional to the temperature difference created between its two plates (information extracted from the datasheet of the thermoelectric module). By including this specific dependence in our simulation, we obtain a theoretical calibration curve in very good agreement with the experimental data **Figure 5.3**d). The measured temperature decrease in our device is fitted by an exponential decay with time-constant τ = 2.23 min, with the temperature at the chip center reaching 80% of its steady-state value in ~4 min and 90% in ~6 min. The slight difference between the measured decay and the simulated one is mainly attributed to imperfections of the thermal contact among the different parts of the assembly, which are not included in the FEM calculations. Much faster cooling is obviously observed at the metallic frame, where the temperature reaches 90% of its final value within 2 min.

5.3.4 Inflow pre-thermalization

As previously described, the fluid entering the microfluidic chip is pre-thermalized during its passage through the metallic frame in which both PDMS chip and tubing are inserted. First, this allows achieving lower on-chip temperatures than without fluid flow, thereby improving the cooling efficiency of the device. Second, fluid pre-thermalization reduces the time constants of the system, thus making temperature changes faster and reducing the overall stabilization time of each experiment. Finally, the speed of the pre-thermalized inflow can be exploited as an additional parameter for temperature control, allowing the fine-tuning of the temperature of the actual microfluidic environment. We experimentally characterize the influence of the pre-thermalized inflow by measuring the steady-state temperature at the chip center for constant electrical power and different flow rates of the liquid entering the chip (**Figure 5.3**e). For this study, we work at constant power P ~ 24 W, since this results in setting the on-chip temperature around 15 °C, which is a critical value for our applications, as will be shown later. In this case, fast inflows (> 1000 nL/s) allow a 25% further reduction of the chip temperature, down to about 11 °C. In certain experiments, such additional cooling by pre-thermalization may, however, be undesirable and can be rendered minimal by working at relatively low flow rates (e.g. 100-200 nL/s) or finely-tuned via proper combinations of thermoelectric and liquid cooling parameters. Finally, we characterize the dynamics of heat exchange during liquid injection at different flow rates: liquid pre-thermalization allows much faster chip cooling, e.g. resulting in a 44% to 87% reduction of the time needed to reach 15 °C at P ~ 24 W, for flow rates from 250 to 2000 nL/s, respectively (**Figure 5.3**f).

5.4 Automated device operation

5.4.1 Worm arraying via passive valves

Passive hydrodynamics allows avoiding the need of additional fluidic control layers or active valving systems, which would complicate use and design of the chip and would reduce its ease of automation. The first critical protocol steps are typically represented by synchronization, loading

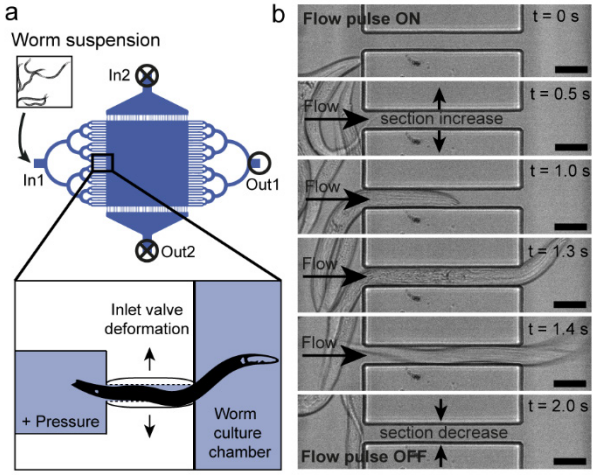

Figure 5.4 | Worm arraying via passive valves. (a) Schematic representation of the worm loading process. A pressure pulse triggers the fast deformation of the PDMS valving channels and allows the injection of worms of desired size into the culture chamber. (b) Time-lapse pictures of a valving channel, during the injection of a L1 worm in the chip of **Figure 5.2**diii. Scale bars = 10 µm.

and distribution of the worms inside the device. In our platform, all these operations are simultaneously accomplished by simply injecting a mixed worm suspension into the microfluidic chip at a proper flow rate, along the In1-Out1 direction (**Figure 5.4**a). We mainly worked with three different chip designs (**Figure 5.2**d) for selecting either L1, L2/L3 or L4 larvae, as these are commonly employed stages for worm synchronization and successive analyses. Size and shape of the microfluidic channels connecting adjacent chambers along the In1-Out1 direction are designed to ensure uniform flow distribution across the chambers and allow access to the chip only to worms which are younger than the desired age – and thus smaller than a certain size. More specifically, we exploit the flexible nature of PDMS to trigger a passive valving mechanism [162] in the channels (zoom of **Figure 5.4**a).

In the "L1 design" (**Figure 5.2**diii), only L1 worms can access the culture chambers because of their smaller size, which is compatible with the passage through microfluidic channels sizing 8 × 14 µm^2 in section. When a 1 s pulse of 2 µL inflow is injected into the device, a slight overpressure instantaneously builds up inside the channels, causing a fast temporary increase of their section. This triggers the passage of L1 larvae through the channels (**Figure 5.4**b). The end of the pulse results then in worm confinement inside the chambers, since each channel immediately returns to its initial shape, preventing any spontaneous passage of worms. A few subsequent inflow pulses allow distributing L1 larvae over the whole matrix of 32 chambers in a few seconds. The same principle is employed in the L2 and L4 chip designs (**Figure 5.2**di-dii), for the automated dispensing of larvae in a single culture chamber or in the 4 chamber array. In this case microchannels (30 × 14 µm^2 and 60 × 14 µm^2 in section for the L2 and L4 designs, respectively) are sized as such to block the passage of adult worms, confine larvae of desired size inside the chambers by the passive valving effect, while directly washing all the smaller larvae out of the chip.

Our passive valve-based worm loading method allows moreover tuning the distribution of worms throughout the microfluidic chamber matrices in very a simple and versatile way. Two main worm

distribution approaches can be implemented in our chips. First, when large data statistics are needed, concentrated worm samples are injected into the microfluidic device and/or chamber matrices of small dimensions are chosen (e.g. 1-4 chambers, **Figure 5.2**di-dii). Passive valves allow automatically distributing the worms over the different chambers in a quite uniform way, resulting in small groups of worms – e.g. 2 to 5 worms – per each chamber. Second, if a reduced number of isolated worms is needed, diluted samples are injected in large chamber matrixes (e.g. 32 chambers, like in **Figure 5.2**diii). In this case, Poisson statistics ensures the presence of single worms in each of the occupied chambers, at the price, however, of having many empty chambers in the matrix. Eventually, direct user control and iteration of the worm loading protocol can be used to adjust the worm distribution until a desired number of worms per chamber is obtained.

5.4.2 Worm culture and imaging protocol

The cross-shape of our chips, with in- and outflows along two orthogonal directions, is designed to decouple the worms' dispensing operation (in the In1-Out1 direction) from the worm culture and imaging protocol. Instead, along the In2-Out2 direction, adjacent chambers are connected by narrow filters – 5 × 14 μm^2 in section – allowing perfusion of liquids across the whole chamber matrix, while preventing any inter-chamber exchange of worms, even under over-pressure conditions. Also, after worm dispensing, the In1-Out1 flow direction can be employed during the culture experiments for evacuating the progeny of the adult worms under analysis. Each switching between the two flow directions is simply controlled by two external valves at the two chip outlets.

We develop a fully automated protocol for worm culture and high-resolution imaging inside the device (**Figure 5.5**a). Worms are cultured on-chip at a desired temperature (typically in the 20-25 °C range) by operating the temperature controller in a closed-loop configuration. *E. coli* suspension is perfused at desired rate along the In2-Out2 direction for worm feeding (**Figure 5.5**ai). For the accurate and repeatable observation of the worms through high-magnification objectives, *C. elegans* need to be temporarily immobilized in a reversible manner. To fulfill this requirement, we employ the thermoreversible gelation of a PF127 solution around the worms, as a minimally invasive *C. elegans* immobilization technique [169]. Prior to imaging, the chip temperature is set at 15 °C and a liquid solution of 25% w/v PF127 is injected into the culture chambers (**Figure 5.5**aii). The chip temperature is then raised to 25 °C, to trigger the gelation of the Pluronic solution. This significant increases the viscosity ensuring stable worm immobilization (**Figure 5.5**aiii). Upon imaging, the chip temperature is brought back to 15 °C, to release the worms and wash the PF127 solution out of the chambers, by replacing it with *E. coli* suspension to restart worm culture and feeding (**Figure 5.5**aiv). The whole protocol can be iterated many times per experiment and strongly relies on accurate temperature control, especially to trigger the worm immobilization/release process [169]. The closed-loop temperature management system plays therefore a crucial role for the system automation. The spatial distribution of temperature over the whole chip geometry is carefully considered, to minimize inter-chamber variations and expose all the worms to the same experimental conditions. We demonstrate via FEM simulations that our device ensures temperature uniformity within 1 °C difference, even when using the largest chamber matrix, and this both during worm culture (at 20 °C) and PF127 injection and washing (at 15 °C) (**Figure 5.5**b).

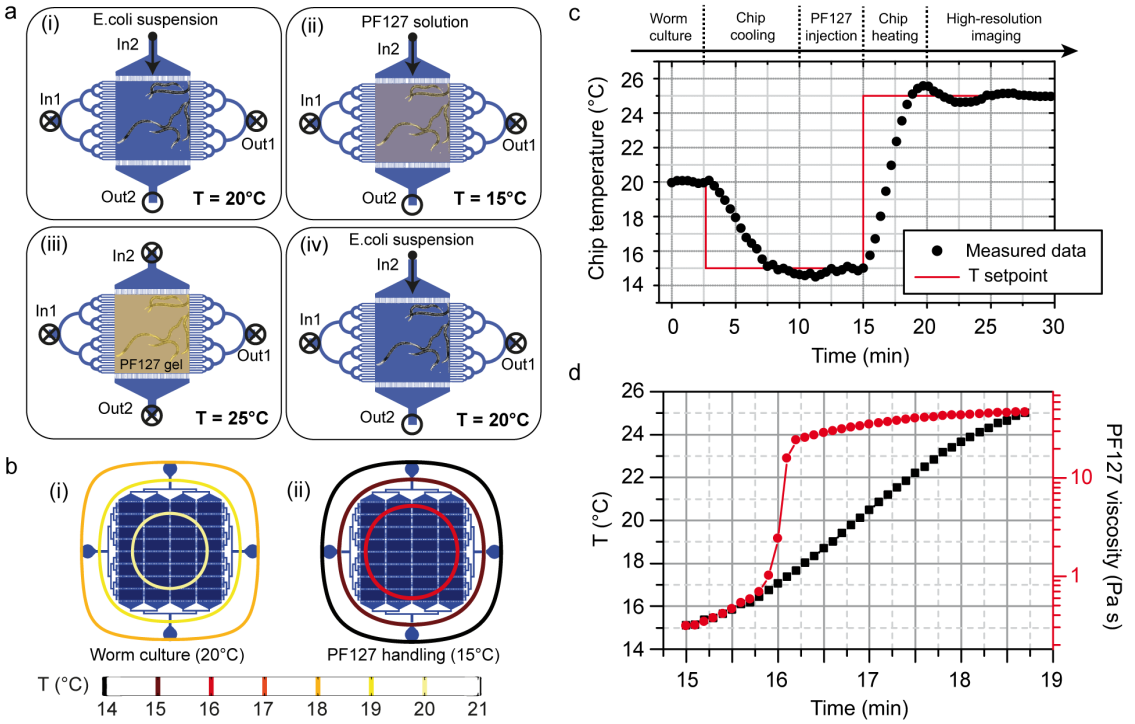

Figure 5.5 | Worm culture, immobilization and imaging. (a) Schematic representation of the iterative worm culture and imaging protocol. (b) FEM simulations of the spatial temperature distribution over the chip area (temperature contour plots) for temperature setpoints (i) at 20 °C for culture and (ii) at 15 °C for imaging. (c) Experimental temperature at the chip center during a worm culture-to-imaging transition, as managed by the active temperature control system, indicating the periods of PF127 injection and chip temperature changes. (d) Temperature rise in the 15-19 min period in more detail. The axis on the right shows the variation of PF127 solution viscosity (25% w/v in water) during the transition from 15 °C to 25 °C in the device. The PF127 sol-gel transition occurs abruptly at about 17 °C, in a time window of ~1 min. Values of PF127 viscosity at the different temperatures are measured through a cone-plate viscometer.

PID parameters are chosen to minimize any overshoots outside of the standard temperature range for worm culture (15-25 °C) (**Figure 5.5**c). Active temperature control allows moreover fast and accurate steering of the sol-gel transition of the PF127 solution. In our device, such a transition occurs about 1 min after the temperature setpoint shift from 15 °C to 25 °C – i.e. worms are ready for high-resolution imaging in about 2 to 3 min, when the viscosity of the PF127 gel reaches its highest value and guarantees worm immobilization (**Figure 5.5**d).

We experimentally determine the viscosity at different temperatures by dispensing a ~2 mL PF127 solution over the bottom plate of a cone-plate viscometer (Bohlin Gemini Malvern, UK) and measuring using a shear rate of 10 s^{-1}. This value is chosen to be comparable with typical shear rates associated to the *C. elegans* swimming motion (1 to 20 s^{-1}) [185]. Finally, we attribute a crucial role to the liquid inflow pre-thermalization as far as the PF127 injection process is concerned. Even in liquid phase, the PF127 solution behaves in fact as a very viscous non-newtonian fluid, and, as such, it is challenging to manipulate through syringes, tubes and microchannels. Pre-thermalizing the PF127 inflow in the metallic frame to temperatures even lower than 15 °C allows further reducing the solution viscosity at the chip inlet and improving the control over its injection.

5.5 Automated longitudinal studies on *C. elegans*

5.5.1 Worm viability and culture tests

Before using our device for answering specific biological questions, we test its capability of automatically running worm cultures over several days and optimize the worm feeding protocol for good worm viability and healthy growth. For this preliminary validation, we employ wild-type *C. elegans* and feed them with HT115 *E. coli* bacteria. Different feeding protocols are tested to establish optimal conditions for worm growth. A delicate balance has to be found between two main competing factors. On the one hand, too strongly diluted *E. coli* suspensions (and/or less frequent injections) might cause worm starvation. On the other hand, too concentrated *E. coli* suspensions (and/or too frequent injections) usually result in the uncontrolled clogging of narrow microfluidic connections, which has then to be eliminated via user-controlled washing steps. A good compromise between these factors is found by injecting in the device ~1.5 µL *E. coli* suspension per microfluidic chamber (e.g. ~6 µL for the 4-chamber matrix) at $1.4 \cdot 10^9$ bacteria mL^{-1} concentration, every 10 minutes. This protocol is automatically handled by the syringe pump software interface and allows attaining reliable worm growth inside the chip over several days, with no significant channel clogging or extra washing steps. Moreover, worm immobilization via thermoreversible PF127 gelation proves neither to affect worms' viability nor to alter their physiological functions, as already reported in previous works [156, 169].

5.5.2 Long-term protein aggregation analysis in amyotrophic lateral sclerosis (ALS) *C. elegans* models

Upon full validation of the capabilities and performance of our device, we employ it to monitor the dynamics of protein aggregation in amyotrophic lateral sclerosis (ALS) disease *C. elegans* models. ALS is a neurodegenerative human disease causing selective death of motor neurons. In Europe and the United States, this disease affects about 2 people per 100,000 per year [186], with average survival form onset to death of only 3 to 5 years and no cure currently available [187]. In ALS, such as in many other neurodegenerative diseases, cellular toxicity could be mediated by the misfolding and aggregation of specific mutant proteins [188-190]. Time-resolved imaging and quantification of these aggregates is hence a key phenotyping method to monitor disease progression. In our study, we employ an ALS *C. elegans* model expressing mutated human SOD1-YFP fusion proteins in the body wall muscle cells (AM725 transgenic worms) [191]. Worms are loaded at the L2 stage into a 4-chamber microfluidic chip (**Figure 5.2**dii), where their distribution is adjusted to isolate a single worm in each chamber. Automated on-chip culture of these worms is then conducted according to the previously described protocols. Correct worm feeding, development and reproduction are constantly monitored via brigthfield time-lapse imaging (**Figure 5.6**a). Automated image processing algorithms on these time-lapse pictures allow moreover extracting detailed information about the worms' growth rate, not only at a population level, but also at single-worm resolution (**Figure 5.6**b-c). Specifically, the area occupied by each worm is here used as a quantitative indicator of growth. Data about the growth rate of individual worms allow preserving detailed information on the development of each nematode (**Figure 5.6**b), while the average growth trend is found to follow a well-defined sigmoidal dependence on time (**Figure 5.6**c).

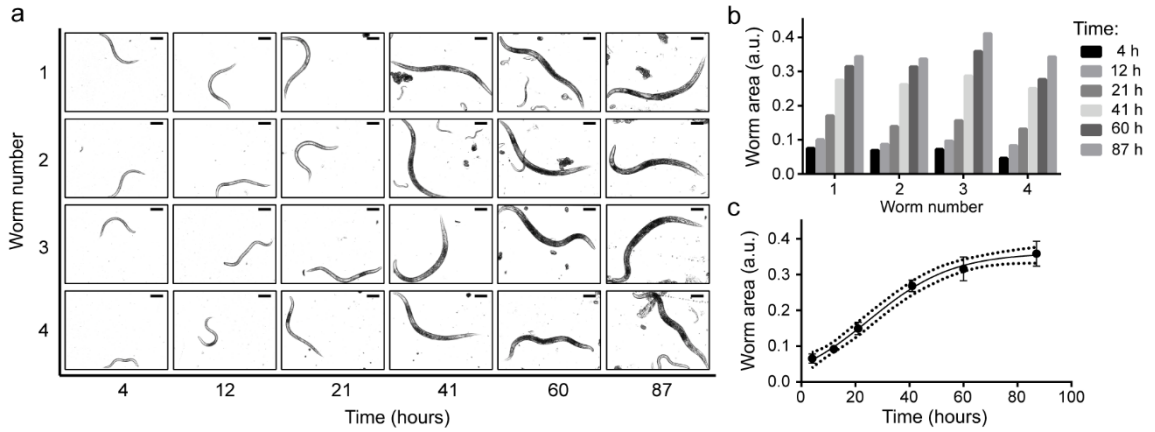

Figure 5.6 | Worm growth monitoring and quantification. (a) Time-lapse brightfield pictures of four AM725 transgenic worms, isolated at t = 0 at the L2 larval stage in the 4 different culture chambers. Scale bars = 100 µm. (b) On-chip growth rate of the four worms over 87 hours, as estimated by measuring the worm area from time-lapse pictures. (c) Average on-chip worm growth, featuring a sigmoidal time-dependence.

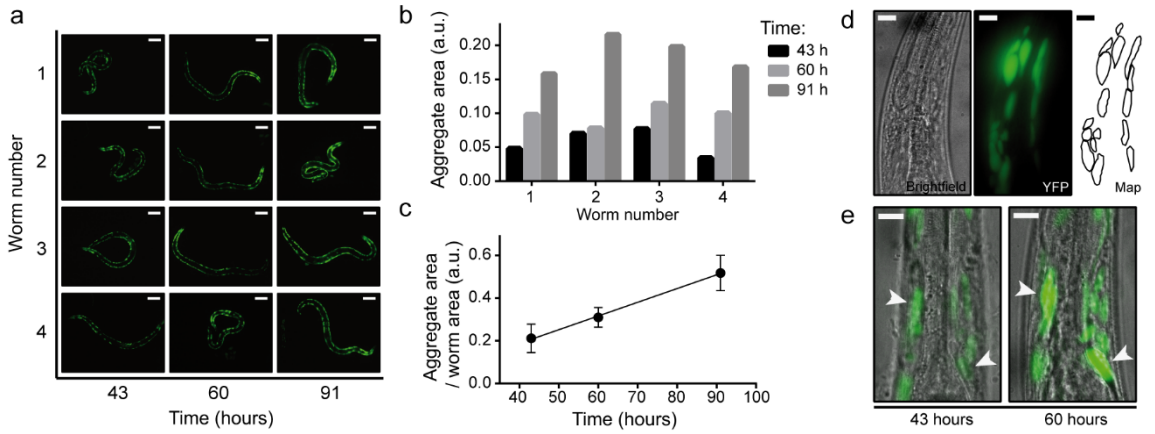

Figure 5.7 | Protein aggregation monitoring and quantification. (a) Time-lapse fluorescent pictures of four AM725 transgenic worms, immobilized in a PF127 gel matrix within the culture chambers. Scale bars = 100 µm. (b) Growth rate of SOD1-YFP aggregates in the body wall muscle cells of each worm, as estimated by measuring YFP expression area across each worm's body during their immobilization in the gel matrix. (c) Average protein aggregate area per worm, normalized by the average worm area. A linear time-dependence of this parameter is observed over the period from 43 to 91 hours upon loading on chip (day 1 to day 3 of worm adulthood). (d) Brightfield and fluorescent images of an immobilized worm (worm 1), as taken through a 63× NA 1.4 oil immersion objective 91 hours upon worm loading into the device. These pictures allow mapping the aggregate morphology at high spatio-temporal resolution. (e) Superimposed brightfield and fluorescent images of an immobilized worm (worm 4), as taken through a 63× NA 1.4 oil immersion objective 43 and 60 hours upon worm loading into the device. Arrows point at specific SOD1-YFP aggregates, which can be re-identified in subsequent images and tracked over time. Scale bars = 20 µm.

At desired moments during worms' development (e.g., in our study, 43 h, 60 h and 91 h upon worm injection), the reversible worm immobilization protocol for high-resolution imaging (see **Figure 5.5**a) is employed. At each observation and in a matter of a few minutes, all the worms are perfectly immobilized in a PF127 gel matrix and SOD1-YFP expression can be monitored within their tissues via fluorescent microscopy through high-magnification objectives. A first analysis at 10× magnification allows observing protein aggregates within the whole body of each worm (**Figure 5.7**a). It is worth noticing that, because of the relatively high exposure times used for the

imaging (120 ms), this analysis would have been impossible to perform on freely moving worms. Perfect image stability is in fact needed for non-distorted observation and accurate estimation of the aggregate size. Interestingly, we find that the temporal evolution of SOD1-YFP aggregation features some observable worm-to-worm variability (**Figure 5.7**b), and follows an overall linear trend in the considered temporal window (43 to 91 hours after on-chip loading at the L2 stage) (**Figure 5.7**c).

A second set of studies is then conducted by imaging the immobilized worms through a 63× oil immersion objective (NA 1.4). Many aggregates in AM725 worms, unlike in other analogous SOD1-transgenic strains, appear as irregular, elongated foci. This feature could be observed before by confocal imaging of paralyzed worms [191]. We are now able to confirm this observation in alive immobilized worms and provide a precise sub-cellular mapping of their protein aggregation pattern at high spatio-temporal resolution by using a standard fluorescent microscope (**Figure 5.7**d). Moreover, the possibility to take quasi-instantaneous brightfield and fluorescent pictures in our chip allows accurately locating each fluorescent signal inside the *C. elegans* body. In combination with reversible worm immobilization, this opens the possibility of following the temporal evolution of protein aggregation at precise locations within the worm tissues and monitoring aggregate progression *in vivo*, not only at single-worm, but even at the single-cell level (**Figure 5.7**e).

5.6 Materials and methods

5.6.1 Chemicals and Materials

4-inch 550 µm thick Si wafers and DIW were obtained from the Center of Micro- and Nanotechnology of EPFL. GM 1070 SU-8 negative photoresist was purchased from Gersteltec (Pully, Switzerland). PDMS Sylgard 184 was acquired from Dow Corning (Wiesbaden, Germany). 1 mL borosilicate H-TLL-PE syringes were purchased from Innovative Laborsysteme GmbH (Stutzerbach, Germany). Microline ethyl vinyl acetate tube with 0.51 mm inner and 1.52 mm outer diameters was bought from Fisher Scientific (Wohlen, Switzerland). Pluronic F-127 was purchased from Sigma-Aldrich (Buchs, Switzerland). M9 buffer was obtained by adding 3 g KH2PO4, 6 g Na2HPO4, 5 g NaCl, 1 mL 1 M MgSO4, H2O to 1 litre and sterilization by autoclaving. S-medium buffer was obtained by adding 10 mL 1 M potassium citrate pH 6, 10 mL trace metals solution (1.86 g disodium EDTA, 0.69 g $FeSO_4 \cdot 7H_2O$, 0.2 g $MnCl_2 \cdot 4H_2O$, 0.29 g $ZnSO_4 \cdot 7H_2O$ and 0.025 g $CuSO_4 \cdot 5H_2O$, H_2O to 1 litre) 3 mL 1 M $CaCl_2$, 3 mL 1M $MgSO_4$, 1 mL [50 mg/mL] carbenicillin, 0.5 mL tween 20 to 1 litre S Basal (5.85 g NaCl, 1 g K_2HPO_4, 6 g KH_2PO_4, 1 mL [5 mg/mL] cholesterol, H_2O to 1 litre) and sterilization by autoclaving. Pluronic F127 solution was prepared by diluting 25% (weight/volume) Pluronic F127 in water. Aluminum and PMMA assembly parts were fabricated at the engineering workshop of EPFL. Thermoelectric modules were bought from TE Technology, Inc. (Traverse City, MI, USA), heat sinks from Advanced Thermal Solutions, Inc. (Norwood, MA, USA) and RTD sensors from Innovative Sensor Technology AG (Ebnat-Kappel, Switzerland), while a PID temperature controller was purchased from BelektroniG GmbH (Freital, Germany).

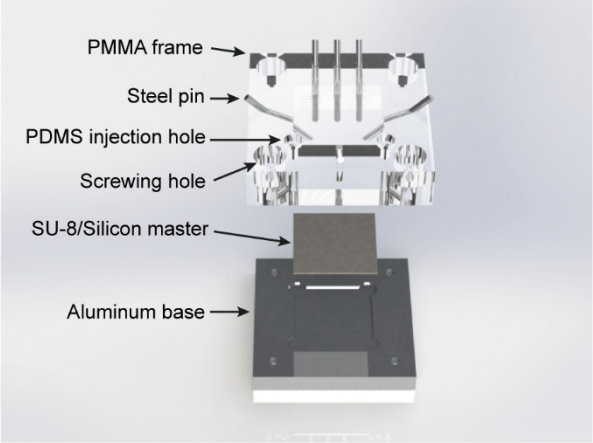

Figure 5.8 | PDMS injection molding technique. Schematic representation of the casting mold designed to shape the whole 3D geometry of our PDMS microfluidic chips. The SU-8/silicon master corresponding to the desired microfluidic design is positioned inside an aluminum base, which is then sealed to a PMMA frame using 4 M3 screws. 1.5 mm diameter steel pins are inserted into the PMMA frame through dedicated holes, machined at 45° angle with respect to the master mold. The flat base of each pin contacts the SU-8 structures at the position of each inlet (or outlet). This specific configuration is conceived to achieve lateral microfluidic connections entering the sidewalls of the chip, leaving hence free access for observation and manipulation both from the top and the bottom faces of the chip. PDMS is injected inside the casting mold through the "PDMS injection hole" using a syringe. The whole assembly is then positioned between two parallel hot plates at 100 °C for PDMS curing, using the aluminum base part to ensure good thermal exchange with the hot plates, so that the liquid PDMS correctly polymerizes.

5.6.2 *C. elegans* strains and culture

C. elegans strains were cultured at 20°C on nematode growth media agar plates seeded with the *Escherichia coli* strain OP50. Strains used were wild-type Bristol N2 and AM725 (rmIs290[unc-54p::Hsa-sod-1(127X)::YFP]). Strains were provided by the Caenorhabditis Genetics Center (University of Minnesota). Worms were suspended in S-medium solution prior to each microfluidic experiment. For microfluidic experiments, the *E. coli* strain HT115 was suspended in S-medium at a concentration of 1.4 x 10^9 cells/mL.

5.6.3 Fabrication of the microfluidic chips

Microfluidic devices were prepared by soft lithography [144] using 2-layer SU-8 molds. Briefly, conventional photolithography was used to pattern a 14 µm-thick layer of SU-8 photoresist on 4-inch wafers. A ~110 µm-thick layer of SU-8 was then patterned on top of the first one. Layer thicknesses were confirmed by mechanical profilometer measurements. The silicon mold was then diced in 20 mm × 20 mm microchips, which were inserted at the bottom of an aluminum/PMMA mold for PDMS casting (**Figure 5.8**). 1.5 mm diameter steel pins were used to define the lateral connections of the device for the external tubing insertion. A liquid PDMS mixture (10:1 base:cross-linker weight ratio) was degassed, injected into the mold and cured at 100 °C for 1 h. Upon extraction from the mold, each PDMS chip was bonded by plasma-activation to a 150 µm-thick, 32 × 24 mm^2 glass coverslip. The chip was then connected to external tubing and enclosed in the device assembly as reported in **Figure 5.2**a.

5.6.4 Image acquisition and processing

The microfluidic platform was placed within an inverted microscope (Axio Observer, Zeiss) equipped with two illumination systems: (i) a precisExcite High-Power LED illumination system (Visitron, Puchheim, Germany) for brightfield imaging and (ii) a Lambda DG4 illumination system (Sutter instruments, Novato, CA, USA) for fluorescence imaging. The microscope had a motorized xy-stage and the automated imaging process was controlled using VisiView Premier Image acquisition software (Visitron, Puchheim, Germany). Images were acquired through a Hamamatsu Orca-ER CCD camera (Hamamatsu, Solothurn, Switzerland). Image processing was performed with Fiji software (http://imagej.nih.gov/ij; version 1.47b).

5.7 Conclusions

We introduce a new device for automated high-resolution imaging and studies on *C. elegans* nematodes down to single-cell resolution. Our platform is based on a multi-functional approach, where several functionalities are integrated in a single miniaturized device, to allow fully automated worm analyses. The device is moreover designed to be compatible with different microfluidic designs and readily suitable for different sets of studies.

In our platform, *C. elegans* nematodes are loaded into a microfluidic chip, where they are directly distributed among a set of culture chambers via a “passive valving” method. Geometrical constraints on the chip allow retaining only worms of desired size inside the device, whereas an automated on-chip culture protocol is established to ensure their correct feeding and development. Active control of the chip temperature ensures moreover running worm cultures at desired temperatures, with minimal variation throughout long-term analyses. To allow longitudinal high-resolution imaging of the worms, we optimize an automated procedure for reversible worm immobilization on-chip. This protocol is based on the thermoreversible gelation of PF127 polymer inside the device, managed by the closed-loop temperature control system as well. Any worms’ progeny is periodically washed out of the chip, with no risk of mixing the identities of the worms under analysis. Therefore, tests at single-worm resolution can be easily performed on our platform. Finally, all the microfluidic designs used in our studies are conceived in a “chamber-matrix” format, which allows easy automation of the imaging process as well.

We fully characterize the different functionalities of our platform, both theoretically and experimentally. We demonstrate fast and precise temperature management on the device and provide calibration curves for its use both in open-loop mode and in closed-loop configuration. We characterize the different integrated worm handling protocols – i.e. on-chip worm loading, feeding, immobilization, imaging – and provide details for their use on the platform. We then employ our device to tackle the challenging task of monitoring the dynamics of protein aggregation in ALS worm models over long-term experiments. Our results show that the device ensures reliable culture and reproducible growth rate of the worms over several days. The possibility of isolating single worms in separated chambers allows collecting population statistics, while preserving at the same time all the information related to the single nematodes under test.

We employ the on-chip immobilization protocol to temporarily immobilize the worms in a reversible way and periodically collect data about protein aggregation in their tissues via high-resolution fluorescent imaging. Our results show that the amount of SOD1-YFP aggregates in ALS *C. elegans* models (AM725 transgenic worms) linearly increases over the whole analysed period (i.e. day 1 to day 4 of adult life). Combined brightfield and fluorescent imaging at high magnification allows moreover mapping the geometry of the aggregates, precisely locate them within the tissues of each worm and following their progression over consecutive days. The relatively short period needed for the quantification of a significant increase in SOD1-YFP aggregates opens the possibility for future studies of rapid identification of ALS modifiers [192]. Because of its unprecedented performance in terms of automation and versatility, we envision that our device could be employed to address many other challenging biological questions on *C. elegans*, related in particular to the study of neurodegenerative diseases – such as Huntington's, Parkinson's, and Alzheimer's disease – which are all modelled in worms [173]. Our platform could moreover be used for studies of movement disorders, for quantifying other phenotypes such as pharyngeal pumping rates, motility, etc., or more generally could be used in non-*C. elegans* biology laboratories. The active temperature control, together with the described on-chip protocols, allow in fact easy and reliable organism culture and analysis, without need of any calibration and no influence of external temperature or other environmental and human factors.

Chapter 6 Conclusions and Outlook

6.1 Results overview

Micro- and nano-science allows nowadays good control and study of the basic building blocks of biological matter, being micro-organisms, cells or even single molecules. Moreover, microfluidics – the technology for manipulating small volumes of fluids – largely demonstrated its potential to miniaturize whole complex laboratory protocols onto single micro-chips, with substantial advantages over standard laboratory procedures. The technological options provided by these so-called "lab-on-a-chip" (LOC) devices are however still far from being standardized solutions, so that even the most groundbreaking LOC components proposed in the last years proved to be less suitable for commercialization, usually because of their fundamental incompatibility with batch-type techniques. In the light of these considerations, we focused our research efforts on the development of versatile, fully automated LOC tools, answering to the urgent need for future commercial solutions. We typically demonstrated the capabilities of our devices to address specific biomedical questions, while always carefully designing them to be mutually compatible and easily readaptable for a manifold of applications. A common feature of all our developed LOC devices is represented by the combination of both microfluidics and "micro-arraying" approaches, which we envision to be key elements towards standardization, full automation and easy scalability of the LOC technology.

We first proposed a new LOC-based method for ultra-sensitive protein detection in serum. Measuring biomarkers at very low concentration in blood or serum samples can allow early disease diagnosis and can thus be crucial for proposing life-saving medical treatments to the patients. Moreover, disease detection via measurement of specific antigens in a serum matrix is often the preferred minimally invasive solution. Very sensitive nucleic acid detection is enabled by polymerase chain reaction (PCR) techniques, but there is no comparable method that can be used to "amplify" proteins, which hence necessitates the development of very sensitive types of assays. With our on-chip assay method, we demonstrated detection down to only 200 molecules of the clinically relevant biomarker TNF- α, in serum sample volumes of 5 µL – the size of a small blood droplet – corresponding to a concentration of 60 attomolar. This result proved that our solution allows attaining unprecedented limits of detection, 10 to 100 times lower than the most sensitive available techniques and only comparable with complex and expensive PCR-based methods. Moreover, we designed our technique to be easily standardizable, by employing micro-arrays of commercially available superparamagnetic beads, as a key technological feature of the assay. In this same framework, we took care of providing the research community with a comprehensive modeling and a deep understanding of our detection method. By combining FEM simulations with analytical calculations, we first built a predictive model for our technique, to be employed as a

guide for its further use, optimization and development. In this study, we elucidated the key role of magnetic bead dipole–dipole interactions, combined with microfluidic viscous forces, to dramatically enhance the selectivity of specific antigen-antibody immunocomplex formation in the so-called “sandwich immunoassays”. In a second study, we included considerations on the probability of the single immunocomplex formation in our assay. This led to a careful investigation of the assay kinetics and ultimately to the full understanding of the peculiar behavior of the assay’s dose-response curves, which remained unexplained, until then. Finally, we introduced the concept of “magnetic particle-scanning”, which we proved to be, both theoretically and experimentally, a new powerful method for building immunoassays with extremely low limit of detection, down to the single-molecule level.

As a further proof of the versatility of our technology, we modified our bead-micro-arraying technique, to make it suitable for the immobilization of particles of various sizes, materials and properties – and even of cells – to be readily applicable in a manifold of research fields. In a first study, we developed a method for the electrostatic self-assembly of dielectric microspheres in well templates, which we employed as a tool for rapid, cost-effective fabrication of microlens arrays. We demonstrated that our method ensured extremely fast and reliable lens array formation (> 99% lens loading efficiency, in a few seconds), while moreover offering the possibility to reversibly assemble and disassemble the array by simply tuning the pH of the microsphere patterning and washing solutions. Different particle sizes and materials could be directly used with our technique, to fabricate microlens arrays with specific light focusing properties. By combining microsphere arrays with microfluidics, we demonstrated single-nanoparticle detection in flowing media via conventional brightfield and fluorescence microscopes – which we made therefore indirectly operate far below their physical diffraction limit. Our microsphere arrays permit in fact enhancing the light scattering and fluorescence intensity of the nanoparticles by up to a factor ~40, over a very wide field of view. This resulted in the possibility of detecting gold nanoparticles down to 50 nm in size, as well as fluorescent nanoparticles down to 20 nm in size, through a common low magnification/low numerical aperture microscope objective. Finally, in the framework of a research collaboration with the biosensors group at KU Leuven, Belgium, we further re-adapted this “microparticle arraying” concept, to be suitable for seeding single non-adherent cells in isolated micro-compartments. This new method was combined with the use of a DMF platform, for the implementation of high-throughput cytotoxicity assays on yeast cells, at significantly enhanced spatio-temporal resolution.

In parallel with the described work, we tackled the challenging task of conceiving technological solutions which allow creating micro-arrays of small living organisms, for their automated study in a high-throughput format. The nematode *Caenorhabditis elegans* is definitely one of the most employed model organisms in biomedical research. In *C. elegans*, many events occurring during larval stages are known to have a strong impact on the animal’s lifespan. Whether conditions in the embryonic phase of life have an influence on the later development is instead a much more challenging question to answer, mainly because systematic *C. elegans* embryonic morphogenesis studies are extremely difficult from a technical viewpoint. *C. elegans* embryos are in fact only a few tens of micrometers in size and almost impossible to handle manually. To solve this issue, we

developed a microfluidic platform for automated on-chip worm culture, creation of synchronized embryo micro-arrays, and for long-term parallel live imaging at the single embryo level. Our device features two main components: a “worm chamber”, where *C. elegans* nematodes are loaded and cultured, and an “embryo-incubator array", where the worms’ progeny is transferred upon natural egg laying in the chamber. The microfluidic device relies on a passive hydrodynamic trapping approach to gently position each embryo in a dedicated micro-incubator. The whole embryo population can then be studied over several hours via fully automated multi-dimensional imaging, covering six independent dimensions: the 3 spatial coordinates, the development time, the exposure (brightfield, fluorescent) duration, and the embryo number in the array. We successfully employed our platform to investigate relevant biological phenomena occurring during the embryonic development, with a particular focus on mitochondrial biogenesis and stress. The incubator array format of our platform provided a unique opportunity to study the intra-embryo variability in terms of viability, development and gene expression. By means of our device, we were able to discriminate variations in terms of embryonic development with unprecedented resolution and describe how perturbations of the mitochondrial functions can profoundly impact the embryogenesis. Our analyses revealed in fact that such perturbations can trigger the mitochondrial unfolded protein response (UPR^{mt}) pathway in the embryos. These observations were the first proof that UPR^{mt} is functional during *C. elegans* embryogenesis.

A very interesting feature of our platform is represented by the fact that worms are directly cultured on-chip and embryos analyzed upon spontaneous egg-laying, so that the whole information related to the natural reproduction process is preserved and the link between parents and progeny is maintained. Starting from these considerations, we designed a “second generation prototype” of our device, with the specific aim of investigating trans-generational properties on worms’ progeny and epigenetic imprints in successive worm generations. In our new device, each micro-incubator is now coupled with an additional worm chamber, where each larva is transferred prior to egg hatching. Also this system automatically operates via pure passive hydrodynamics and allows not only potentially observing on-chip, for the first time, the *entire* lifespan of *C. elegans* from embryogenesis to death – and at single-worm resolution –, but also relating it to conditions or events occurred to the previous generation. When arrays of living organisms need to be studied, the fact that the animal can freely move typically complicates observation and analysis. Our microfluidic devices allow confining single worms in culture chambers of desired size, thus ensuring that worms can always be found within a well-defined field of view. However, high-magnification imaging is usually needed to extract relevant biological information, while studies on transgenic animals often require the accurate observation of highly localized fluorescent signals inside the worms. During imaging, hence, animals have usually to be fully immobilized to prevent their movement, which would result in image distortion. Moreover, to observe the dynamics of biological processes, while ensuring minimal impact during the imaging phase, the same worm has to be immobilized repeatedly in a reversible manner, and under normal physiological conditions. Based on these needs, we developed our “third generation prototype”, which features: (i) a new microfluidic design tailored for the isolation of L1 or L4 larvae from a mixed larval population and for their successive culture and treatment; (ii) a worm immobilization method, based on the thermoreversible gelation of a biocompatible polymer inside the microfluidic chip, thereby enabling

high-resolution imaging; (iii) an integrated temperature control system, both to ensure viable environmental conditions for *C. elegans* culture and to steer the worm immobilization/release process. The chip geometry is again conceived in an array-format, and parallel multi-dimensional imaging over the device allows gathering plenty of information on the whole worm population in an automated way. We successfully employed this device to pursue challenging time-resolved studies, in particular the long-term *in vivo* observation at single-animal resolution of SOD1 aggregation in the AM725 *C. elegans* transgenic strain, which we use as a biological model system for the investigation of the human ALS disease. In particular, we exploited the on-chip immobilization protocol to temporarily immobilize the worms in a reversible way and periodically collect data about protein aggregation in their tissues via high-resolution fluorescent imaging. Our results showed that the amount of SOD1-YFP aggregates in ALS *C. elegans* models (AM725 transgenic worms) linearly increases over the whole analysed period (i.e. day 1 to day 4 of adult life). Combined brightfield and fluorescent imaging at high magnification allowed moreover mapping the geometry of single aggregates, precisely locate them within the tissues of each worm and following their progression over consecutive days.

6.2 Future opportunities

The combination of passive microfluidics and micro-arraying approaches will likely represent one of the answers to the need of versatile, commercializable LOC systems. The use of pure passive hydrodynamics, rather than complex microfluidic architectures with active components, could significantly help evolving towards the industrialization phase, in which key requirements are typically represented by the ease of integration and control of the device itself. The micro-array format provides then any microfluidic geometry with even more precious features for commercialization purposes, which are modularity, scalability and versatility of the design. At the same time, these characteristics are particularly convenient in the research environment as well, where they allow the same devices and techniques being rapidly re-adapted for different applications.

6.2.1 New research directions for micro-arrays of beads, lenses and single-cells

Our “magnetic bead-scanning” immunoassay method (see chapter 1) could be readily used for the detection of any biomarker in serum, provided that their capture antigen is available in a biotinylated form. The behavior of the system for any modification of the microfluidic or magnetic protocol can be easily predicted through our modeling tools, while the use of parallel detection channels would directly allow the simultaneous detection of a whole set of different molecules. Microwell array templates (see chapter 2) of different materials, size and geometries will be fabricated for the creation of microlens arrays with tailored optical properties. Moreover, our technique recently proved to be useful not only for NPs detection, but also for immunodetection of biomolecules immobilized on gold NPs (data not shown). In future, it may develop into a versatile tool to detect other nanoscale objects of environmental or biological relevance – such as cancerous nanomaterial or viruses – or even to directly observe the nanoscale dynamics of biological phenomena within living cells. Eventually, multiple single-cell arrays could be employed on a single microfluidic device for multiplexed testing of compound libraries on the same cell type or even on different cell strains or mutants.

6.2.2 New research directions for micro-arrays of *C. elegans* embryos

The live imaging capabilities of the device presented in chapter 3 can be extended to include other types of microscopies, like differential interference contrast microscopy, for high-contrast bright-field live imaging, and confocal microscopy to achieve extreme spatial resolution. Computer-enhanced image processing can be used to further extend the analytical possibilities of the platform for real-time embryonic screening and phenotyping, or even automated cell lineage and expression profiling in the developing embryos. In our device embryos are isolated immediately after they are naturally laid, thus their monitoring typically starts at the 26 to 44-cell stage. However, with our system, earlier cell division events may be optionally observed by directly injecting embryo suspensions prepared via standard manual bleaching protocols into the device. However, as in our platform worms are directly cultured on-chip and embryos analyzed upon spontaneous egg-laying, the whole information related to the natural reproduction process is preserved, maintaining the link between parents and progeny. Therefore, the platform is directly suitable for investigating trans-generational properties on the embryos and, with the adaptation of the microfluidic design proposed in chapter 4, even studying the progeny and epigenetic imprints in successive worm generations. Devices for related parasitic nematodes can be readily designed by re-adapting the incubator size, for example to study the effects of anti-parasitic drugs. Finally, we expect that similar microfluidic devices will be used to perform live imaging of a multitude of development events, like gastrulation and tissue morphogenesis during embryogenesis in other species of nematodes or other model organisms.

6.2.3 New research directions for micro-arrays of *C. elegans* nematodes

C. elegans recently gained a lot of attention as a model organism for the investigation of neurodegenerative diseases, such as ALS, Alzheimer's, Parkinson's, and Huntington's disease (see chapter 5). Studies on *C. elegans* are increasingly leading towards high-throughput screens for the identification of new genes and novel pharmaceuticals which could modify the course of different neurodegenerative diseases. These kind of studies would enormously benefit from microfabricated solutions in which different compounds and conditions can be tested at the same time, under accurate control of all the other long-term culture conditions. Moreover, extremely precious tools in this field will be represented by software interfaces for "worm tracking" and motility assessment, as well as other image processing tools which allow automatically extracting multi-phenotypic profiles of the worms, including data such as body volume, growth rate, reproduction rate and – by means of transgenic strains – gene and protein expression. Moreover, we are currently employing our "worm-chips" to address some crucial biological questions: (i) what is the progression of the different neurodegenerative diseases in *C. elegans* and how protein aggregation phenomena relate to other phenotypes over long-term analyses? (ii) Which are the effects of specific antibiotic treatments on the worms' mitochondrial activity and how is this reflected on different worms' phenotypes? (iii) Can we reliably identify new anti-parasitic drugs by screening compound libraries through our device? Keeping in mind that more than 80% of the *C. elegans* proteome has human homologous genes, by answering to these biological questions, we expect to get precious insights about human neurodegenerative and metabolic diseases as well as possibly discover new cures to parasitic infections in humans. The versatility and automation

levels that we could reach with our worm-chip designs will hopefully set a new standard in the *C. elegans* research community. The proposed devices might have large impact in the drug discovery field, with a future potential as new platforms for high-content drug-screening.

Curriculum Vitae

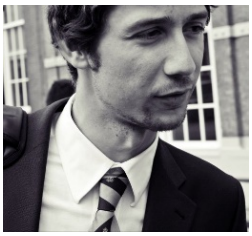

Matteo Cornaglia

1, Chemin de Villars
CH-1030, Bussigny, Switzerland
matteo.cornaglia@epfl.ch
+41 21 69 34834
http://people.epfl.ch/matteo.cornaglia

Education

2011 - present	Ph.D., Microsystems and Microelectronics *École polytechnique fédérale de Lausanne (EPFL)*, Lausanne, Switzerland
2008-2010	M.Sc., Micro & Nanotechnologies, *110/110 cum laude* *École polytechnique fédérale de Lausanne (EPFL)*, Lausanne, Switzerland *Institut National Polytechnique de Grenoble (INPG),* Grenoble, France *Politecnico di Torino,* Turin, Italy
2005-2008	B.S., Physics engineering, *110/110 cum laude* *Politecnico di Torino,* Turin, Italy

Experience

Apr 2011 - present	Research and teaching assistant, Microsystems and Microelectronics *École polytechnique fédérale de Lausanne (EPFL)*, Lausanne, Switzerland - Research activities: design, modeling and simulation of microfluidic devices and bio-MEMS; optimization of cleanroom fabrication processes; development of biological protocols for lab-on-a-chip devices; use of advanced microscopy techniques, image processing and data analysis tools; publication writing. - Project supervision: 3 M.Sc. projects, 4 B.S. projects, 3 summer internships - Teaching: cleanroom practical trainings for B.S. students
Nov 2010-Mar 2011	Research assistant, Electronics and ICT, NEMS *French Atomic Energy Commission (CEA) - Leti*, Grenoble, France Performance analysis of piezoelectric nanocantilevers for gas detection.
Mar-Aug 2010	M.Sc. project intern, Nanophotonics and Plasmonics, nanofabrication *Lawrence Berkeley National Laboratory (LBNL)* – Berkeley, CA, USA Design, fabrication and characterization of plasmonic nanoantennae; conception of plasmonic elements for optical circuits.

Jun-Aug 2009	Summer project intern, Microfluidics and MEMS *Royal Institute of Technology (KTH)*, Stockholm, Sweden Development of a novel microfabrication technique for prototyping of 3D polymeric lab-on-a-chip devices.
Mar-Jul 2008	B.S. project intern, Laser systems and optoelectronics *Microla Optoelectronics*, Turin, Italy Performance enhancement of laser micromachining processes.

Honors and awards

Jun 2015	Top 10 business ideas – venture.ch 2015 competition Initiative of ETH Zurich, Knecht Holding, CTI and McKinsey & Company
May 2015	1st prize Business Concept – CTI entrepreneurship training Business idea contest, sponsored by CVCI and EPFL innovation park
Oct 2011/Oct 2012	Finalist in the EUREL Management cup 2011 and 2012 Strategic business simulation contest at European level.
Sep 2010	Scholarship: "Future Leaders Program", 20000 € + travelling and training events. Awarded to 20 selected Italian students at the end of their M.Sc. career.
Mar 2010	Scholarship for thesis abroad, 5000$. Awarded to excellent students, pursuing a M.Sc. internship project abroad.
Oct 2005	Sign of honor from the President of the Italian Republic: "Alfiere del lavoro". Awarded to the best 25 students in Italy at the end of their high school career.

Personal skills and competences

Language skills	Italian (native language), English (fluent, spoken and written), French (fluent, spoken and written).
IT skills	MATLAB, COMSOL Multiphysics, OriginLab, L-edit, AutoCAD, SolidWorks, ImageJ, Adobe Illustrator and Photoshop, C programming, Microsoft Office
Social skills	Organization of summer camps for children and educator for 8 years. School representative of high school institute for 2 years.
Artistic/Sport skills	15-year experience as electric and acoustic guitar player. Group leader (organization, lead guitar and voice) of rock/acoustic bands. Soccer team player for 15 years. Volleyball team player for 3 years. Other practiced sports: tennis, snowboard.

List of publications

Jounal papers

1. **M. Cornaglia**, M. C. Letizia, L. Mouchiroud, D. Dumont-Fillon, T. Lehnert, J. Auwerx, and M.A.M. Gijs, An automated microfluidic platform for *C. elegans* phenotyping from the embryo till the adult stage at single-organism resolution, Lab Chip, in preparation
2. L. Dong, **M. Cornaglia**, T. Lehnert, and M. A. M. Gijs, Versatile size-dependent sorting of *C. elegans* nematodes and embryos using a tunable microfluidic filter structure, Lab Chip, in preparation
3. **M. Cornaglia**, G. Krishnamani, L. Mouchiroud, T. Lehnert, J. Auwerx, and M. A. M. Gijs, Automated longitudinal monitoring of *in vivo* protein aggregation in a neurodegenerative disease *C. elegans* model, Mol Neurodegener, under revision
4. E.G. Williams, L. Mouchiroud, **M. Cornaglia**, A.A. Nicolet-dit-Félix, G. Krishnamani, T. Ouhmad, M.V. Frochaux, B. Deplancke, M. A. M. Gijs, and J. Auwerx, The Movement Tracker: a flexible system for automated movement analysis in model organisms, Nat Protocols, in preparation
5. **M. Cornaglia**, L. Mouchiroud, A. Marette, S. Narasimhan, T. Lehnert, V. Jovaisaite, J. Auwerx, and M. A. M. Gijs, An automated microfluidic platform for *C. elegans* embryo arraying, phenotyping, and long-term live imaging, Sci Rep 5, 10192, doi: 10.1038/srep10192 (2015)
6. **M. Cornaglia**, R. Trouillon, H. C. Tekin, T. Lehnert, and M. A. M. Gijs, Dose-response curve of a microfluidic magnetic bead-based surface coverage sandwich assay, New Biotechnol 32, 433-440, doi: 10.1016/j.nbt.2015.03.008 (2015)
7. H. Yang, **M. Cornaglia**, and M. A. M. Gijs, Photonic Nanojet Array for Fast Detection of Single Nanoparticles in a Flow. Nano Lett 15, 1730-1735, doi: 10.1021/Nl5044067 (2015)
8. P. Tewari Kumar, K. Vriens, **M. Cornaglia**, M. A. M. Gijs, T. Kokalj, K. Thevissen, A. Geeraerd, B.P.A. Cammue, R. Puers and J. Lammertyn, Digital microfluidics for time-resolved cytotoxicity studies on single non-adherent yeast cells. Lab Chip, doi: 10.1039/C4LC01469C (2015)
9. **M. Cornaglia**, R. Trouillon, H. C. Tekin, T. Lehnert, and M. A. M. Gijs, Magnetic particle-scanning for ultrasensitive immunodetection on-chip. Anal Chem 86, 8213-8223, doi:10.1021/ac501568g (2014)
10. B. Verbruggen, T. Tóth, **M. Cornaglia**, R. Puers, M. A. M. Gijs, and J. Lammertyn. Separation of magnetic microparticles in segmented flow using asymmetric splitting regimes. Microfluid Nanofluid 18, 91-102, doi: 10.1007/s10404-014-1409-8 (2014)
11. N. Vergauwe, S. Vermeir, J. B. Wacker, F. Ceyssens, **M. Cornaglia**, R. Puers, M. A. M. Gijs, J. Lammertyn, and D. Witters. A highly efficient extraction protocol for magnetic particles on a

digital microfluidic chip. Sensor Actuat B-Chem 196, 282-291, doi: 10.1016/j.snb.2014.01.076 (2014)

12. **M. Cornaglia**, H. C. Tekin, T. Lehnert & M. A. M. Gijs. Fine-tuning of magnetic and microfluidic viscous forces for specific magnetic bead-based immunocomplex formation. J Appl Phys 114, doi: 10.1063/1.4817663 (2013)
13. H. C. Tekin, **M. Cornaglia** & M. A. M. Gijs. Attomolar protein detection using a magnetic bead surface coverage assay. Lab Chip 13, 1053-1059, doi: 10.1039/C3lc41285g (2013)
14. A. Weber-Bargioni, A. Schwartzberg, **M. Cornaglia**, A. Ismach, J. J. Urban, Y. J. Pang, R. Gordon, J. Bokor, M. B. Salmeron, D. F. Ogletree, P. Ashby, S. Cabrini & P. J. Schuck. Hyperspectral Nanoscale Imaging on Dielectric Substrates with Coaxial Optical Antenna Scan Probes. Nano Lett 11, 1201-1207, doi: 10.1021/Nl104163m (2011)
15. C. F. Carlborg, T. Haraldsson, **M. Cornaglia**, G. Stemme & W. van der Wijngaart. A High-Yield Process for 3-D Large-Scale Integrated Microfluidic Networks in PDMS. J Microelectromech S 19, 1050-1057, doi: 10.1109/Jmems.2010.2067203 (2010)

Conference contributions

16. M. C. Letizia, **M. Cornaglia**, and M.A.M. Gijs, Accurate quantification of bacteria concentration as a nutrient for *C. elegans* worm culture on chip. NanoBioTech 2015, Montreux, Switzerland, November 2015. Poster presentation
17. **M. Cornaglia**, L. Mouchiroud, A. Marette, S. Narasimhan, T. Lehnert, V. Jovaisaite, J. Auwerx, and M. A. M. Gijs, Multi-dimensional imaging and phenotyping of *C. elegans* embryos via an automated microfluidic device. Proc. of 19th International Conference on Miniaturized Systems for Chemistry and Life Sciences (microTAS 2015), Gyeongju, Korea, October 2015. Poster presentation
18. **M. Cornaglia**, G. Krishnamani, M. Meurville, L. Mouchiroud, T. Lehnert, J. Auwerx, and M.A.M. Gijs. A microfluidic device for longitudinal studies of *C. elegans* neurodegenerative models. Proc. of 19th International Conference on Miniaturized Systems for Chemistry and Life Sciences (microTAS 2015), Gyeongju, Korea, October 2015. Poster presentation
19. H. Yang, **M. Cornaglia**, and M.A.M. Gijs, Fast detection of single nanoparticles in a microfluidic channel by a microlens array in combination with conventional optical microscope. Proc. of 19th International Conference on Miniaturized Systems for Chemistry and Life Sciences (microTAS 2015), Gyeongju, Korea, October 2015. Poster presentation
20. G. Huszka, H. Yang, **M. Cornaglia**, and M.A.M. Gijs, Patterning of melamine and SiO_2 microsphere lens arrays. MNE 2015 - the 41th International Conference on Micro and Nano Engineering, The Hague, The Netherlands, September 2015. Poster presentation
21. **M. Cornaglia**, L. Mouchiroud, J. Auwerx, and M.A.M. Gijs, Automated microfluidic platforms for *C. elegans* arraying, phenotyping, and long-term analysis. BioInnovation Day 2015, CHUV, Lausanne, Switzerland, June 2015. Oral presentation
22. G. Krishnamani, **M. Cornaglia**, L. Mouchiroud, M.A.M. Gijs, and J. Auwerx, Long-term culture and high-resolution imaging of *C. elegans* using an automated microfluidic platform. Third

Lausanne Integrative Metabolism and Nutrition Alliance (LIMNA) Symposium, Lausanne, Switzerland, March 2015. Poster presentation

23. H. Yang, **M. Cornaglia**, T. Lehnert and M.A.M. Gijs, Study of constrained Brownian motion of nanoparticles near an interface using optical tweezers. Proc. of SPIE, Vol. 9379, Photonics West, San Francisco, CA, USA, February 2015. Poster presentation
24. P. Tewari Kumar, K. Vriens, **M. Cornaglia**, M.A.M. Gijs, T. Kokalj, K. Thevissen, A. Geeraerd, B.P.A.Cammue, R. Puers, and J. Lammertyn. Digital microfluidic chip technology for cytotoxicity studies on yeast cells at spatio-temporal resolution. NanoBioTech 2014, Montreux, Switzerland, November 2014. Oral presentation
25. H. Yang, **M. Cornaglia**, T. Lehnert, and M.A.M. Gijs. Lens array by electrostatic patterning of dielectric microspheres in a parylene-c well template. Proc. of 18th International Conference on Miniaturized Systems for Chemistry and Life Sciences (microTAS 2014), San Antonio, TX, USA, October 2014. Poster presentation
26. **M. Cornaglia**, G. Krishnamani, M. Meurville, L. Mouchiroud, T. Lehnert, J. Auwerx, and M.A.M. Gijs. An automated microfluidic platform for long-term high-resolution imaging of *C. elegans*. Proc. of 18th International Conference on Miniaturized Systems for Chemistry and Life Sciences (microTAS 2014), San Antonio, TX, USA, October 2014. Poster presentation
27. **M. Cornaglia**, R. Trouillon, H.C. Tekin, T. Lehnert, and M.A.M. Gijs. A random-walk based model to explain ultrasensitive magnetic bead-based immunoassays. Proc. of 18th International Conference on Miniaturized Systems for Chemistry and Life Sciences (microTAS 2014), San Antonio, TX, USA, October 2014. Oral presentation
28. P. Tewari Kumar, K. Vriens, **M. Cornaglia**, M.A.M. Gijs, T. Kokalj, K. Thevissen, A. Geeraerd, B.P.A. Cammue, R. Puers, and J. Lammertyn. Spatio-temporal analysis of yeast cells responses on a digital microfluidic platform. Diatech 2014 - Novel technologies for in vitro diagnostics, Leuven, Belgium, October 2014. Poster presentation
29. **M. Cornaglia**, R. Trouillon, H.C. Tekin, T. Lehnert, and M.A.M. Gijs. Random-walk model of magnetic bead-based surface coverage immunoassays. Diatech 2014 - Novel technologies for in vitro diagnostics, Leuven, Belgium, October 2014. Oral presentation
30. B. Verbruggen, F. Ceyssens, K. Leirs, **M. Cornaglia**, M.A.M. Gijs, T. Kokalj, R. Puers, and J. Lammertyn. DNA extraction with magnetic microbeads in segmented flow microfluidic chip. Diatech 2014 - Novel technologies for in vitro diagnostics, Leuven, Belgium, October 2014. Poster presentation
31. **M. Cornaglia**, H. Yang, T. Lehnert, and M.A.M. Gijs. Electrostatic self-assembly of microsphere lens arrays. MNE 2014 - the 40th International Conference on Micro and Nano Engineering, Lausanne, Switzerland, September 2014. Poster presentation
32. **M. Cornaglia**, G. Krishnamani, M. Meurville, L. Mouchiroud, T. Lehnert, J. Auwerx, and M.A.M. Gijs. An automated microfluidic platform for reversible immobilization and imaging of *C. elegans*. EMBL Microfluidics 2014, Heidelberg, Germany, July 2014. Poster presentation
33. **M. Cornaglia**, H.C. Tekin, T. Lehnert, M.A.M. Gijs. Magnetic Bead-Rolling for Ultrasensitive Surface-Based Immunoassays. Proc. of 17th International Conference on Miniaturized Systems for Chemistry and Life Sciences (microTAS 2013), October 2013, Freiburg, Germany. Oral presentation

34. **M. Cornaglia**, H.C. Tekin, T. Lehnert, M.A.M. Gijs. Balancing Magnetic Dipolar and Viscous Forces on Superparamagnetic Beads for Improving the Specificity of Microfluidic Surface-based Immunoassays. 9th International Conference on the Scientific and Clinical Applications of Magnetic Carriers, Minneapolis, Minnesota, USA, May 2012. Poster presentation
35. **M. Cornaglia**, H.C. Tekin, T. Lehnert, M.A.M. Gijs. A Combined Finite Element Method/Analytical Model of the Magnetophoretic Manipulation of Superparamagnetic Particles for Microfluidic Immunoassays. EMBL Microfluidics 2012, Heidelberg, Germany, July 2012. Poster presentation
36. H.C. Tekin, **M. Cornaglia**, C. Razaname, M.A.M. Gijs. Analysis of protein biomarkers via magnetic bead surface coverage detection. NanoBioTech 2011, Montreux, Switzerland, November 2011. Poster presentation
37. A. Weber-Bargioni, A. Schwartzberg, **M. Cornaglia**, A. Ismach, J. J. Urban, Y. J. Pang, R. Gordon, D. F. Ogletree, S. Cabrini & P. J. Schuck. Hyperspectral Nanoscale Imaging on Dielectric Substrates with Coaxial Optical Antenna Scan Probes. 2011 Conference on Lasers and Electro-Optics (Cleo) (2011)
38. **M. Cornaglia**, A. Weber-Bargioni, S. Dhuey, A. McLeod, J. Neaton, D.F. Ogletree, P.J. Schuck, S. Cabrini. Manipulating Resonance and Radiative Properties of Optical Bowtie Antennae by Modifying the Antenna's Aspect Ratio while Maintaining the Enhancement. MNE - International Conference on Micro & Nano Engineering, Genova, Italy, September 2010, Oral presentation
39. C. F. Carlborg, K. T. Haraldsson, **M. Cornaglia**, G. Stemme & W. van der Wijngaart. Large Scale Integrated 3D Microfluidic Networks through High Yield Fabrication of Vertical Vias in Pdms. Proc Ieee Micr Elect, 240-243 (2010)

Patents pending

40. **M. Cornaglia**, D. Migliozzi, and M. A. M. Gijs. Microfluidic device, system and method for worm culture and studies, International Patent Application (provisional) n° PCT/IB2014/065472 filed on October 20, 2014
41. H. Yang, **M. Cornaglia**, and M. A. M. Gijs, System for optical detection and imaging of sub-diffraction-limited nano-objects, International Patent Application (provisional) n° PCT/IB2014/063747 filed on August 6, 2014

References

[1] H. C. Tekin, M. Cornaglia, and M. A. Gijs, "Attomolar protein detection using a magnetic bead surface coverage assay," *Lab on a Chip,* vol. 13, pp. 1053-9, 2013.

[2] V. N. Morozov and T. Y. Morozova, "Active bead-linked immunoassay on protein microarrays," *Analytica Chimica Acta,* vol. 564, pp. 40-52, 2006.

[3] S. P. Mulvaney, K. M. Myers, P. E. Sheehan, and L. J. Whitman, "Attomolar protein detection in complex sample matrices with semi-homogeneous fluidic force discrimination assays," *Biosensors & Bioelectronics,* vol. 24, pp. 1109-1115, 2009.

[4] M. Cornaglia, H. C. Tekin, T. Lehnert, and M. A. M. Gijs, "Fine-tuning of magnetic and microfluidic viscous forces for specific magnetic bead-based immunocomplex formation," *Journal of Applied Physics,* vol. 114, 2013.

[5] M. Cornaglia, R. Trouillon, H. C. Tekin, T. Lehnert, and M. A. Gijs, "Magnetic particle-scanning for ultrasensitive immunodetection on-chip," *Anal Chem,* vol. 86, pp. 8213-23, 2014.

[6] M. Cornaglia, R. Trouillon, H. C. Tekin, T. Lehnert, and M. A. M. Gijs, "Dose-response curve of a microfluidic magnetic bead-based surface coverage sandwich assay," *New Biotechnology,* vol. 32, pp. 433-440, 2015.

[7] R. Etzioni, N. Urban, S. Ramsey, M. McIntosh, S. Schwartz, B. Reid, J. Radich, G. Anderson, and L. Hartwell, "The case for early detection," *Nature Reviews Cancer,* vol. 3, pp. 243-252, 2003.

[8] C. S. Thaxton, R. Elghanian, A. D. Thomas, S. I. Stoeva, J. S. Lee, N. D. Smith, A. J. Schaeffer, H. Klocker, W. Horninger, G. Bartsch, and C. A. Mirkin, "Nanoparticle-based bio-barcode assay redefines "undetectable'' PSA and biochemical recurrence after radical prostatectomy," *Proceedings of the National Academy of Sciences of the United States of America,* vol. 106, pp. 18437-18442, 2009.

[9] R. Etzioni, C. Kooperberg, M. Pepe, R. Smith, and P. H. Gann, "Combining biomarkers to detect disease with application to prostate cancer," *Biostatistics,* vol. 4, pp. 523-538, 2003.

[10] P. R. Srinivas, B. S. Kramer, and S. Srivastava, "Trends in biomarker research for cancer detection," *Lancet Oncology,* vol. 2, pp. 698-704, 2001.

[11] J. M. Barletta, D. C. Edelman, and N. T. Constantine, "Lowering the detection limits of HIV-1 viral load using real-time immuno-PCR for HIV-1 p24 antigen," *Am J Clin Pathol,* vol. 122, pp. 20-7, 2004.

[12] D. de Jong, B. P. Kremer, M. G. Olde Rikkert, and M. M. Verbeek, "Current state and future directions of neurochemical biomarkers for Alzheimer's disease," *Clin Chem Lab Med,* vol. 45, pp. 1421-34, 2007.

[13] D. Galasko, "Biomarkers for Alzheimer's disease--clinical needs and application," *J Alzheimers Dis,* vol. 8, pp. 339-46, 2005.

[14] D. A. Giljohann and C. A. Mirkin, "Drivers of biodiagnostic development," *Nature,* vol. 462, pp. 461-464, 2009.

[15] N. L. Anderson and N. G. Anderson, "The human plasma proteome - History, character, and diagnostic prospects," *Molecular & Cellular Proteomics,* vol. 1, pp. 845-867, 2002.

[16] R. J. Chen, S. Bangsaruntip, K. A. Drouvalakis, N. W. Kam, M. Shim, Y. Li, W. Kim, P. J. Utz, and H. Dai, "Noncovalent functionalization of carbon nanotubes for highly specific electronic biosensors," *Proc Natl Acad Sci U S A,* vol. 100, pp. 4984-9, 2003.

[17] R. S. Gaster, D. A. Hall, C. H. Nielsen, S. J. Osterfeld, H. Yu, K. E. Mach, R. J. Wilson, B. Murmann, J. C. Liao, S. S. Gambhir, and S. X. Wang, "Matrix-insensitive protein assays push the limits of biosensors in medicine," *Nature Medicine,* vol. 15, pp. 1327-U130, 2009.

[18] S. Krishnan, V. Mani, D. Wasalathanthri, C. V. Kumar, and J. F. Rusling, "Attomolar Detection of a Cancer Biomarker Protein in Serum by Surface Plasmon Resonance Using Superparamagnetic Particle Labels," *Angewandte Chemie-International Edition,* vol. 50, pp. 1175-1178, 2011.

[19] V. N. Morozov, S. Groves, M. J. Turell, and C. Bailey, "Three minutes-long electrophoretically assisted zeptornolar microfluidic immunoassay with magnetic-beads detection," *Journal of the American Chemical Society,* vol. 129, pp. 12628-+, 2007.

[20] J. M. Nam, C. S. Thaxton, and C. A. Mirkin, "Nanoparticle-based bio-bar codes for the ultrasensitive detection of proteins," *Science,* vol. 301, pp. 1884-1886, 2003.

[21] D. M. Rissin, C. W. Kan, T. G. Campbell, S. C. Howes, D. R. Fournier, L. Song, T. Piech, P. P. Patel, L. Chang, A. J. Rivnak, E. P. Ferrell, J. D. Randall, G. K. Provuncher, D. R. Walt, and D. C. Duffy, "Single-molecule enzyme-linked immunosorbent assay detects serum proteins at subfemtomolar concentrations," *Nature Biotechnology,* vol. 28, pp. 595-U25, 2010.

[22] G. F. Zheng, F. Patolsky, Y. Cui, W. U. Wang, and C. M. Lieber, "Multiplexed electrical detection of cancer markers with nanowire sensor arrays," *Nature Biotechnology,* vol. 23, pp. 1294-1301, 2005.

[23] M. A. Gijs, F. Lacharme, and U. Lehmann, "Microfluidic applications of magnetic particles for biological analysis and catalysis," *Chemical Reviews,* vol. 110, pp. 1518-63, 2010.

[24] H. C. Tekin and M. A. M. Gijs, "Ultrasensitive protein detection: a case for microfluidic magnetic bead-based assays," *Lab on a Chip,* vol. 13, pp. 4711-4739, 2013.

[25] J. W. Choi, K. W. Oh, J. H. Thomas, W. R. Heineman, H. B. Halsall, J. H. Nevin, A. J. Helmicki, H. T. Henderson, and C. H. Ahn, "An integrated microfluidic biochemical detection system for

protein analysis with magnetic bead-based sampling capabilities," *Lab on a Chip,* vol. 2, pp. 27-30, 2002.

[26] M. A. Hayes, N. A. Polson, and A. A. Garcia, "Active control of dynamic supraparticle structures in microchannels," *Langmuir,* vol. 17, pp. 2866-2871, 2001.

[27] F. Lacharme, C. Vandevyver, and M. A. Gijs, "Full on-chip nanoliter immunoassay by geometrical magnetic trapping of nanoparticle chains," *Anal Chem,* vol. 80, pp. 2905-10, 2008.

[28] S. A. Peyman, A. Iles, and N. Pamme, "Mobile magnetic particles as solid-supports for rapid surface-based bioanalysis in continuous flow," *Lab on a Chip,* vol. 9, pp. 3110-3117, 2009.

[29] U. Lehmann, C. Vandevyver, V. K. Parashar, and M. A. M. Gijs, "Droplet-based DNA purification in a magnetic lab-on-a-chip," *Angewandte Chemie-International Edition,* vol. 45, pp. 3062-3067, 2006.

[30] M. Shikida, K. Takayanagi, H. Honda, H. Ito, and K. Sato, "Development of an enzymatic reaction device using magnetic bead-cluster handling," *Journal of Micromechanics and Microengineering,* vol. 16, pp. 1875-1883, 2006.

[31] S. J. Osterfeld, H. Yu, R. S. Gaster, S. Caramuta, L. Xu, S. J. Han, D. A. Hall, R. J. Wilson, S. H. Sun, R. L. White, R. W. Davis, N. Pourmand, and S. X. Wang, "Multiplex protein assays based on real-time magnetic nanotag sensing," *Proceedings of the National Academy of Sciences of the United States of America,* vol. 105, pp. 20637-20640, 2008.

[32] R. S. Gaster, L. Xu, S. J. Han, R. J. Wilson, D. A. Hall, S. J. Osterfeld, H. Yu, and S. X. Wang, "Quantification of protein interactions and solution transport using high-density GMR sensor arrays," *Nature Nanotechnology,* vol. 6, pp. 314-320, 2011.

[33] Y. M. Shlyapnikov, E. A. Shlyapnikova, M. A. Simonova, A. O. Shepelyakovskaya, F. A. Brovko, R. L. Komaleva, E. V. Grishin, and V. N. Morozov, "Rapid Simultaneous Ultrasensitive Immunodetection of Five Bacterial Toxins," *Analytical Chemistry,* vol. 84, pp. 5596-5603, 2012.

[34] D. M. Rissin and D. R. Walt, "Digital concentration readout of single enzyme molecules using femtoliter arrays and Poisson statistics," *Nano Letters,* vol. 6, pp. 520-523, 2006.

[35] L. O. Narhi and T. Arakawa, "Dissociation of Recombinant Tumor-Necrosis-Factor-Alpha Studied by Gel-Permeation Chromatography," *Biochemical and Biophysical Research Communications,* vol. 147, pp. 740-746, 1987.

[36] J. Baudry, C. Rouzeau, C. Goubault, C. Robic, L. Cohen-Tannoudji, A. Koenig, E. Bertrand, and J. Bibette, "Acceleration of the recognition rate between grafted ligands and receptors with magnetic forces," *Proceedings of the National Academy of Sciences of the United States of America,* vol. 103, pp. 16076-16078, 2006.

[37] A. Ranzoni, G. Sabatte, L. J. van IJzendoorn, and M. W. J. Prins, "One-Step Homogeneous Magnetic Nanoparticle Immunoassay for Biomarker Detection Directly in Blood Plasma," *Acs Nano,* vol. 6, pp. 3134-3141, 2012.

[38] H. C. Tekin, "Automated Analysis of Rare Biomarkers Using a Magnetic Bead Surface Coverage Assay Coupled with Chaotic Mixing on a Microfluidic Chip," PhD, Microsystems and Microtechnology, EPFL, 2012.

[39] V. Sivagnanam, A. Sayah, C. Vandevyver, and M. A. M. Gijs, "Micropatterning of protein-functionalized magnetic beads on glass using electrostatic self-assembly," *Sensors and Actuators B-Chemical,* vol. 132, pp. 361-367, 2008.

[40] R. Zaouk, B. Y. Park, and M. J. Madou, "Introduction to microfabrication techniques," *Methods Mol Biol,* vol. 321, pp. 5-15, 2006.

[41] T. Henighan, A. Chen, G. Vieira, A. J. Hauser, F. Y. Yang, J. J. Chalmers, and R. Sooryakumar, "Manipulation of Magnetically Labeled and Unlabeled Cells with Mobile Magnetic Traps," *Biophysical Journal,* vol. 98, pp. 412-417, 2010.

[42] D. MacDougall and W. B. Crummett, "Guidelines for Data Acquisition and Data Quality Evaluation in Environmental Chemistry," *Analytical Chemistry,* vol. 52, pp. 2242-2249, 1980.

[43] D. A. Brenner, M. Ohara, P. Angel, M. Chojkier, and M. Karin, "Prolonged Activation of Jun and Collagenase Genes by Tumor Necrosis Factor-Alpha," *Nature,* vol. 337, pp. 661-663, 1989.

[44] A. McTiernan, "Mechanisms linking physical activity with cancer," *Nature Reviews Cancer,* vol. 8, pp. 205-211, 2008.

[45] H. Bruus, *Theoretical Microfluidics*. New York: Oxford Univ Press, 2008.

[46] G. Fonnum, C. Johansson, A. Molteberg, S. Morup, and E. Aksnes, "Characterisation of Dynabeads (R) by magnetization measurements and Mossbauer spectroscopy," *Journal of Magnetism and Magnetic Materials,* vol. 293, pp. 41-47, 2005.

[47] Y. Moser, T. Lehnert, and M. A. M. Gijs, "Quadrupolar magnetic actuation of superparamagnetic particles for enhanced microfluidic perfusion," *Applied Physics Letters,* vol. 94, 2009.

[48] E. P. Furlani and X. Xue, "A model for predicting field-directed particle transport in the magnetofection process," *Pharm Res,* vol. 29, pp. 1366-79, 2012.

[49] D. C. Duffy, J. C. McDonald, O. J. A. Schueller, and G. M. Whitesides, "Rapid prototyping of microfluidic systems in poly(dimethylsiloxane)," *Analytical Chemistry,* vol. 70, pp. 4974-4984, 1998.

[50] A. E. Saliba, L. Saias, E. Psychari, N. Minc, D. Simon, F. C. Bidard, C. Mathiot, J. Y. Pierga, V. Fraisier, J. Salamero, V. Saada, F. Farace, P. Vielh, L. Malaquin, and J. L. Viovy, "Microfluidic sorting and multimodal typing of cancer cells in self-assembled magnetic arrays," *Proceedings of the National Academy of Sciences of the United States of America,* vol. 107, pp. 14524-14529, 2010.

[51] Y. Wang, Y. Gao, H. Wyss, P. Anderson, and J. den Toonder, "Out of the cleanroom, self-assembled magnetic artificial cilia," *Lab on a Chip,* 2013.

[52] A. Pierres, D. Touchard, A. M. Benoliel, and P. Bongrand, "Dissecting streptavidin-biotin interaction with a laminar flow chamber," *Biophysical Journal,* vol. 82, pp. 3214-23, 2002.

[53] Y. R. Chemla, H. L. Crossman, Y. Poon, R. McDermott, R. Stevens, M. D. Alper, and J. Clarke, "Ultrasensitive magnetic biosensor for homogeneous immunoassay," *Proceedings of the National Academy of Sciences of the United States of America,* vol. 97, pp. 14268-14272, 2000.

[54] S. Y. Choi, J. M. Karp, and R. Karnik, "Cell sorting by deterministic cell rolling," *Lab on a Chip,* vol. 12, pp. 1427-1430, 2012.

[55] N. K. Lee, A. Johner, F. Thalmann, L. Cohen-Tannoudji, E. Bertrand, J. Baudry, J. Bibette, and C. M. Marques, "Ligand-receptor interactions in chains of colloids: When reactions are limited by rotational diffusion," *Langmuir,* vol. 24, pp. 1296-1307, 2008.

[56] L. Cohen-Tannoudji, E. Bertrand, J. Baudry, C. Robic, C. Goubault, M. Pellissier, A. Johner, F. Thalmann, N. K. Lee, C. M. Marques, and J. Bibette, "Measuring the kinetics of biomolecular recognition with magnetic colloids," *Physical Review Letters,* vol. 100, 2008.

[57] S. Condamin, O. Benichou, V. Tejedor, R. Voituriez, and J. Klafter, "First-passage times in complex scale-invariant media," *Nature,* vol. 450, pp. 77-80, 2007.

[58] E. B. Saff and A. B. J. Kuijlaars, "Distributing many points on a sphere," *Mathematical Intelligencer,* vol. 19, pp. 5-11, 1997.

[59] W. Habicht and B. L. van der Waerden, "Lagerung von Punkten auf der Kugel," *Math. Ann.,* vol. 123, pp. 223–234, 1951.

[60] I. Langmuir, "The Adsorption of Gases on Plane Surfaces of Glass, Mica and Platinum.," *Journal of the American Chemical Society,* vol. 40, pp. 1361-1403, 1918.

[61] I. Langmuir, "Vapor pressures, evaporation, condensation and adsorption," *Journal of the American Chemical Society,* vol. 54, pp. 2798-2832, 1932.

[62] A. Holmberg, A. Blomstergren, O. Nord, M. Lukacs, J. Lundeberg, and M. Uhlen, "The biotin-streptavidin interaction can be reversibly broken using water at elevated temperatures," *Electrophoresis,* vol. 26, pp. 501-510, 2005.

[63] W. C. Chiu, Y. P. Lai, and M. Y. Chou, "Humanization and Characterization of an Anti-Human TNF-alpha Murine Monoclonal Antibody," *Plos One,* vol. 6, 2011.

[64] H. Y. Tsai, Y. C. Hsieh, Y. M. Su, J. R. Chan, Y. C. Chang, and C. B. Fuh, "Effects of particle characteristics on magnetic immunoassay in a thin channel," *Biosensors & Bioelectronics,* vol. 28, pp. 38-43, 2011.

[65] N. Modak, D. Kejriwal, K. Nandy, A. Datta, and R. Ganguly, "Experimental and numerical characterization of magnetophoretic separation for MEMS-based biosensor applications," *Biomedical Microdevices,* vol. 12, pp. 23-34, 2010.

[66] M. A. Tahir, L. Gao, L. N. Virgin, and B. B. Yellen, "Transport of superparamagnetic beads through a two-dimensional potential energy landscape," *Physical Review E,* vol. 84, 2011.

[67] H. Ottevaere, R. Cox, H. P. Herzig, T. Miyashita, K. Naessens, M. Taghizadeh, R. Volkel, H. J. Woo, and H. Thienpont, "Comparing glass and plastic refractive microlenses fabricated with different technologies," *Journal of Optics a-Pure and Applied Optics,* vol. 8, pp. S407-S429, 2006.

[68] J. N. Anker, W. P. Hall, O. Lyandres, N. C. Shah, J. Zhao, and R. P. Van Duyne, "Biosensing with plasmonic nanosensors," *Nature Materials,* vol. 7, pp. 442-453, 2008.

[69] D. J. Maxwell, J. R. Taylor, and S. M. Nie, "Self-assembled nanoparticle probes for recognition and detection of biomolecules," *Journal of the American Chemical Society,* vol. 124, pp. 9606-9612, 2002.

[70] F. Vollmer and S. Arnold, "Whispering-gallery-mode biosensing: label-free detection down to single molecules," *Nature Methods,* vol. 5, pp. 591-596, 2008.

[71] J. G. Zhu, S. K. Ozdemir, Y. F. Xiao, L. Li, L. N. He, D. R. Chen, and L. Yang, "On-chip single nanoparticle detection and sizing by mode splitting in an ultrahigh-Q microresonator (vol 4, pg 46, 2010)," *Nature Photonics,* vol. 4, pp. 122-122, 2010.

[72] H. Yang, N. Moullan, J. Auwerx, and M. A. M. Gijs, "Super-Resolution Biological Microscopy Using Virtual Imaging by a Microsphere Nanoscope," *Small,* vol. 10, pp. 1712-1718, 2014.

[73] J. J. Schwartz, S. Stavrakis, and S. R. Quake, "Colloidal lenses allow high-temperature single-molecule imaging and improve fluorophore photostability," *Nature Nanotechnology,* vol. 5, pp. 127-132, 2010.

[74] S. Lee, L. Li, and Z. B. Wang, "Optical resonances in microsphere photonic nanojets," *Journal of Optics,* vol. 16, 2014.

[75] S. Yang, A. Taflove, and V. Backman, "Experimental confirmation at visible light wavelengths of the backscattering enhancement phenomenon of the photonic nanojet," *Optics Express,* vol. 19, pp. 7084-7093, 2011.

[76] H. Yang and M. A. M. Gijs, "Microtextured Substrates and Microparticles Used as in Situ Lenses for On-Chip Immunofluorescence Amplification," *Analytical Chemistry,* vol. 85, pp. 2064-2071, 2013.

[77] D. Witters, K. Knez, F. Ceyssens, R. Puers, and J. Lammertyn, "Digital microfluidics-enabled single-molecule detection by printing and sealing single magnetic beads in femtoliter droplets," *Lab on a Chip,* vol. 13, pp. 2047-2054, 2013.

[78] R. R. Jahan-Tigh, C. Ryan, G. Obermoser, and K. Schwarzenberger, "Flow Cytometry," *Journal of Investigative Dermatology,* vol. 132, pp. 1-6, 2012.

[79] D. Di Carlo, N. Aghdam, and L. P. Lee, "Single-cell enzyme concentrations, kinetics, and inhibition analysis using high-density hydrodynamic cell isolation arrays," *Analytical Chemistry,* vol. 78, pp. 4925-4930, 2006.

[80] D. Wlodkowic, S. Faley, M. Zagnoni, J. P. Wikswo, and J. M. Cooper, "Microfluidic Single-Cell Array Cytometry for the Analysis of Tumor Apoptosis," *Analytical Chemistry,* vol. 81, pp. 5517-5523, 2009.

[81] S. H. Kim, T. Yamamoto, D. Fourmy, and T. Fujii, "Electroactive Microwell Arrays for Highly Efficient Single-Cell Trapping and Analysis," *Small,* vol. 7, pp. 3239-3247, 2011.

[82] X. L. Wang, S. X. Chen, M. Kong, Z. K. Wang, K. D. Costa, R. A. Li, and D. Sun, "Enhanced cell sorting and manipulation with combined optical tweezer and microfluidic chip technologies," *Lab Chip,* vol. 11, pp. 3656-3662, 2011.

[83] V. Lecault, M. VanInsberghe, S. Sekulovic, D. J. H. F. Knapp, S. Wohrer, W. Bowden, F. Viel, T. McLaughlin, A. Jarandehei, M. Miller, D. Falconnet, A. K. White, D. G. Kent, M. R. Copley, F. Taghipour, C. J. Eaves, R. K. Humphries, J. M. Piret, and C. L. Hansen, "High-throughput analysis of single hematopoietic stem cell proliferation in microfluidic cell culture arrays," *Nature Methods,* vol. 8, pp. 581-U93, 2011.

[84] H. M. Wyss, D. L. Blair, J. F. Morris, H. A. Stone, and D. A. Weitz, "Mechanism for clogging of microchannels," *Physical Review E,* vol. 74, 2006.

[85] N. L. W. Xiao-Peng Bi, Brian P. Crum, Wen Li, "Plasma-treated Switchable Wettability of Parylene-C Surface " *Proc of IEEE NEMS 2012,* pp. 296-299, 2012.

[86] A. K. Diallo, J. Tardy, Z. Q. Zhang, F. Bessueille, N. Jaffrezic-Renault, and M. Lemiti, "Trimethylamine biosensor based on pentacene enzymatic organic field effect transistor," *Applied Physics Letters,* vol. 94, 2009.

[87] M. Demelas, S. Lai, A. Spanu, S. Martinoia, P. Cosseddu, M. Barbaro, and A. Bonfiglio, "Charge sensing by organic charge-modulated field effect transistors: application to the detection of bio-related effects," *Journal of Materials Chemistry B,* vol. 1, pp. 3811-3819, 2013.

[88] A. R. Wheeler, "Chemistry - Putting electrowetting to work," *Science,* vol. 322, pp. 539-540, 2008.

[89] P. T. Kumar, K. Vriens, M. Cornaglia, M. Gijs, T. Kokalj, K. Thevissen, A. Geeraerd, B. P. A. Cammue, R. Puers, and J. Lammertyn, "Digital microfluidics for time-resolved cytotoxicity studies on single non-adherent yeast cells," *Lab Chip,* vol. 15, pp. 1852-1860, 2015.

[90] A. J. Phillips, I. Sudbery, and M. Ramsdale, "Apoptosis induced by environmental stresses and amphotericin B in Candida albicans," *Proceedings of the National Academy of Sciences of the United States of America,* vol. 100, pp. 14327-14332, 2003.

[91] J. Giacomotto and L. Segalat, "High-throughput screening and small animal models, where are we?," *Br J Pharmacol,* vol. 160, pp. 204-16, 2010.

[92] L. P. O'Reilly, C. J. Luke, D. H. Perlmutter, G. A. Silverman, and S. C. Pak, "C. elegans in high-throughput drug discovery," *Advanced Drug Delivery Reviews,* vol. 69, pp. 247-253, 2014.

[93] C. e. S. Consortium, "Genome sequence of the nematode C-elegans: A platform for investigating biology," *Science,* vol. 282, pp. 2012-2018, 1998.

[94] L. Timmons and A. Fire, "Specific interference by ingested dsRNA," *Nature,* vol. 395, pp. 854-854, 1998.

[95] J. E. Sulston, E. Schierenberg, J. G. White, and J. N. Thomson, "The Embryonic-Cell Lineage of the Nematode Caenorhabditis-Elegans," *Developmental Biology,* vol. 100, pp. 64-119, 1983.

[96] Z. F. Altun and D. H. Hall. (2015). *Handbook of C. elegans Anatomy*.

[97] M. F. Yanik, C. B. Rohde, and C. Pardo-Martin, "Technologies for Micromanipulating, Imaging, and Phenotyping Small Invertebrates and Vertebrates," *Annual Review of Biomedical Engineering, Vol 13,* vol. 13, pp. 185-217, 2011.

[98] M. M. Crane, K. Chung, J. Stirman, and H. Lu, "Microfluidics-enabled phenotyping, imaging, and screening of multicellular organisms," *Lab Chip,* vol. 10, pp. 1509-1517, 2010.

[99] D. Wlodkowic, K. Khoshmanesh, J. Akagi, D. E. Williams, and J. M. Cooper, "Wormometry-on-a-Chip: Innovative Technologies for In Situ Analysis of Small Multicellular Organisms," *Cytometry Part A,* vol. 79A, pp. 799-813, 2011.

[100] N. Chronis, "Worm chips: Microtools for C. elegans biology," *Lab Chip,* vol. 10, pp. 432-437, 2010.

[101] M. Baker, "Screening: the age of fishes," *Nature Methods,* vol. 8, pp. 47-51, 2011.

[102] N. A. Bakhtina and J. G. Korvink, "Microfluidic laboratories for C. elegans enhance fundamental studies in biology," *Rsc Advances,* vol. 4, pp. 4691-4709, 2014.

[103] V. Sivagnanam and M. A. Gijs, "Exploring living multicellular organisms, organs, and tissues using microfluidic systems," *Chemical Reviews,* vol. 113, pp. 3214-47, 2013.

[104] S. E. Hulme and G. M. Whitesides, "Chemistry and the Worm: Caenorhabditis elegans as a Platform for Integrating Chemical and Biological Research," *Angewandte Chemie-International Edition,* vol. 50, pp. 4774-4807, 2011.

[105] S. P. Curran and G. Ruvkun, "Lifespan regulation by evolutionarily conserved genes essential for viability," *PLoS Genet,* vol. 3, 2007.

[106] J. Hardin, "Imaging Embryonic Morphogenesis in C. elegans," *Caenorhabditis Elegans: Molecular Genetics and Development, Second Edition,* vol. 106, pp. 377-412, 2011.

[107] N. Chronis, "Worm chips: Microtools for C. elegans biology," *Lab on a Chip,* vol. 10, pp. 432-437, 2010.

[108] A. Ben-Yakar, N. Chronis, and H. Lu, "Microfluidics for the analysis of behavior, nerve regeneration, and neural cell biology in C. elegans," *Current Opinion in Neurobiology,* vol. 19, pp. 561-567, 2009.

[109] C. Fang-Yen, C. V. Gabel, A. D. T. Samuel, C. I. Bargmann, and L. Avery, "Laser Microsurgery in Caenorhabditis elegans," *Caenorhabditis Elegans: Cell Biology and Physiology, Second Edition,* vol. 107, pp. 177-206, 2012.

[110] S. E. Hulme, S. S. Shevkoplyas, A. P. McGuigan, J. Apfeld, W. Fontana, and G. M. Whitesides, "Lifespan-on-a-chip: microfluidic chambers for performing lifelong observation of C. elegans," *Lab Chip,* vol. 10, pp. 589-597, 2010.

[111] C. B. Rohde, F. Zeng, R. Gonzalez-Rubio, M. Angel, and M. F. Yanik, "Microfluidic system for on-chip high-throughput whole-animal sorting and screening at subcellular resolution," *Proceedings of the National Academy of Sciences of the United States of America,* vol. 104, pp. 13891-13895, 2007.

[112] K. H. Chung, M. M. Crane, and H. Lu, "Automated on-chip rapid microscopy, phenotyping and sorting of C. elegans," *Nature Methods,* vol. 5, pp. 637-643, 2008.

[113] S. K. Gokce, S. X. Guo, N. Ghorashian, W. N. Everett, T. Jarrell, A. Kottek, A. C. Bovik, and A. Ben-Yakar, "A fully automated microfluidic femtosecond laser axotomy platform for nerve regeneration studies in C. elegans," *PLoS One,* vol. 9, p. e113917, 2014.

[114] D. R. Albrecht and C. I. Bargmann, "High-content behavioral analysis of Caenorhabditis elegans in precise spatiotemporal chemical environments," *Nature Methods,* vol. 8, pp. 599-605, 2011.

[115] K. Chung, Y. Kim, J. S. Kanodia, E. Gong, S. Y. Shvartsman, and H. Lu, "A microfluidic array for large-scale ordering and orientation of embryos," *Nature Methods,* vol. 8, pp. 171-U103, 2011.

[116] J. Akagi, K. Khoshmanesh, B. Evans, C. J. Hall, K. E. Crosier, J. M. Cooper, P. S. Crosier, and D. Wlodkowic, "Miniaturized Embryo Array for Automated Trapping, Immobilization and Microperfusion of Zebrafish Embryos," *Plos One,* vol. 7, 2012.

[117] W. H. Tan and S. Takeuchi, "A trap-and-release integrated microfluidic system for dynamic microarray applications," *Proceedings of the National Academy of Sciences of the United States of America,* vol. 104, pp. 1146-1151, 2007.

[118] S. Kobel, A. Valero, J. Latt, P. Renaud, and M. Lutolf, "Optimization of microfluidic single cell trapping for long-term on-chip culture," *Lab Chip,* vol. 10, pp. 857-63, 2010.

[119] M. Porta-de-la-Riva, L. Fontrodona, A. Villanueva, and J. Ceron, "Basic Caenorhabditis elegans methods: synchronization and observation," *J Vis Exp,* p. e4019, 2012.

[120] B. Xian, J. Shen, W. Chen, N. Sun, N. Qiao, D. Jiang, T. Yu, Y. Men, Z. Han, Y. Pang, M. Kaeberlein, Y. Huang, and J. D. Han, "WormFarm: a quantitative control and measurement device toward automated Caenorhabditis elegans aging analysis," *Aging Cell,* vol. 12, pp. 398-409, 2013.

[121] T. Yoneda, C. Benedetti, F. Urano, S. G. Clark, H. P. Harding, and D. Ron, "Compartment-specific perturbation of protein handling activates genes encoding mitochondrial chaperones," *J Cell Sci,* vol. 117, pp. 4055-66, 2004.

[122] C. Benedetti, C. M. Haynes, Y. Yang, H. P. Harding, and D. Ron, "Ubiquitin-like protein 5 positively regulates chaperone gene expression in the mitochondrial unfolded protein response," *Genetics,* vol. 174, pp. 229-39, 2006.

[123] J. Durieux, S. Wolff, and A. Dillin, "The cell-non-autonomous nature of electron transport chain-mediated longevity," *Cell,* vol. 144, pp. 79-91, 2011.

[124] N. Ishii, K. Takahashi, S. Tomita, T. Keino, S. Honda, K. Yoshino, and K. Suzuki, "A methyl viologen-sensitive mutant of the nematode Caenorhabditis elegans," *Mutat Res,* vol. 237, pp. 165-71, 1990.

[125] D. M. Raizen, R. Y. Lee, and L. Avery, "Interacting genes required for pharyngeal excitation by motor neuron MC in Caenorhabditis elegans," *Genetics,* vol. 141, pp. 1365-82, 1995.

[126] J. Feng, F. Bussiere, and S. Hekimi, "Mitochondrial electron transport is a key determinant of life span in Caenorhabditis elegans," *Dev Cell,* vol. 1, pp. 633-44, 2001.

[127] N. Ishii, M. Fujii, P. S. Hartman, M. Tsuda, K. Yasuda, N. Senoo-Matsuda, S. Yanase, D. Ayusawa, and K. Suzuki, "A mutation in succinate dehydrogenase cytochrome b causes oxidative stress and ageing in nematodes," *Nature,* vol. 394, pp. 694-7, 1998.

[128] B. Lakowski and S. Hekimi, "The genetics of caloric restriction in Caenorhabditis elegans," *Proc Natl Acad Sci USA,* vol. 95, pp. 13091-6, 1998.

[129] S. Kumar, C. Aninat, G. Michaux, and F. Morel, "Anticancer drug 5-fluorouracil induces reproductive and developmental defects in Caenorhabditis elegans," *Reproductive Toxicology,* vol. 29, pp. 415-420, 2010.

[130] C. M. Haynes and D. Ron, "The mitochondrial UPR - protecting organelle protein homeostasis," *J Cell Sci,* vol. 123, pp. 3849-3855, 2010.

[131] V. Jovaisaite, L. Mouchiroud, and J. Auwerx, "The mitochondrial unfolded protein response, a conserved stress response pathway with implications in health and disease," *Journal of Experimental Biology,* vol. 217, pp. 137-143, 2014.

[132] E. A. Schroeder, N. Raimundo, and G. S. Shadel, "Epigenetic Silencing Mediates Mitochondria Stress-Induced Longevity," *Cell Metabolism,* vol. 17, pp. 954-964, 2013.

[133] S. S. Lee, R. Y. N. Lee, A. G. Fraser, R. S. Kamath, J. Ahringer, and G. Ruvkun, "A systematic RNAi screen identifies a critical role for mitochondria in C-elegans longevity," *Nature Genetics,* vol. 33, pp. 40-48, 2003.

[134] L. Mouchiroud, R. H. Houtkooper, N. Moullan, E. Katsyuba, D. Ryu, C. Canto, A. Mottis, Y. S. Jo, M. Viswanathan, K. Schoonjans, L. Guarente, and J. Auwerx, "The NAD(+)/Sirtuin Pathway Modulates Longevity through Activation of Mitochondrial UPR and FOXO Signaling," *Cell,* vol. 154, pp. 430-41, 2013.

[135] A. D. Chisholm and J. Hardin, "Epidermal morphogenesis," *WormBook,* pp. 1-22, 2005.

[136] M. Levin, T. Hashimshony, F. Wagner, and I. Yanai, "Developmental Milestones Punctuate Gene Expression in the Caenorhabditis Embryo," *Dev Cell,* vol. 22, pp. 1101-1108, 2012.

[137] L. Piko and K. D. Taylor, "Amounts of Mitochondrial-DNA and Abundance of Some Mitochondrial Gene Transcripts in Early Mouse Embryos," *Developmental Biology,* vol. 123, pp. 364-374, 1987.

[138] W. Y. Tsang and B. D. Lemire, "Mitochondrial genome content is regulated during nematode development," *Biochemical and Biophysical Research Communications,* vol. 291, pp. 8-16, 2002.

[139] R. H. Houtkooper, L. Mouchiroud, D. Ryu, N. Moullan, E. Katsyuba, G. Knott, R. W. Williams, and J. Auwerx, "Mitonuclear protein imbalance as a conserved longevity mechanism," *Nature,* vol. 497, pp. 451-7, 2013.

[140] C. M. Haynes, K. Petrova, C. Benedetti, Y. Yang, and D. Ron, "ClpP mediates activation of a mitochondrial unfolded protein response in C-elegans," *Dev Cell,* vol. 13, pp. 467-480, 2007.

[141] K. Kimura, N. Tanaka, N. Nakamura, S. Takano, and S. Ohkuma, "Knockdown of mitochondrial heat shock protein 70 promotes progeria-like phenotypes in caenorhabditis elegans," *J Biol Chem,* vol. 282, pp. 5910-8, 2007.

[142] E. D. Runkel, S. Liu, R. Baumeister, and E. Schulze, "Surveillance-activated defenses block the ROS-induced mitochondrial unfolded protein response," *PLoS Genet,* vol. 9, p. e1003346, 2013.

[143] R. C. Taylor, K. M. Berendzen, and A. Dillin, "Systemic stress signalling: understanding the cell non-autonomous control of proteostasis," *Nat Rev Mol Cell Biol,* vol. 15, pp. 211-7, 2014.

[144] Y. N. Xia and G. M. Whitesides, "Soft lithography," *Angewandte Chemie-International Edition,* vol. 37, pp. 551-575, 1998.

[145] A. Dillin, A. L. Hsu, N. Arantes-Oliveira, J. Lehrer-Graiwer, H. Hsin, A. G. Fraser, R. S. Kamath, J. Ahringer, and C. Kenyon, "Rates of behavior and aging specified by mitochondrial function during development," *Science,* vol. 298, pp. 2398-401, 2002.

[146] K. Ziolkowska, R. Kwapiszewski, and Z. Brzozka, "Microfluidic devices as tools for mimicking the in vivo environment," *New Journal of Chemistry,* vol. 35, pp. 979-990, 2011.

[147] I. Zaretsky, M. Polonsky, E. Shifrut, S. Reich-Zeliger, Y. Antebi, G. Aidelberg, N. Waysbort, and N. Friedman, "Monitoring the dynamics of primary T cell activation and differentiation using long term live cell imaging in microwell arrays," *Lab Chip,* vol. 12, pp. 5007-5015, 2012.

[148] A. Weltin, K. Slotwinski, J. Kieninger, I. Moser, G. Jobst, M. Wego, R. Ehret, and G. A. Urban, "Cell culture monitoring for drug screening and cancer research: a transparent, microfluidic, multi-sensor microsystem," *Lab Chip,* vol. 14, pp. 138-146, 2014.

[149] L. G. Griffith and M. A. Swartz, "Capturing complex 3D tissue physiology in vitro," *Nature Reviews Molecular Cell Biology,* vol. 7, pp. 211-224, 2006.

[150] M. Markaki and N. Tavernarakis, "Modeling human diseases in Caenorhabditis elegans," *Biotechnology Journal,* vol. 5, pp. 1261-1276, 2010.

[151] Q. Wen, M. D. Po, E. Hulme, S. Chen, X. Y. Liu, S. W. Kwok, M. Gershow, A. M. Leifer, V. Butler, C. Fang-Yen, T. Kawano, W. R. Schafer, G. Whitesides, M. Wyart, D. B. Chklovskii, M. Zhen, and A. D. T. Samuel, "Proprioceptive Coupling within Motor Neurons Drives C. elegans Forward Locomotion," *Neuron,* vol. 76, pp. 750-761, 2012.

[152] T. V. Chokshi, D. Bazopoulou, and N. Chronis, "An automated microfluidic platform for calcium imaging of chemosensory neurons in Caenorhabditis elegans," *Lab Chip,* vol. 10, pp. 2758-2763, 2010.

[153] Y. Zhang, H. Lu, and C. I. Bargmann, "Pathogenic bacteria induce aversive olfactory learning in Caenorhabditis elegans," *Nature,* vol. 438, pp. 179-184, 2005.

[154] X. C. I. Solvas, F. M. Geier, A. M. Leroi, J. G. Bundy, J. B. Edel, and A. J. deMello, "High-throughput age synchronisation of Caenorhabditis elegans," *Chemical Communications,* vol. 47, pp. 9801-9803, 2011.

[155] C. L. Gilleland, C. B. Rohde, F. Zeng, and M. F. Yanik, "Microfluidic immobilization of physiologically active Caenorhabditis elegans," *Nat Protoc,* vol. 5, pp. 1888-1902, 2010.

[156] J. Krajniak, Y. Hao, H. Y. Mak, and H. Lu, "CLIP-continuous live imaging platform for direct observation of C. elegans physiological processes," *Lab on a Chip,* vol. 13, pp. 2963-2971, 2013.

[157] M. M. Crane, J. N. Stirman, C. Y. Ou, P. T. Kurshan, J. M. Rehg, K. Shen, and H. Lu, "Autonomous screening of C-elegans identifies genes implicated in synaptogenesis," *Nature Methods,* vol. 9, pp. 977-+, 2012.

[158] S. E. Hulme, S. S. Shevkoplyas, J. Apfeld, W. Fontana, and G. M. Whitesides, "A microfabricated array of clamps for immobilizing and imaging C-elegans," *Lab Chip,* vol. 7, pp. 1515-1523, 2007.

[159] D. B. Weibel, M. Kruithof, S. Potenta, S. K. Sia, A. Lee, and G. M. Whitesides, "Torque-actuated valves for microfluidics," *Analytical Chemistry,* vol. 77, pp. 4726-4733, 2005.

[160] J. Clausell-Tormos, D. Lieber, J. C. Baret, A. El-Harrak, O. J. Miller, L. Frenz, J. Blouwolff, K. J. Humphry, S. Koster, H. Duan, C. Holtze, D. A. Weitz, A. D. Griffiths, and C. A. Merten, "Droplet-based microfluidic platforms for the encapsulation and screening of mammalian cells and multicellular organisms," *Chemistry & Biology,* vol. 15, pp. 427-437, 2008.

[161] W. W. Shi, J. H. Qin, N. N. Ye, and B. C. Lin, "Droplet-based microfluidic system for individual Caenorhabditis elegans assay," *Lab Chip,* vol. 8, pp. 1432-1435, 2008.

[162] K. Chung, M. Zhan, J. Srinivasan, P. W. Sternberg, E. Gong, F. C. Schroeder, and H. Lu, "Microfluidic chamber arrays for whole-organism behavior-based chemical screening," *Lab Chip,* vol. 11, pp. 3689-3697, 2011.

[163] M. Cornaglia, L. Mouchiroud, A. Marette, S. Narasimhan, T. Lehnert, V. Jovaisaite, J. Auwerx, and M. A. M. Gijs, "An automated microfluidic platform for C-elegans embryo arraying, phenotyping, and long-term live imaging," *Scientific Reports,* vol. 5, 2015.

[164] N. Chronis, M. Zimmer, and C. I. Bargmann, "Microfluidics for in vivo imaging of neuronal and behavioral activity in Caenorhabditis elegans," *Nature Methods,* vol. 4, pp. 727-731, 2007.

[165] F. Zeng, C. B. Rohde, and M. F. Yanik, "Sub-cellular precision on-chip small-animal immobilization, multi-photon imaging and femtosecond-laser manipulation," *Lab Chip,* vol. 8, pp. 653-656, 2008.

[166] T. V. Chokshi, A. Ben-Yakar, and N. Chronis, "CO2 and compressive immobilization of C. elegans on-chip," *Lab Chip,* vol. 9, pp. 151-157, 2009.

[167] P. Rezai, A. Siddiqui, P. R. Selvaganapathy, and B. P. Gupta, "Behavior of Caenorhabditis elegans in alternating electric field and its application to their localization and control," *Applied Physics Letters,* vol. 96, 2010.

[168] X. Y. Ding, S. C. S. Lin, B. Kiraly, H. J. Yue, S. X. Li, I. K. Chiang, J. J. Shi, S. J. Benkovic, and T. J. Huang, "On-chip manipulation of single microparticles, cells, and organisms using surface acoustic waves," *Proceedings of the National Academy of Sciences of the United States of America,* vol. 109, pp. 11105-11109, 2012.

[169] J. Krajniak and H. Lu, "Long-term high-resolution imaging and culture of C. elegans in chip-gel hybrid microfluidic device for developmental studies," *Lab on a Chip,* vol. 10, pp. 1862-1868, 2010.

[170] S. Lockery, "Channeling the worm: microfluidic devices for nematode neurobiology," *Nature Methods,* vol. 4, pp. 691-692, 2007.

[171] A. Kunze, S. Lengacher, E. Dirren, P. Aebischer, P. J. Magistretti, and P. Renaud, "Astrocyte-neuron co-culture on microchips based on the model of SOD mutation to mimic ALS," *Integrative Biology,* vol. 5, pp. 964-975, 2013.

[172] S. H. Choi, Y. H. Kim, M. Hebisch, C. Sliwinski, S. Lee, C. D'Avanzo, H. C. Chen, B. Hooli, C. Asselin, J. Muffat, J. B. Klee, C. Zhang, B. J. Wainger, M. Peitz, D. M. Kovacs, C. J. Woolf, S. L. Wagner, R. E. Tanzi, and D. Y. Kim, "A three-dimensional human neural cell culture model of Alzheimer's disease," *Nature,* vol. 515, pp. 274-U293, 2014.

[173] J. Li and W. Le, "Modeling neurodegenerative diseases in Caenorhabditis elegans," *Exp Neurol,* vol. 250, pp. 94-103, 2013.

[174] C. H. Lai, C. Y. Chou, L. Y. Ch'ang, C. S. Liu, and W. C. Lin, "Identification of novel human genes evolutionarily conserved in Caenorhabditis elegans by comparative proteomics," *Genome Research,* vol. 10, pp. 703-713, 2000.

[175] C. I. Nussbaum-Krammer and R. I. Morimoto, "Caenorhabditis elegans as a model system for studying non-cell-autonomous mechanisms in protein-misfolding diseases," *Dis Model Mech,* vol. 7, pp. 31-39, 2014.

[176] M. Zimmer, J. M. Gray, N. Pokala, A. J. Chang, D. S. Karow, M. A. Marletta, M. L. Hudson, D. B. Morton, N. Chronis, and C. I. Bargmann, "Neurons Detect Increases and Decreases in Oxygen Levels Using Distinct Guanylate Cyclases," *Neuron,* vol. 61, pp. 865-879, 2009.

[177] S. H. Chalasani, N. Chronis, M. Tsunozaki, J. M. Gray, D. Ramot, M. B. Goodman, and C. I. Bargmann, "Dissecting a circuit for olfactory behaviour in Caenorhabditis elegans," *Nature,* vol. 450, pp. 63-+, 2007.

[178] J. H. Qin and A. R. Wheeler, "Maze exploration and learning in C-elegans," *Lab Chip,* vol. 7, pp. 186-192, 2007.

[179] H. Ma, L. Jiang, W. W. Shi, J. H. Qin, and B. C. Lin, "A programmable microvalve-based microfluidic array for characterization of neurotoxin-induced responses of individual C. elegans," *Biomicrofluidics,* vol. 3, 2009.

[180] S. R. Lockery, S. E. Hulme, W. M. Roberts, K. J. Robinson, A. Laromaine, T. H. Lindsay, G. M. Whitesides, and J. C. Weeks, "A microfluidic device for whole-animal drug screening using

electrophysiological measures in the nematode C. elegans," *Lab Chip,* vol. 12, pp. 2211-2220, 2012.

[181] S. X. Guo, F. Bourgeois, T. Chokshi, N. J. Durr, M. A. Hilliard, N. Chronis, and A. Ben-Yakar, "Femtosecond laser nanoaxotomy lab-on-achip for in vivo nerve regeneration studies," *Nature Methods,* vol. 5, pp. 531-533, 2008.

[182] C. Samara, C. B. Rohde, C. L. Gilleland, S. Norton, S. J. Haggarty, and M. F. Yanik, "Large-scale in vivo femtosecond laser neurosurgery screen reveals small-molecule enhancer of regeneration," *Proceedings of the National Academy of Sciences of the United States of America,* vol. 107, pp. 18342-18347, 2010.

[183] I. D. Caceres, N. Valmas, M. A. Hilliard, and H. Lu, "Laterally Orienting C. elegans Using Geometry at Microscale for High-Throughput Visual Screens in Neurodegeneration and Neuronal Development Studies," *PLoS One,* vol. 7, 2012.

[184] C. B. Rohde and M. F. Yanik, "Subcellular in vivo time-lapse imaging and optical manipulation of Caenorhabditis elegans in standard multiwell plates," *Nature Communications,* vol. 2, 2011.

[185] X. N. Shen and P. E. Arratia, "Undulatory Swimming in Viscoelastic Fluids," *Physical Review Letters,* vol. 106, 2011.

[186] M. C. Kiernan, S. Vucic, B. C. Cheah, M. R. Turner, A. Eisen, O. Hardiman, J. R. Burrell, and M. C. Zoing, "Amyotrophic lateral sclerosis," *Lancet,* vol. 377, pp. 942-55, 2011.

[187] M. C. Kiernan, "ALS and neuromuscular disease: in search of the Holy Grail," *Lancet Neurol,* vol. 13, pp. 13-4, 2014.

[188] P. A. Jonsson, K. Ernhill, P. M. Andersen, D. Bergemalm, T. Brannstrom, O. Gredal, P. Nilsson, and S. L. Marklund, "Minute quantities of misfolded mutant superoxide dismutase-1 cause amyotrophic lateral sclerosis," *Brain,* vol. 127, pp. 73-88, 2004.

[189] R. Rakhit, J. Robertson, C. Vande Velde, P. Horne, D. M. Ruth, J. Griffin, D. W. Cleveland, N. R. Cashman, and A. Chakrabartty, "An immunological epitope selective for pathological monomer-misfolded SOD1 in ALS," *Nature Medicine,* vol. 13, pp. 754-9, 2007.

[190] A. J. Pratt, D. S. Shin, G. E. Merz, R. P. Rambo, W. A. Lancaster, K. N. Dyer, P. P. Borbat, F. L. Poole, 2nd, M. W. Adams, J. H. Freed, B. R. Crane, J. A. Tainer, and E. D. Getzoff, "Aggregation propensities of superoxide dismutase G93 hotspot mutants mirror ALS clinical phenotypes," *Proc Natl Acad Sci U S A,* vol. 111, pp. E4568-76, 2014.

[191] T. Gidalevitz, T. Krupinski, S. Garcia, and R. I. Morimoto, "Destabilizing protein polymorphisms in the genetic background direct phenotypic expression of mutant SOD1 toxicity," *PLoS Genet,* vol. 5, p. e1000399, 2009.

[192] G. Riboldi, M. Nizzardo, C. Simone, M. Falcone, N. Bresolin, G. P. Comi, and S. Corti, "ALS genetic modifiers that increase survival of SOD1 mice and are suitable for therapeutic development," *Progress in Neurobiology,* vol. 95, pp. 133-148, 2011.